FLOW, SEDIMENT TRANSPORT AND BEDFORMS UNDER COMBINED FLOWS

BY

MAURICIO M. PERILLO

DISSERTATION

Submitted in partial fulfillment of the requirements
for the degree of Doctor of Philosophy in Geology
in the Graduate College of the
University of Illinois at Urbana-Champaign, 2013

Urbana, Illinois

Doctoral Committee:

Professor James L. Best, Chair and Director of Research
Professor Marcelo H. Garcia, Co-Director of Research
Professor Jaco H. Baas, Bangor University, UK
Professor Gary Parker

Abstract

Combined flow, which refers to a combination of unidirectional and wave-induced oscillatory flows, is omnipresent in natural environments and generates a range of bedforms on sandy beds. Combined-flow bedforms are abundant in coastal and lacustrine environments, as well as in their ancient counterparts in the rock record. However, few experimental studies have focused on the relationship between the morphology and formative hydraulic conditions of combined-flow bedforms. There is thus a wide range of unexplored stability conditions for such bedforms, especially with intermediate oscillation periods. The aim of this research is to undertake new experimental work in the Large Oscillatory Water-Sediment Tunnel (LOWST) in order to address this gap in knowledge. The LOWST has a test section 12.5 m long, 0.8 m wide and 1.2 m high, with the oscillatory motion generated by three pistons. Unidirectional currents were superimposed on these water oscillations using two centrifugal pumps. Fifty-five experiments were conducted in the LOWST, both with and without an initially flattened bed. Bedform development in a 250 μm diameter sand bed was studied under pure oscillatory and combined flow conditions with oscillation periods of 4, 5 and 6 s. The maximum orbital velocity (U_o) was varied from 0.10 to 0.70 $m\,s^{-1}$ while the unidirectional component (U_u) was varied from 0 to 0.50 $m\,s^{-1}$.

This thesis presents new experimental data on bedform initiation and development under unidirectional, oscillatory and, more extensively, under combined flows. In particular, this study was able to populate zones of the *Terra incognita* region previously defined in the literature (Southard, 1991). In this thesis, the stable bedform configurations under a diverse range of flow conditions were studied and divided into *no motion (NM), 2D symmetric rip-*

ples (SR), 3D symmetric ripples (SR), 3D symmetric dunes (SR), 3D asymmetric ripples (AR), 3D quasi-asymmetric ripples (QAR), 3D asymmetric dunes (AD), 3D current ripples (CR), 3D current dunes (CD) and *upper-stage plane bed (USPB)*. Each of these bedform stages was described, characterized and reproduced in dimensional and dimensionless phase diagrams. A complete re-evaluation of the nomenclature for combined flow bedforms is proposed, which includes their planform and cross-sectional geometries in order to better represent the bed morphologies. This new nomenclature was carefully selected in order to integrate the bedform studies both in the unidirectional and oscillatory flow literature. One of the main changes that allows the integration with the nomenclature used in unidirectional flows is the reclassification of large ripples as dunes. Additionally, the introduction of the planform and cross-sectional geometries as properties to classify bedforms leads to the definition of a stable phase space for two-dimensional symmetrical ripples and three-dimensional quasi-asymmetrical ripples. Furthermore, the experimental data collected under unidirectional flows larger than 0.30 $m\,s^{-1}$ allows expansion of the current understanding of the bed configurations within the *Terra Incognita* zone (Southard, 1991), where the phase boundary between combined flow bedforms and current ripples was uncertain. Based on dimensionless analysis, the oscillatory and unidirectional mobility numbers were used to represent the dimensionless phase diagram under combined flows. This set of dimensionless numbers provides a better representation than previous studies that use a friction factor to compute the Shields number. In addition, a quantitative analysis of the bedform cross-sectional geometries has allowed development of new bedform shape predictors based on the formative flow and sediment transport conditions. Moreover, based on the bedform initiation and development experiments, it was concluded that the genesis and growth processes are unique for all types of flows. This result was reflected in the same geometric pattern and development-path of bedforms regardless of the flow conditions. Furthermore, the development-path or bedform growth exhibit the same general trend for different bedform size (e.g., ripples vs dunes), bedform shape (e.g., symmetric or rounded), bedform planform geometry (e.g., 2D

vs 3D) and sediment grain sizes. The development of bed defects during the genesis of bedforms shows a strong relationship with the direction and magnitude of the bed shear stress throughout the oscillation. In conditions with a symmetric bed shear stress, the defects grew and propagated symmetrically, whereas when the bed shear stress was asymmetric, the defects grew and propagated with a predominant downstream direction. Furthermore, for the case of current-dominated combined flow, the maximum upstream bed shear stress was not large enough to entrain sediment in the upstream direction, resulting in solely downstream migration transport. Bedform development was divided and characterized into four main stages: (1) incipient bedforms, (2) growing bedforms, (3) stabilizing bedforms, and (4) fully-developed bedforms, consistent with the scheme proposed by Baas (1994, 1999) for pure unidirectional flows. Finally, a probabilistic model based on the cross-sectional bedform geometries is proposed in order to differentiate between unidirectional, oscillatory and combined flows from their preserved strata. This probabilistic model provides a significant improvement on the present tools to differentiate bedforms in the modern and ancient record.

10 mil km de amor...

Acknowledgments

This dissertation would not have been accomplished without the support of several people. First and foremost I want to thank my advisors Jim Best and Marcelo García whose support and advice allowed me to begin, do and complete this work. Both of them in different ways, and in their particular times and manners helped me in each step of this adventure of becoming a doctorate in Geology. I also want to thank the rest of my PhD committee members, Gary Parker and Jaco H. Baas, for their willingness to sit and chat multiple times to review and evaluate my work. In particular, I want to thank the large effort that Prof. Parker did in enriching my knowledge of stand-up comedy, an asset that will be definitely of great use in the near future. I wish to make a special distinction to John Southard, who not only inspired me by his seminal work, but also by the time he invested in me during the many times we met. Prof. Miwa Yokokawa, Prof. Tomohiro Sekiguchi and Dr. Tomohiro Takagawa deserve an special distinction as well, since they not only helped a lot during the first stages of experimentation, but also became amazing colleagues and good friends. I want to acknowledge the contributions of Diego Margot, as his insights on multinomial logistic regression made a huge difference in Chapter 8. I acknowledge Prof. Bruce Fouke, Prof. Susan Kieffer and Prof. Bruce Rhoads for their insights, assistance, and invaluable contributions to this work. Also, I want to thank my friends Eric Prokocki and Frank Engel for countless hours of discussions, I never knew one topic of conversation could last so many years!. In the same way, the experimental work conducted at the Large Oscillating Water-Sediment Tunnel would not have been possible without the help of Dr. Francisco Pedocchi, whose early contribution to this work made a huge impact in the way the

experiments were conducted. Finally, I am very grateful to all the present and past students, staff and colleagues that helped me in many ways. Luckily for me, the list of people is huge, but I do not want to miss Lori Baker, Dr. Gianluca Blois, Alexander Bryk, Ron Cash, Shelley Campbell, Dr. Yovanni Catano, Scott David, Julie Dyar, Dr. Anjali Fernandes, Dr. Duncan Keenan-Jones, Dr. Blake Landry, Dr. Suzanne Leclair, Dr. Ezequiel Martin, Raleigh Martin, Jose M. Mier, Prof. Sara Mclafferty, Dr. Jeff Nittrouer, Dr. Eduardo Puhl, Nils Oberg, Dr. Rob Sanford, Domenico Santoro, Dr. Octavio Sequeiros, Travis Swanson, Erik van Dusen, Prof. Jeremy Venditti, Andrew Waratuke, Marilyn Whalen and Jessica Zinger. Financial support was provided through research and teaching assistantships thanks to Jim Best and the Dept of Geology. The Large Oscillating Water-Sediment Tunnel was built with support from the DURIP Program ONR Grant No. N00014-01-1-0540. In addition, the completion of my thesis was made possible by the Leighton Graduate Student Research Award, established and supported by Dr. Morris W. Leighton.

My family provided unfailing support. There is not enough space to adequately express my gratitude to my wife Luján, none of this was possible without her. To my family in Argentina, Dad, Mom and Vanesa... skype every Sunday for the last five years, millions of emails and phone calls made it like there was no distance between us, I will always be thankful for everything.

Table of Contents

List of Tables

List of Figures

List of Abbreviations

mADV	micro Acoustic Doppler Velocimeter
BI	Bedform Index
BSI	Bedform Symmetry Index
BRI	Bedform Roundness Index
FFT	Fast Fourier Transform
LBL	Laminar Boundary Layer
LOWST	Large Oscillatory Water Sediment Tunnel
RI	Ripple Index
RSI	Ripple Symmetry Index
RRI	Ripple Roundness Index
SFD	Sedimentological Fluid Dynamics
SLR	Single-Lens Reflex
TBL	Turbulent Boundary Layer
UVDP	Ultrasonic Doppler Velocity Profiler

List of Symbols

β	$1/\delta_w$ $[m^{-1}]$
β_{bf}	Bedform Shape Factor $[\beta_{bf} = A_{bf}/\eta\,\lambda]$
δ	Boundary Layer Thickness $[m]$
$\dot{\delta}$	Displacement Thickness $[m]$
δ_ν	Viscous Sublayer Thickness $[m]$
δ_w	Stokes Length or Wave Boundary Layer Thickness $[m]$
δ_{cw}	Combined Flow Boundary Layer Thickness $[m]$
ϵ	Eddy Viscosity $[kg\,m^{-1}s^{-1}$ or $Pa\,s]$
φ	Critical Angle of Sediment Repose $\varphi \approx 32°$ $[°]$
γ	Angle between the Waves and the Current $[°]$
η	Bedform Height $[m]$
η_e	Bedform Height at Bed-Flow Equilibrium $[m]$
η_t	Bedform Height at Time T $[m]$
κ	von Kármán Constant ($\kappa = 0.4$)
λ_η	Bedform Wavelength $[m]$
λ_e	Bedform Wavelength at Bed-Flow Equilibrium $[m]$
λ_p	Bed Porosity $[\lambda_p \approx 0.3]$
λ_t	Bedform Wavelength at Time T $[m]$
λ_w	Wave Wavelength $[m]$
λ_{ci}	Turbulent Swirling Strength

μ	Dynamic Viscosity $[kg\,m^{-1}s^{-1}$ or $Pa\,s]$
ν	Kinematic Viscosity $[m^2\,s^{-1}]$
θ	Dimensionless Shear Stress or Shields Number
ρ	Fluid Density $[kg\,m^{-3}]$
ρ_s	Sediment Density $[kg\,m^{-3}]$
τ	Fluid Shear Stress $[kg\,m^{-1}s^{-2}$ or $Pa]$
τ_0	Bed Shear Stress $[kg\,m^{-1}s^{-2}$ or $Pa]$
$\tau^{(\nu)}$	Viscous Shear Stress $[kg\,m^{-1}s^{-2}$ or $Pa]$
$\tau^{(R)}$	Turbulent Shear $[kg\,m^{-1}s^{-2}$ or $Pa]$
ω	Angular Frequency $[s^{-1}]$
ω_s	Settling Velocity $[m\,s^{-1}]$
ψ	Mobility Number
ψ_c	Current Mobility Number
ψ_w	Wave Mobility Number
A	Wave Amplitude $[m]$
A_{bf}	Bedform Cross-sectional Area $[m^2]$
c_η	Height Adaptation Constant $[hr^{-1}]$
c_λ	Wavelength Adaptation Constant $[hr^{-1}]$
C_{bf}	Instantaneous Bedform Celerity $[m\,s^{-1}]$
$\overline{C_{bf}}$	Mean Bedform Celerity $[m\,s^{-1}]$
C_D	Drag Coefficient
C_z	Chezy Coefficient
d_0	Wave Orbital Diameter [m]
D_{50}	Median Grain Size $[m]$
D_*	Dimensionless Grain Size $[D_* = Re_p^{2/3}]$
$\mathbf{f}$	Body Forces in Navier-Stokes Equation
f	Instrument Sampling Frequency $[Hz]$

f_{DW}	Darcy-Weisbach resistance Coefficient
g	Gravitational Acceleration $[m\,s^{-2}]$
h	Water Depth $[m]$
k_s	Bed/Nikuradse Roughness Length $[m]$
n	Gauckler-Manning-Strickler Coefficient $[m^{1/3}\,s^{-1}]$
p	Fluid Pressure $[kg\,m^{-1}s^{-2}$ or $Pa]$
q_s	Bedload Transport per unit Width $[cm^2\,s^{-1}]$
R	Submerged Specific Density $[R = \rho_s/\rho - 1]$
R^2	Square of the Sample Correlation Coefficient
Re	Reynolds Number
Re_w	Wave Reynolds Number
Re_p	Particle Reynolds Number
Re_*	Roughness Reynolds Number
Rep	Dimensionless Grain Size
t	Time $[hr$ to $s]$
t_e	Time until Flow-Bedform Equilibrium $[hr]$
t_f	Duration of Experiment or Total/Final Time$[hr]$
T	Oscillation Period $[s]$
$\mathbf{u}$	Fluid Velocity Vectorial Form $[m\,s^{-1}]$
u	Streamwise Fluid Velocity $[m\,s^{-1}]$
$\overline{u}$	Mean Streamwise Fluid Velocity $[m\,s^{-1}]$
u'	Streamwise Turbulent Fluctuations $[m\,s^{-1}]$
$\sqrt{\overline{u'^2}}$	Mean Streamwise Turbulent Fluctuations $[m\,s^{-1}]$
u_*	Friction or Shear Velocity $[m\,s^{-1}]$
$\hat{u}_*$	Maximum Value of the Shear Velocity $[m\,s^{-1}]$
u^+	Streamwise Fluid Velocity made Dimensionless with the Shear Velocity

U_1	Streamwise Outer Edge Boundary Layer Velocity $[m\,s^{-1}]$
U_o	Maximum Orbital Velocity $[m\,s^{-1}]$
U_u	Mean Free Flow Unidirectional or Current Velocity $[m\,s^{-1}]$
v	Transverse Fluid Velocity $[m\,s^{-1}]$
$\overline{v}$	Mean Transverse Fluid Velocity $[m\,s^{-1}]$
v'	Transverse Turbulent Fluctuations $[m\,s^{-1}]$
$\sqrt{\overline{v'^2}}$	Mean Transverse Turbulent Fluctuations $[m\,s^{-1}]$
w	Vertical Fluid Velocity $[m\,s^{-1}]$
$\overline{w}$	Mean Vertical Fluid Velocity $[m\,s^{-1}]$
w'	Vertical Turbulent Fluctuations $[m\,s^{-1}]$
$\sqrt{\overline{w'^2}}$	Mean Vertical Turbulent Fluctuations $[m\,s^{-1}]$
W	Wake Function
W_0	Coles Wake Parameter
z^+	Dimensionless Wall Distance
z_0	Non-zero Constant in Log-Law Velocity Distribution $[m]$

Chapter 1

Introduction

Coastal areas are zones of major economic importance since harbors, seaside resorts, marinas and offshore constructions like pipelines, wind farms and oil platforms are located in these regions. In addition, rapid population growth and tourism are increasing infrastructure near the shore, and thus efforts to ensure the safety of such structures and/or survival of ecosystems in such areas, are of great significance. All these activities require a better understanding of the physical processes occurring at the coast. Tides, waves, currents, and the combination of these flows, are periodic processes that interact with the shore. The most general distinction between these three characteristic flows is that waves and tides are oscillatory flows whereas currents are classified as unidirectional. Consequently, coastal environments are characterized by a combination of unidirectional and oscillatory flows, with the superimposition of an oscillatory flow upon a unidirectional flow being defined as a *combined flow* (Figure 1.1). Combined flows are of great interest in a wide range of disciplines (e.g. coastal engineering, sediment transport, construction, sedimentology and stratigraphy) since the complexity of the flow is key for understanding many sedimentary environments, such as estuaries, beaches, tidal flats, lakes and deltas. In most cases, tides may be considered as unidirectional flows of known directional change over time (except near the high and low water slack periods). Such a statement holds since the period of the tides (≈ 44000 s) is more than three orders of magnitude longer than waves, even for waves generated by open-ocean storm conditions where the period may be ≈ 25 s. Such a distinction is important, not only to define the extent of oscillatory periods that are characteristic of the environment, but also to consider the range of angles between the waves and currents.

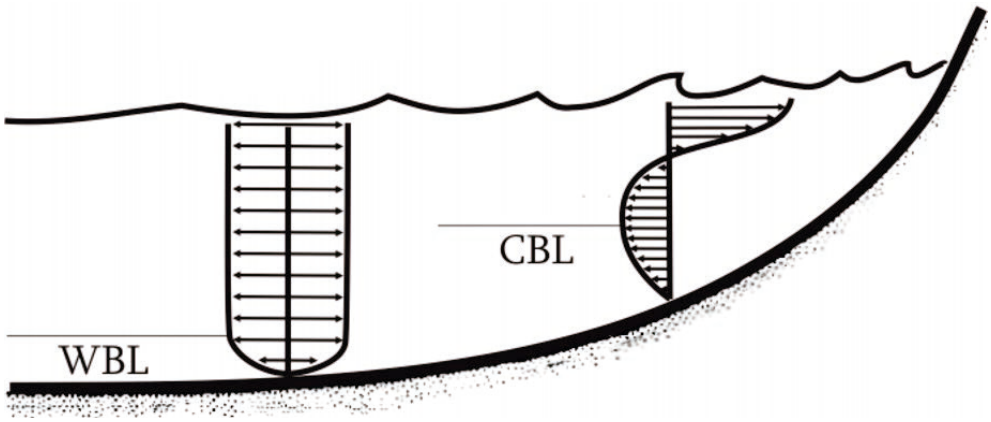

Figure 1.1: Shoreline profile with the action of combined flows. WBL and CBL denote the Wave and Current Boundary Layer respectively. After Duke (1990).

However, it is important to account for a change in flow orientation, since that reversal is crucial in many sedimentological reconstructions.

Morphodynamic systems can be represented as a coupling between flow, sediment transport and bed morphology. Spatial and temporal changes in flow conditions, sediment characteristics, sediment transport, linear and non-linear mechanisms, and large and small-scale changes in bed topography can be summarized in three main interlinked areas; fluid, sediment transport and bed morphology. Hence, all the processes linking flow, sediment transport and bedform development define the sedimentological fluid dynamic (SFD) "trinity" (Figure 1.2).

In the context of any morphodynamic system, all components of the SFD "trinity"are connected with the others.Water in motion develops turbulent sweeps and bursts that entrain sediment in movement (Heathershaw and Thorne, 1985; Lapointe, 1992; Cao, 1997; Niño et al., 2003) and generates differential transport of grains, these areas of erosion and accumulation leading to development of a bedform. Bedforms change the flow and turbulence characteristics, inducing a new condition for transport, which will modify the original bedforms. This is just one example of the many feedback loops that are continually occurring in the vicinity of the bed.

Many of the interactions between the elements in the SFD "trinity"are inherently non-

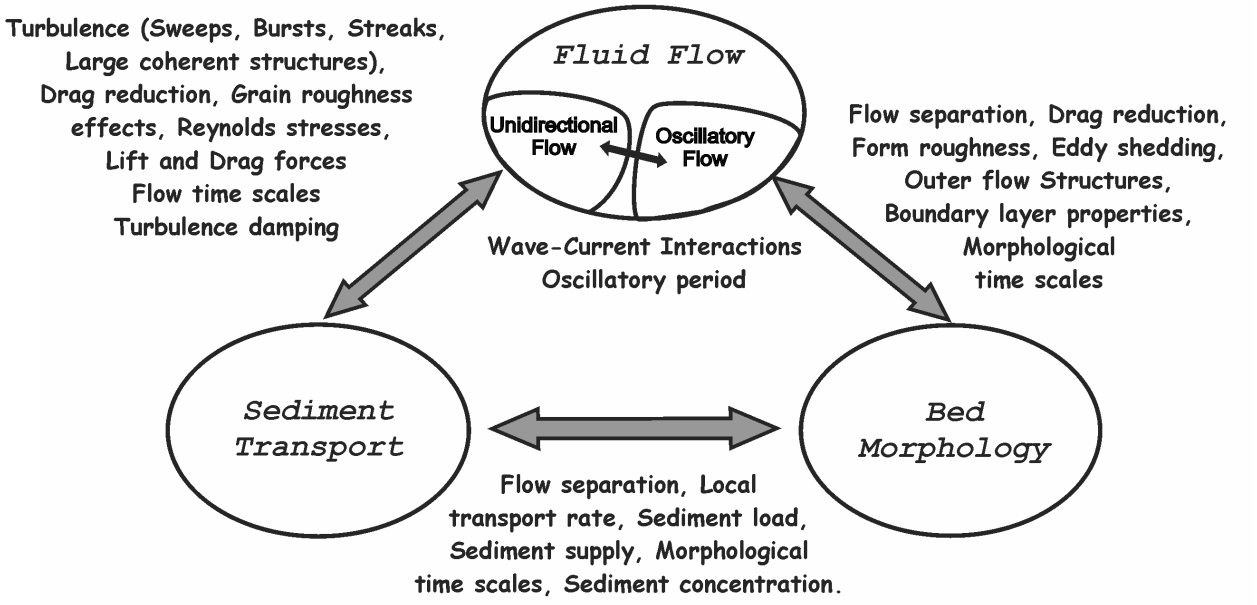

Figure 1.2: Inter-relationships and feedbacks between the elements of the SFD "trinity" for the case of combined flows. Modified after Leeder (1983) and Best (1993) .

linear and time-dependent. This temporal dependence not only needs to take into account the fact that the conditions of the SFD "trinity" change over time, but also that there may be a lag between a change in one variable and the response of the system or hysteresis. In other words, the different components of the SFD "trinity" have a particular time-scale within which they react to changes. In the case of combined flows, the presence of an oscillatory flow introduces a regular, but dynamically changing, time scale, to which each element of the SFD "trinity" needs to adjust. These dynamics are reflected in the presence of two boundary layers, one due to waves and the other due to the current alone (Mathisen and Madsen, 1996a,b, 1999; Fredsøe et al., 1999). The boundary layer formed by wave-current interactions is relatively thin and behaves as an additional roughness to the overall unidirectional current. However, within the wave-current boundary layer, which is the closest to the bed, the flow changes with the oscillation cycle producing characteristic sedimentary features associated with the combined flow condition.

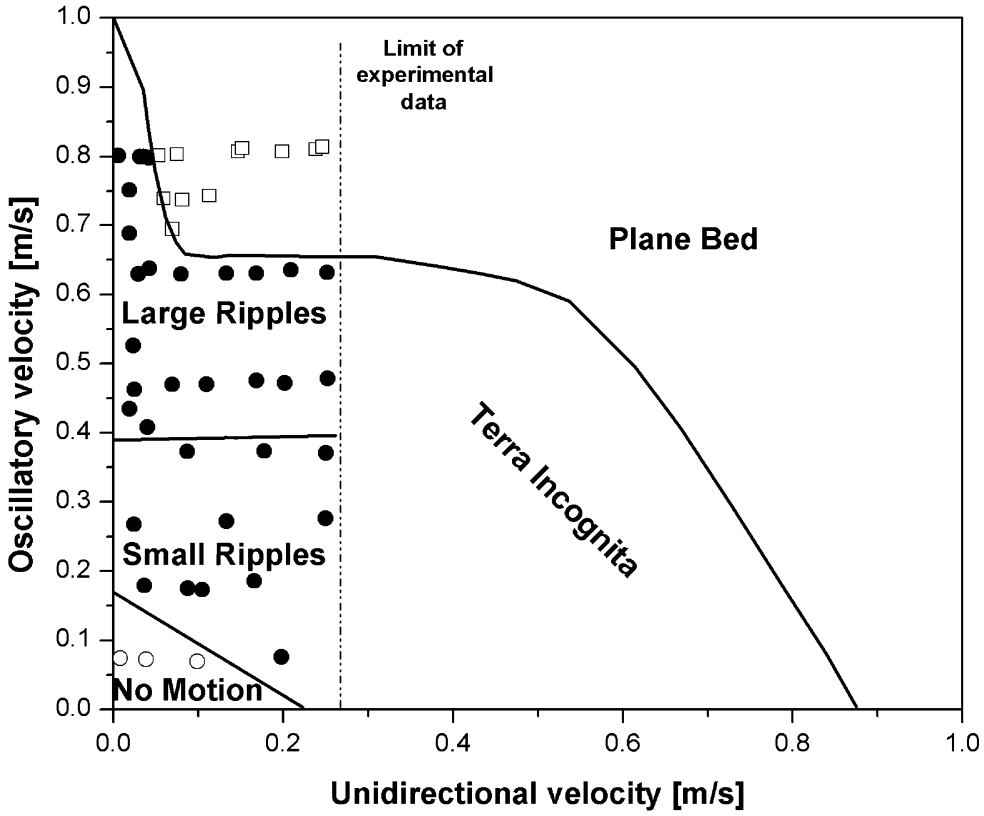

Figure 1.3: Combined flow phase diagram. Experimental data for a grain diameter of 0.09 mmand a wave period of 8.5 s from Arnott and Southard (1990). Terra incognita is an area of no experimental data.

Some work has been conducted in the study of bedforms at a range of relatively short oscillation periods and low unidirectional flow velocities (Inman and Bowen, 1963; Harms, 1969; Brevik and Bjørn, 1979; Brevik, 1980; Arnott and Southard, 1990; Southard et al., 1990; Yokokawa, 1995; Dumas et al., 2005; Sekiguchi and Yokokawa, 2008). The laboratory data set from Arnott and Southard (1990) is summarized in Figure 1.3, where the unidirectional velocity ranges from 0 to 0.26 ms^{-1} and the oscillatory component varies from 0 to 0.8 ms^{-1}. Figure 1.3 is a phase, or stability diagram that shows the regimes of existence of one or more stable bed states. The stability of the bed can be defined when the bedform is in equilibrium and does not change in time for the same flow condition. This invariance over time must not be confused with a static morphology or frozen equilibrium; on the contrary, the bed moves and adjusts in a dynamic equilibrium with the flow and the sediment transport for

that particular condition. Despite the work of Arnott and Southard (1990), Dumas et al. (2005) and Sekiguchi and Yokokawa (2008), the general understanding of bed morphology generated in combined flow is rather limited. There are still areas in the phase diagram in which there are no, or very few, data (Figure 1.3: *Terra incognita*).

Therefore, the aim of this thesis is to understand and characterize the bed morphology present in wave-current conditions, with special attention to the *Terra incognita* region. Thus, the thesis is divided into the following structure;

Chapter 2 briefly discusses our present knowledge on boundary layers for unidirectional, oscillatory and combined flows.

Chapter 3 briefly discusses our present knowledge of stable bed configurations for unidirectional, oscillatory and combined flows.

Chapter 4 describes the experimental facility used, the instrumentation employed and the data acquired and processed.

Chapter 5 illustrates the different bed morphologies for combined flows and proposes two new phase diagrams with dimensionless variables and dimensional units.

Chapter 6 analyzes the initiation of bedforms under combined flows. This study builds on previous work conducted under unidirectional and oscillatory flows.

Chapter 7 discusses the development of bedforms from flat bed to equilibrium conditions under pure oscillatory and combined flows. Relationships between the equilibrium time and planform geometry are established for equilibrium bed morphologies.

Chapter 8 examines the cross-sectional characteristics of the unidirectional, oscillatory and combined flow bedforms and establishes a probabilistic model to distinguish between them.

Chapter 9 concludes on the principal findings of the thesis and outlines areas of future research.

Chapter 2

SFD *trinity* : Fluid Flow

2.1 Unidirectional Flows

Unidirectional flows are flows moving in only one direction through space and time. These currents may be caused by tidal motions, density or pressure driven gradients, wind-stress or river flows that experience friction due to the bed roughness, resulting in the development of a boundary layer (Prandtl, 1904).

2.1.1 Unidirectional boundary layer

The velocity distribution within the boundary layer goes from zero at the bed to a maximum value at, or near, the water surface. This velocity profile can be decomposed into two main regions: the inner layer and outer layers (Fig. 2.1).

Inner layer

The inner layer was first described by Prandtl (1925) and is normally divided into three sublayers:

- *Viscous Sublayer*: a small layer very close to the bed that is mainly dominated by viscous forces. The flow can be characterized by

$$u^+ = z^+ \tag{2.1}$$

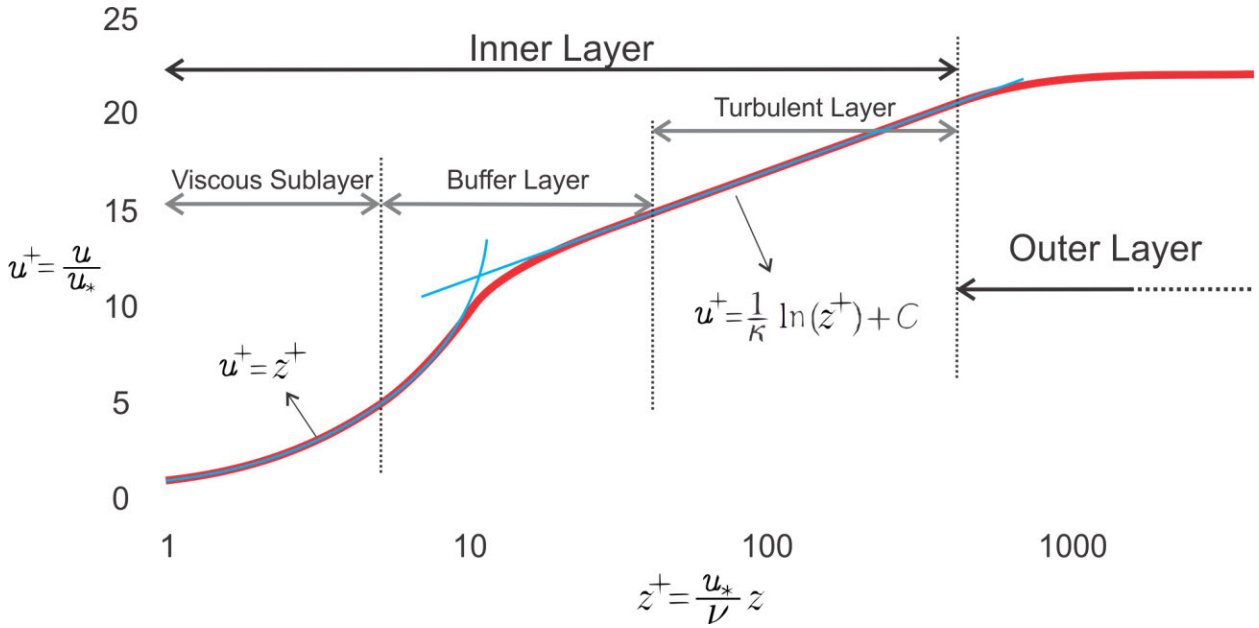

Figure 2.1: Theoretical velocity distribution for a unidirectional boundary layer

where u^+ is a dimensionless velocity defined as

$$u^+ = \frac{u}{u_*} \tag{2.2}$$

and z^+ is the dimensionless distance from the wall

$$z^+ = \frac{u_*}{\nu} z \tag{2.3}$$

The thickness of the viscous sublayer (δ_ν) is usually smaller than 5 dimensionless wall units ($z^+ < 5$) and is normally expressed as

$$\delta_\nu = 5\frac{\nu}{u_*} \tag{2.4}$$

where $u_* = \sqrt{\frac{\tau}{\rho}}$ is the shear velocity, ν is the kinematic viscosity, ρ is the fluid density and τ is the fluid shear stress. However, other researchers (e.g., García, 2008) define the viscous sublayer thickness at z^+ values smaller than 11.6. This difference arises

since the linear behavior can be observed in part of the buffer layer.

- *Transition Layer or Buffer Layer*: the name of this layer derives from the fact that the velocity profile in this region is transitional between two different behaviors, viscosity dominated in the viscous sublayer to turbulent in the turbulent layer (Fig. 2.1). The location of this layer is somewhat arbitrary but starts above the viscous sublayer ($z^+ > 5\frac{\nu}{u_*}$) and below the turbulent layer ($z^+ < 30$ or $z < 0.044\,U_1\,\dot{\delta}/u_*$), where U_1 is the velocity at the outer edge of the boundary layer, κ is the von Kármán constant and $\dot{\delta}$ is the displacement thickness defined as

$$\dot{\delta} = \int_0^\infty \left(1 - \frac{u}{U_1}\right) \mathrm{d}z \tag{2.5}$$

In order to obtain an analytical expression for the velocity distribution in this region, Clauser (1956) proposed a model that assumes that the mean flow is the same as a laminar flow, except that the kinematic viscosity should be replaced by an eddy viscosity (ϵ) in Newton's (1687) viscous stress (τ) formulation,

$$\tau = \epsilon\rho\frac{\partial\, u}{\partial\, z} \tag{2.6}$$

where ϵ changes in the vertical

$$\epsilon = \begin{cases} \nu & \text{if } 0 < z < 5\frac{\nu}{u_*} \\ \kappa\, u_*\, z & \text{if } 5\frac{\nu}{u_*} < z < 0.044\; U_1\,\dot{\delta}/u_* \\ 0.018\, U_1\,\dot{\delta} & \text{if } z > 0.044\, U_1\,\dot{\delta}/u_* \end{cases} \tag{2.7}$$

- *Turbulent Layer*: this was first outlined by Reynolds (1883) and later described by von Kármán (1930) using a logarithmic velocity profile

$$u^+ = \frac{1}{\kappa}\ln(z^+) + C = \frac{1}{\kappa}\ln\left(\frac{z}{z_0}\right) \tag{2.8}$$

where z_0 is a non-zero constant, whose magnitude depends on the bed roughness length (k_s) and the roughness Reynolds number $\left(Re_* = \frac{u_* \, k_s}{\nu}\right)$

$$z_0 = \begin{cases} \nu / 9 \, u_* & \text{if } \delta_\nu / k_s \ll 1 \text{ (hydraulically smooth beds)} \\ k_s / 30 & \text{if } \delta_\nu / k_s \gg 1 \text{ (hydraulically rough beds)} \end{cases}$$

The bed roughness length, or the Nikuradse equivalent sand-grain roughness (k_s), is often assumed to be proportional to a characteristic sediment size

$$k_s = \alpha_s \, D_x \tag{2.9}$$

Values of α_s can vary between $\alpha_s = 1$ to 6, and the sediment size can change between D_{35} to D_{90} depending on the characteristics of the system under study (e.g. van Rijn, 2006; García, 2008). Some of the most common expressions of Equation 2.9 are:

Meyer-Peter and Müller (1948)	$k_s = D_{90}$
van Rijn (1982)	$k_s = 3 \, D_{90}$
Ikeda (1983)	$k_s = 1.5 \, D_{84}$
García (2008)	$k_s = 2.5 \, D_{50}$

Alternatively, Christoffersen and Jonsson (1985) suggested a way to estimate z_0 as a function of k_s

$$z_0 = \frac{k_s}{30} \left(1 - e^{-u_* \, k_s / 27 \, \nu}\right) + \frac{\nu}{9 \, u_*} \tag{2.10}$$

A synthesized formulation of Equation 2.8 for all Re_* was proposed by Yalin (1992)

$$u^+ = \frac{1}{\kappa} \ln\left(\frac{z}{k_s}\right) + B_s$$

where B_s is a function of Re_*

$$B_s = 8.5 + (2.5 \ln[Re_*] - 3) \, e^{-0.121 \, (\ln[Re_*])^{2.42}}$$

Outer layer

Following the work of Prandtl, von Kármán (1930) described an area above the inner layer that is characterized by inviscid forces and where the velocity profile resembles a wall-free turbulent flow. Such a layer is generally termed the outer layer or wake layer. The logarithmic formulation presented in Equation 2.8 is commonly called the *law of the wall* and is a good approximation for the entire velocity profile - including the outer layer (Schlichting, 1979; Nezu and Rodi, 1986). However, if a more detailed description of the velocity profile is needed, especially in the outer layer, an additional term should be added to Equation 2.8

$$u^+ = \frac{1}{\kappa}\ln(z^+) + C + W\left(\frac{z}{h}\right) \tag{2.11}$$

where h is the water depth and W is the wake function defined by Coles (1956) as:

$$W\left(\frac{z}{h}\right) = \frac{2\,W_0}{\kappa}\sin^2\left(\frac{\pi}{2}\frac{z}{h}\right) \tag{2.12}$$

where W_0 is the Coles wake parameter which has a mean value of 0.2 for turbulent flows.

However, Gad el Hak and Bandyopadhyay (1994) proposed that the velocity profile has a dependence on the bed roughness and also that the structure of the velocity profile changes as a function of the Reynolds number. Moreover, Smits et al. (2011) suggested that the true mean velocity profile remains an open question and that the classical structure presented in Fig. 2.1 is a robust first-order representation.

2.1.2 Bed shear stress and Reynolds stresses

The effect of the no-slip condition is not only reflected by the development of a boundary layer, but also by the presence of a shear stress on that boundary. For a turbulent boundary

layer, the total shear-stress can be described by the sum of two terms:

$$\tau = \tau^{(\nu)} + \tau^{(R)} \tag{2.13}$$

the viscous shear stress

$$\tau^{(\nu)} = \mu \frac{\partial u}{\partial z} \tag{2.14}$$

and the turbulent stress

$$\tau^{(R)} = \rho \overline{u'w'} \tag{2.15}$$

where u' and w' are the fluctuations around the mean for the longitudinal and vertical velocities. The turbulent stress is also known as the *Reynolds Stress* and can be theoretically derived by using the Reynolds decomposition (Equation 2.16) of the Navier-Stokes equations,

$$u = \overline{u} + u' \tag{2.16}$$

where $\overline{u}$ denotes the time average of u,

$$\overline{u} = \int u \, \mathrm{d}t \tag{2.17}$$

and u' is the fluctuating part (or perturbations).

The bed shear stress (τ_0) can also be approximated by using the friction coefficient (C_f)

$$\tau_0 = \rho \, C_f \, \overline{U}^2 \tag{2.18}$$

where $\overline{U}$ is the depth-averaged current velocity and C_f is given by

$$C_f = \left[\frac{1}{\kappa} \ln \left(11 \frac{h}{k_s} \right) \right]^{-2} \tag{2.19}$$

or if Equation 2.8 is approximated by a power law

$$\frac{U}{u_*} = \frac{1}{\kappa} \ln\left(\frac{z}{z_0}\right) \approx 8.1 \left(\frac{h}{k_s}\right)^{1/6} \tag{2.20}$$

by

$$C_f = \left[8.1 \left(\frac{h}{k_s}\right)^{1/6}\right]^{-2} \tag{2.21}$$

Alternatively, several other coefficients can be used instead of C_f

$$C_f = \frac{f_{\text{DW}}}{8} = \frac{g}{C_z^2} = \frac{g\, n^2}{h^{1/3}} \tag{2.22}$$

where f_{DW} is the Darcy-Weisbach resistance coefficient, C_z is the Chezy coefficient, n is the Manning coefficient and g is acceleration due to gravity.

2.1.3 Coherent turbulent structures

Pioneering studies by Kline et al. (1967) provided the first evidence for well-organized spatially and temporally dependent structures within the "viscous sublayer". These motions lead to the formation of low-speed streaks that interact with the outer portions of the flow through a process of gradual 'lift-up', concluding in bursting, and ejection. Bursting is associated with the lifting and stretching of vortex loops (e.g. Christensen and Adrian, 2001) that occur in the steep velocity gradient that is immediately followed by violent mixing. On the other hand, the sweep is associated with the intensification of near-boundary vorticity by lateral spanwise stretching (Williams, 1996).

Fluid bursting and sweeping can be classified by quadrant analysis (Lu and Willmarth, 1973). Four quadrants can be defined based on the fluid motion relative to the mean flow: i) Quadrant 1 - inward interactions, ii) Quadrant 2 - ejections, iii) Quadrant 3 - outward interactions, and iv) Quadrant 4 - sweeps (Figure 2.2). Quadrant 2 and Quadrant 4 events have significant importance since they are the dominant contributors to the Reynolds stress

close to the bed (Willmarth and Lu, 1972).

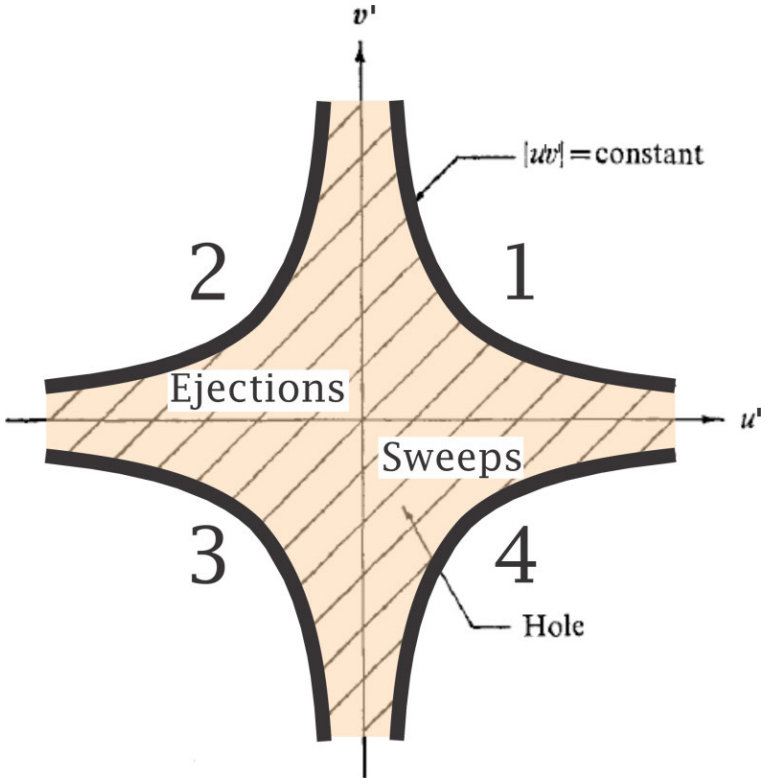

Figure 2.2: Quadrant analysis identifying turbulent bursts and sweeps. Modified from Lu and Willmarth (1973)

Contributions to the Reynolds stress from the four quadrants are computed from

$$\frac{\tilde{u'v'}(H_z)}{\overline{u'v'}} = \frac{1}{\overline{u'v'}} \lim_{T\to\infty} \frac{1}{T} \int_0^T u'v'(t) S_j(t,H) \mathrm{d}t \text{ for j = 1,2,3,4} \tag{2.23}$$

where the subscript j refers to the jth quadrant and

$$S_j(t,H) = \begin{cases} 1 & \text{if } |u'v'| > H_z \\ 0 & \text{otherwise} \end{cases}$$

where H_z is called the hole size and its function is to filter the small perturbations.

As the technology to quantify turbulence improved with time, the idea of an unmanageable fluid motion started to disappear (Cantwell, 1981). This stochastic fluid motion (bursting

and sweeping) with a complex multiscaled structure has a quasi-periodic repeating pattern of coherent motion, and this finding revolutionized studies of turbulent flows (Robinson, 1991). These temporal and spatial coherent structures (also called eddies, Adrian, 2007) can be viewed as individual entities that live long enough to contribute significantly to time-averaged statistics (e.g. turbulence kinetic energy, $\overline{u}$). Recent and ongoing studies of turbulence are providing new insights on the size, shape, energy, origin, stability, growth and development of these structures (e.g. Green et al., 2007; Willis and Kerswell, 2008; Hertwig et al., 2011). The quadrant analysis introduced earlier can be used to evaluate the mean values of several relevant quantities (e.g. turbulence kinetic energy, dissipation, Reynolds stresses) but does not provide any information on the form of such eddies or structures. Despite the initial lack of acceptance by the research community, the hairpin or horseshoe vortex described for the first time by Theodorsen (1952) became an elemental structure to study turbulent boundary layers (Zhou et al., 1999; Adrian, 2007). These structures have a hairpin shape inclined at approximately 45 degrees to the wall, with a pair of counter-rotating quasi-streamwise vortices near the wall (Figure 2.3, Robinson, 1991; Adrian, 2007). Theodorsen's (1952)

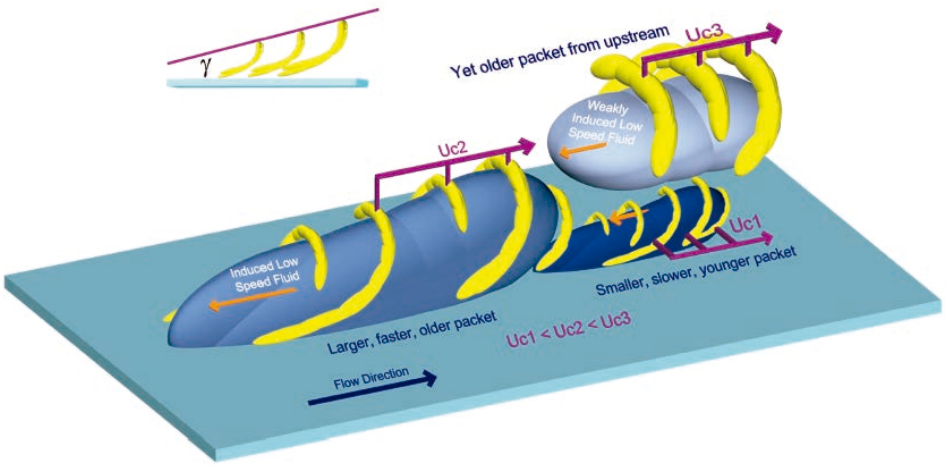

Figure 2.3: Idealized sketch of a set of hairpins attached to the wall. Note the presence of an environment with several hairpin packets at different stages of growth. From Adrian et al. (2000).

smoke visualizations showed that the hairpin structures have a small upward motion. The

head or arch of this filament would experience higher mean flow velocity and be convected downstream faster than its lower-lying parts, producing a stretching of the hairpin structure. Hence, this stretching and intensification causes the lifting of the vortex from the wall into still higher mean velocity resulting in still greater stretching (Figure 2.4, Haidari and Smith, 1994). These processes occur until the vortex is dissipated (Acarlar and Smith, 1987a,b).

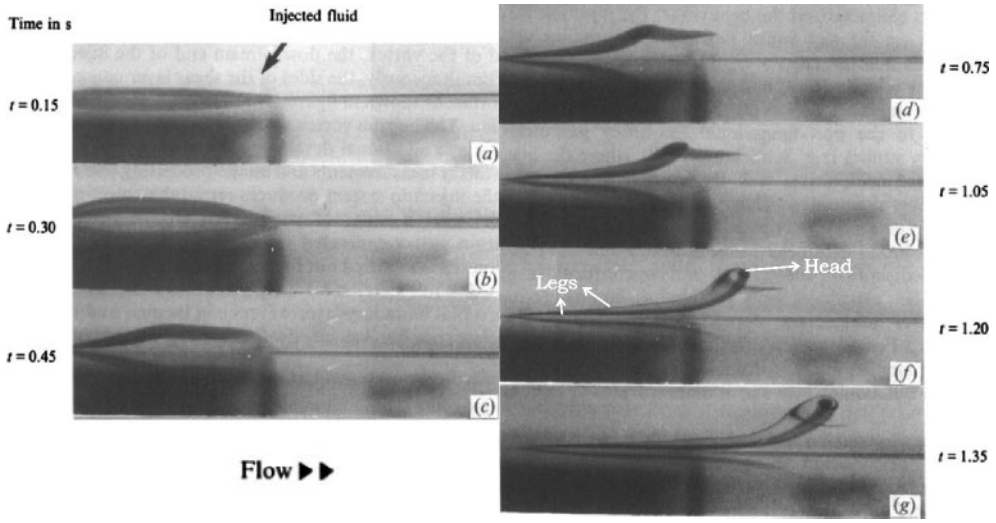

Figure 2.4: Hairpin-vortex generation for $Re = 354$. Modified from Haidari and Smith (1994).

The Reynolds shear stress can be obtained from the mean turbulent flow field (2.15). In this case, the mean is given by the conditional average

$$\langle u_i\left(x_i,t\right)|u_i\left(x_{i,0},t\right)=u_{i,0}\rangle \tag{2.24}$$

of the fluctuating velocity at a fixed point $x_{i,0}$. Figure 2.5 represents a direct numerical simulation of a Q2 event in a channel with $Re_* = u_*\delta/\nu = 300$ by plotting iso-surfaces of the turbulent swirling strength, λ_{ci}, defined as the imaginary part of the complex eigenvalue of $\left(\nabla\langle u_i|u_{i,0}\rangle\right)x_i = \lambda x_i$ (Adrian and Liu, 2002). Turbulent swirling strength is a kinematic quantity that allows a good visualization of the rotation terms of the vorticity (Adrian, 2007). The hairpin-like eddy represented in Figure 2.5 is a combination of a hairpin eddy and two short counter-rotating quasi-streamwise vortices. Most coherent structures can

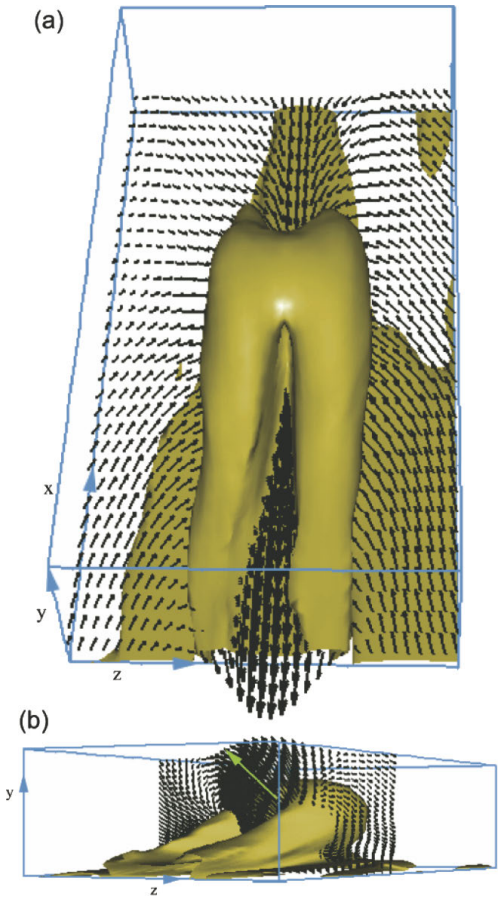

Figure 2.5: Visualization of a direct numerical simulation of a Q2 event. a) top and b) oblique view of a conditional average of the flow around a Q2 event in a channel flow with $Re_* = u_*\delta/\nu = 300$. From Adrian, 2007, after Adrian and Liu (2002).

be classified as hairpin or quasi-streamwise vortices (Johnson, 1998). The main difference between these two turbulent structures is that quasi-streamwise vortices are primarily single structures rather than counter-rotating pairs, which are oriented streamwise but skewed in the spanwise direction and angled away from the wall (Figure 2.6). These two structures are responsible for the Q2 and Q4 events (Figure 2.6b, Robinson, 1991). Near the wall, ejection and sweep motions are associated with the quasi-streamwise vortices in the near-wall region as single burst or sweeps, or as a burst and sweep as a pair. In the outer region, Q2 events occurred on the upstream side of an hairpin-vortex, and Q4 events occur along the side of the head.

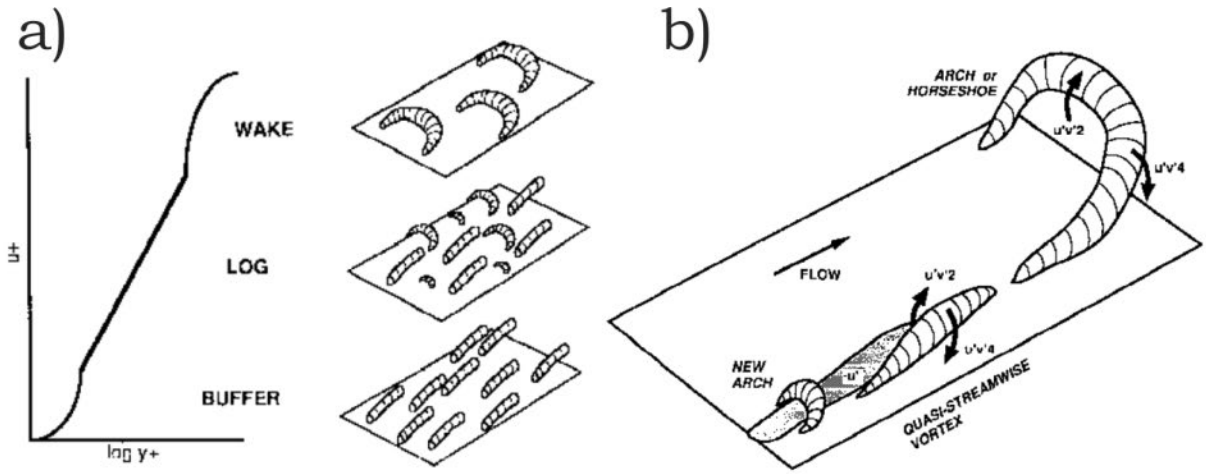

Figure 2.6: Schematic of the population of coherent flow structures in different regions of the turbulent boundary layer and their interactions with the wall. a) Idealized schematic of vortical-structure populations in different regions of the turbulent boundary layer. b) Conceptual model proposed for low-Reynolds number boundary layers. See text for description. Both diagrams are from Robinson (1991).

2.2 Oscillatory Flows or Waves

A pure oscillatory flow has surface waves as its only source of motion. Surface waves, in this context, are a mechanical wave that propagates along the interface between two fluids with different densities. In this study, waves are associated with wind-generated waves, which occur on the free surface of oceans, seas, lakes, rivers, and canals as the result of wind blowing over a long stretch of the fluid surface.

2.2.1 Oscillatory boundary layer

Once the water depth is smaller than half the wave wavelength (λ_w), the flow starts to interact with the bed. For the case of laminar flows, the boundary layer (BL) can be solved analytically.

Laminar Case

The fundamental equation for flow in the BL for a uniform oscillatory flow is

$$\frac{\partial u}{\partial t} = -\frac{1}{\rho}\frac{\partial p}{\partial x} + \frac{\partial \tau}{\partial z} \tag{2.25}$$

where u is the velocity in the BL, p is the pressure, and ρ and ν are the density and the kinematic viscosity of the fluid. Moreover, if the boundary layer is very thin, the pressure in the layer can be considered constant and equal to the pressure in the limit of the boundary layer,

$$\rho\frac{\partial u_0}{\partial t} = -\frac{\partial p}{\partial x} \tag{2.26}$$

where u_0 is the longitudinal velocity outside the boundary layer given by linear Airy wave theory

$$\begin{aligned} u_0 &= \overbrace{\frac{d_0\omega}{2}}^{U_o} \cos(\omega t - k\,x) \\ &= U_o \cos(\omega t - k\,x) \end{aligned} \tag{2.27}$$

where d_0 is the orbital diameter outside the boundary layer defined by

$$d_0 = \frac{A}{\sinh(k\,h)} \tag{2.28}$$

where A is the wave amplitude or height, and k is the wavenumber defined as

$$k = \frac{2\,\pi}{\lambda_w} \tag{2.29}$$

and ω is the angular frequency defined as

$$\omega = \frac{2\,\pi}{T} \tag{2.30}$$

where T is the wave period. The solution above is valid for a two-dimensional, incompressible and irrotational flow. In addition, it is assumed that the wave height (A) is small compared with both the wavelength (λ_w) and the water depth (h)

$$\frac{A}{\lambda_w} \ll 1 \tag{2.31}$$

$$\frac{A\lambda_w^2}{h^3} \ll 1 \tag{2.32}$$

Replacing Equation 2.26 in Equation 2.25, and taking into account that the flow is laminar, the governing equation for the BL is

$$\frac{\partial}{\partial t}\left(u - u_0\right) = \nu \frac{\partial^2 u}{\partial z^2}$$

which has a solution of the form

$$u = \Re\left[f\left(z\right) e^{i(\omega t - kx)}\right]$$

where $f\left(z\right)$ satisfies

$$\frac{\partial^2 f}{\partial z^2} - \frac{i\omega}{\nu} f = -\frac{i\omega}{\nu} U_o$$

By assuming that

$$u\left(z \to \infty\right) = u_0 = U_o \cos\left(\omega\, t - k\, x\right) \tag{2.33}$$

$$u\left(z \to 0\right) = 0 \tag{2.34}$$

we obtain

$$u\left(x, z, t\right) = U_o\left[\cos\left(\omega t - k\, x\right) - e^{-\beta z} \cos\left(\omega t - k\, x - \beta z\right)\right] \tag{2.35}$$

where β^{-1} is the thickness of the laminar boundary layer

$$\frac{1}{\beta} = \delta_w = \sqrt{\frac{2\nu}{\omega}} \tag{2.36}$$

that is also called the Stokes length. Figure 2.7 shows that the velocity profile given in Equation 2.35 varies during the different phases of the wave cycle. Relating Equation 2.35

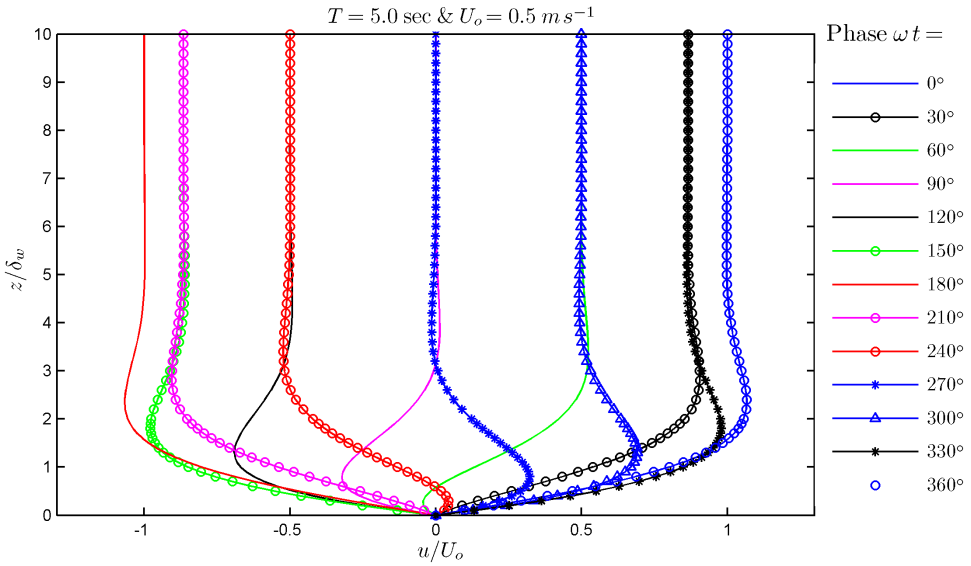

Figure 2.7: Velocity profiles in the laminar boundary layer at various phases in the wave cycle for laminar flows. The distance from the bed (z) was normalized with the thickness of the oscillatory boundary layer defined by Eq 2.36. The profiles were computed from Eq 2.35 with $x = 0$ m, $T = 5$ sand $U_o = 0.5$ ms^{-1} .

with the motion of free flow (Equation 2.27), it can be seen that the maximum velocity, and therefore the bed shear stress, are out of phase.

$$\frac{\tau_0}{\rho} = \nu \left.\frac{\partial u}{\partial z}\right|_{z=0} = \frac{\nu U_o}{\delta} \left[\sin(\omega t - kx) + \cos(\omega t - kx)\right] \tag{2.37}$$

From Eqs 2.27 and 2.37, it can be seen that there is a phase shift of 45° between the shear stress and the outer flow velocity. Despite the fact that Equation 2.35 is a first-order approximation, the curve conforms with experimental results (Fig. 2.8)

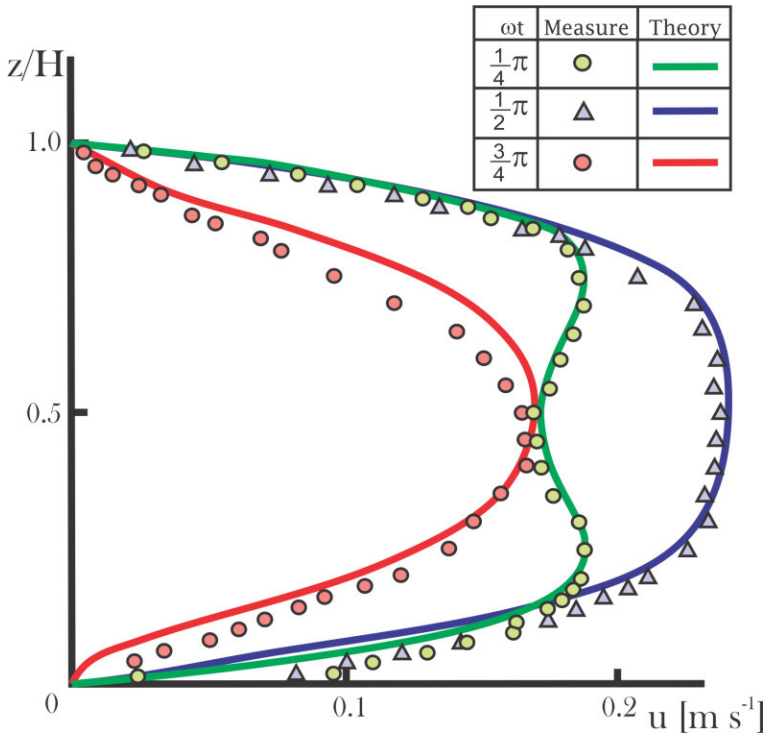

Figure 2.8: Comparison between theory (Equation 2.35) and experiments conducted in an oscillatory wind tunnel. Modified from Hino *et al.* (1983).

Turbulent Case

Due to the impossibility of an analytical solution for a turbulent flow over a flat bed, several models have been proposed in the literature with unidirectional flow assumptions (e.g. Agnew, 1965; Jonsson, 1966; Kajiura, 1968; Bakker, 1974; Johns, 1975; Johns, 1977; Jonsson, 1980 and Brevik, 1981). The model proposed by Kajiura (1968) assumes an eddy

Oscillatory Models	**Assumption**	**UMA**[1]
Agnew (1965)	2 Layer Eddy Viscosity Model	—
Jonsson (1966,1980)	Law of the wall Model	—
Kajiura (1968)	3 Layer Eddy Viscosity Model	Clauser (1956)
Bakker (1974)	Mixing Length Model	Prandtl (1925)
Johns (1975,1977)	Mixing Length Model	Launder and Spalding (1972)
Grant and Madsen (1979)	1 Layer Eddy Viscosity Model	—
Brevik (1981)	2 Layer Eddy Viscosity Model	Simplified Clauser (1956)

Table 2.1: Incomplete list of oscillatory flow models to describe the turbulent oscillatory boundary layer.
[1] UMA = Unidirectional Flow Assumptions.

viscosity model following the work of Clauser (1956) in unidirectional flows (Equation 2.7). Thus, the shear stress can be expressed as

$$\tau = \epsilon \rho \frac{\partial u}{\partial z}$$

where ϵ changes in the vertical.

1. Smooth beds

$$\epsilon = \begin{cases} \nu & \text{if } 0 < z < 12\,\nu/\hat{u}_* \\ \kappa\,\hat{u}_*\,z & \text{if } 12\,\nu/\hat{u}_* < z < \Delta \\ \kappa\,\hat{u}_*\,\Delta & \text{if } z > \Delta \end{cases} \tag{2.38}$$

2. Rough beds

$$\epsilon = \begin{cases} 0.185\,\kappa\,\hat{u}_*\,k_s & \text{if } 0 < z < 12\,\nu/\hat{u}_* \\ \kappa\,\hat{u}_*\,z & \text{if } 12\,\nu/\hat{u}_* < z < \Delta \\ \kappa\,\hat{u}_*\,\Delta & \text{if } z > \Delta \end{cases} \tag{2.39}$$

where $\hat{u}_*$ is the maximum value of the shear velocity $(\tau_0/\rho)^{1/2}$ at the bed and Δ is the thickness of the wall layer defined as (Kajiura, 1968)

$$\Delta = 0.05 \frac{\hat{u}_*}{\omega} \tag{2.40}$$

Kajiura (1968) proposed that for overlapping layers the velocity can be described as

- For $0 < z < \delta_w$

$$u = \Re\left[U_o\,(1 - \, e^{\alpha_1\,z} + A_1 \sinh(\alpha_1\,z))\; e^{i\,\omega\,t}\right] \tag{2.41}$$

- For $z > \delta_w$

$$u = \Re\left[U_o\left(1 - A_2\,e^{-\alpha_2\,z}\right)\; e^{i\,\omega\,t}\right] \tag{2.42}$$

where

$$A_1 = \frac{(\alpha_1 + \alpha_2)\ e^{\alpha_1\,\delta_w}}{\alpha_1 \cosh(\alpha_1\,\delta) + \alpha_2\ \sinh(\alpha_1\,\delta_w)} \tag{2.43}$$

and

$$A_2 = \frac{\alpha_1\, A\, e^{(\alpha_2 - \alpha_1)\,\delta}}{\alpha_1 + \alpha_2} \tag{2.44}$$

- For a smooth bed

$$\begin{aligned} \delta_w &= 12\,\nu/\hat{u}_* \\ \alpha_1 &= (i\,\omega/\nu)^{1/2} \\ \alpha_2 &= \left(i\,\omega^2/0.05\,\kappa\,\hat{u}_*^2\right)^{1/2} \end{aligned} \tag{2.45}$$

- For a rough bed

$$\begin{aligned} \delta_w &= k_s/2 \\ \alpha_1 &= (i\,\omega/0.185\,\kappa\,\hat{u}_*\,k_s)^{1/2} \\ \alpha_2 &= \left(i\,\omega^2/0.05\,\kappa\,\hat{u}_*^2\right)^{1/2} \end{aligned} \tag{2.46}$$

The model of Kajiura (1968) shows a relatively good agreement with high Reynolds number experiments, although the model is far from explaining most oscillatory flows since it assumes an eddy viscosity that does not change with time. Figure 2.9 shows an example of how the eddy viscosity fluctuates during the course of a cycle at two different heights. In particular, the singularities when $\frac{\partial u}{\partial z} = 0$ are not unexpected since the turbulence, and hence Reynolds stresses, do not instantly disappear as the velocity gradient passes through zero. In addition, the model proposed by Kajiura (1968) has two 'unrealistic' assumptions; i) that the thickness of the wave boundary layer is a time-independent quantity, and ii) that the variation in bed shear stress is assumed to be sinusoidal.

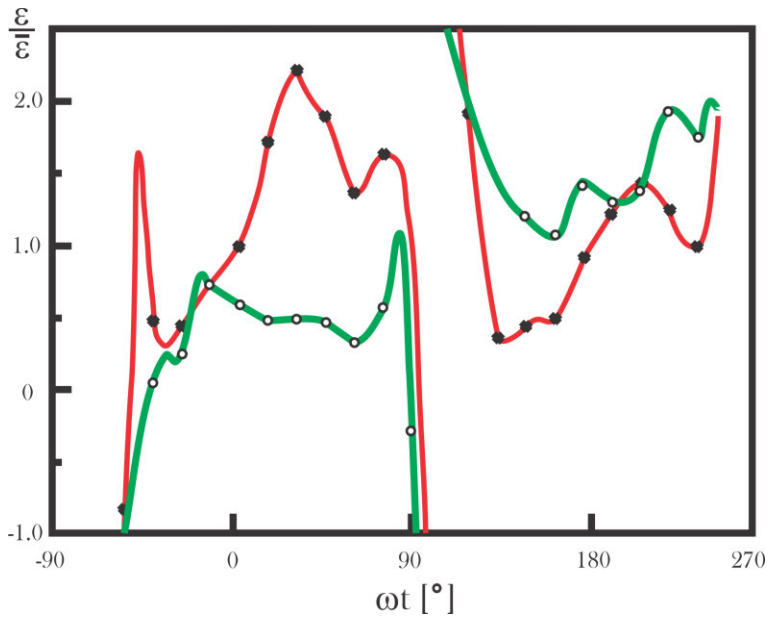

Figure 2.9: Variation of eddy viscosity during the wave cycle: red line measurements were taken at z = 3.5 mm and green lines at 30 mm. Modified from Sleath (1987).

The model of Brevik (1981) follows the original idea from Kajiura (1968) with the simplification that for high values of A/k_s, or wave Reynolds number

$$Re_w = \frac{U_o\, A}{\nu} \tag{2.47}$$

the inner layer may be relatively unimportant so it can be eliminated from the equation. Therefore, for the model of Brevik (1981), Eqs 2.38 and 2.39 from the model of Kajiura (1968) become

1. Smooth beds

$$\epsilon = \begin{cases} \kappa\, \hat{u}_*\, z & \text{if } 0 < z < \Delta \\ \kappa\, \hat{u}_*\, \Delta & \text{if } z > \Delta \end{cases} \tag{2.48}$$

2. Rough beds

$$\epsilon = \begin{cases} \kappa\, \hat{u}_*\, z & \text{if } 0 < z < \Delta \\ \kappa\, \hat{u}_*\, \Delta & \text{if } z > \Delta \end{cases} \tag{2.49}$$

where Brevik (1981) redefines Δ as

$$\Delta = \frac{\delta_1}{2} \tag{2.50}$$

where

$$\delta_1 = \frac{1}{\hat{u}_*}\text{Amp.}\int_0^{\delta_w}(u - U_o)\,\mathrm{d}z$$

Although this approach produces some simplifications, the solutions still involve Kelvin functions that are related to the vth order Bessel function of the first kind (see Abramowitz and Stegun (1972) for more details) and these solutions are far from straightforward (Sleath, 1984).

On the other hand, the model of Jonsson (1966,1980) assumes, as in steady flows, a fully developed turbulent oscillatory flow with two regions: i) a wall region in which the velocity distribution is determined by the local conditions, and, ii) a defect layer in which the velocities are independent of viscosity. Consequently, if the bed is assumed to be rough, the velocity distribution would be written as

- For the wall region

$$\frac{u}{\hat{u}_*} = f\left(\frac{z}{k_s}\right) \tag{2.51}$$

- For the defect layer

$$\frac{u - u_0}{\hat{u}_*} = f\left(\frac{z}{\delta_w}\right) \tag{2.52}$$

where δ_w is the thickness of the boundary layer and u_0 is the velocity in the freestream outside. If it is assumed that there is little variation in phase within the boundary layer, and there is an overlapping region between the wall layer and the defect layer, a logarithmic profile can be proposed:

$$\frac{u}{\hat{u}_*} = \frac{1}{\kappa}\ln\left(\frac{z}{z_0}\right)\cos\left(\omega\, t + \phi_0\right) \tag{2.53}$$

where $z_0 = k_s/30$ and ϕ_0 is independent of height but varies with A/k_s. From comparison with experiments, Jonsson (1980) suggests $\phi_0 = 25^\circ$ for $A/k_s = 100$ and $\phi_0 = 11^\circ$ when

$A/k_s = 1000$. In addition, if it is assumed that the logarithmic profile is valid for the whole boundary layer instead of only the overlapping area, the thickness of the boundary layer for $\omega t = 0$ can be expressed by:

$$\frac{30\,\delta_w}{k_s} \ln\left(\frac{30\,\delta}{k_s}\right) = \vartheta \frac{A}{k_s} \tag{2.54}$$

where ϑ equals 1.64, although from experimental data a value of 1.2 gives a better fit. The success of the model of Jonsson (1980) in describing the boundary layer over a rough bed depends on how large the overlap region is as compared with the full length of the boundary layer. The region where the velocity distribution can be expected to be logarithmic is generally strongly related with A/k_s. Hino *et al.* (1983) examined the boundary layer of an oscillatory turbulent flow using laser-Doppler velocimetry and hot-wire anemometry in a rectangular duct. Although the experiments of Hino *et al* (1983) were above the limits for overlapping conditions ($Re_w < 4.7 \times 10^4$), the area in which a logarithmic profile could be fitted were small (Figure 2.10).

Bakker (1974) and Johns (1975, 1977) made use a single layer mixing length, which is not applicable to the viscous sublayer and, from steady flow results, it seems unlikely it would

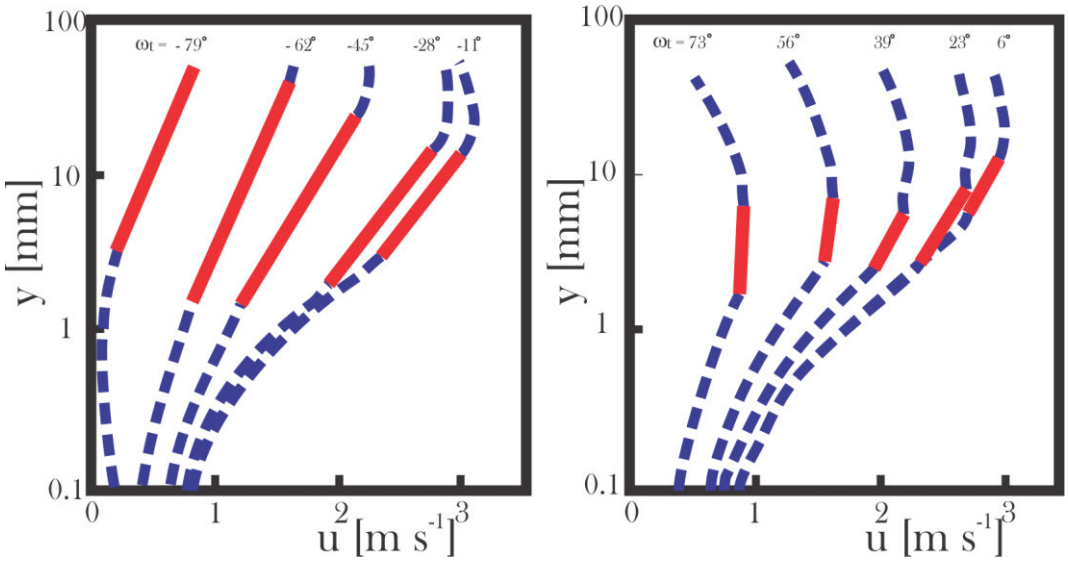

Figure 2.10: Velocity profiles in a turbulent oscillatory boundary layer. Broken curves represent the measured velocity and the heavy lines show the segments to which it was possible to fit a logarithmic distribution. Modified from (Sleath, 1984) after Hino *et al.*, (1983).

apply in the wake region above the overlap layer (Sleath, 1984). In addition, measurements by Sleath (1987) have shown that the temporal variation of the mixing length with height are similar to that for eddy viscosity (Figure 2.9).

As discussed for unidirectional flows, the structure of the boundary layer changes as a function of the Reynolds number (Jensen *et al.*, 1989), with the additional complication that such characteristics are quite different from wall turbulence that is steady in the mean. Turbulence intensities fluctuate significantly during the course of the wave cycle. As the flow decelerates, the maximum turbulence intensity is reached as well as the maximum Reynolds stress (Sleath, 1987). This phenomenon was also described by Hino *et al.* (1983), where it was observed that during flow acceleration bursts of turbulence are triggered by the shear instability at a slight distance from the wall, but are suppressed and did not develop further. However, with the beginning of flow deceleration, turbulence grows explosively and violently and is maintained by a bursting type of motion (Hino *et al.*, 1983).

In turbulent oscillatory flow over rough beds, turbulence intensities during the cycle show significant variation. The root-mean-square fluctuations in the horizontal component of the velocity vary during the course of the cycle at various heights above the grains (Figure 2.11). The RMS values in Fig. 2.11 were measured relative to the maximum negative velocity in the freestream. Thus, the freestream velocity is a minimum at $0\,^\circ$, a maximum at $180\,^\circ$, and zero at $-90\,^\circ$, and $+90\,^\circ$. It can be seen that the maximum turbulence intensity propagates out from the bed at a more or less constant velocity.

2.2.2 Wave friction factor

The relation between the wave conditions and the bed shear stress can be described by:

$$\tau_w = \frac{1}{2}\,\rho\, f_w\, U_o^2 \tag{2.55}$$

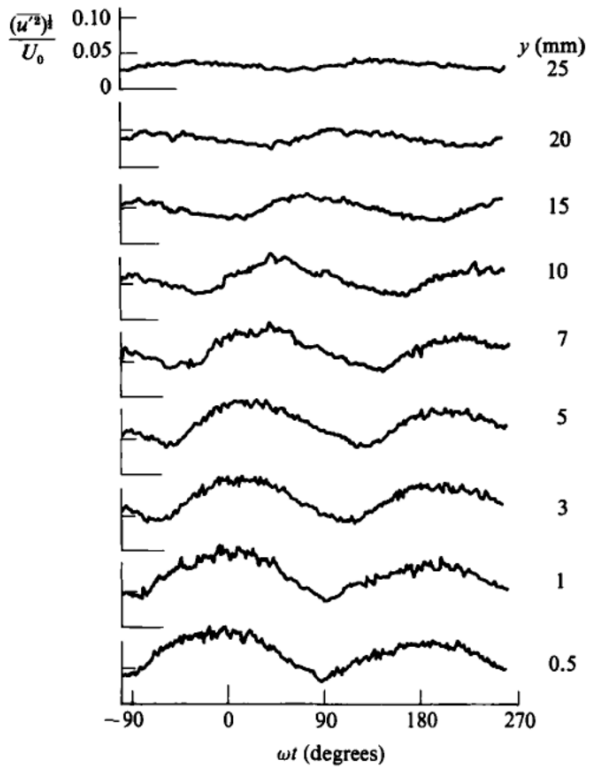

Figure 2.11: Variation of $(\sqrt{u'^2})$ during the course of a cycle of 4.58 seconds over a flat bed of 1.63 mm sand. From Sleath (1987).

where τ_w is the wave shear stress and f_w is the wave friction factor. There are several expressions for the wave friction factor, but all can be generalized as a function of the wave Reynolds number (Re_w) and the relative roughness $\left(\frac{A}{k_s}\right)$

$$f_w = \mathbf{f}\left(\frac{A}{k_s}, Re_w\right) \tag{2.56}$$

Myrhaug (1989) proposed an implicit relationship for smooth, transitional and rough turbulent flows by using Equation 2.10

$$\frac{0.32}{f_w} = \left\{\ln\left(6.36\,\frac{A\,f_w^{1/2}}{k_s}\right) - \ln\left[1-\exp\left(1-0.0262\,\frac{Re_w\,k_s\,f_w^{1/2}}{A}\right)\right] + 4.71\,\frac{A}{k_s\,Re_w\,f_w^{1/2}}\right\}^2 + 1.64 \tag{2.57}$$

For rough and transitional turbulent flow, a number of expressions can be found in the literature:

Swart (1974):

$$f_w = \begin{cases} 0.3 & \text{if } \frac{A}{k_s} \leq 1.57 \\ 0.00251 \exp\left[5.21 \left(\frac{A}{k_s}\right)^{-0.19}\right] & \text{if } \frac{A}{k_s} > 1.57 \end{cases} \tag{2.58}$$

Nielsen (1992):

$$f_w = \exp\left[5.5 \left(\frac{A}{k_s}\right)^{-0.2} - 6.3\right] \tag{2.59}$$

Soulsby (1997):

$$f_w = 0.237 \left(\frac{A}{k_s}\right)^{-0.52} \tag{2.60}$$

Pedocchi and García (2009a):

$$\frac{1}{\sqrt{f_w}} = G_w \left(\frac{\delta_w}{k_s} L_w\right) = 1.9 \ln\left(\frac{1}{1.5} \frac{u_* L_w}{\omega k_s}\right) \tag{2.61}$$

where L_w

$$L_w \left(\frac{u_* k_s}{\nu}\right) = \left\{ \frac{1}{7.5} \left[1 - \exp\left(-\left[\frac{1}{90} \frac{u_* k_s}{\nu}\right]^2\right)\right] + \frac{1}{2.1} \frac{\nu}{u_* k_s} \right\}^{-1} \tag{2.62}$$

2.2.3 Coherent turbulent structures

Section 2.1.3 briefly discussed the extensive literature on coherent turbulent flow structures in unidirectional flows and the relationship with bursts and sweeps. However, the studies that focus on coherent flow structures in oscillatory flows are less common than unidirectional flows. Recent work by Carstensen et al. (2010) has provided some enlightenment into the subject for oscillatory flows that show the existence of two kinds of coherent flow structures: i) vortex tubes, and ii) turbulent spots.

Vortex tubes are a set of flow structures oriented transverse to flow that are generated as a result of the inflectional-point in the shear field (See section 2.2.1) generated (for $\omega t = 135°$) due to the oscillatory nature of the flow (Figure 2.7). These vortex tubes are the concentration of vorticity that develops in the oscillatory boundary layer (Carstensen et al.,

2010), which is unstable due to Kelvin-Helmholtz instabilities (Blondeaux and Vittori, 1994). During the experiment of Carstensen et al. (2010) at $Re_w = 2.9 \times 10^5$, the vortex tubes first emerged at the phase value of approximately $\omega t \approx 165°$, growing stronger as the structure was convected until it gradually lost coherence at $\omega t \approx 225°$ (Figure 2.12). The spacing between adjacent vortices was of the order of $6.1\,\delta$, and remained relatively constant throughout the vortex lifespan. In addition, Carstensen et al. (2010) showed that these two-dimensional vortices emerged for Re_w larger than 7×10^4. However, this flow structure does not form for Re_w larger than $5{\times}10^5$. This absence of vortex tubes can be explained since, for large Reynolds numbers, the flow becomes fully turbulent for the phases corresponding to the inception of the vortex tubes ($\omega t = 150 - 170°$) and there is no inflectional-point shear layer instability, and hence no vortex tubes are generated.

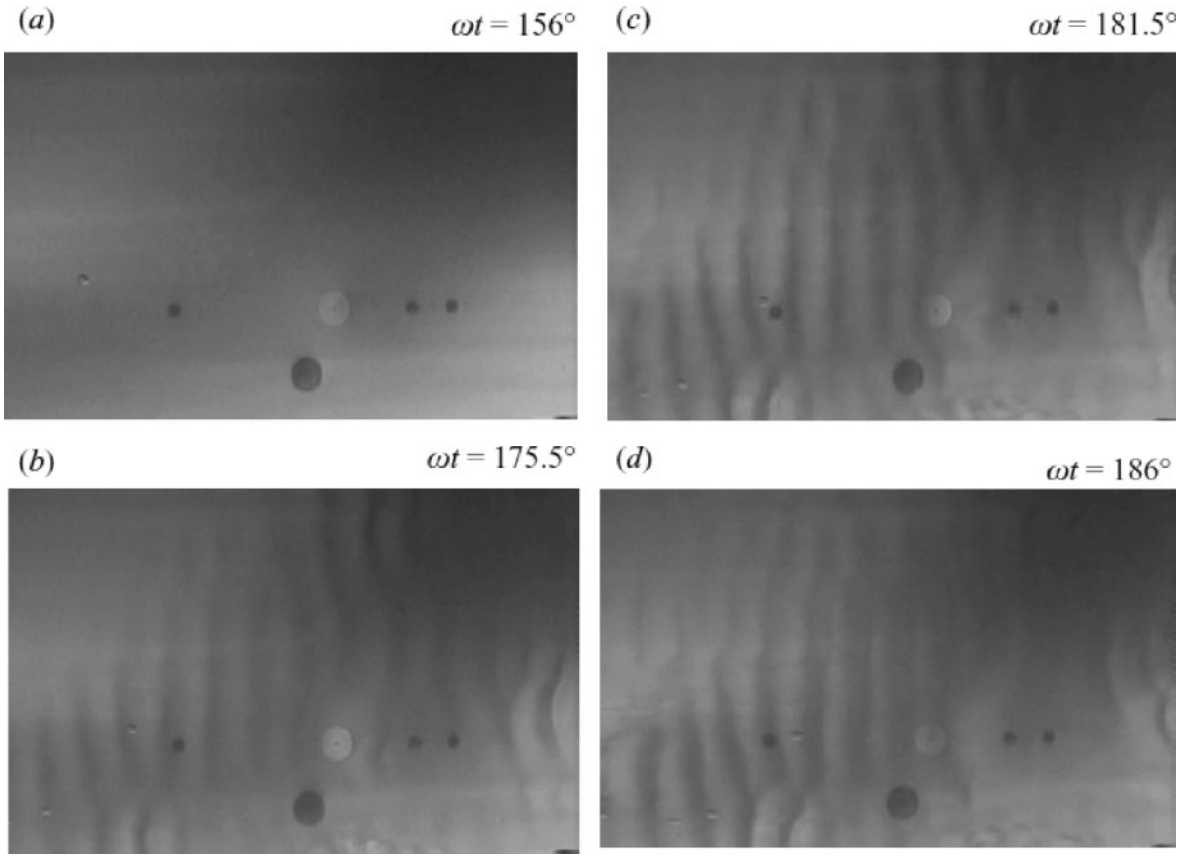

Figure 2.12: Time evolution of vortex tubes. Near the bed flow is from left to right. Several circular hot-film probes are located at the bottom of the bed. From Carstensen et al. (2010).

Turbulent spots are isolated areas with relatively high turbulence close to the bed (burst-like features), in an otherwise laminar boundary-layer flow (Carstensen et al., 2010). The influence of turbulent spots has been observed by other researchers such as Hino et al. (1983), Jensen et al. (1989) and Fredsoe (1984) but, influenced by the 'old bursting' theory (Lu and Willmarth, 1973), they did not interpret such effects as coherent structures. Carstensen et al. (2010) classify these features as new structures, but the pictures of this structure (Figure 2.13) looks like a localized set of quasi-streamwise vortices (i.e. Section 2.1.3).

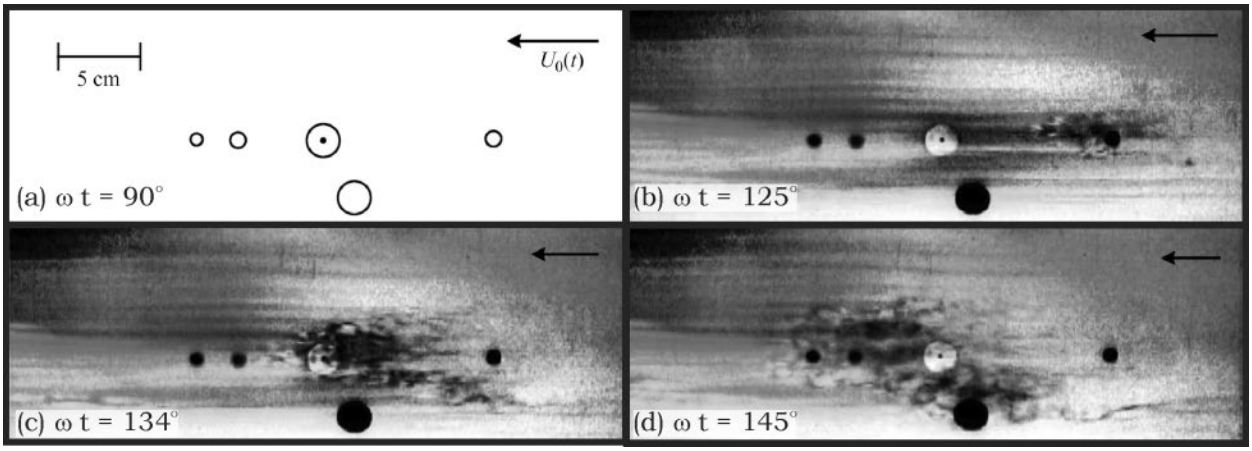

Figure 2.13: a) Sketch of the multiple circular hot-film probes that are located at the bottom of the bed. b-d) Time evolution of turbulent spots. Near the bed flow is from right to left. From Carstensen et al., 2010.

The series of frames taken by Carstensen et al. (2010) (Figure 2.13) show that the turbulent spots originate at a phase value $\omega\, t = 125°$ ($Re_w = 4.5 \times 10^5$) and evolve until their dissipation by the time the flow reverses. These spots start as very small zones of local turbulence (finite-length streaks) and grow in size by twisting and turning motions as they move in the flow direction throughout half of the wave cycle (Figure 2.13). For a range of Re_w ($1.5 - 3 \times 10^5$), turbulent spots can occur simultaneously with vortex tubes, but there is no clear interaction between them. Carstensen et al. (2010) propose that the turbulent spots are generated during the laminar-to-turbulent transition throughout the wave cycle. This assumption can be supported since the first turbulent spot structures are seen for flows with $Re_w = 1.5 \times 10^5$, a value that is very close to the experimental value estimated for the

laminar-to-turbulent transition (e.g. Sleath, 1984; Jensen et al., 1989). In addition, as the wave Reynolds number increases, the turbulent spots emerge earlier in the cycle to values that agree with the laminar-to-turbulent transition measured by Jensen et al. (1989).

2.3 Combined Flows or Current-Wave flows

The superimposition of an oscillatory flow upon an unidirectional flow can be defined as a combined flow. For the rest of this thesis, the wave propagation will be assumed to be co-linear to the mean unidirectional flow unless specified otherwise. Co-linear conditions are common in many coastal environments but are not necessarily the only combined-flow present in nature. Further information on non-collinear currents is given in Longuet-Higgins and Stewart (1960), Soulsby et al. (1993), Myrhaug et al. (2001), Faraci et al. (2008) and Hasanat Zaman and Baddour (2011). For example, the effect on the wave height (η_w) and wavelength (λ_w) produced by a steady current can be described as a simple first approximation by

$$\frac{\eta_w}{\eta_{w_0}} = \left[\frac{\left(1 + \frac{2\,k_0\,d_0}{\sinh 2\,k_0\,d_0}\right)\left(1 - \frac{k\,U_u}{k_0\,c_0}\right)}{\left(\frac{k_0}{k} - \frac{U_u}{c_0}\right)\left(1 + \frac{2\,k\,d}{\sinh 2\,k\,d}\right) + 2\,\frac{U_u}{c_0}} \right]^{1/2} \tag{2.63}$$

$$(g\,k_0\,\tanh k_0\,d_0)^{1/2} = (g\,k\,\tanh k\,d)^{1/2} + k\,U_u \tag{2.64}$$

where the subscript 0 refers to quantities in the absence of the current and U_u is the mean free flow unidirectional velocity. Equations 2.63 and 2.64 show that when the current is in the same direction as the wave, the height is decreased and the wavelength becomes longer (Figure 2.14), whereas, for opposing directions, the height is increased and the wavelength decreased. These theoretical curves are in remarkably good agreement with experiments (Figure 2.14) despite the fact that they assume no change from the current due to the waves.

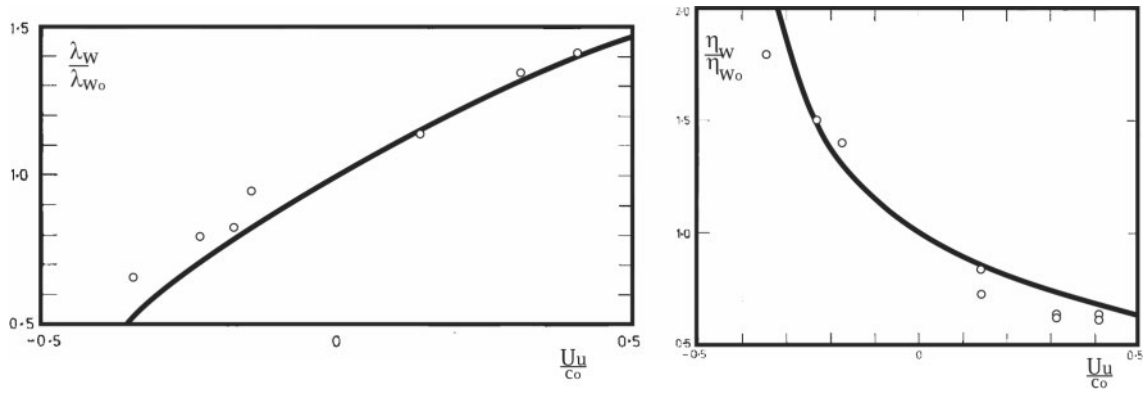

Figure 2.14: Variation of the wave height (right) and wavelength (left) produced by a steady current. The subscript 0 refers to quantities in the absence of the current. Measurements are taken from Brevik (1980) and the theoretical line is given by Equation 2.63 for the wave height and Equation 2.64 for the wave wavelength with $k_o\, d_o = 0.65$.

The interactions between waves and currents are manifested in various ways throughout the water column. These complex systems have been studied by numerous researchers such as Lighthill (1954), Bijker (1967), Peregrine (1976), Soulsby (1980), Kemp and Simons (1982, 1983), Sleath (1991), Soulsby et al. (1993), Héquette et al. (2008), Uchiyama et al. (2009), Ojha and Mazumder (2010) and Olabarrieta et al. (2011). There appears to be a general consensus that shows the main features of combined flows are:

- the mean velocity profile may be split into two sections: an inner region close to the bed that is affected by the wave boundary layer, and an outer region above it that is unaffected by waves. Hence, the mean velocity profile in the outer region can be characterized by Equation 2.8 with a modified bed roughness length (k_{wc}) that takes into account the inner layer.

- The inner region can be divided into two layers: a wave-dominated layer near the bed and a logarithmic layer.

- For rough beds, the waves reduce the mean current velocity in the outer region.

- The mean bed shear stress may increase ($U_u/U_o \leq 1$ and $Re_w > 1.5 \times 10^5$), or remain constant ($U_u/U_o \geq 1$ and $Re_w < 1.5 \times 10^5$), or even decrease ($U_u/U_o \leq 1$ and $Re_w <$

1.5×10^5) with respect to its steady-current value (Lodahl *et al.*, 1998). The maximum bed shear stress may increase, or it may retain its steady current value when waves are introduced.

Even though the previously mentioned research has provided a clear basis for the main interactions between waves and currents in a boundary layer, relatively little is known about the physical mechanics of these flow interactions.

2.3.1 The Laminar Case

Experiments by Lighthill (1954) concerning combined steady currents and oscillatory flows had showed that if the frequency of the wave oscillation is high enough ($\delta_w << \delta_c$), the interactions between waves and currents can be negligible at a first order approximation. Following this approximation, Collins (1964) gives the velocity distribution in the vicinity of the bed as

$$u_{cf}\,(x, z, t) = U_o \left[\cos\left(\omega t - k\,x\right) - e^{-\beta z} \cos\left(\omega t - k\,x - \beta z\right)\right] \pm U_1 \left[0.4\,\beta\,z - 0.04\,\beta^2\,z^2\right] \tag{2.65}$$

where U_1 is the velocity of the unidirectional component at $z = 5/\beta$. Velocity profiles for different phases ($\omega\,t$) throughout the wave cycle are plotted in Figure 2.15. The oscillatory flow condition plotted in Figure 2.15 is the same as the one plotted for the pure oscillatory case in Figure 2.7, with the exception that a unidirectional current is superimposed. The effect of the unidirectional component is reflected by a clear downstream 'shift' of the profile (i.e., weaker upstream flow and stronger downstream flows).

2.3.2 The Turbulent Case

Like unidirectional and oscillatory flows, the main problem in obtaining a solution for the velocity profile of combined flows lies in the relationship between the fluid velocity and shear

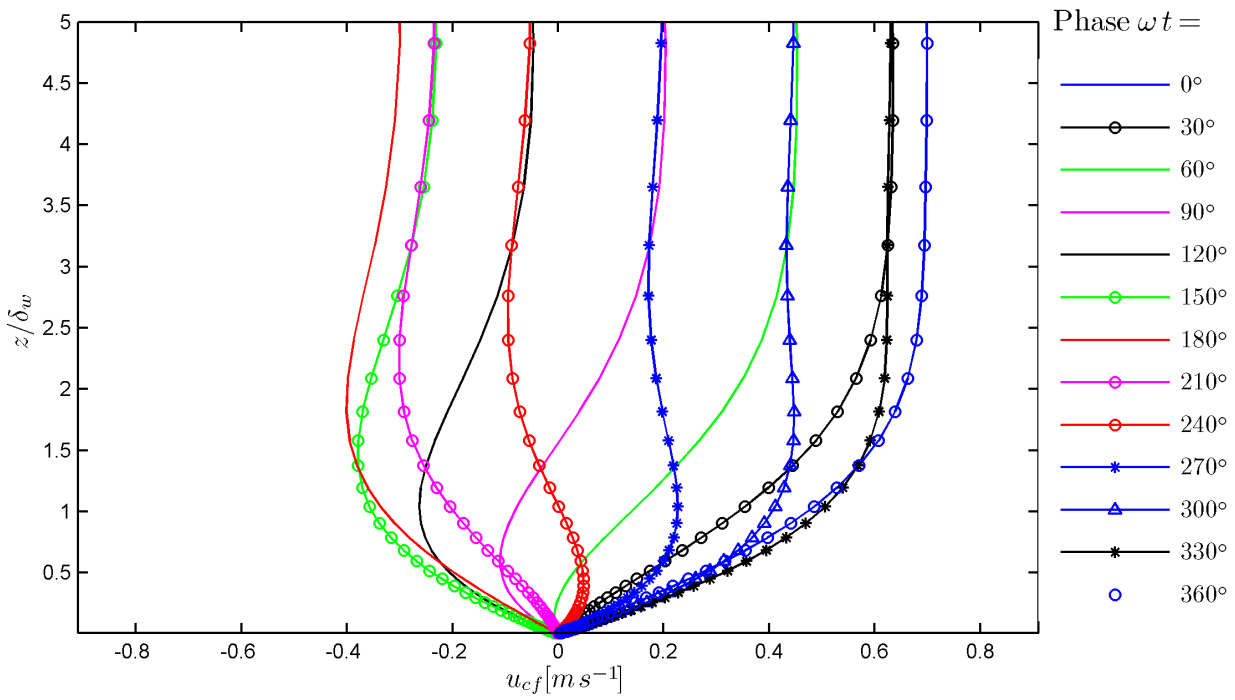

Figure 2.15: Velocity profiles in the laminar boundary layer at various phases in the wave cycle. The distance from the bed (z) was normalized with the thickness of the oscillatory boundary layer defined by Equation 2.36. The profiles were computed from Equation 2.65 with $x = 0$ m, $T = 5$ s, $U_o = 0.5$ ms^{-1} $U_1 = 0.2$ ms^{-1}.

stress. The simplest, and most used, model to relate the velocity field and shear stress in combined flows is by using the eddy viscosity concept

$$\tau = \rho\,\epsilon\frac{\partial\,u}{\partial\,z} \tag{2.66}$$

Like Kajiura (1968), Smith (1977) made use of an eddy viscosity for the inner layer that does not vary with time

$$\epsilon = \kappa\,(u_{*\,c} + u_{*\,w})\,z \tag{2.67}$$

where $u_{*\,c}$ is the shear velocity for the steady current and $u_{*\,w}$ is the amplitude of the oscillatory shear velocity. On the other hand, the eddy viscosity proposed by Grant and

Madsen (1979) is of the form

$$\epsilon = \kappa u_* \, z \tag{2.68}$$

where u_* is a characteristic shear velocity representing the level of turbulence in the flow. Both Grant and Madsen (1979) and Smith (1977) used an eddy viscosity that does not vary with time, so the solutions to Equation 2.25 are similar. The solution obtained by Smith (1977) is

$$u_{cf} = \frac{u_{*\,c}^2}{\kappa \left(u_{*\,c} + u_{*\,w}\right)} \ln\left(\frac{z}{z_0}\right) + U_o \left[(1 - \Phi)\, \cos\omega\, t - \Psi\, \sin\omega\, t\right] \tag{2.69}$$

where

$$\Phi = \frac{\mathrm{Ker}\left(\xi\right)\, \mathrm{Ker}\left(\xi_0\right) + \mathrm{Kei}\left(\xi\right)\, \mathrm{Kei}\left(\xi_0\right)}{\mathrm{Ker}^2\left(\xi_0\right) + \mathrm{Kei}^2\left(\xi_0\right)} \tag{2.70}$$

$$\Psi = \frac{\mathrm{Ker}\left(\xi\right)\, \mathrm{Kei}\left(\xi_0\right) - \mathrm{Kei}\left(\xi\right)\, \mathrm{Ker}\left(\xi_0\right)}{\mathrm{Ker}^2\left(\xi_0\right) + \mathrm{Kei}^2\left(\xi_0\right)} \tag{2.71}$$

where Ker and Kei are zero-order Kelvin functions (see Abramowitz and Stegun,1972) and

$$\xi = 2\left(\frac{\omega\, z}{\kappa\left(u_{*\,c} + u_{*\,w}\right)}\right)^{1/2} \tag{2.72}$$

$$\xi_0 = 2\left(\frac{\omega\, z_0}{\kappa\left(u_{*\,c} + u_{*\,w}\right)}\right)^{1/2} \tag{2.73}$$

It is important to note that, regardless of the complexity in the velocity profile in Equation 2.69, the equations still predict a logarithmic time-mean velocity distribution. These can be easily seen in the velocity profiles plotted for different phases ($\omega\, t$) throughout the wave cycle in Figure 2.16. Grant and Madsen (1986) provided a more explicit solution for the inner region by providing a different eddy viscosity for the two layers (Figure 2.17): the

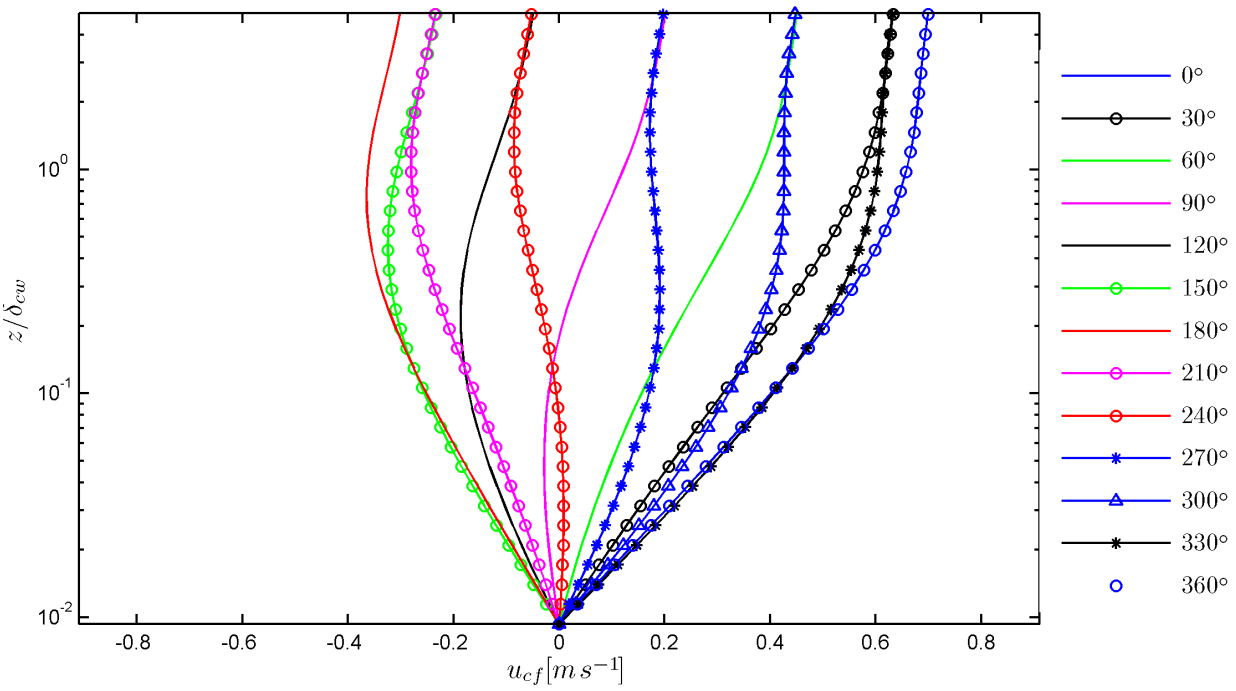

Figure 2.16: Velocity profiles in the turbulent boundary layer at various phases in the wave cycle for laminar flows. The distance from the bed (z) was normalized with the thickness of the wave-current boundary layer defined by Equation 2.75. The profiles were computed from Equation 2.69 with $x = 0$ m, $T = 5$ s, $U_o = 0.5$ ms^{-1} $U_u = 0.2$ ms^{-1}.

wave dominated layer ($z < \delta_{cw}$) and the logarithmic layer ($z > \delta_{cw}$)

$$\epsilon = \begin{cases} \kappa u_{*\,cw}\, z & \text{if } z < \delta_{cw} \\ \kappa u_{*\,c}\, z & \text{if } z > \delta_{cw} \end{cases} \tag{2.74}$$

where δ_{cw} is the wave-current boundary layer thickness defined by

$$\delta_{cw} = \frac{\kappa\, u_{*\,cw}}{\omega} \tag{2.75}$$

The wave-current boundary layer thickness defines the limit of the wave-dominated layer, which is embedded in a large-scale rotating boundary layer where both waves and currents contribute to the turbulence. Above this height, turbulence is associated only with the

low-frequency current in the logarithmic layer. The solutions from Grant and Madsen (1986) are very similar to that presented in Equation 2.69. The high turbulence intensities generated

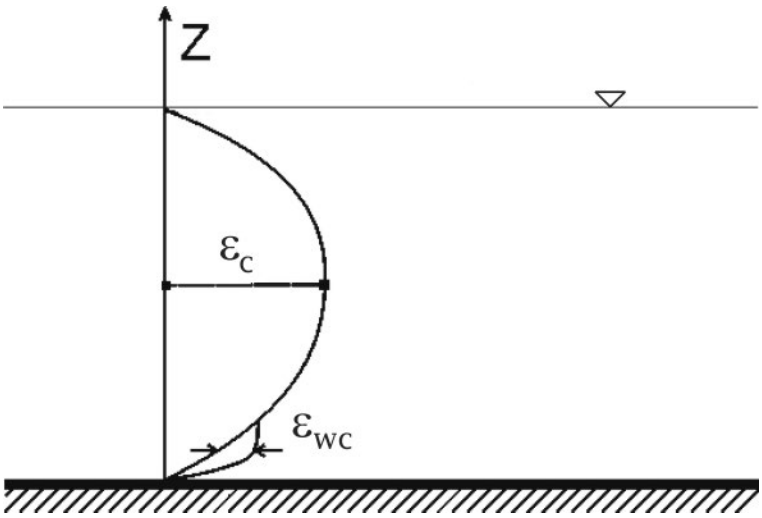

Figure 2.17: Schematic illustration of the time-averaged eddy viscosity. Using the Boussinesq hypothesis, the momentum transfer caused by turbulent eddies can be modeled with an eddy viscosity. Modified after Fredsøe and Deigaard (1992).

by the wave boundary layer affect the unidirectional current velocity in the outer region, generating a higher resistance to flow that can be represented as an "apparent" higher roughness coefficient in the logarithmic velocity profile

$$u = \frac{u_{*\,cw}}{\kappa} \ln\left(\frac{z}{z_0 + z_a}\right) \tag{2.76}$$

where z_a is the "apparent" roughness coefficient. This assumption holds for relatively low period waves, since the time scales in which the mean velocity of the waves change are several orders of magnitude smaller than the rate of change in the currents. The boundary layer associated with the current is generated by the real bed roughness, and the apparent bed roughness, which is of a larger magnitude, and is induced by the wave motion. These results raise an unanswered question; why are waves able to change the boundary layer of the current but not the other way around?

2.4 General Overview

The sedimentological fluid dynamic (SFD) "trinity", as explained in Chapter 1, is a conceptual framework to study the coupling effects between flow, sediment transport and bed morphology (Figure 1.2). This chapter had provided a brief discussion of some of the key concepts on boundary layers for unidirectional (Section 2.1), oscillatory (Section 2.2) and combined flows (Section 2.3). The inter-relationships and feedbacks between the elements of the SFD "trinity"for combined flows are strictly associated with the interaction between currents and waves. No existing model is able to quantitatively describe the individual effects of waves and currents on the bed. However, it can qualitatively be stated that a combined flow is more efficient at transporting material than waves or currents alone (Soulsby, 1997). Based on studies of pure oscillatory and unidirectional flows, waves are found to be relatively more efficient in entraining sediment into suspension than currents (Soulsby and Clarke, 2005). On the other hand, unidirectional currents have a higher net transport than that generated by waves (Soulsby and Clarke, 2005). Therefore, even although there is no evidence of linear interactions, these two sediment transport processes can be added linearly, giving a flow which entrains and transports more than the individual components of the flow.

In addition, one of the most important phenomena occurring in the combined flow boundary layer, and a major factor in determining the bed morphology, is the interaction between the two boundary layers (i.e., current boundary layer and wave boundary layer). One of the most obvious, but yet crucial, factors to understanding wave-current interactions is the simple fact that the wave boundary layer oscillates. This oscillation forces the wave velocity to go back and forth while crossing to a zero-velocity stage. This has many important implications for the transport of sediments; for example, coarser grains that are entrained only at the maximum velocities/bed shear stresses may settle very quickly from suspension during the low velocity phases after the flow reversal. In addition, if a 'Bagnoldian' view is taken

on how sediment is kept in suspension, the settling velocity of the sand grains (ω_s) needs to be opposed by the turbulent lift that is proportional to the shear velocity u_* (Bagnold, 1966). However, as it has been proven by many researches (e.g. Jensen et al., 1989), the oscillatory boundary layer is not always turbulent since flow velocity changes throughout the wave cycle. For example, the experiments of Jensen et al. (1989) indicate that the transition to turbulence for $Re_w \approx 10^5$ only occurs just prior to the near-bed flow reversal. Of course, as the flow Re_w is increased, more half-cycle wave phases develop a fully turbulent motion. However, for Re_w as high as 1.6×10^6 there are still some portions of the half-cycle ($\omega\, t < 45°$) where the flow regime is not fully turbulent (Jensen et al., 1989), which means that if the background turbulence is not strong enough to maintain sediment in suspension, the grains will settle. On the other hand, the experiments of Jensen et al. (1989) were conducted under flat bed conditions, and yet the bed roughness generated by bed topography places a very significant role in sediment transport dynamics. Therefore, in the next chapter (Chapter 3) a brief discussion on the present knowledge of stable bed configurations for unidirectional, oscillatory and combined flows will be presented to fully address the SFD "trinity".

Chapter 3

SFD *trinity* : Bed Morphology

3.1 Bedform phase diagrams

Phase or stability diagrams are defined as graphs that show the regimes of existence of one or more stable bed states. The stability of the bed can be defined when the bedform is in equilibrium and does not change in time for the same flow condition. This invariance over time must not be confused with a static morphology or frozen equilibrium; on the contrary, the bed moves and adjusts in a dynamic equilibrium with the flow and sediment transport for that particular condition. These phase diagrams (e.g. Southard, 1991) are used for two main purposes: i) for prediction of bed states in a known flow and sediment transport condition, and, ii) as a tool for the reconstruction of paleoenvironments from a known bed state or sedimentary structure. Despite the great utility of such diagrams, they are very difficult to construct, making them either incomplete or very hard to interpret. This complexity lies in the number of variables needed to quantify the system. As an example, consider the simplest case for a system with co-existing waves and currents in water at a fixed temperature. The simplest representation of the system can be achieved by selecting

- the oscillation period (T) and the maximum orbital speed (U_o) for the oscillatory component.
- the water depth (h) and the mean velocity (U_u) for the unidirectional component.
- the angle γ between the waves and the current to quantify the wave-current interaction.
- the median grain size (D_{50}) to quantify the sediment.

This yields five variables for the flow and one for the sediment. To simplify the case even more, consider that the waves and the currents are co-linear and the change in water elevation, h, is so small that it can be neglected. Despite the fact that this approximation holds for only a limited number of scenarios, four-variables are needed to describe the problem (considering equilibrium conditions only). Therefore, in order to plot the simplest phase diagram, a non-intuitive four-dimensional graphic is needed. Nevertheless, two possible solutions are proposed in the literature: dimensionless quantities (e.g., flow Reynolds number [$Re = \frac{U\,L}{\nu}$], Einstein parameter [$\theta = \frac{\tau_b}{\rho g R D_{50}}$], dimensionless particle size [$R_{ep} = \frac{\sqrt{gRD_{50}}D_{50}}{\nu}$]) or fixed parameters (e.g., $D_{50} = 250\ \mu\text{m},\ h = 0.5\ \text{m},\ T = 10\ \text{s}$).

The use of dimensionless parameters for the axis of phase diagrams is generally used by the engineering community (e.g., Figure 3.1a). Such quantities are a combination of relevant variables that describe a characteristic process of the system. In this way, the diagram is able to include more than two of the relevant variables while quantifying a significant process. Dimensionless diagrams can be applied to a wide range of conditions even if there is no data available on such states (e.g., change in D_{50}). On the other hand, geologists have often used

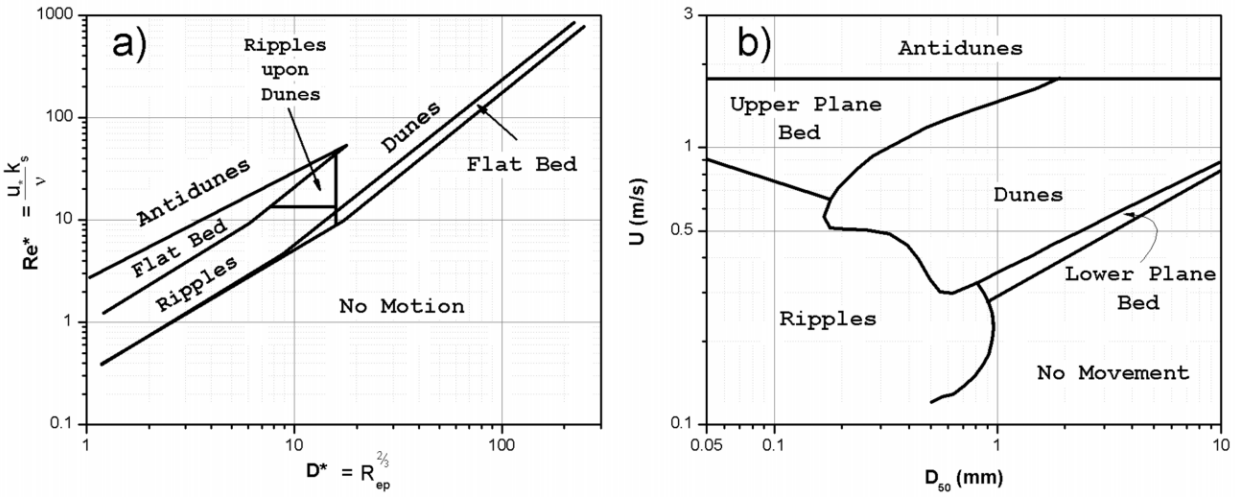

Figure 3.1: Unidirectional bedform diagrams. (a) Shear Reynolds number (dimensionless shear velocity) versus Bonnefille parameter, D_* (dimensionless grain size), where u_* is the shear velocity, k_s is a skin friction coefficient and ν is the dynamic viscosity. After Bonnefille-Pernecker (from Bechteler et al., 1991) (b) Velocity [$m\ s^{-1}$] versus mean diameter [mm] for a fixed water depth of 0.25-0.40 m. Modified after Southard and Boguchwal (1990).

phase diagrams with a number of fixed variables (e.g., Figure 3.1b). Such simplification allows the use of standard variables on the axes, making it easier to relate with natural conditions (more intuitive but more restrictive). In addition, zones of the phase diagram can be defined for a single morphological stage (data collapse). In general, this holds true in all dimensional diagrams, but it is not the case for dimensionless diagrams. The data collapse in the non-dimensionless diagrams is achieved by the lack of variability in the data generated by the fact that some of the parameters are fixed. It is important to note that the dimensions used in the phase diagrams proposed by Southard and colleagues (e.g., Southard and Boguchwal, 1990; Arnott and Southard, 1990; Dumas et al., 2005) are standardized to an arbitrary water temperature (10°C). This standardization was accomplished by multiplying the variables in the axes to the ratio of the dynamic viscosities (μ) at the reference temperature (10°C) and the actual temperature

$$\begin{aligned} d_{10} &= d\left(\frac{\mu_{10}}{\mu}\right)^{2/3} \\ U_{10} &= U\left(\frac{\mu_{10}}{\mu}\right)^{1/3} \\ D_{10} &= D\left(\frac{\mu_{10}}{\mu}\right)^{2/3} \end{aligned} \tag{3.1}$$

where d_{10}, U_{10} and D_{10} are the standardized water depth, velocity and grain size respectively.

Both approaches have been used to obtain phase diagrams for unidirectional, oscillatory and combined flows (e.g. Liu, 1957; Simons et al., 1965; van Rijn, 1984b; Southard, 1991; García, 2008). However, there are still many controversies on what the bed states are, how they may be classified and where the transitions are between each stage (e.g., Ashley, 1990). Therefore, it is important to define the bed configuration for each flow condition. The following subsection will present a brief overview of the bedforms formed under unidirectional, oscillatory and combined flows.

3.2 Unidirectional Flows

3.2.1 Initiation of Bedforms

Bedforms generated in aqueous flows are omnipresent in many environments (e.g., fluvial, glaciofluvial, deltaic and deep sea), although there is still some debate on how they develop. The initiation of bedforms have two - not mutually exclusive - models: defect initiation and instantaneous initiation (e.g. Best, 1992; Coleman and Melville, 1996; Venditti et al., 2005a). The defect theory proposes that the turbulent sweeps that are generated in turbulent flows (Willmarth and Lu, 1972; Lu and Willmarth, 1973) entrain sediment (Grass, 1983) that upon deposition generates defects in a non-cohesive material. These deposits then propagate downstream via a flow separation process, thus developing bedform fields. Furthermore, Best (1992) suggested that the origin of the defects is linked to packets of hairpin vortex structures. These coherent turbulent flow structures give rise to entrainment corridors on the mobile bed, forming grain lineations that interact with the low-speed streaks generating an agglomeration of grains. Once a critical height of grains is reached, flow separation occurs over the new structure. Sediment will be eroded close from the reattachment point and deposited downstream creating a new defect. This new defect will thus induce formation of another defect and the process will continue, propagating downstream while the accumulations of grains quickly evolve into small bedforms (Figure 3.2).

In general, the defect propagation theory plays a bigger role at low sediment transport rates since for high rates defects maybe washed away and bedforms generally initiated across the entire bed spontaneously (Venditti et al., 2005a, 2006). Venditti et al. (2005a) report that instantaneous initiation begins with the formation of a cross-hatch pattern, which leads to chevron-shaped forms that migrate independently of the pattern structure. This chevron-like structure reorganizes to form the future crest lines of the bedforms (Figure 3.2). Venditti et al. (2006), based on the earlier model by Liu (1957), proposed that instantaneous initiation is a manifestation of an interfacial hydrodynamic instability of Kelvin-Helmholtz type

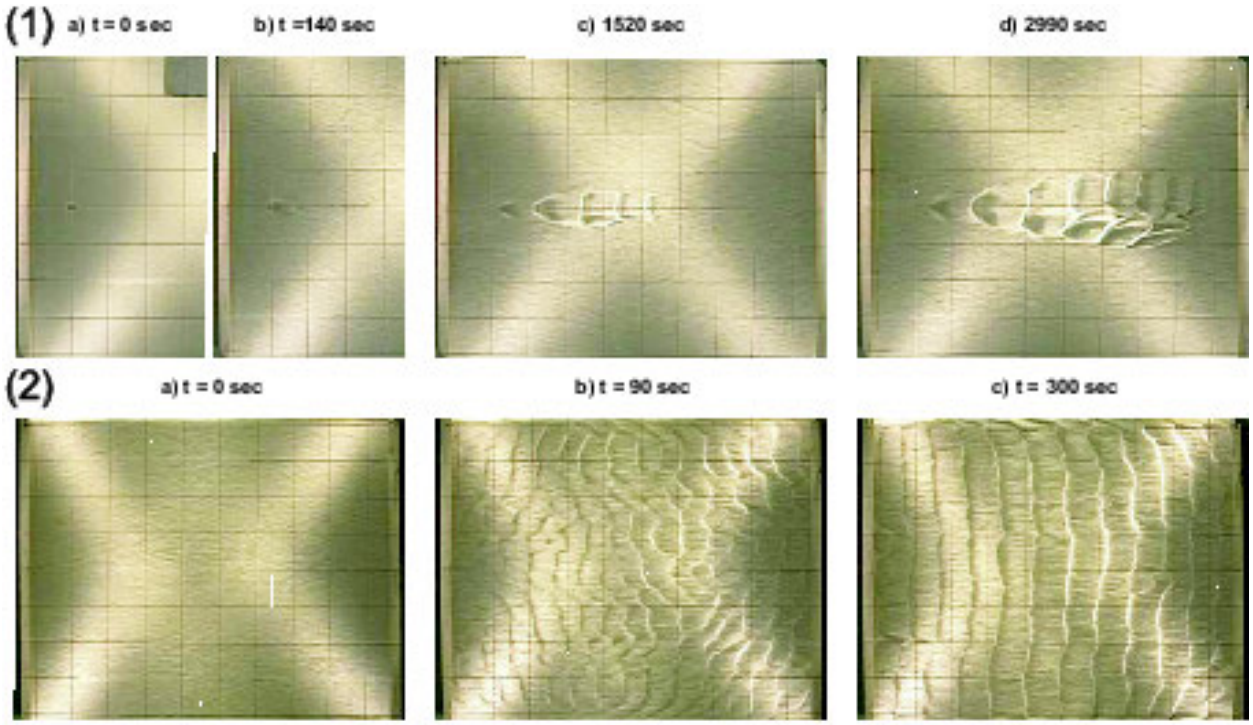

Figure 3.2: Initiation of bedforms under unidirectional flows. 1) Evolution of bedforms from a negative defect. 2) Evolution of the bed through instantaneous initiation of bedforms. Grid spacing is 0.115 m, and flow is left to right. After Venditti et al. (2005a).

between a highly active pseudofluid sediment layer and the fluid above it. In addition, Venditti et al. (2005a) imply that there is no linkage between the instantaneous initiation and coherent turbulent flow structures, since spatially- and temporally-random events should lock in place to generate the cross-hatch pattern. Moreover, there is no clear explanation of the effect of turbulence in the formation of bedforms since bedforms may also occur under laminar flows (e.g., Coleman and Eling, 2000;Devauchelle et al., 2010). It is important to note, that laminar-generated bedform studies used the temporally-averaged flow conditions to determine the degree of turbulence, indicating Reynolds number in the laminar regime. However, instantaneous process, such as burst and sweeps, which are infrequent at low Reynolds number but still present, can be the driving mechanisms to generate the bedforms. The generation of bedforms in laminar flows is still a topic of debate within the scientific community, since if true, it suggests that there should be other processes for defect devel-

opment other than the one suggested by Best (1992). This alternative model for bedform development at low sediment transport rates should explain the generation of defects and bedforms for cases where the flow is not turbulent.

3.2.2 Current Ripples

Current ripples are more or less regularly-spaced flow-transverse bedforms with height (η) generally smaller than 50 mm and length (λ_η) up to 0.5 m. In addition to η and λ_η, a set of dimensionless parameters can be defined for description of bedform geometry:

$$\begin{aligned} RI &= \lambda_\eta\ \eta^{-1} && \text{Ripple Index} \\ RSI &= \lambda_s\ \lambda_l^{-1} && \text{Ripple Symmetry Index} \\ RRI &= \lambda_{0.5\,s}\ \lambda_s^{-1} && \text{Ripple Roundness Index} \end{aligned} \tag{3.2}$$

where λ_s is the length of the stoss side, $\lambda_{0.5\,s}$ is the length from crest to stoss at half the height of the bedform and λ_l is the length of the lee side (Figure 3.3). The set of dimensionless

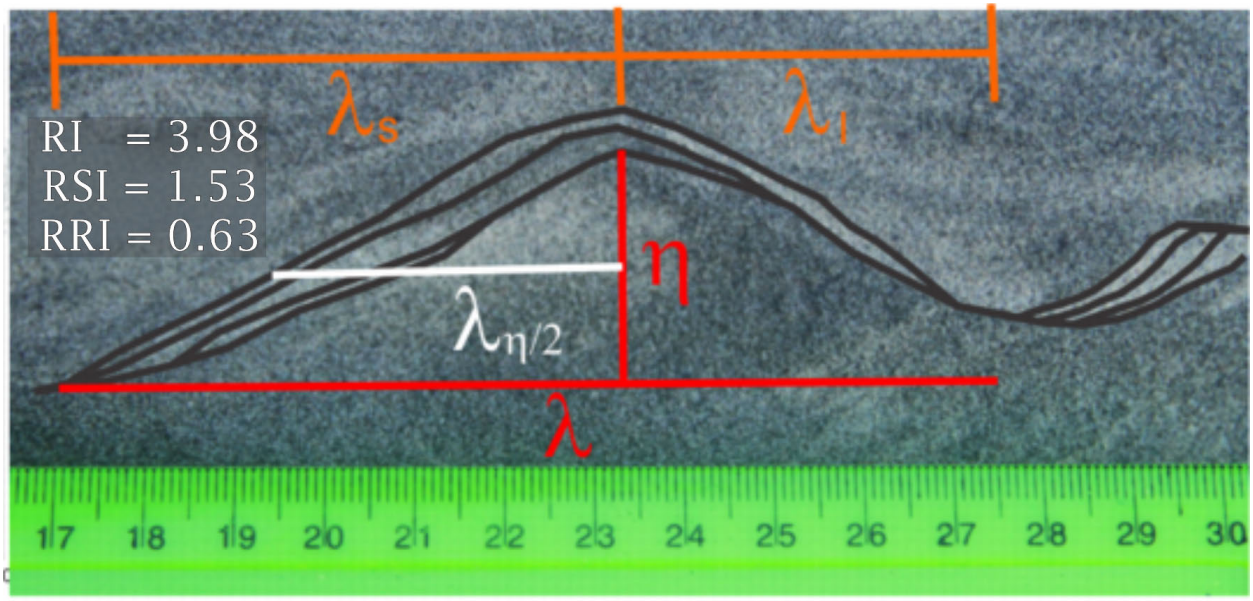

Figure 3.3: Ripple index measured in an outcrop, Rio Negro Formation, Argentina. Ripple indices are obtained using Equation 3.2.

numbers defined in Equation 3.2 are generally called ripple indices but can be applied to

larger bedforms such as dunes. For the case of unidirectional ripples, the range of ripple indices are (Tanner, 1967, 1965, 1964; Yokokawa, 1995; Dumas et al., 2005)

$$\begin{aligned} 10 \leq \quad & RI & \leq 60 \\ & RSI & \geq 5 \\ & RRI & \approx 0.5 \end{aligned} \tag{3.3}$$

In addition, ripples are characterized by an angle-of-repose ($20 - 35\,^{\circ}$) leeside and a more gentle stoss side ($5 - 10\,^{\circ}$). Ripples are stable for sediment sizes smaller than 0.7 mm and for a range of low flow velocities (Southard and Boguchwal, 1990). The geometry of current ripples has been proposed to have a strong relationship with grain size

$$\begin{aligned} \lambda &= 1000\, D_{50} && \text{Yalin, 1964} \\ \lambda &= 75.4 \log D_{50} + 197 && \text{Baas, 1993} \\ \lambda &= 245\, D_{50}^{0.35} && \text{Raudkivi, 1997} \end{aligned} \tag{3.4}$$

but no evident relationship with flow strength or flow depth.

Another characteristic feature of fully developed current ripples is a three-dimensional planform geometry (Figure 3.4). Experimental work by Baas (1994, 1999) has shown that there are four stages in the development of current ripples starting from a flat bed: a very early (α) stage where a few grains are transported in patches, or incipient ripples a few grains in height and a few cm long. These incipient ripples gradually grow up to 10 mm in height and 0.1 m in wavelength, forming straight and sinuous ripples in the β stage. As the height and wavelength keep increasing in size, the bedforms become more three-dimensional reaching a more linguoid shape (γ stage). Once the γ stage is reached, the planform geometry stays in a three-dimensional linguoid shape. The main difference between ripples in the γ and δ stages is that ripples in the γ stage are still growing (non-equilibrium). Once the equilibrium height and wavelength are reached, the ripples are in the δ stage. Experimental work by Baas

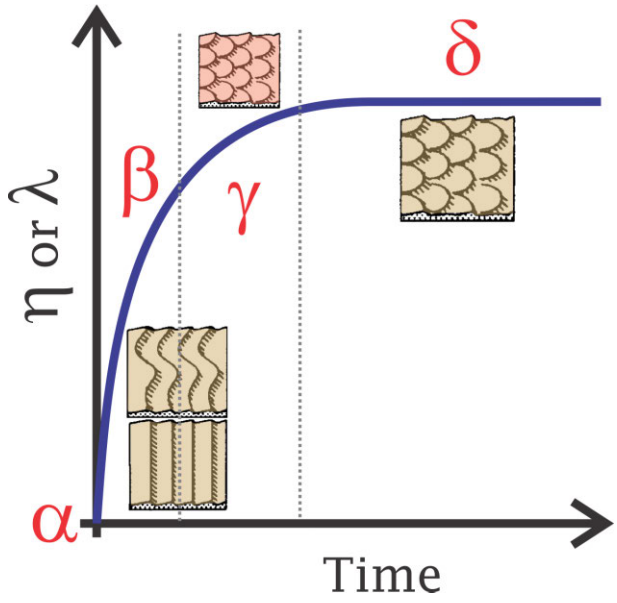

Figure 3.4: Conceptual model of planform geometry development for unidirectional flow ripples. See text for description on the stages of development ($\alpha - \delta$). The dotted lines illustrate the overall time where the transition between stages occurs. Modified from Baas (1994, 1999)

(1994, 1999) shows that two-dimensional (straight and sinuous ripples) are non-equilibrium bedforms for a wide range of flow velocities. Venditti et al. (2005b) found a similar result for dunes. Furthermore, Venditti et al. (2005b) describe that the origin of three-dimensionality is produced by the abundance of deficiencies of sand, or crest defects that are passed from one bedform crest to another. The bedform field is capable of absorbing some small number of those defects but, once the number grows, the constant change in the crestline leads to the disruption of the continuous crest, therefore generating three-dimensionality.

In addition, the flow must adjust to the presence of a geometry in the bed; as the flow moves over the stoss side of the current ripple, it accelerates and becomes detached from the bed at the brinkpoint of the ripple forming a separation zone and a shear layer (Figure 3.5) in the leeside. The generation of such shear layers is characterized by the presence of vortices. Four quadrants can be defined from the fluctuations in horizontal velocity, $u = \bar{u} + u'$, and vertical velocity, $v = \bar{v} + v'$: quadrant 1 [+u' +v'], quadrant 2 [-u' +v'], quadrant 3 [-u' -v'], and quadrant 4 [+u' -v'], where an overbar indicates the time-averaged value of this

component of velocity and the prime denotes the instantaneous variations from that mean (see Section 2.1.3). Positive values of vertical flow indicate flow upward and away from the

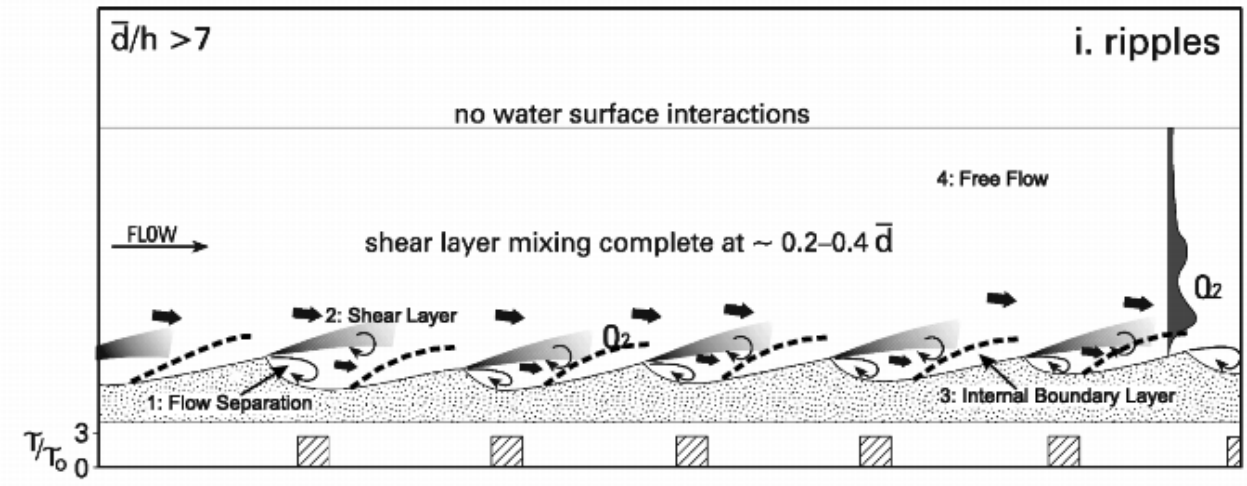

Figure 3.5: A conceptual model of flow over a ripple. From Fernandez et al. (2006), after Bennett and Best (1996) . τ and τ_0 represent the bed shear stress and threshold bed shear stress for sediment entrainment, respectively. Q_2 and Q_4 (arrows) denote quadrant 2 and 4 events. $\bar{d}$ is the flow depth and h bedform height.

bed, with the vortices generated along the shear layer and at flow reattachment being largely manifested as quadrant 2 events. In addition, the near-bed flow is decelerated and reversed in the flow-separation zone. In the internal boundary layer that develops on the stoss side of the downstream ripple (Figure 3.5), the near-bed velocity increases progressively from the flow-reattachment zone towards the bedform crest. Ripples do not interact with the water surface, generating a zone between the shear layer and the water surface where flow can be assumed to be free of the individual structures generated by the bed. However, the flow still feels an average roughness that is a function of all the individual ripples and their flow structures (Figure 3.5).

3.2.3 Dunes

Dunes are also sometimes mistakenly called megaripples due to their similar shape but larger size compared with ripples (e.g., Allen, 1982; Ashley, 1990; Gallagher, 2003; Passchier and

Kleinhans, 2005). However, ripples and dunes are different bedforms, that differ not only in size but also in their interaction with the flow, hence with each element of the SFD "trinity". Dunes generally have a wavelength larger than 0.6 m and heights greater than 40 mm, with a relatively higher RI than ripples, varying from 40 to 100. No previous work was found to address the characteristic values for RRI or RSI. However, it can be assumed that the values should not differ much from these for current ripples. Dunes form in sediments ranging from 0.1 mm up to gravels, with moderate to strong flows with Froude numbers ($Fr^2 = \frac{U^2}{g\,h}$) lower than unity (these range of flow conditions depend strongly on the water depth). Unlike ripples, most researchers agree that equilibrium dunes do not scale with the grain size, but rather with water depth (h) where their size increases with flow depth;

$$\lambda \approx [1 - 16]\, h \tag{3.5}$$

$$\eta \approx [0.025 - 0.16]\, h \tag{3.6}$$

where numbers in the brackets indicate the range of valid values for the relations (Allen,

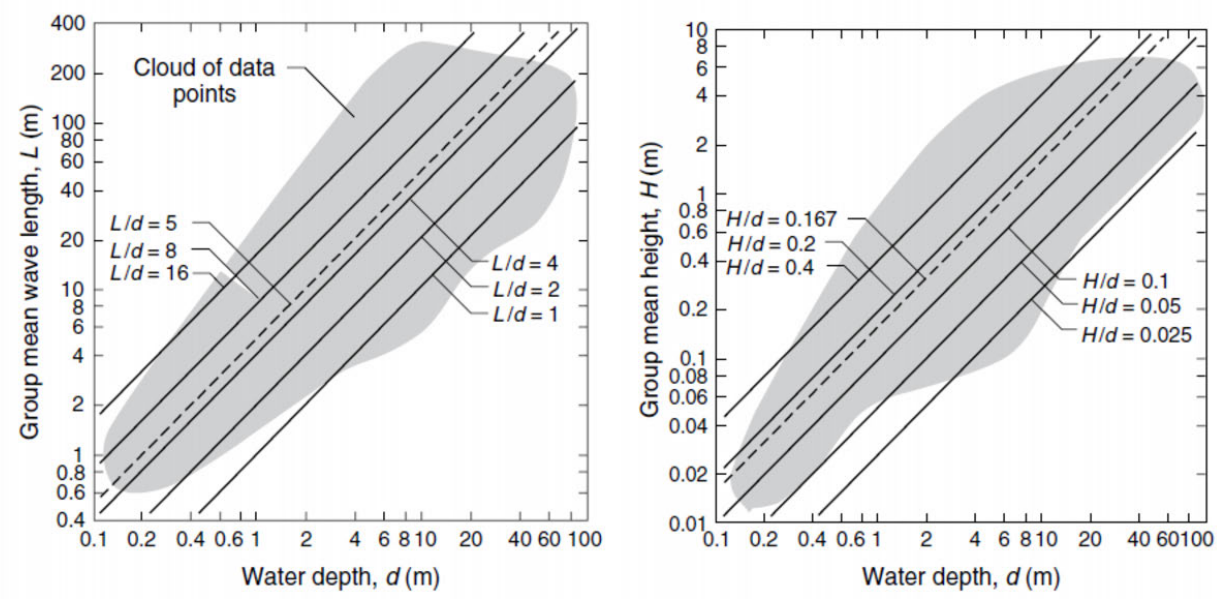

Figure 3.6: Height and length of dunes as a function of water depth. From Bridge and Demicco (2008, Page 164).

1982). However, due to the large scatter in the relationships between water depth and dune size, several studies have raised the question if dunes really scale with water depth. Following this argument, recent work proposed by Bartholdy et al. (2005) suggests that dunes are primarily controlled by grain size and flow strength and are independent of flow depth. Furthermore, Bartholdy et al. (2005) infer that, for small enough water depths, the limitation of the flow depth will influence any bedform (including current ripples) making it a scaling factor. On the other hand, it has been proposed that dunes actually scale with the bedform-generated-boundary-layer (Southard, 1991). Nevertheless, there is also a large

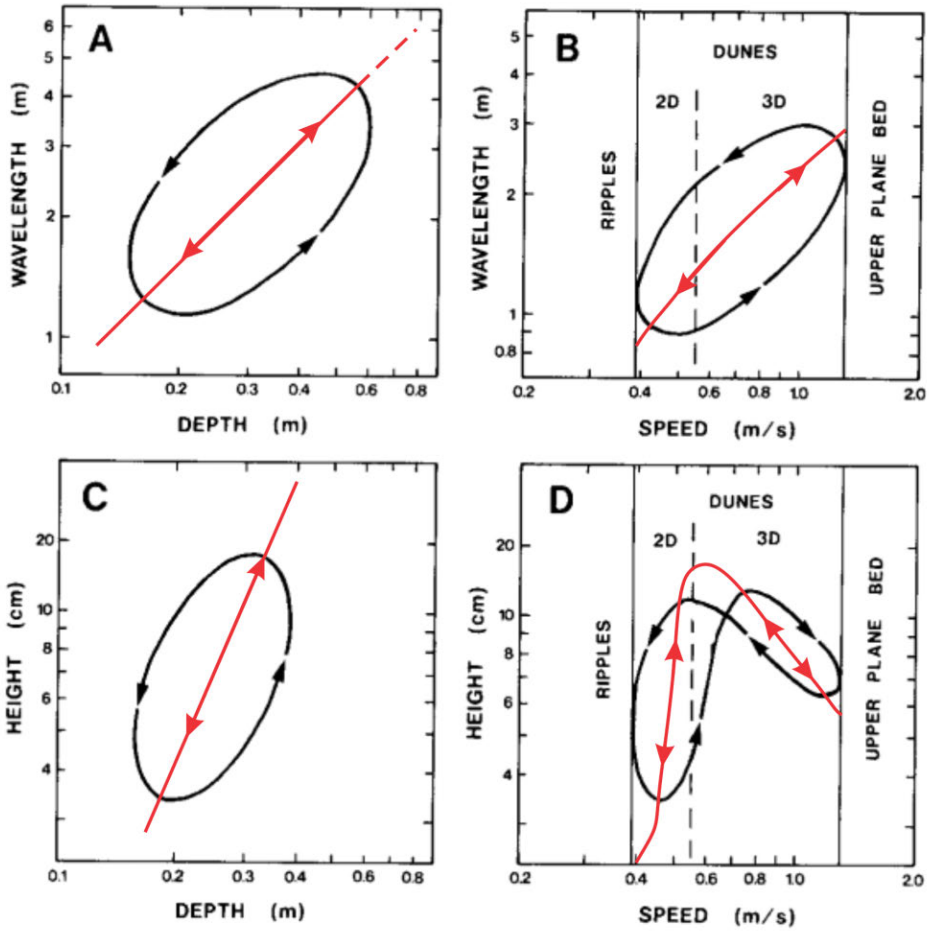

Figure 3.7: Idealized representation of hysteresis loops expected for dune wavelength and height, due to variations in water depth and current speed. The red line in each section is the equilibrium relationship predicted from Equation 3.6. The black line in each section represents the idealized behavior of the dunes by changing flow depth (a and c) or flow speed (b and d). From Dalrymple and Rhodes (1995).

scatter in the boundary layer dune size relationships. The majority of the scatter could be associated to the difficulties of measuring a single height or wavelength in a generally very three-dimensional environment that has a dune size distribution instead of a single value (Paola and Borgman, 1991; Leclair et al., 1997). In addition, unstable dune fields - which do not scale with water depth - might be left from a previous short-duration stronger flow condition due to the large lag between flow and morphological changes (e.g., Allen and Friend, 1976; Allen, 1976; Dalrymple and Rhodes, 1995). This lag is called bedform hysteresis and can easily be seen by plotting dune height or wavelength against a flow parameter that is changing (Figure 3.7). If the bedform size were fully developed and in equilibrium with the flow, all points would follow a single path (red lines in Figure 3.7). However, due to hysteresis, paths can follow a wide range of pathways depending on changes in the flow (black lines in Figure 3.7).

Nevertheless, even though dunes might not scale with water depth, it has been shown that the presence of dunes produces a distinct flow structure throughout the entire flow depth (Figure 3.8), often generating large-scale turbulence that erupts on the water surface as 'boils' or a 'kolk-boil vortex' (e.g., Coleman, 1969; Jackson, 1976; Best, 2005). Dunes that have an angle-of-repose leeside will have a well-developed separation zone (Figure 3.8) of permanent recirculating flow, a very high turbulence intensity shear layer (Figure 3.8) and the near-bed velocity will accelerate from the flow-reattachment point to the downstream crest (e.g., Kostaschuk, 2000). However, such overall flow structure is not characteristic of all dunes. Recent field studies, especially in large sand bed rivers, have shown that a common feature is either more symmetrical dunes that have a gently sloping lee/stoss sides without flow separation or low-angle asymmetrical dunes with intermittent to no separation (e.g., Kostaschuk and Villard, 1996; Best and Kostaschuk, 2002). The 'symmetric' dunes have stoss and lee sides of similar length, stoss and lee slope angles lower than 8 °, and rounded crests, whilst asymmetric dunes have sharp crests, stoss sides longer than their lee sides, stoss side slopes lower than 3 ° and straight lee side slopes up to 19 °, and generally have

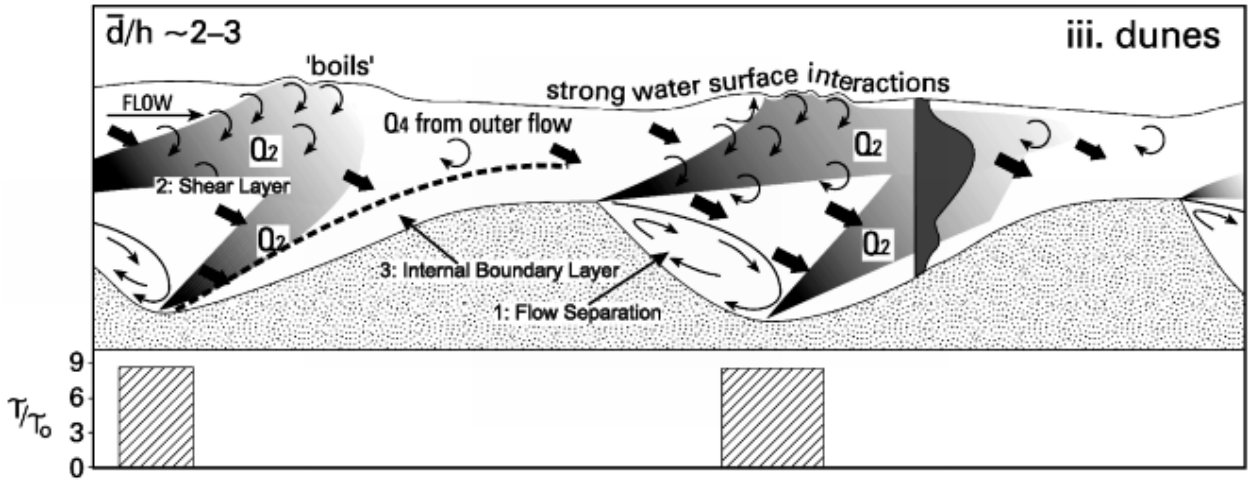

Figure 3.8: A conceptual model of flow over a dune. From Fernandez et al. (2006), after Bennett and Best (1996). τ and τ_0 represent the bed shear stress and threshold bed shear stress for sediment entrainment, respectively. Q_2 and Q_4 (arrows) denote quadrant 2 and 4 events, respectively (Q_2: -u', +w' ; Q_4: +u', -w').

superimposed small dunes or ripples on their stoss sides. Crestal rounding of the bedforms is associated with high sediment transport rates and high near-bed velocities (Figure 3.9). This type of dune cannot be classified as a traditional dune which assumes a highly asymmetric shape, sharp crest and lee side flow separation (e.g., Bennett and Best, 1995; Kostaschuk, 2000). However, there is presently no better classification scheme other than calling *dunes* a bedform that is characteristic of unidirectional flows, that are larger than ripples when fully developed, can be three-dimensional, asymmetrical, with flow-separation and with flow depth as a scaling parameter. On occasion, dunes can be more two-dimensional, symmetrical, without permanent flow-separation and possess a bedform geometry that is independent of flow depth.

3.2.4 Upper-stage plane beds

Ripples and dunes transition to upper-stage plane beds (USPB) as the bed shear stress and sediment-transport rate are increased. As ripples and dunes get closer to the transitional zone, the increase in shear stress makes the bedform become more rounded and smaller in

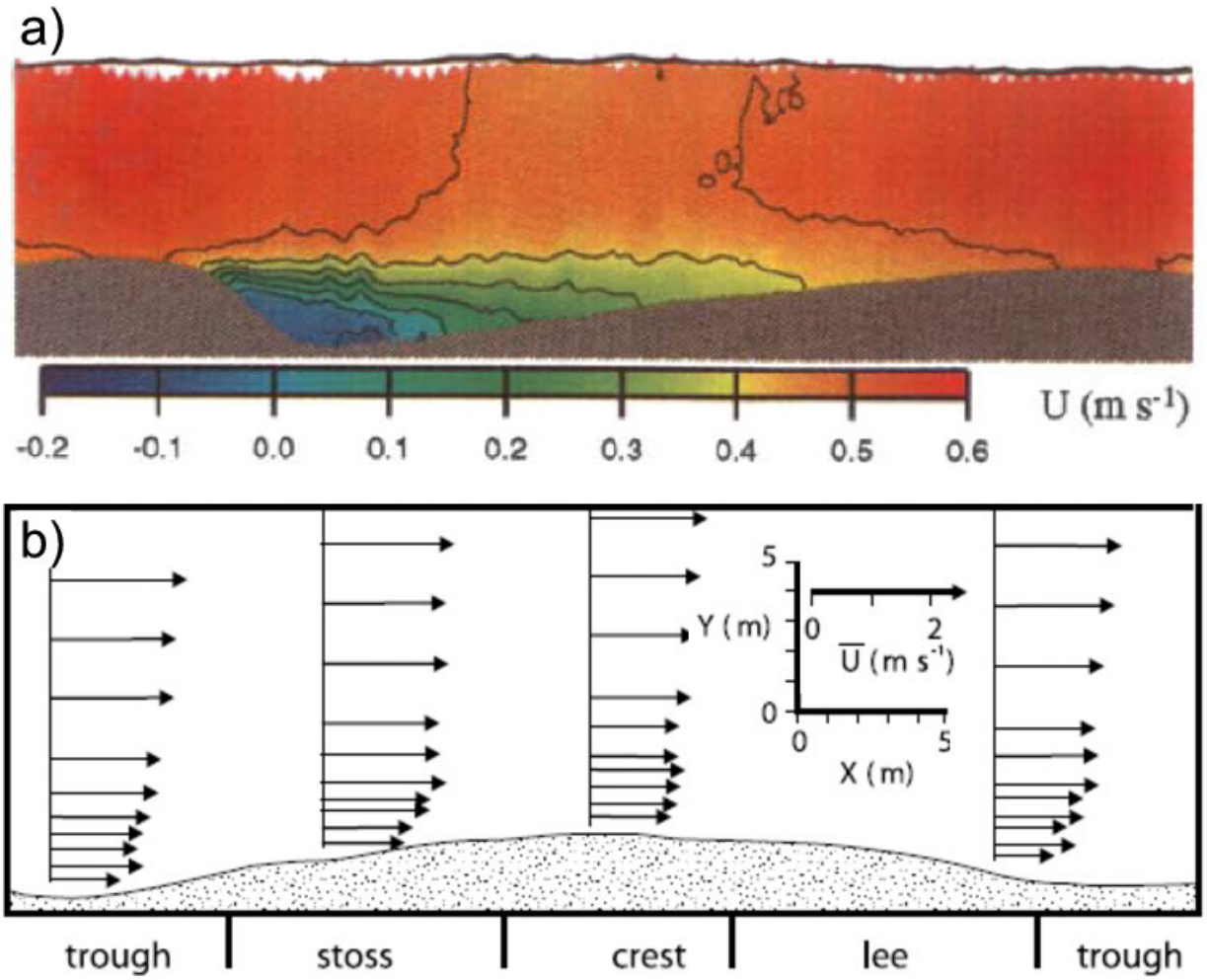

Figure 3.9: Flow structure for angle-of-repose leeside (a) and low-angle dunes (b). a) Contour maps of time-averaged downstream velocity from flume experiments. Vertical exaggeration is 1.3 x. After Bennett and Best (1995). b) Mean horizontal velocity over a low-angle dune in the Fraser River, Canada. After Best and Kostaschuk (2002).

height compared with their length (Figure 3.10). In addition, the previous brink point of the dune will gradually move downstream of the slip face until no flow separation occurs (Saunderson and Lockett, 1983). As dunes become rounded in the transition to USPB, the horizontal and vertical turbulent motions in the troughs decrease progressively while horizontal turbulence intensities increase near the bed on the dune backs (similar to low-angle dunes, Figure 3.9b). As the bed shear stress rises during the transition, the suspended and bedload concentrations increase progressively and the near-bed transport rate decreases

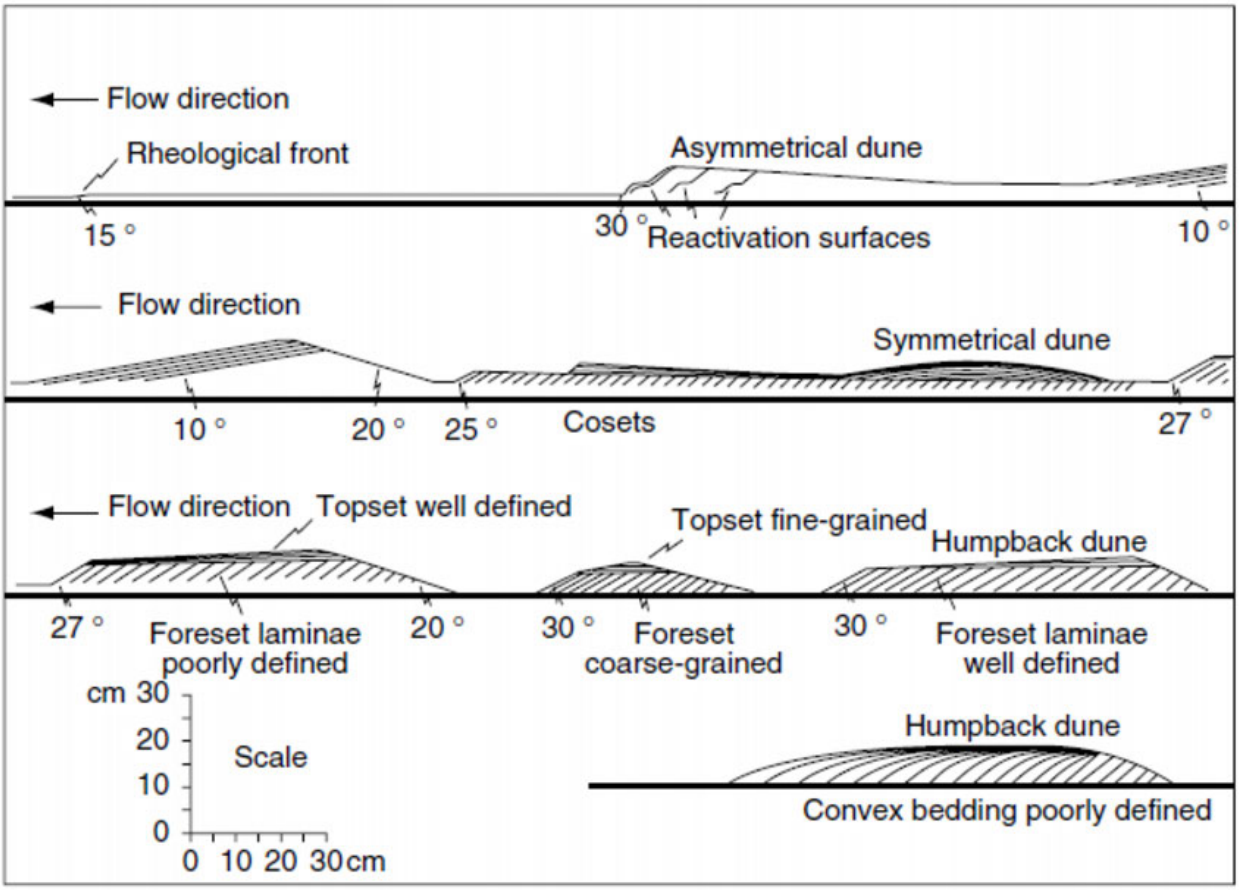

Figure 3.10: Types of experimental dunes and their internal structures formed near the transition to upper-stage plane beds. From Saunderson and Lockett (1983).

in the vicinity of the dune crests relative to the region immediately downstream of flow reattachment (Saunderson and Lockett, 1983). The increase in sediment transport near the reattachment zone has been linked to suppression of upward-directed turbulence by increased sediment concentration (Bridge and Best, 1988). In addition, upper-stage plane beds are rarely completely flat, and low-relief bedforms several millimeters in height and meters in length are present. These bedforms are asymmetrical in the flow direction, but the lee slope rarely approaches the angle of repose. The mean length/height ratio of these bedforms is similar to that of curved-creasted dunes, suggesting that these low-relief bedforms are dunes that cannot grow in height.

3.3 Oscillatory Flows

Bagnold (1946) classified bedforms produced by oscillatory flows into two main groups : rolling grain ripples and vortex ripples. Vortex ripples are bedforms with a height-to-length ratio large enough to form vortices in the lee of the crest, and those that are too small for vortex formation are called rolling grain ripples. Most researchers have been concerned principally with vortex ripples, although there is an agreement on using the name ripple to refer to any bedform that has been produced by an oscillatory flows (Bagnold, 1946; Stokes, 1950; Davis, 1965; Komar, 1974; Lofquist, 1978; Allen, 1979; Clifton and Dingler, 1984; Southard, 1991; Wiberg and Harris, 1994; Sekiguchi and Sunamura, 2004; Cummings et al., 2009; Pedocchi and García, 2009b,c). In the following subsections, the most common bed morphologies for wave ripples will be discussed.

3.3.1 Initiation of Bedforms

Experiments on bedform initiation under oscillatory flows have shown the same two mechanisms as unidirectional flows: defect initiation and instantaneous initiation (Lofquist, 1978). Unlike unidirectional flow research, these two models lack a detailed study such as that conducted by Venditti et al. (2005a, 2006). However, it has been observed that a slight local elevation or depression on the sand surface of a flat bed enhances the formation of ripples in that locality (Figure 3.11) and, once begun, the ripples spread out over the surface while growing in size (Bagnold, 1946; Lofquist, 1978). Lofquist (1978) proposed that there is a critical maximum orbital velocity, not defined, at which spontaneous ripples form. Lofquist (1978) suggested that spontaneous generation occurs since the instantaneous ripples develop faster than those generated by local perturbations. Figure 3.11 shows the formation of vortex ripples. Away from the defect, development begins with the generation of a low height to length ratio, transient bedforms, that are called rolling grain ripples.

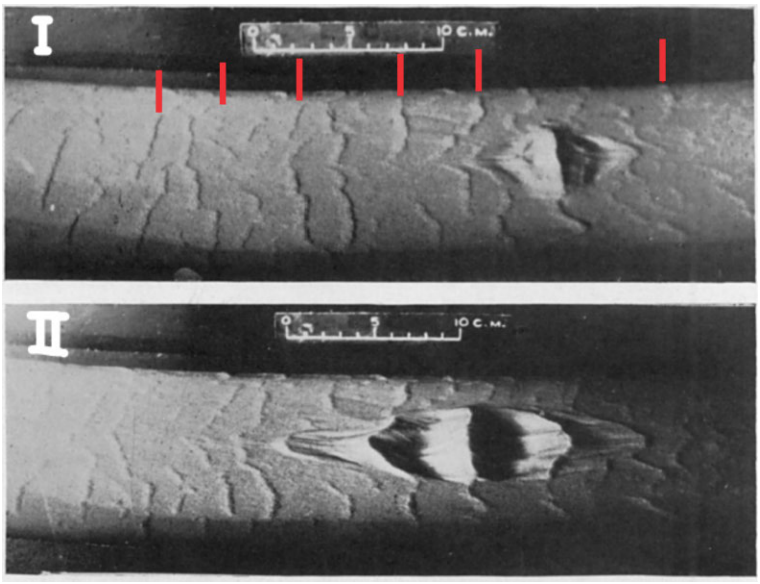

Figure 3.11: Initiation of bedforms under oscillatory flows from a positive defect. I) Evolution of bedform field after a few wave oscillations have occurred. The defect begins to propagate whilst small rolling grain ripples (red lines) form from the flat bed. II) Later evolution of the bed, with the original defect now evolving to a more developed bedform, and the presence of rolling grain ripples has decreased significantly. After Bagnold (1946).

3.3.2 Rolling grain ripples

Rolling-grain ripples are the first bedforms to appear on an initially plane bed when oscillatory flows start entraining sediment. As described above, the most characteristic feature of rolling grain ripples is that, due to the low height-to-length ratio (about 0.1), this bedform does not form vortices in the lee side of the crest. Andersen (2001) proposed a simple model for the formation of rolling grain ripples by evolving an equation of motion for each particle. In the model of Andersen (2001), the particles originally represent grains, but as the single grains quickly merge, the particles in the model represent a larger amount of grains which can be considered ripples. Based on this model, Andersen (2001) proposes that the final distance between the ripples is proportional to $(\theta - \theta_c)^{0.5}$, where θ is the Shields parameter and θ_c is the critical Shields parameter. On the other hand, experiments conducted by Lofquist (1978) with 0.18 and 0.21 mm sand grains produced bedforms resembling the rolling-grain ripples reported by Bagnold (1946). However, such bedforms were not present

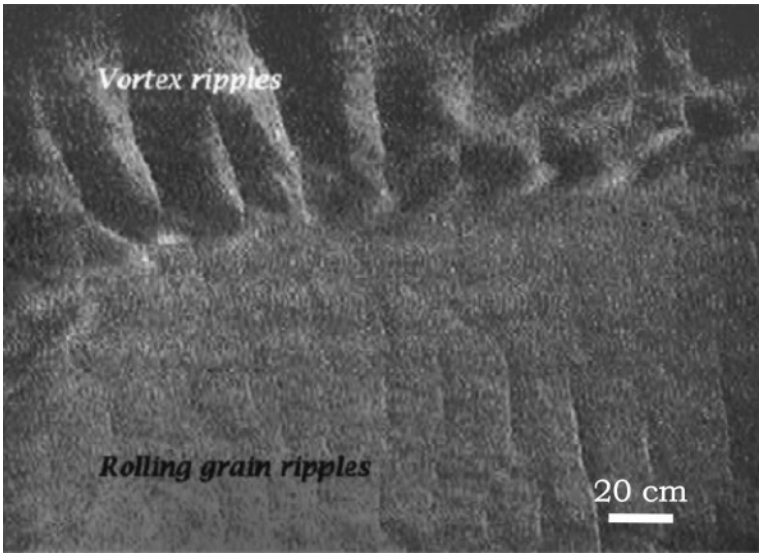

Figure 3.12: Rippled bed consisted of rolling grain ripples (bottom) and vortex ripples (top). Sand size has a median diameter of 0.2 mm. From Andersen (2001).

in experiments conducted with 0.55 mm sand grains (Lofquist, 1978).

3.3.3 Vortex ripples

The essential feature of vortex ripples is the presence of recirculating cells of fluid in the leeside of each crest. For this reason, a brief description on the formation of vortex eddies will be discussed. For the case of small height-to-length ratios, explicit analytical solutions for a pure oscillatory flow can be obtained from the governing equations. It is convenient to define a curvilinear coordinate system (χ, ζ)

$$\chi = x + \frac{\eta}{2} e^{-k\zeta} \sin(k\chi) \tag{3.7}$$

$$\zeta = z - \frac{\eta}{2} e^{-k\zeta} \cos(k\chi) \tag{3.8}$$

where z is measured from the mean bed level (Figure 3.13). If the bed is taken to be $\zeta = 0$,the bottom profile is

$$z = \frac{\eta}{2} \cos(k\chi) \tag{3.9}$$

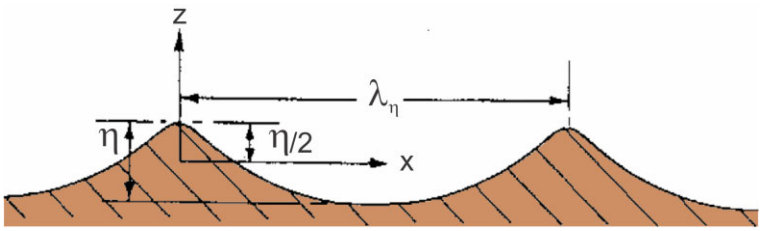

Figure 3.13: Sketch for the ripple profile defined by Eqs (3.7) and (3.8). After Sleath (1984).

When the height (η) to length (λ_η) ratio is very small, the bed profile is sinusoidal, but, as it gets larger, the crest becomes more pointed and the troughs become flatter. Consequently, assuming that Equation 2.35 uses ζ instead of z to represent the flow displacement per unit of time for this bed profile, a first approximation of the velocity profile is:

$$u = U_\infty \left[\cos(\omega t - kx) - e^{-\beta\zeta}\cos(\omega t - kx - \beta\zeta)\right] \tag{3.10}$$

If the solution of the velocity is carried to higher orders of η/λ_η, Equation (3.10) not only becomes more complex, but the result also has terms that are independent of time. These steady currents are reflected in recirculating cells of fluid over the bedform (Figure 3.14). For small values of $\beta\lambda_\eta$, there are only two recirculating cells for each ripple, but if $\beta\lambda_\eta$ becomes larger, which is the general case, four vortices are produced by the flow conditions. Kaneko and Honji (1979) were able to demonstrate experimentally that when the ratio of the wavelength of the wavy wall to the thickness of the Stokes layer becomes larger than about $\beta\lambda \cong 26$, the streaming that has two recirculating cells transforms into a double structure consisting of regions of upper and lower pairs of recirculation cells (Figure 3.14).

These mechanisms are of vital importance in the growth and stability of bedforms in pure oscillatory flows. Such oscillation will cause equal eddies in each side of the ripple, which eventually will form very regular straight-crested ripples. In contrast with the relative paucity of work conducted on rolling grain ripples, numerous experiments have studied vortex ripples (*Field*: Komar (1974); Dingler (1974); Doucette (2002); Xu (2005), *Experimental*: Bagnold (1946); Carstens et al. (1969); Mogridge and Kamphuis (1972); Sato (1987);

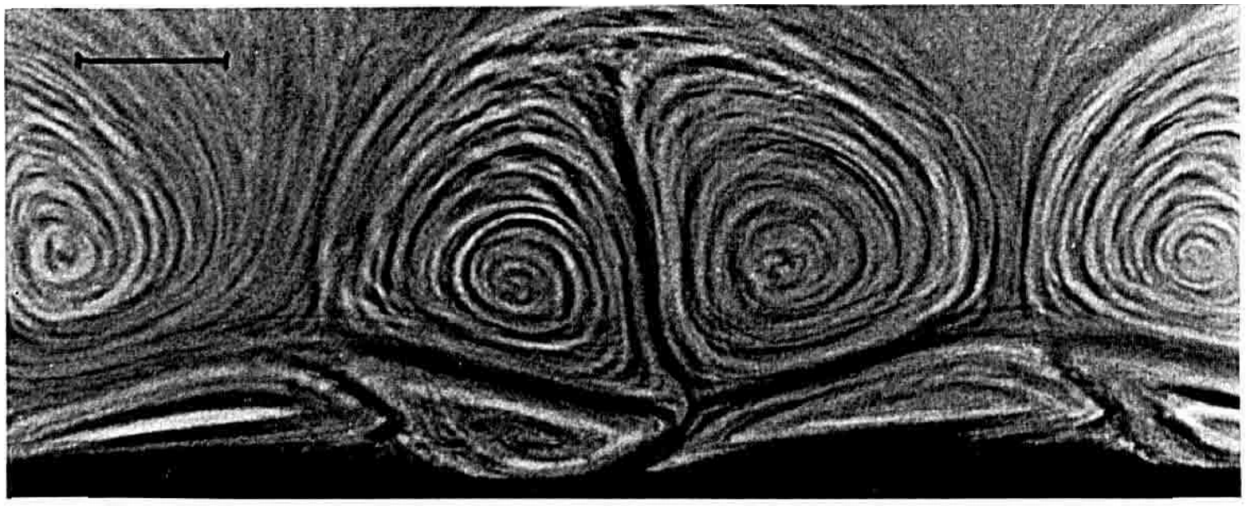

Figure 3.14: Streamlines above vortex ripples of glass beads in a viscous fluid visualized by dye. Scale bar: 20 mm. Note the presence of standing vortices. From Honji et al. (1980).

Southard (1991); Wiberg and Harris (1994); Ribberink and Al-Salem (1994); Earnshaw and Greated (1998); Traykovski et al. (1999); Sekiguchi and Sunamura (2004); Cummings et al. (2009); Pedocchi and García (2009b,c) *Theoretical*: Kennedy and Falcon (1965); Clifton and Dingler (1984)). Following the work done by Yalin and Russell (1962), Carstens et al. (1969), Mogridge and Kamphuis (1972) and Dingler (1974), Pedocchi and García (2009b) introduced three dimensionless numbers to characterize the oscillatory boundary layer and therefore geometry of vortex ripples:

$$\frac{\sqrt{g\,R\,D_{50}}\,D_{50}}{\nu}, \quad \frac{U_o\,D_{50}}{\nu}, \quad \frac{T\,\nu}{D_{50}^2} \tag{3.11}$$

where $\sqrt{g\,R\,D_{50}}\,D_{50}/\nu$ is a dimensionless particle size, Re_p (García, 2008), $U_o\,D_{50}/\nu$ is a a dimensionless maximum oscillation velocity written as a Reynolds number, and $T\,\nu/D_{50}^2$ is a dimensionless oscillation period (Yalin and Karahan, 1979). Based on Equation 3.11, Pedocchi and García (2009b) produced a diagram that provides insight on the hydrodynamics of oscillatory boundary layer flows (Figure 3.15). Figure 3.15 provides a good representation of the hydraulic conditions that would prevail for different sediment sizes. Data plotted in Figure 3.15 is a compilation of several studies with U_o varying between 0.2 and 2.0 $m\,s^{-1}$ and

T varying between 2.5 and 20 s for three sand sizes 500, 250 and 100 μm (references of the studies used are given in Pedocchi, 2009). For medium and small sand grains ($D_{50} = 100$ and 250 μm) the diagrams predicts that, depending on the flow conditions, there will be a region where the boundary layer is laminar, a region where the boundary layer is hydraulically smooth, and a region of transition. However, for the case of $D_{50} = 500\,\mu$m, the flow can be either transitional or fully rough without a smooth regime.

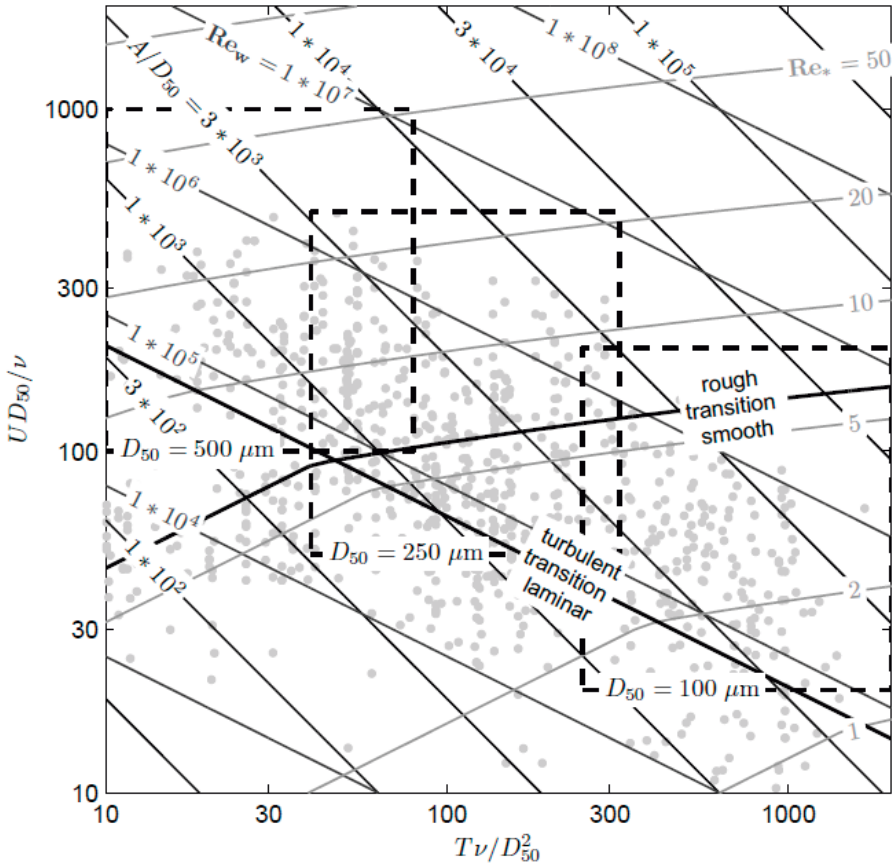

Figure 3.15: Dimensionless diagram showing the different dimensionless parameters controlling the hydrodynamics of the oscillatory boundary layer over a sediment bed. From Pedocchi and García (2009b).

Unlike unidirectional ripples, vortex ripples have a well-defined and stable two-dimensional planform geometry. Ongoing debate exists as to the role of grain size on the planform geometry of vortex ripples. Southard (1991) observed that for $D_{50} > 0.5$ mm, vortex ripples tend to be more two-dimensional. This value was later modified by O'Donoghue and Clubb

(2001) and O'Donoghue et al. (2006) to $D_{50} > 0.3$ mm. In addition, O'Donoghue and Clubb (2001) and O'Donoghue et al. (2006) observed that for normal to large water excursions, sands finer than 0.2 mm always developed three-dimensional vortex ripples. Several predictors for vortex ripple planform geometry can be found in the literature (Carstens et al., 1969; Lofquist, 1978; Vongvisessomjai, 1984; Sato, 1987; Pedocchi and García, 2009b) but none are fully able to predict the influence of grain size. Sato (1987) proposed that ripples are three-dimensional if

$$\frac{d}{D_{50}} > 1550 \quad \text{and} \quad \theta > 0.9 \left(\frac{d}{D_{50}}\right)^{-1/4} \tag{3.12}$$

On the other hand, Vongvisessomjai (1984) suggests that vortex ripples become three-dimensional when

$$\frac{A\,U_o}{\sqrt{g\,R\,D_{50}}\,D_{50}} > 5500 \tag{3.13}$$

However, recent work by Pedocchi and García (2009b) proposed a much clearer division between two and three dimensional ripples (Figure 3.16:a). For coarse sands ($Re_p > 13$ from Equation 3.11) ripples become two-dimensional if

$$Re_p > 0.06\,\sqrt{Re_w} \tag{3.14}$$

when Re_w is the wave Reynolds number. However, for values of Re_p smaller than 9, a mixed behavior is observed and the division is no longer clear. Equations 3.13 and 3.14 mainly associate the change in planform geometry to a change in grain size (D_{50}) and wave amplitude (A). However, the experimentally-obtained phase diagram of Southard (1991) (Figure 3.16:b) proposes that the 2D-3D transition depends strongly on wave period. The diagram predicts regular and straight-crested ripples (two-dimensional ripples) at low oscillatory speeds and small period and irregular (three-dimensional) ripples at high oscillatory speeds and long periods.

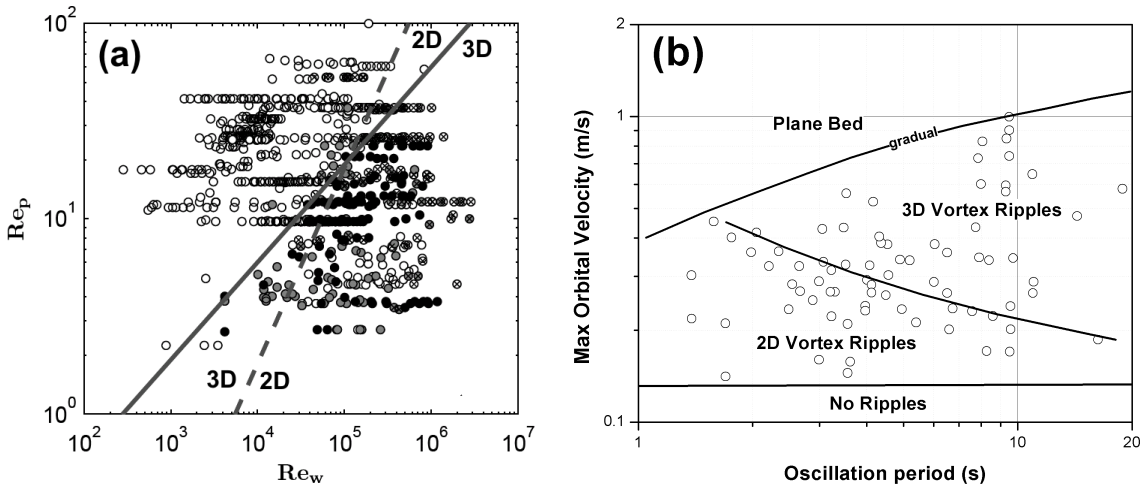

Figure 3.16: Planform geometry phase diagrams for oscillatory flows. a) Dimensionless prediction for vortex ripples. Notice the change of behavior for fine materials ($Re_p < 9$). Re_w is the wave Reynolds number. After Pedocchi and García (2009b). b) Velocity versus oscillation period diagram. Modified after Southard (1991).

Another method of ripple classification is to relate the characteristic parameters of the ripple with those of the flow. In particular, the relationship between the water orbital diameter d_0 (Equation 3.15) near the bed and the ripple wavelength λ (Figure 3.17) is important. Komar (1974) compiled several experimental data sets (Figure 3.18) and concluded that for

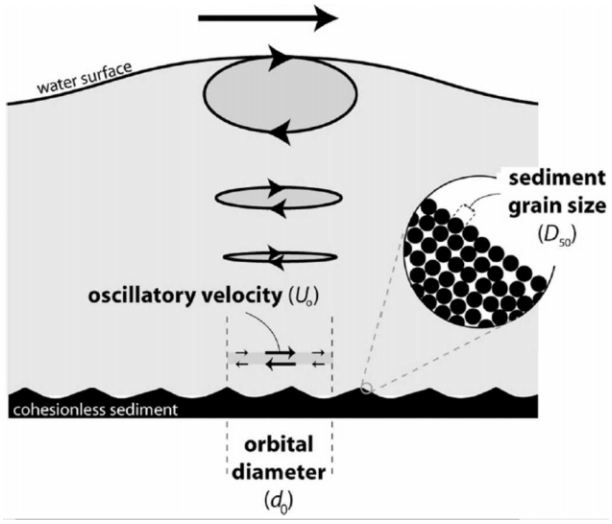

Figure 3.17: Three key controls on vortex-ripple shape and size: orbital diameter (d_0), maximum oscillatory velocity (U_o) and sediment grain size (D_{50}). From Cummings et al. (2009).

shallow water of low period, the orbital diameter and the ripple length had a linear relation of the form

$$\lambda_\eta = 0.8\, d_0 \tag{3.15}$$

With the incorporation of new data, Equation 3.15 has been updated to (e.g. Clifton, 1976; Pedocchi and García, 2009b):

$$\lambda_\eta = 0.65\, d_o \tag{3.16}$$

However, at larger orbital diameters, this relation ceases to exist and ripple size decreases

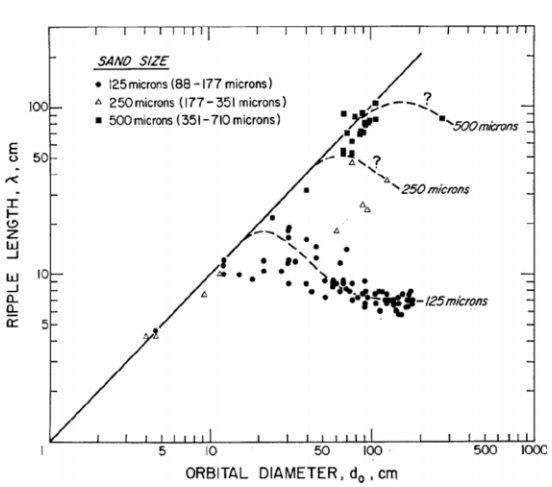

(a) From Komar (1974).

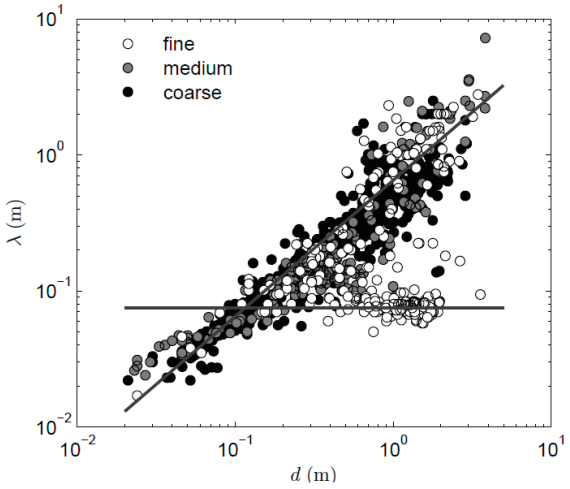

(b) The two lines correspond to 'orbital' $\lambda_\eta = 0.65\, d_o$ and 'anorbital' $\lambda_\eta = 0.075$ m trends. From Pedocchi (2009).

Figure 3.18: Experimental data relating d_0 with the wave ripple spacing.

until it appears to approach a value that is stable for each particular grain size (denoted by the question marks in Figure 3.18a). Clifton and Dingler (1984) were able to demonstrate that different bedforms exist in different regions of a λ_η/D vs d_0/D phase diagram and that all of these areas overlapped (Figure 3.19). Hence, following the divisions presented in Figure 3.19, wave ripples can also be classified as orbital, suborbital or anorbital. Orbital ripples are those that are described by $\lambda_\eta = 0.65\, d_0$ and where there is one orbital wave motion per ripple. On the other hand, the wavelength of anorbital ripples is independent of

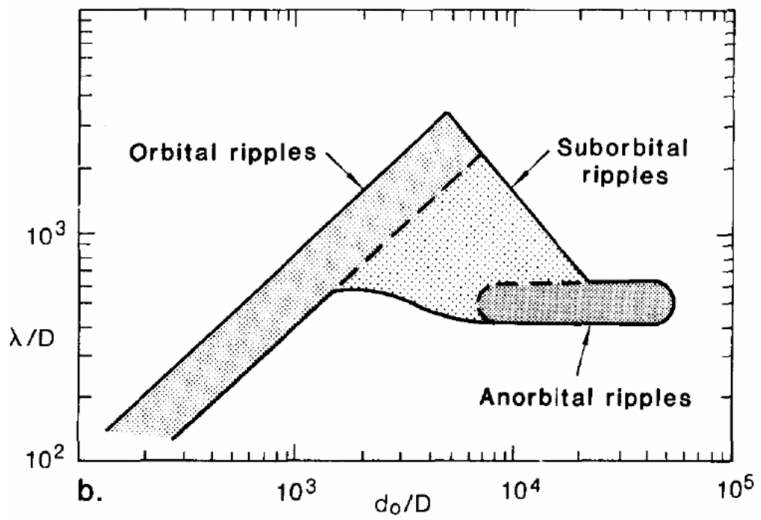

Figure 3.19: Plot of ratio of ripple spacing to grain size against ratio of orbital diameter to grain size. From Clifton and Dingler (1984).

d_0, and many ripples can be present under a single orbital diameter. Suborbital ripples are a transitional stage between orbital and anorbital ripples. Wiberg and Harris (1994) were also able to classify these different modes according to the relation between ripple height and the water orbital diameter.

$$\frac{d_0}{\eta} < 20 \quad \text{Orbital ripples} \tag{3.17}$$

$$20 < \frac{d_0}{\eta} < 100 \quad \text{Suborbital ripples} \tag{3.18}$$

$$\frac{d_0}{\eta} > 100 \quad \text{Anorbital ripples} \tag{3.19}$$

On the other hand, Nielsen (1981) proposes that there is not a constant relationship between the water orbital diameter and the ripples geometries, but a dependence on the wave mobility number ψ_w,

$$\psi_w = \frac{\rho_f \, U_{ob}^2}{(\rho_s - \rho_f) \, g \, D_{50}} \tag{3.20}$$

Hence, Nielsen (1981) proposes that for regular waves

$$\frac{\lambda}{d_0} = 4.4 - 0.69\,\psi_w^{-0.34} \tag{3.21}$$

$$\frac{\eta}{d_0} = 0.55 - 0.044\,\psi_w^{0.5} \tag{3.22}$$

and for irregular waves

$$\frac{\lambda}{d_0} = 2\,\exp\left[\frac{693 - 0.37\ln^7\psi_w}{1000 + 0.75\ln^8\psi_w}\right] \tag{3.23}$$

$$\frac{\eta}{d_0} = 42\,\psi_w^{-1.85} \tag{3.24}$$

The presence of orbital or anorbital ripples on a sandy bed is strongly modulated by grain size (Cummings et al., 2009; Pedocchi, 2009). Orbital ripples can be formed in all grain sizes, but recent work by Cummings et al. (2009) has shown that anorbital ripples do not occur in coarse sands (Figure 3.20). In addition, the slope of the flanks of larger ripples (wavelength > 0.3 m) changes with grain size, with coarse grains having steeper leesides angles ($> 15\,^\circ$) than very fine grains ($< 15\,^\circ$).

3.3.4 Hummocks

Most stratigraphers and sedimentologies prefer to use dimensional diagrams, like Southard's (1991) phase diagram where oscillation period is plotted against the maximum orbital velocity (Figure 3.16b). The diagram presents two abrupt transitions: no ripple-2D vortex ripples and 2D vortex ripples-3D vortex ripples and a gradual transition: vortex ripples-plane bed. The phase diagram of Southard (1991) predicts that for a fixed oscillation period, as the maximum orbital velocity increases, then the bedforms will gradually become smaller until a high-transport plane stage is reached. However, experimental work by Pedocchi and García (2009c) has shown that there is an intermediate state (maximum orbital velocity $\geq 0.5\,m\,s^{-1}$) where the wavelength of the oscillatory bedform is approximately double (from

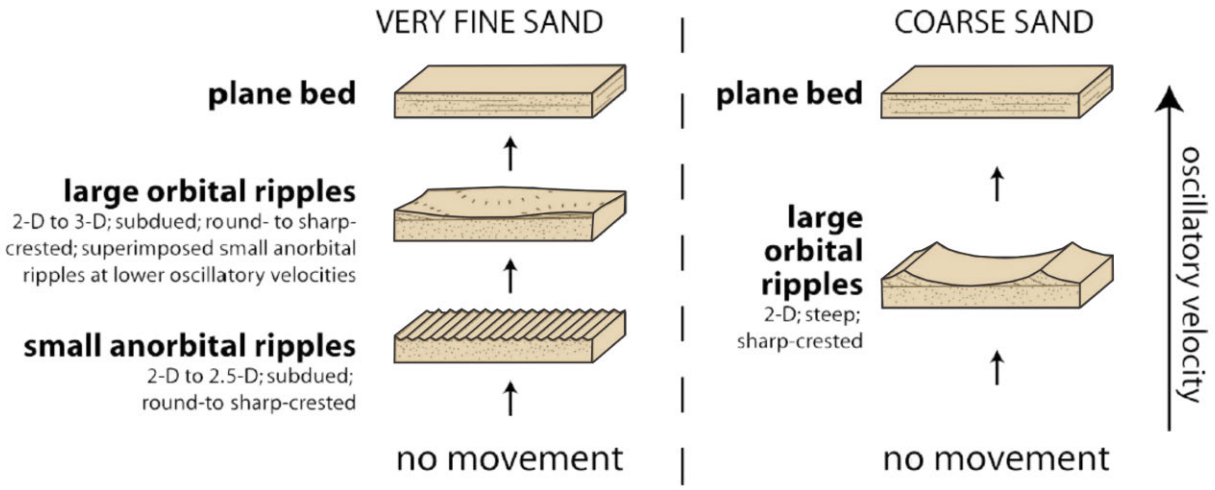

Figure 3.20: Schematic diagram of equilibrium bed configuration generated for very fine and coarse sand under oscillatory flows as the maximum orbital velocity is increased. From Cummings et al. (2009).

0.5 m to 1-1.5 m) before the transition to a plane bed occurs. This intermediate state is associated with a change in the crest shape of the ripple, which becomes rounder as the orbital velocity increases. The understanding of these rounded large ripples is restricted, but there is enough information to suggest that they are a stable configuration between vortex ripples and plane bed. It has been proposed that these rounded features are 'hummocks' (Dumas et al., 2005; Dumas and Arnott, 2006; Cummings et al., 2009) that have been well-described in the sedimentological literature (Figure 3.21a).

Hummocks and Hummocky Cross-Stratification (HCS) were first described by Harms et al. (1975), although it had been earlier reported under different names: truncated wave-ripple laminae (Campbell, 1966), crazy bedding (Howard, 1971) or truncated megaripples (Howard, 1972). Hummocky morphology (Figure 3.21) is characterized by convex upward (hummocks) and concave upward (swales) laminae with bounding surfaces gently dipping in different directions (generally less than 10°). The hummocks have wavelengths ranging from fractions (0.2-0.5) to several (1-2 m) meters with heights between 0.1 and 0.5 meters (e.g., Harms et al., 1975; Dumas et al., 2005). Hummocks are present in fine-grained sediments (Figure 3.22b;

e.g., Dott and Bourgeois, 1982; Brenchley, 1985; Swift et al., 1987). However, coarser grains can be present in the strata but in a significantly smaller percentage (Cheel and Leckie, 1993). Following Campbell (1966), Dott and Bourgeois (1982), Bourgeois (1980), Brenchley (1985) and Cheel and Leckie (1993), three hierarchies of surface can be established:

First-order surfaces are surfaces that are nearly flat and erosional (scratches, grooves, prodmarks might occur), although some relief might be present. The surfaces might bound HCS cosets or beds containing a sequence of various structures.

Second-order surfaces are normally the surfaces where the classic, laterally-alternating, swales and hummocks are generally preserved.

Third-order surfaces are surfaces with laminae that tend to pinch and swell laterally and are most commonly thin in the antiforms (hummocks) and thicker in the synforms (swales).

Since 1975, the presence of hummocks or HCS has been proposed to be the single most diagnostic sedimentary structure to represent the deposits of paleo-storms in relatively shallow marine or lake environments (e.g. Harms et al., 1975; Swift et al., 1983; Duke et al., 1991; Ito et al., 2001). However, there is still a great debate regarding the hydraulic conditions that lead to their formation. Researchers have associated their structure with pure oscillatory flows (e.g. Dott and Bourgeois, 1982), combined flows (e.g. Hamblin et al., 1979; Allen,

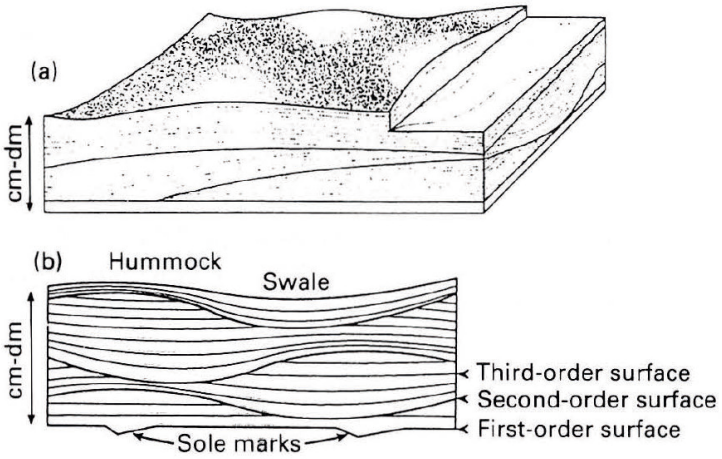

Figure 3.21: Morphology of Hummocky Cross-Stratification (HCS). a) Original block diagram of HCS presented by Harms et al. (1975). b) Characteristic strata found in HCS. From Cheel and Leckie (1993).

1985; Duke et al., 1991; Dumas et al., 2005; Tinterri, 2011) or purely unidirectional flows (e.g. Prave and Duke, 1990; Mulder et al., 2009). However, there is almost total consensus that strong waves ($U_o \gtrsim 0.5\, m\, s^{-1}$, Figure 3.22) are the key process in hummock genesis and the presence of a unidirectional current might be secondary (e.g. Greenwood and Sherman, 1986).

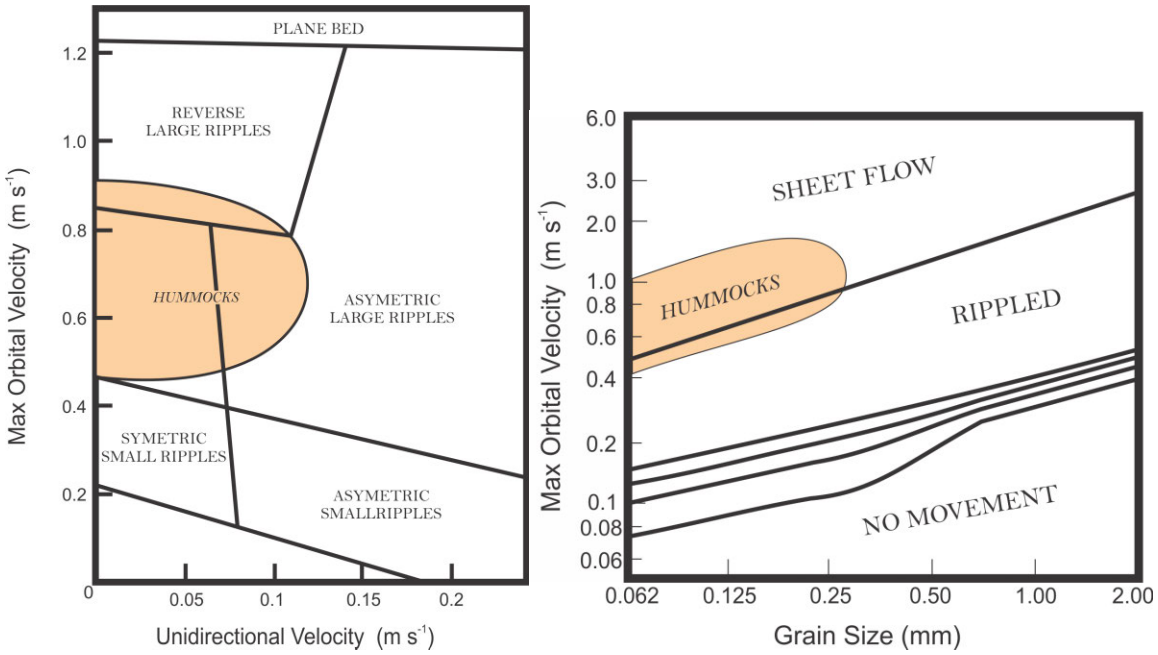

(a) From Dumas et al. (2005).

(b) Velocity thresholds for initiation of motion for different wave periods (2,5,10 and 15 sec). From Dott and Bourgeois (1982) based on Clifton (1976).

Figure 3.22: Different stability fields proposed for hummocky beds.

Greenwood and Sherman (1986) described HCS structures from the surf zone of Lake Huron, Canada at water depths of less than 2 m. On the other hand, other researchers had associated HCS with deep marine environments (water depths up to approximately 180 m; e.g., Tillman, 1985; Cheel and Leckie, 1993; Smith and Jacobi, 2001). Therefore, hummocks or HCS strata can be found in different environments ranging from the intertidal zone and lacustrine to the outer shelf.

3.3.5 Plane Bed or Sheet Flow

Similar to unidirectional flows (Section 3.2.4), there is a high regime stage where oscillatory ripples transition to a plane bed (PB) or sheet flow as the bed shear stress and sediment-transport rate are increased. This stable configuration is characterized by a highly mobile active layer of the order of 10 mm in thickness (McLean et al., 2001) and a suspended sediment layer which is confined to a few centimeters above the bed (Ribberink and Al-Salem, 1994). There is no consensus on when such conditions are achieved or what the relevant threshold criteria is to characterize the phenomenon; some of the most widely used threshold conditions are:

Kennedy and Falcon (1965)

$$\frac{A}{D_{50}} = 8000 \tag{3.25}$$

Carstens et al. (1969)

$$\frac{A}{D_{50}} = 1700 \tag{3.26}$$

Komar and Miller (1975)

$$\theta = 0.413\, D_{50}^{-2/5} \tag{3.27}$$

where D_{50} is measured in cm. Dingler and Inman (1976) proposed a threshold condition to a plane bed using a wave mobility number ψ_w,

$$\psi_w = \frac{\rho_f\, U_{ob}^2}{(\rho_s - \rho_f)\, g\, D_{50}} = 240 \tag{3.28}$$

Nielsen (1979) proposed a Shields number criteria

$$\theta = 0.83 \tag{3.29}$$

However, a few years later Nielsen updated the conditions to Nielsen (1981)

$$\theta = 1 \quad \& \quad \psi_w = 240 \tag{3.30}$$

Li and Amos (1999b) proposed a dual criterion for θ and ψ_w depending on D_{50}

$$\theta = 0.172\, D_{50}^{-0.376} \quad \& \quad \psi_w = 12.13\, D_{50}^{-0.707} \tag{3.31}$$

where D_{50} is measured in cm.

3.4 Combined Flows

As previously stated, the information concerning the bed morphology generated under combined flows is rather limited. Some work has been conducted in the laboratory to study bedforms at a range of relatively short oscillation periods ($\lesssim$ 12 s) and low unidirectional flow velocities ($\lesssim$ 0.3 $m\,s^{-1}$) (Inman and Bowen, 1963; Harms, 1969; Brevik and Bjørn, 1979; Brevik, 1980; Arnott and Southard, 1990; Southard et al., 1990; Yokokawa et al., 1995; Dumas et al., 2005; Sekiguchi and Yokokawa, 2008). The absence of data at higher unidirectional velocities and longer oscillation periods is due to the great expense involved in construction, and maintenance, of a facility capable of producing both flows at the same time.

The laboratory data set for combined flows from Arnott and Southard (1990) is summarized in Figure 3.23, where the unidirectional velocity ranges from 0 to 0.26 $m\,s^{-1}$ and the oscillatory component varies from 0 to 0.8 ms^{-1}. The oscillation period was 8.5 s and the mean sediment size used was 90 μm. The equilibrium stages of the bed observed were *no motion*, *small* or *large ripples* and a *plane bed*. No criteria were given in this study to discriminate between large and small ripples. However, if such a classification is compared with the data of Dumas et al. (2005), it can be assumed that the ripple classification was based

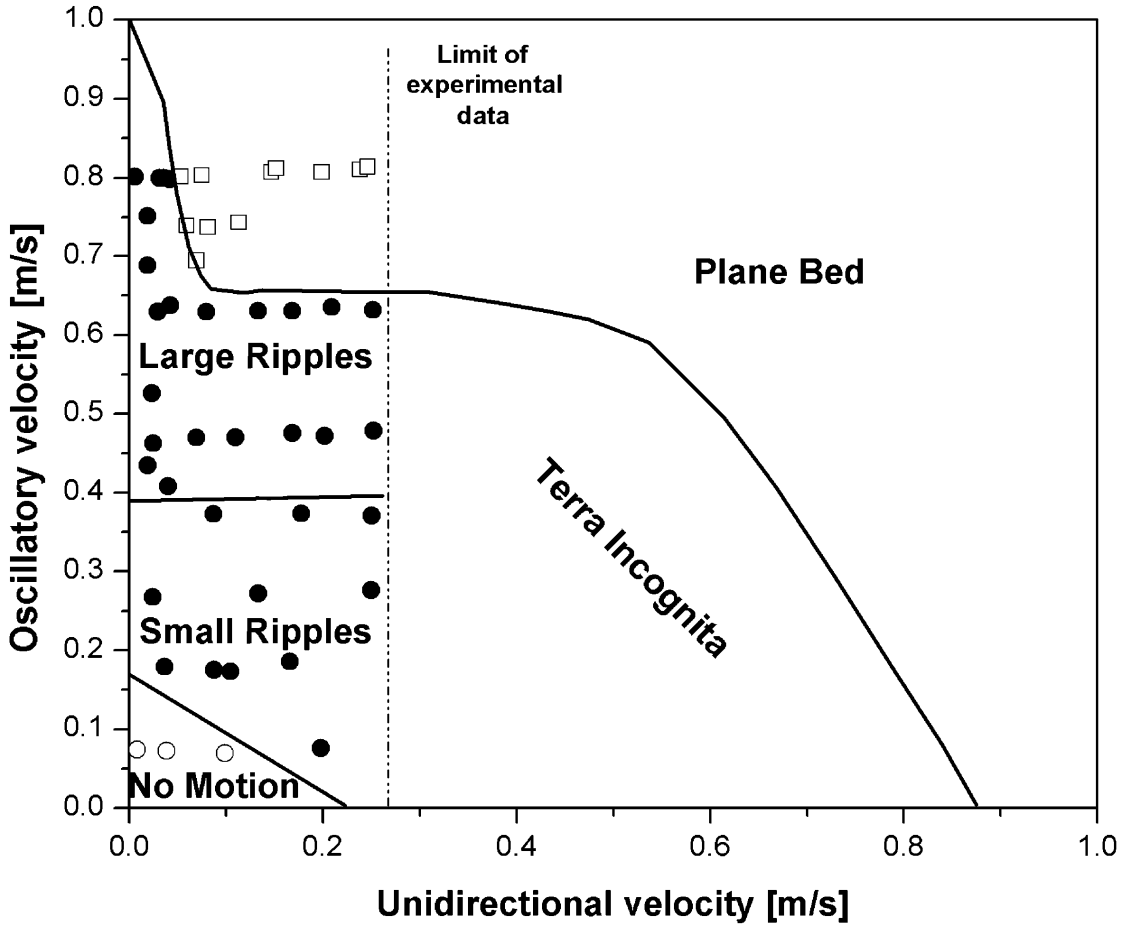

Figure 3.23: Combined flow bedform phase diagram. Experimental data for $D_{50} = 90\mu m$ and $T = 8.5$ s. Terra incognita is an area of no experimental data. Modified after Arnott and Southard (1990) and Southard (1991).

on the wavelength (λ), where small ripples are those with wavelengths smaller than 0.30 m and large ripples have wavelengths larger than 1 m. One of the major problems described by Arnott and Southard (1990) was the lack of accuracy in their flow measurements. The absence of any flow meter resulted in the characterization of the flow being achieved by the tracking and measurement of buoyant particles through the viewing windows. Despite the lack of accuracy, this bedform phase diagram is still the most widely used in the literature due to its simplicity and good description of bedforms in the area of wave-dominated conditions ($U_u \lesssim 30\ m\,s^{-1}$). Following the work and suggestions proposed by Arnott and Southard (1990), Dumas et al. (2005) investigated the same range of unidirectional conditions (less

than 0.25 $m\,s^{-1}$), but increased the oscillatory velocity to 1.25 $m\,s^{-1}$. Two different grain sizes (110 and 170 μm) and two wave periods (9.4 and 7 s) were used to quantify the effect of grain size and oscillation period (Figure 3.24). The equilibrium stages of the bed were similar to those found by Arnott and Southard (1990) with the difference being that Dumas et al. (2005) make a distinction between symmetrical and asymmetrical ripples. Taking this symmetry into account, the bed can be described in terms of:

No Motion (NM) is characterized by a plane bed with the absence of sediment movement.

Symmetrical Small Ripples (SSR) are characterized by a symmetrical profile ($RSI < 3$) with sharp and narrow crests. Wavelength varies between 70 and 110 mm and the ripple height between 5 to 20 mm. The average lee side has an angle of 14°.

Asymmetrical Small Ripples (ASR) are characterized by an asymmetrical profile ($RSI > 3$). The angle of the lee side is in the range of 10° to 20°. The ripple wavelength ranges between 0.11 and 0.21 m and the ripple height between 12 to 30 mm.

Symmetrical Large Ripples (SLR) are generally formed by increasing the oscillatory velocity over the SSR. The ripple wavelength varies between 1.11 and 2.24 m and the ripple height between 0.06 to 0.27 m. The average lee slope angle is 16°.

Asymmetrical Large Ripples (ALR) are characterized by both sharp crests, deep troughs, and round stoss sides ($RRI > 0.4$). The angle of the lee side varies between 10° to 30°, but in general it is close to the angle-of-repose ($\approx 32°$). These large bedforms have a wavelength ranging between 1 to almost 5 m with a ripple height between 0.1 to 0.4 m.

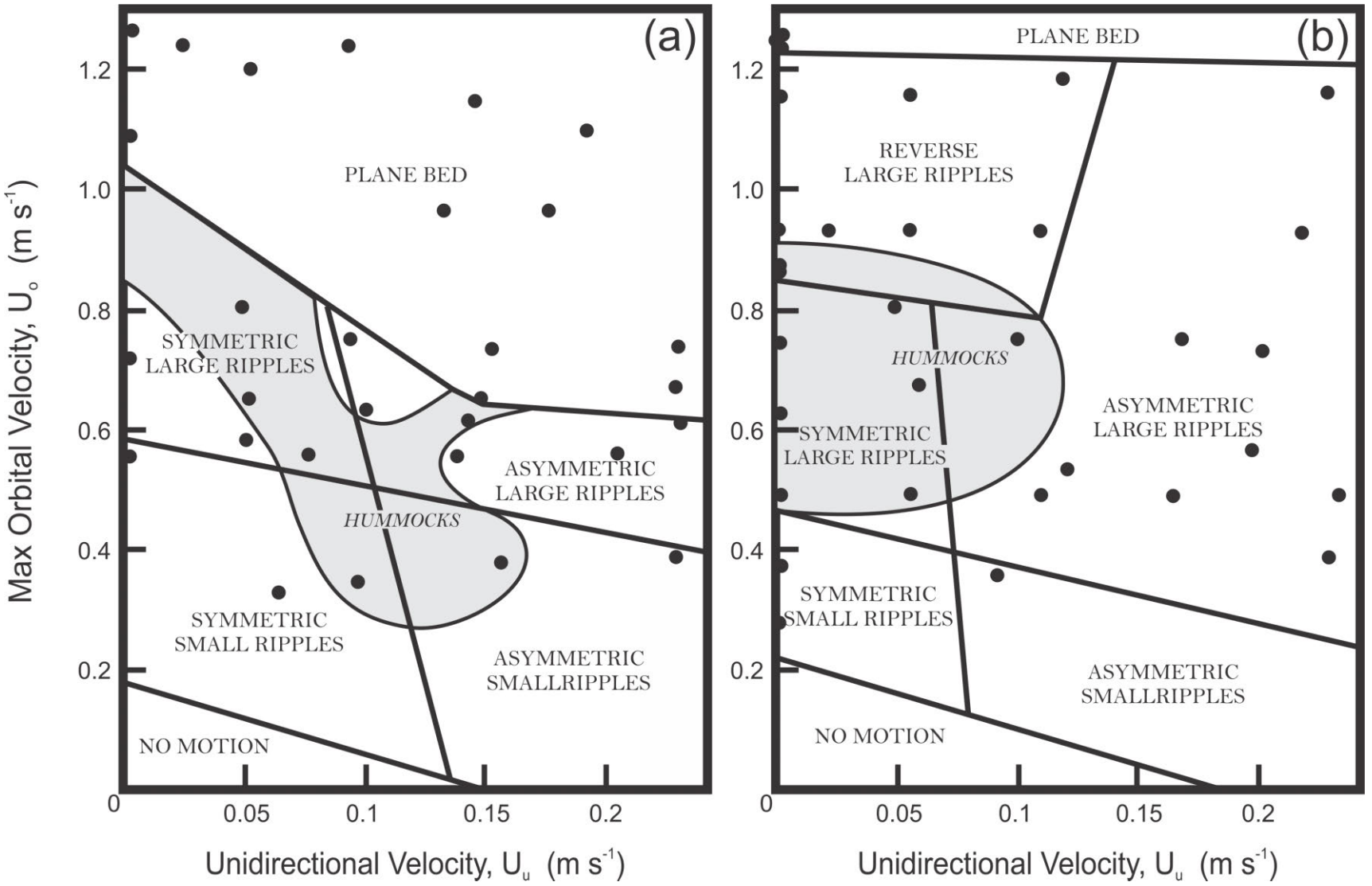

Figure 3.24: Combined flow bedform phase diagram. (a) Phase diagram 1 - $D_{50} = 110\mu$m and $T = 9.4$ s . (b) Phase diagram 2 - $D_{50} = 110$ μm and $T = 7$ s.. For phase description see text. Modified after Dumas et al. (2005)

Reverse Large Ripples (RLR) are characterized by ripple migration in the direction opposite to their sense of asymmetry. This is explained by sediment being eroded on the short, steep, lee side due to the high velocities generated when the wave and current are in the same direction and deposited along the longer and gently-dipping stoss side when the current and wave are in opposite directions. The ripple wavelength varies between 2 and 5 m and the ripple height between 0.3 to 0.4 m.

Plane Bed (PB) is characterized by a flat bed generated by intense sediment movement.

In addition to the laboratory research mentioned above, some work has been conducted in the field by Amos et al. (1988, 1999) where flow and bed measurements were taken during a range of oscillatory and tidal flows. Amos et al. (1988, 1999) recorded mean current velocity, statistics on near-bed wave motion, wave height, period and time-lapse photographs of the seabed (Figure 3.25) over 12 days in 22 m of water on Sable Island Bank, Scotian Self. Oscillatory flows throughout the 12 days recorded oscillation periods between 6 and 11 s and maximum orbital velocity ranged from 0 to $0.4\,m\,s^{-1}$ with an average value of $\sim 0.2\,m\,s^{-1}$. On the other hand, unidirectional velocities changed between 0 and $0.13\,m\,s^{-1}$ with an average value of $\sim 0.06\,m\,s^{-1}$. Based on the time-lapse photographs, Amos et al. (1988) distinguished eight bed types over the 0.23 mm bottom sand: (1) wave ripples (Figure 3.25b); (2) straight-crested current ripples (Figure 3.25a); (3) linguoid current ripples; (4) wave and current ripples (Figure 3.25c); (5) transitional wave ripples; (6) transitional current ripples; (7) poorly developed ripples; and (8) flat bed (Figure 3.25d). Amos et al. (1988) describe the different bedforms as:

Straight-crested current ripples are characterized by straight and continuous crests throughout the whole photograph. Brink points were estimated to be sharp and slipfaces appeared to be tabular. Wavelengths varied between 0.12 to 0.17 m. Based on the asymmetrical (RSI > 3) and the propagation direction (same as tidal current direction) these ripples are interpreted to have been formed by unidirectional flows.

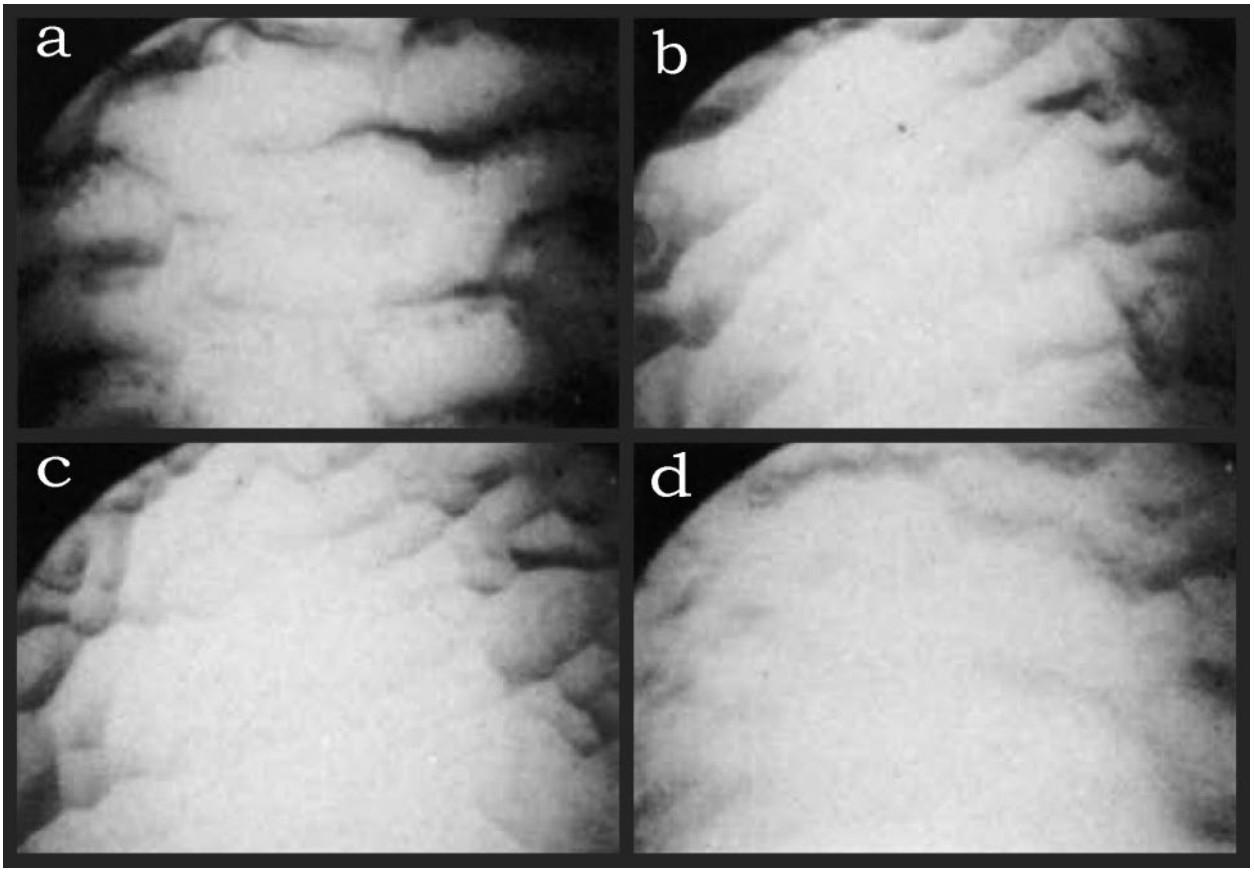

Figure 3.25: Time-lapse photographs of the seabed on Sable Island Bank, Scotian Self. a) straight-crested or linguoid ripples, b) wave-formed ripples, c) wave and current ripples and d) flattened bed

Linguoid current ripples are characterized by sharply-defined brink points and slipfaces. The wavelength and shape changed across the frames between 0.10 and 0.27 m and different linguoid shapes. Like their straight-crested current ripples, their origin is associated with unidirectional flows based on the asymmetry (RSI > 3) and the similarity between the tides and the propagation direction.

Wave ripples had regularly-spaced crests oriented normal to the direction of wave propagation. The ripples are characterized by sharp symmetrical-crested bedforms (RSI < 2). Once ripples were fully developed, the wavelength remained stationary through time at approximately 0.20 m in wavelength.

Wave and current ripples showed 'distinct' superimposed patterns of current and wave ripples.

Wave ripples are characterized by sharp and discontinuous crests, whilst current ripples are characterized by a triangular planform geometry. These ripples migrated in the direction of the tidal flow, whereas wave ripples were stationary.

Transitional current ripples are characterized by current ripples with superimposed wave ripples. The bed was dominated by well-developed, active, current ripples. Symmetrical wave ripples were present intermittently in their troughs. Crestlines of wave ripples were discontinuous, broken by the current ripple crests. Current ripples migrated, whereas the wave ripples were stationary.

Transitional wave ripples are characterized by wave ripples with superimposed current ripples. Wave ripples were predominant, but small (40 mm in wavelength), asymmetric, straight-crested current ripples were seen in wave ripple troughs.

Poorly developed ripples are characterized by rounded brink points and substantial biodegradation.

Flat beds are characterized by the absence of bedforms and by recognizable biodegradation.

3.5 General Overview

The sedimentological fluid dynamic (SFD) "trinity", as explained in Chapter 1, is a conceptual framework to study the coupling effects between flow, sediment transport and bed morphology (Figure 1.2). The present chapter provided a brief discussion on the bed morphologies generated under unidirectional (Section 3.2), oscillatory (Section 3.3) and combined flows (Section 3.4). Despite the extensive work studying unidirectional bedforms over several centuries, there is no standard classification or nomenclature to unambiguously define a particular bed feature (i.e. dunes vs megaripples, Section 3.2.3). In addition, researchers studying oscillatory and combined flow bedforms term all bed features ripples, making it a very difficult task to directly compare results between bidirectional and unidirectional

flows. Moreover, the very limited data on combined flows still lacks statistical validation of any of the relevant characteristics of the bedforms (e.g., the effects of oscillation period or grain size on bed morphology). Therefore, it is essential for any bedform study to clearly define the bedform nomenclature that will be used. An ideal nomenclature or classification scheme should address the characteristic changes in bedform structure or geometry (e.g., planform, height, wavelength) and functionality (e.g., type of flow, flow separation, grain or depth dependence) for all the potential bed morphologies. Despite the fact that both the structure and functionality of bedforms are strictly related to one another (SFD "trinity"), the information necessary to fully characterize each of the SFD "trinity"products are different and generally not reported (e.g. Dumas et al., 2005). Therefore, based on the limited data on combined flow bedforms, and the lack of a consistent nomenclature on oscillatory and unidirectional flows, a new nomenclature has been proposed to produce a geometrical-process based bedform classification (Table 3.1). The nomenclature consists of several terms, including the following:

Flow Type

Unidirectional Flow $U_u \neq 0$ and $U_o = 0$.

Oscillatory Flow $U_u = 0$ and $U_o \neq 0$.

Combined Flow $U_u \neq 0$ and $U_o \neq 0$

Wave-Dominated Combined Flow

Maximum shear stress at flow reversal (maximum oscillatory velocity in the upstream direction) larger than the critical shear stress for sediment entrainment ($|\theta^{(-)}_{max}| > \theta_c$).

Current-Dominated Combined Flow

Maximum shear stress at flow reversal smaller than the critical shear stress for sediment entrainment ($|\theta^{(-)}_{max}| < \theta_c$).

Bedform Type

No Motion $\theta < \theta_c$ and flat bed

Ripple $\lambda_\eta < 0.5$ m and $\eta < 0.05$ m

Dunes $\lambda_\eta > 0.5$ m and $\eta > 0.05$ m

Lower-Stage Bed $\theta \approx \theta_c$ and flat bed

Upper-Stage Bed $\theta \gg \theta_c$ and flat bed

The methodology to differentiate ripples from dunes in the absence of a free surface was based on the classification proposed by Ashley (1990). However, a slight modification was made: $\lambda_\eta = 0.5$ m was used instead of $\lambda_\eta = 0.6$ m as the bedform wavelength threshold between ripples and dunes, since this value better represented the separation of the two bedform sizes.

Planform Geometry

Two Dimensional (2D)

Bedform crestline is continuous and straight (Figure 3.26a).

Two and a half Dimensional (2.5D)

Bedform crestline is either continuous or straight (Figure 3.26b).

Three Dimensional (3D)

Bedform crestline is neither continuous or straight (Figure 3.26c).

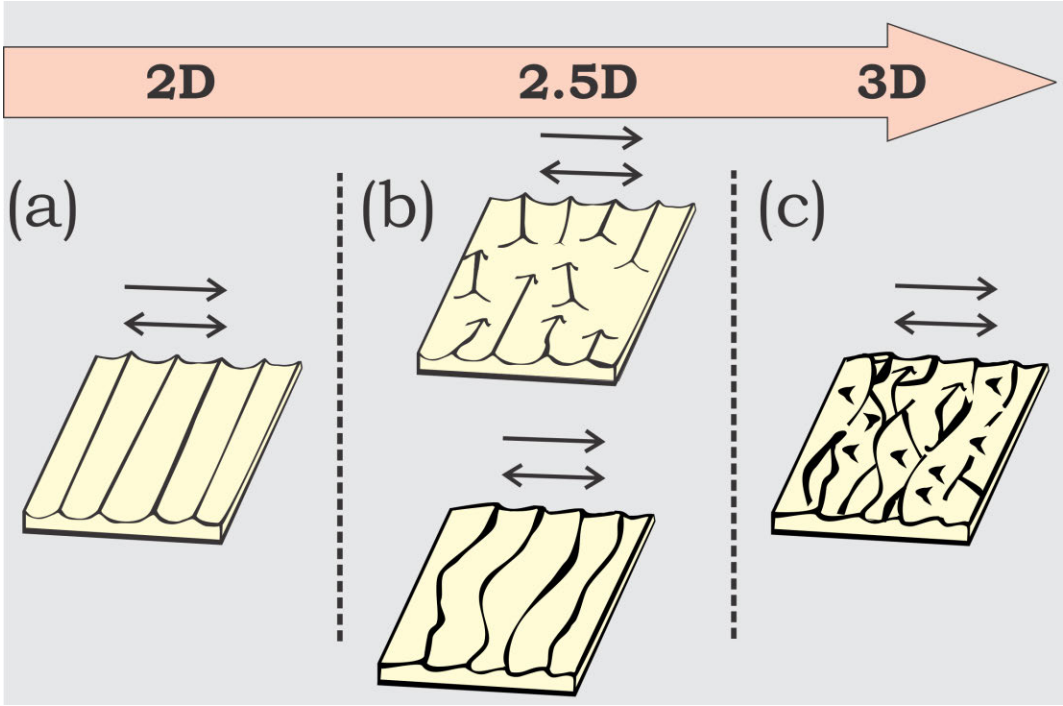

Figure 3.26: Planform Geometry Classification: differences between 2D, 2.5D and 3D bedforms. (a) Two dimensional (2D); bedform crestline is continuous and straight. (b) Two and a half dimensional (2.5D); bedform crestline is either not continuous and straight (upper case) or continuous and not straight (lower case). (c) Three Dimensional (3D); bedform crestline is not continuous and not straight.

Cross-Section Form Geometry

Asymmetric	$BSI > 1.5$	**Quasi-asymmetric**	$BSI \sim 1.3 - 1.5$
Symmetric	$BSI < 1.5$		
Rounded	$BRI \geq 0.6$	**Not-rounded**	$BRI < 0.6$
Low-angled	$BI < 3.$		

where

$$\begin{aligned} BI &= \lambda_\eta \, \eta^{-1} && \text{Bedform Index} \\ BSI &= \lambda_s \, \lambda_l^{-1} && \text{Bedform Symmetry Index} \\ BRI &= \lambda_{0.5\,s} \, \lambda_s^{-1} && \text{Bedform Roundness Index} \end{aligned} \tag{3.32}$$

Therefore, if a bedform is two-dimensional with a wavelength of 0.3 m, a $BSI = 1.2$ and if it is produced under oscillatory flow, it would be termed a 2D symmetric oscillatory ripple.

Nomenclature Used	Unidirectional Flows	Oscillatory Flows	Combined Flows	
	Southard (1991)[a]	Pedocchi and García (2009c)[a]	Dumas et al. (2005)[a]	Amos et al. (1988)[a]
No Motion	No Motion	No Motion	No Motion	Flat Beds
Unidirectional Ripples	Ripples	N/A N/A	N/A N/A	Straight Current Ripples Linguoid Current Ripples
Unidirectional Dunes	Dunes	N/A	N/A	N/A
2D Oscillatory Ripples 3D Oscillatory Ripples	N/A N/A	2D Vortex Ripples 3D Vortex Ripples	Symmetrical Small Ripples	Wave Ripples
Combined Flow Ripples	N/A	N/A	Asymmetrical Small Ripples	Wave and Current Ripples Transitional Current Ripples Transitional Wave Ripples
Oscillatory Dunes	N/A	Round-Crested Ripples	Symmetrical Large Ripples Isotropic 3-D Hummocks	N/A
Combined Flow Dunes	N/A	N/A	Asymmetrical Large Ripples Anisotropic 3-D Hummocks	N/A
Upper-Stage Plane Bed	Upper Stage Plane Bed	Plane Bed or Sheet Flow	Plane Bed	N/A
Lower-Stage Plane Bed[b]	Lower Stage Plane Bed	N/A	N/A	N/A

Table 3.1: Bedform Nomenclature

[a]These studies are used as an example to illustrate the general nomenclature used for that particular type of flow.
[b]There are no current studies that address the existence of lower-stage beds for oscillatory and combined flows.

Chapter 4

Experimental Facility, Instrumentation and Data Processing

4.1 Experimental Apparatus

4.1.1 Description

Experiments were conducted in the Large Oscillatory Water Sediment Tunnel (LOWST) at the Ven Te Chow Hydrosystems Laboratory, University of Illinois at Urbana Champaign, which enables a combination of oscillatory and unidirectional flow velocities of up to 2 and 0.55 ms^{-1} respectively. The tunnel is U-shaped, with one leg containing three pistons generating the water oscillation and the other leg forms an open reservoir (Figure 4.1). The pistons move inside cylinders of 0.78 m diameter with a maximum nominal stroke of 2.1 m that is generated by three servo motors controlled by a computer. The unidirectional component of the flow is generated by two centrifugal pumps. In addition, flow straighteners

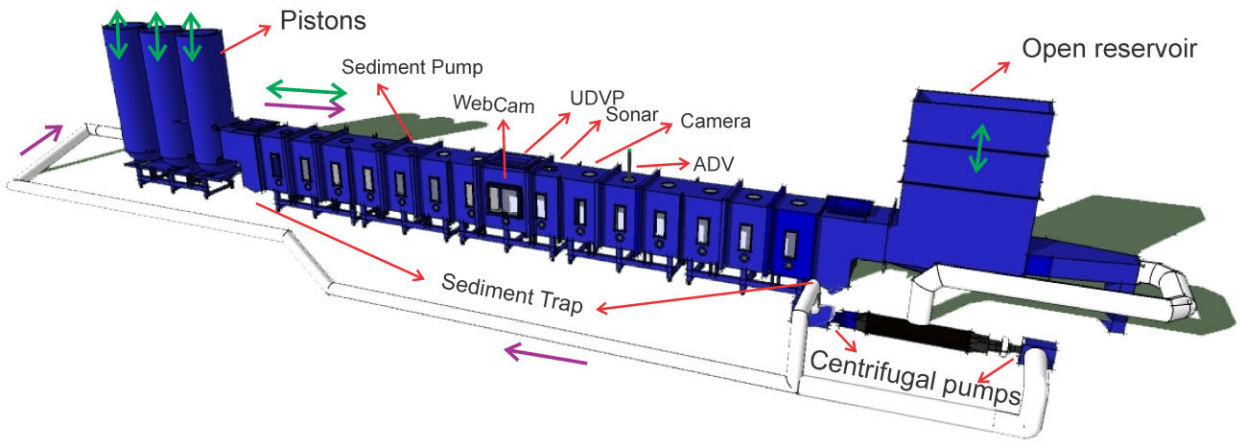

Figure 4.1: Sketch of the Large Oscillating Water-Sediment Tunnel (LOWST)

are located at both ends of the main test section to reduce the flow distortion produced by the "elbow type" entrance of the pumped water. Finally, gravel is located at both ends of the sediment bed to prevent local erosion.

The tunnel has a working cross-section 0.8 m wide by 1.2 m deep and 12.5 m long. Two large windows (0.6 m high by 0.7 m wide) are located in each side of the central region and allow observation of the interior of the tunnel. In addition, twenty-eight smaller windows (0.6 m high by 0.2 m wide) are equally spaced on both sides of the rest of the working section. On the top of the tunnel, three access hatches and fifteen 0.2 m diameter circular ports give access to the inside of the tunnel. These circular ports give direct access to the bed and provide an easy way to insert instrumentation for the measurement of bed and flow properties.

4.1.2 Operational range

The LOWST was designed to produce a wide range of wave-current flows with oscillatory periods ranging between 2 to 20 s. However, not all oscillatory conditions can be achieved for every period (Figure 4.2). The limits given by the black line in Figure 4.2 are produced by the physical limitation of the system, e.g. maximum water displacement driven by the piston 0.8 m^3s^{-1}, maximum nominal velocity 2.0 ms^{-1} and maximum nominal piston acceleration 2.1 ms^{-2}. Moreover, to prolong the lifetime of the facility and minimize the creation of any potential malfunction, an empirical curve (Figure 4.2: Green line) is proposed to be the safe limit for the operational range. Such a curve is consistent with the experiments conducted during this work and that of Pedocchi (2009).

4.1.3 Sand

Half of the flume working area was filled with 250 µm diameter quartz sand ($D_{10} = 185\,\mu m$ and $D_{90} = 373\,\mu m$; Figure 4.3). The total volume occupied by sand was 6 m^3 ($\sim$ 5.2 tonnes),

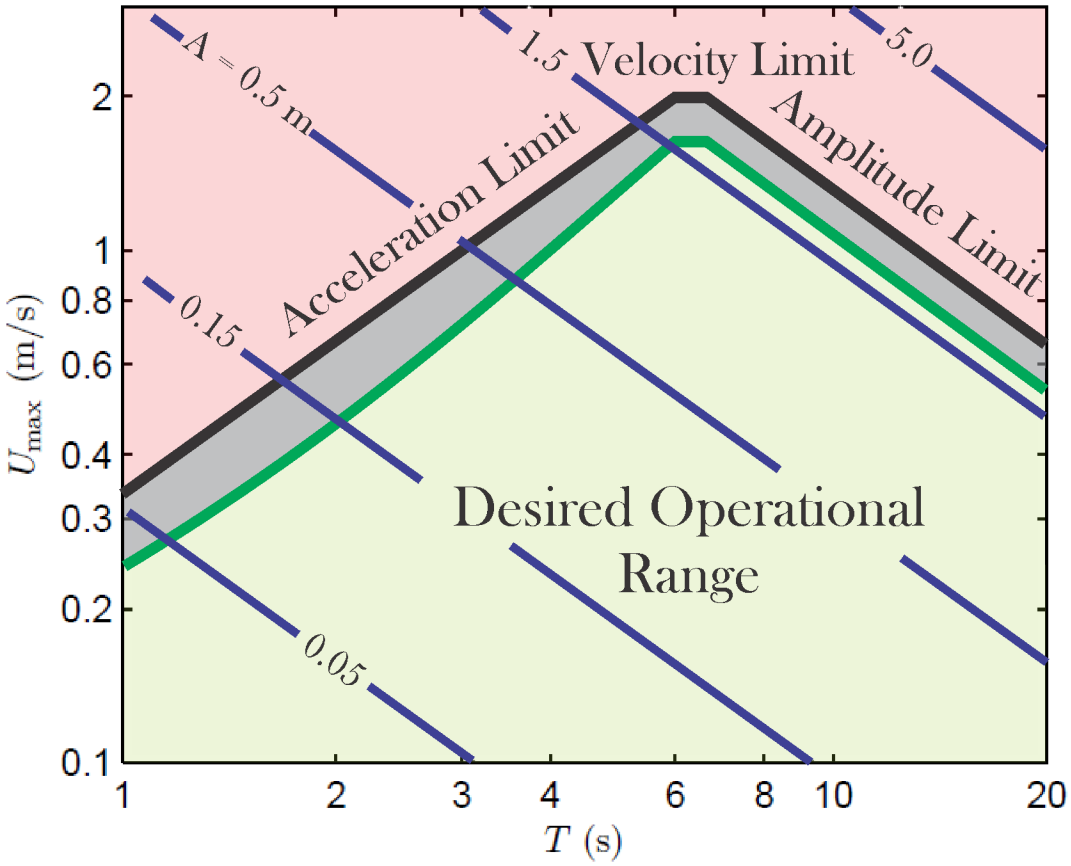

Figure 4.2: Desired operational range of the LOWST for oscillatory flows. The tunnel was designed to operate below the black curve. However, set by empirical results, it is recommended to run conditions below the green curve.

although for most experiments around 1 m^3 ($\sim$ 0.9 tonnes) was mobilized. Sediment traps are located at both ends of the test section to collect the sediment that has been transported as bedload. For a typical experiment, the average amount of sand transported to the ends of the flume and retained in the sand traps was around 150 kg, but for high sediment transport experiments the traps held up to 300 kg. In addition, for the case of combined flows, the downstream trap contained up to 5 times more sand than the one upstream.

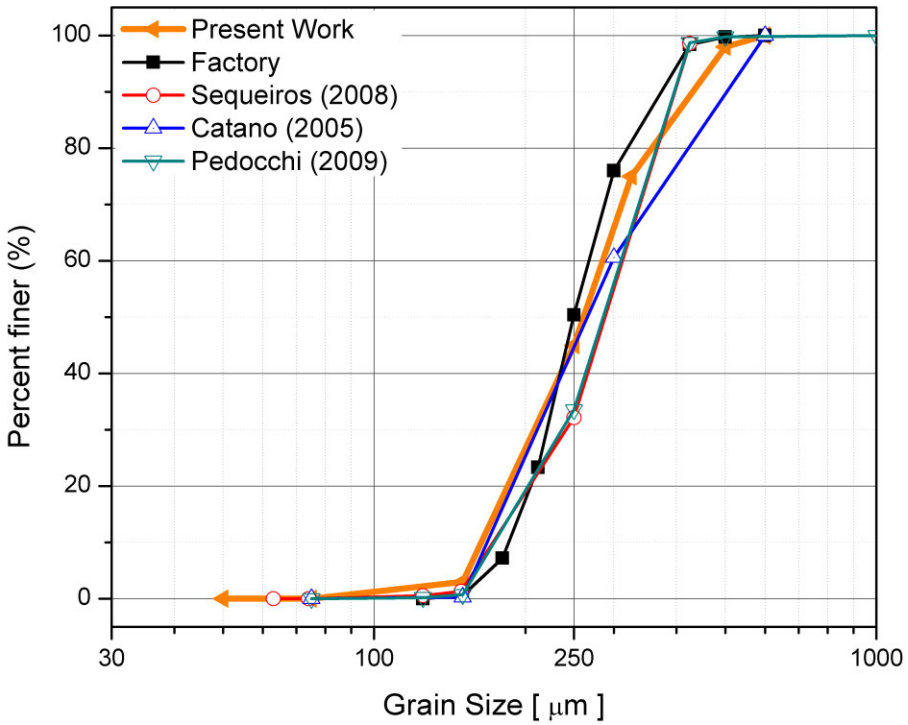

Figure 4.3: Grain size distribution obtained by different researchers using the same facility for the same sand.

4.2 Experimental Description

Each experiment could be divided into three main steps: *pre-experiment, experiment* and *post-experiment.*

- The *pre-experiment stage* : this generally began with clearing sediment from the two sediment traps that are at both ends of the test section. This sediment was placed in the tunnel and at the same time a cart was pulled by a winch to flatten the bed (Figure 4.4: a-c). The cart was composed of two blades that covered the entire width of the tunnel (Figure 4.4: b), and it was pulled back and forward along the tunnel in order to redistribute the wet sand and leave a smooth and flat sand surface (Figure 4.4: d-f). Small defects of the order of a few grain diameters were present after the bed was flattened, but there is no clear association between such defects and the location where bedforms were initiated.

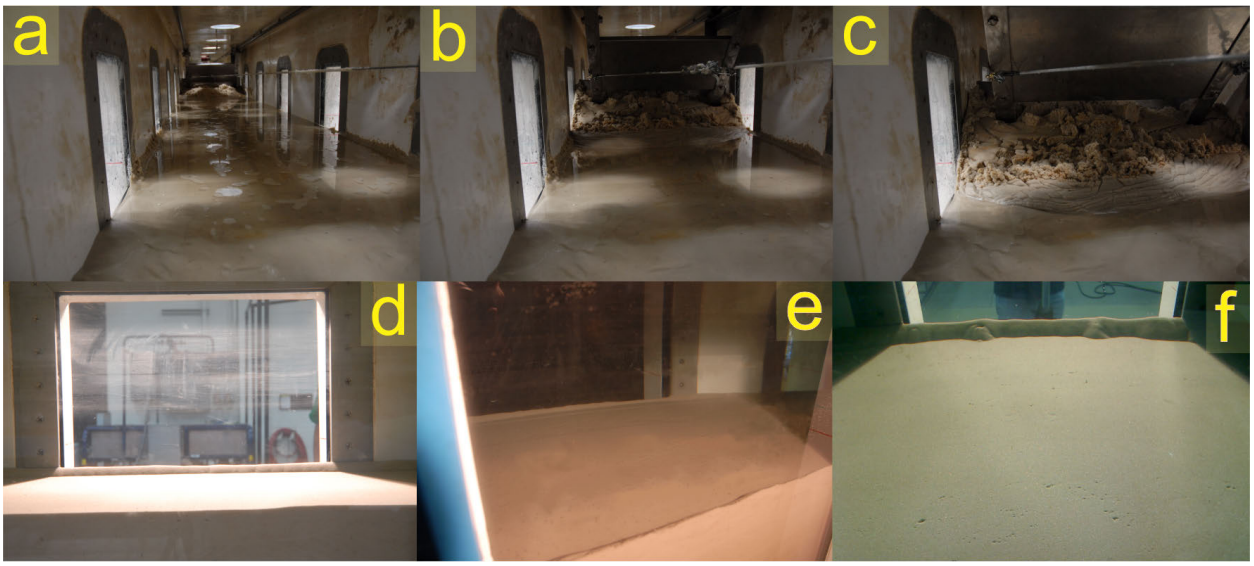

Figure 4.4: a-c) Sand redistribution as the cart is pulled by the winch. d-f) Resulting flat bed for three different experiments.

- During the *experimental stage* : a maximum orbital velocity and period were set on the computer and the unidirectional velocity was set on the pump controller to obtain the desired combined flow conditions. Once the experiment was started, the pistons increased their motion amplitude in about 5 to 10 oscillations until the desired condition was reached. Meanwhile, measurements were begun. The tunnel was equipped with a micro Acoustic Doppler Velocimeter (ADV), Ultrasonic Doppler Velocity Profiler (UDVP), a custom-designed sonar system, pressure transducers, a peristaltic pump to extract suspended sediment samples and a digital camera (Figure 4.5). Two-dimensional bathymetric data (Section 4.3.2) and side-view webcam photographs (Section 4.3.4) were taken every 3 s and 5 s respectively, throughout the whole experiment. At least one UDVP and sediment sample measurement were synchronized to later correlate the sediment in suspension with the UDVP backscatter intensity (Section 4.3.3). The beginning of each ADV and UDVP measurement was synchronized with the motion of the piston with a electrical circuit in order to start the measurements at the same phase of the oscillation period. For more detailed information on the equipment and data recorder, see Section 4.3).

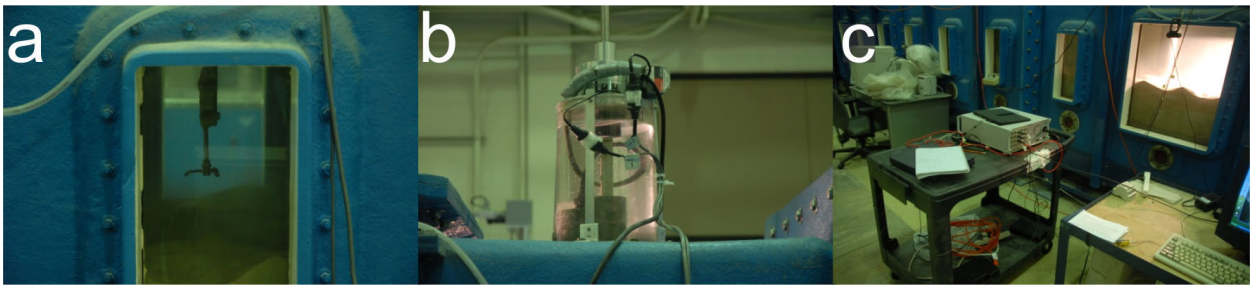

Figure 4.5: a) micro Acoustic Doppler Velocimeter measuring the three components of velocity. b) Custom-designed sonar system measuring two-dimensional bed profiles. c) Ultrasonic Doppler Velocity Profiler on the left measuring velocity profiles and web-camera obtaining images at a set frequency.

- Once the bed configuration reached equilibrium, the experiment was stopped and the *post-experiment* analysis was conducted. Detailed sketches of the experimented stratigraphy and morphology were conducted with measurement of the height and wavelength of the bedforms.

4.3 Instrumentation

4.3.1 Acoustic Doppler Velocimeter

A SonTek micro acoustic Doppler velocimeter with a 1.01 cm^3 sampling volume was used to measure three-dimensional flow velocities using the Doppler shift principle. The instrument consists of a sound emitter, three sound receivers, and a signal conditioning electronics module (Figure 4.6). The sound emitter generates an acoustic signal at a known frequency f (up to 50 Hz), which is reflected back by sound-scattering particles present in the water, which are assumed to move at the velocity of the water. The scattered sound signal is detected by the receivers and used to compute the Doppler phase shift, from which the flow velocity in the radial or beam direction is calculated using

$$u_i = \frac{C}{4\,\pi\,f}\frac{\Delta\phi}{\Delta t} \tag{4.1}$$

where $\Delta\phi$ is the phase shift, Δt is the measurement period and C is the speed of sound (McLelland and Nicholas, 2000). The micro-ADV is attached to a Velmex BiSlide positioning system which allows three-dimensional point velocity measurements with a vertical movement accuracy of 0.5 mm. Velocity measurements were taken in the fifth circular port from the open reservoir (Figure 4.1). A detailed list of flow conditions under which velocity was measured can be found in Table 4.1. Consequently, the velocity field in the vertical could be determined with great precision (Kraus et al., 1994; Voulgaris and Trowbridge, 1998; Lopez and García, 2001; García et al., 2004, 2005).

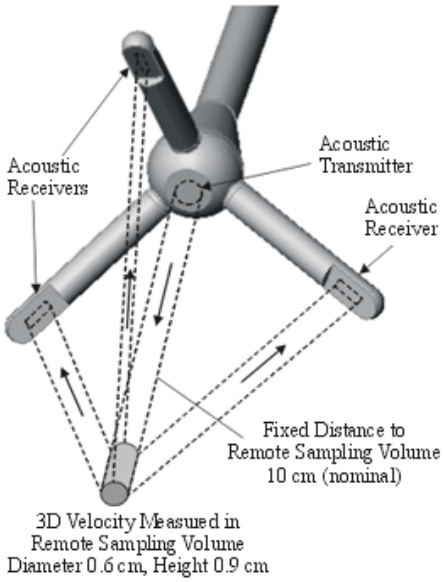

Figure 4.6: ADV Beam Geometry. From Sontek (2011)

Data Acquisition

The sampling frequency f was selected following Pedocchi (2009)

$$f = \frac{2^n}{2^m T} \tag{4.2}$$

Table 4.1: Summary of flow parameters for the morphology experiments with velocity measurements

#[a]	Init.[b] Cond.	T (s)	U_o ($m\,s^{-1}$)	d_o (m)	U_u ($m\,s^{-1}$)	ADV[c] (m)	UVDP[d]	Bedform[e] Type
01	00	04	0.25	0.32	0.00	-	2	SR
02	00	04	0.25	0.32	0.10	-	1	QAR
03	00	04	0.25	0.32	0.20	0.05, 0.1, 0.15, 0.2, 0.35	1	AR
04	00	04	0.25	0.32	0.30	-	1	ARR
05	00	04	0.25	0.32	0.40	-	1	ARD
06	04	04	0.25	0.32	0.40	-	1	ARD
08	00	05	0.20	0.32	0.00	0.05. 0.1, 0.2, 0.35	2	SR
11	00	05	0.20	0.32	0.10	0.35	2	QAR
13	01	05	0.20	0.32	0.20	-	1	QAR
14	09	05	0.20	0.32	0.20	-	1	QAR
15	00	05	0.20	0.32	0.30	0.1, 0.35	3	ARR
16	00	05	0.20	0.32	0.40	0.02, 0.1, 0.35	2	ARD
17	00	05	0.20	0.32	0.50	0.1, 0.35	3	ARD
18	00	05	0.40	0.64	0.00	-	3	SR
19	00	05	0.40	0.64	0.10	0.05, 0.1, 0.35	3	QAR
20	00	05	0.40	0.64	0.20	-	2	QARR
21	00	05	0.40	0.64	0.30	0.1, 0.35	2	QARR
23	17	05	0.40	0.64	0.40	-	1	ARD
24	00	05	0.40	0.64	0.50	0.05, 0.1, 0.35	1	USPB
25	00	05	0.50	0.80	0.40	0.1, 0.35	1	ARD
26	41	06	0.10	0.19	0.20	0.02, 0.35	13^C	AR
27	00	06	0.10	0.19	0.50	0.02, 0.05, 0.1, 0.35	8^C	CR
28	28	06	0.15	0.29	0.40	0.02, 0.05, 0.35	11^C	AD
29	39	06	0.20	0.38	0.00	0.35	20^C	SR
30	00	06	0.25	0.48	0.00	0.05, 0.1, 0.35	3	SR
31	00	06	0.25	0.48	0.05	0.1, 0.35	3	SR
32	00	06	0.25	0.48	0.10	0.35	2	QAR
33	00	06	0.25	0.48	0.20	0.35	2	QAR
34	00	06	0.25	0.48	0.30	0.35	4	ARR

[a] Experiment Number

[b] Initial condition of the sediment bed at the beginning of the experiment: 00 indicates flat bed, other numbers indicate the number of the experiment run before.

[c] Distance away from the bed where velocity was measured.

[d] Number of velocity profiles measured when the bed morphology was in equilibrium with the flow condition. [C] Measurements taken during evolution of the bed.

[e] S-R = Symmetric Ripples, SR-R = Symmetric Rounded Ripples, S-D = Symmetric Dunes, SR-D = Symmetric Rounded Dunes, A-R = Asymmetric Ripples, AR-R = Asymmetric Rounded Ripples, QA-R = Quasi-Asymmetric Ripples, QAR-R = Quasi-Asymmetric Rounded Ripples, A-D = Asymmetric Dunes, AR-D = Asymmetric Rounded Dunes, USPB = Upper Stage Plane Bed and CR = Current Ripples.

Table 4.1: continued from previous page

#[a]	Init.[b] Cond.	T (s)	U_o ($m\,s^{-1}$)	d_o (m)	U_u ($m\,s^{-1}$)	ADV[c] (m)	UVDP[d]	Bedform[e] Type
35	00	06	0.25	0.48	0.40	0.35	2	ARD
36	00	06	0.25	0.48	0.50	-	2	ARD
37	16	06	0.30	0.57	0.00	0.02, 0.05, 0.35	-	SR
38	40	06	0.30	0.57	0.10	0.01, 0.04, 0.06, 0.35	13^C	QAR
39	42	06	0.30	0.57	0.20	0.01, 0.05, 0.1, 0.15, 0.35	12^C	QAR
40	44	06	0.40	0.76	0.20	0.02, 0.05, 0.1, 0.35	13^C	ARR
41	45	06	0.40	0.76	0.30	0.01, 0.35	-	ARD
42	00	06	0.50	0.95	0.00	0.15, 0.2	-	SR
43	29	06	0.50	0.95	0.30	0.02, 0.05, 0.35	5	ARD
44	00	06	0.60	1.15	0.40	0.1, 0.35	1	USPB
46	29	06	0.80	1.53	0.20	0.2, 0.35	1	SD
47	00	06	1.00	1.91	0.50	0.01, 0.05, 0.35	2	USPB
49	00	-	-	-	0.10	0.01, 0.35	1	NM
50	00	-	-	-	0.20	0.01, 0.35	1	NM
52	00	-	-	-	0.30	0.01, 0.35	1	NM
53	00	-	-	-	0.40	-	1	CR
55	00	-	-	-	0.50	0.02, 0.05, 0.07, 0.1, 0.35	3	CR

and the criteria proposed by García et al. (2005)

$$f > 20\frac{U}{L} \tag{4.3}$$

where 2^n is the total number of samples, 2^m is the number of periods to be sampled, T is the flow period, U is the maximum convective velocity and L is the length scale of the energy containing eddies. By selecting f as described by Equation 4.2, the error that is introduced in the energy peaks when performing Fast Fourier Transform (FFT) is minimized, whereas by following Equation 4.3 the Doppler noise (low-pass filtering) generated by the ADV is reduced. In addition to improving the quality of the data, selecting an f which conforms to Equation 4.2 allows study of the turbulence statistics by ensemble averaging. For oscillatory and combined flows, the turbulence statistics should be computed by phase averaging, which makes it necessary to have several realizations of the same data point at the same time along

the oscillation (Figure 4.7).

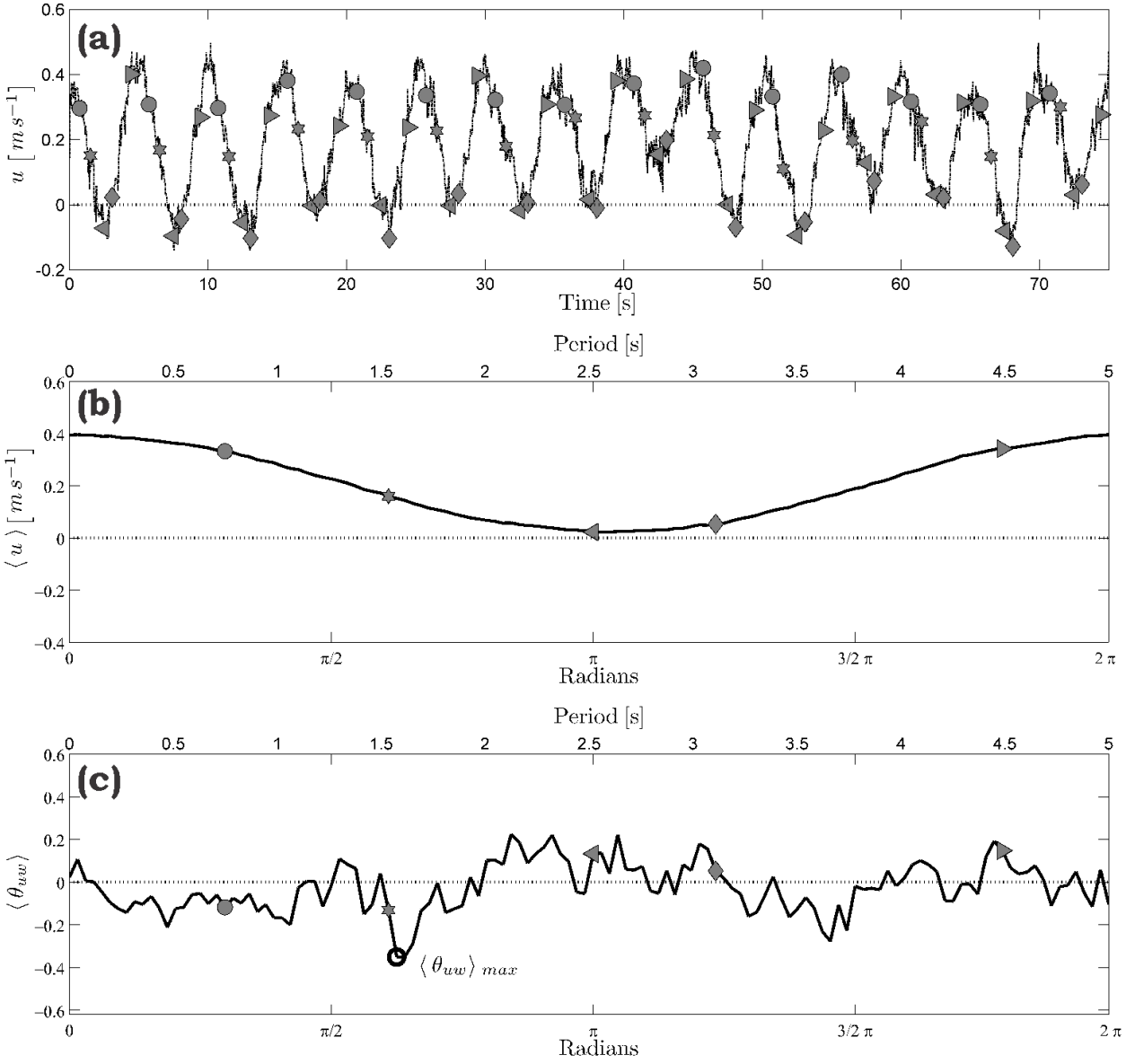

Figure 4.7: Oscillatory Condition: $U_o = 0.50\,m\,s^{-1}$ and $T = 5$ s. Unidirectional Condition: $U_u = 0.40\,m\,s^{-1}$. a) Streamwise velocity as a function of time. Each individual symbol will be averaged to produce a single data point in the phase average data. b) Streamwise phase-averaged mean velocity along the oscillation cycle. c) Phase-averaged Shields number.

Despite the benefits of using Equations 4.2 and 4.3, the accuracy of these measurements

from the ADV will still have three main sources of uncertainty

$$\Delta v = \sqrt{\sigma_M^2 + \sigma_D^2 + \sigma^2} \tag{4.4}$$

where σ is the standard deviation, σ_M is a systematic sampling error due to instrument uncertainties to resolve the phase shift (Equation 4.1) and σ_D is the Doppler-noise or error due to random scatterer motions within the sample volume (Nikora and Goring, 1998; Voulgaris and Trowbridge, 1998; McLelland and Nicholas, 2000). van Rijn (1986) assumed that Δv was approximately 1 % of the reading value. However, recent studies conducted by Voulgaris and Trowbridge (1998) estimated σ_M by still water measurements with errors up to $3\,mm\,s^{-1}$. In addition, the experiments of Voulgaris and Trowbridge (1998) showed that ADV measurements were within 1 % of those measured with an LDV.

Velocity and Shear Stress Computations

The SonTek micro-ADV was used to capture three-dimensional flow measurements at several control volume locations above the bed. In particular, the measurements at 10 mm from the flat bed were used to compute shear stresses. For simplicity, an index notation will be used to describe the three components of the instantaneous velocity, $u_i(t)$. From now on, the index i will be assumed to go from 1 to 3, where $i = 1$ is the longitudinal direction (x), $i = 2$ is the transverse direction (y) and $i = 3$ is the vertical direction (z). The Reynolds triple-decomposition (Hussain and Reynolds, 1970) is used to the characterize $u_i(t)$ as

$$u_i(t) = \overline{u_i} + \tilde{u_i}(t) + u_i'(t) \tag{4.5}$$

where $\overline{u_i}$ is the mean value, $\tilde{u_i}(t)$ is the periodic component of the velocity and $u_i'(t)$ are the turbulent fluctuations. The mean velocity, $\overline{u_i}$, is computed as

$$\overline{u_i} = \frac{1}{N} \sum_{k=1}^{N} [u_i(t)]_k \tag{4.6}$$

and the periodic velocity $\tilde{u_i}(t)$, is calculated as the difference of the phase-averaged velocity, $\langle u_i(t) \rangle$, and the mean velocity $\overline{u_i}$.

$$\tilde{u_i}(t) = \langle u_i(t) \rangle - \overline{u_i} \tag{4.7}$$

The phase-averaged velocity can be computed as

$$\langle u_i(t) \rangle = \frac{1}{N_c} \sum_{k=1}^{N_c} u_i(t + k\,T) \tag{4.8}$$

where T (e.g., 5 s) is the period and N_c (e.g., 32 cycles) are the number of cycles measured.

Introducing the Reynolds triple-decomposition to the Navier-Stokes equations and doing a Reynolds averaging, it can be shown that the Reynolds stresses of the background turbulence can be written as

$$R_{ij}(t) = \left\langle u_i'(t)\, u_j'(t) \right\rangle - \overline{u_i'(t)\, u_j'(t)} \tag{4.9}$$

which can be transformed to a dimensionless shear stress or near-bed Shields number $\theta_{uw}(t)$, by

$$\theta_{uw}(t) = \frac{\tau_{uw}(t)}{(\rho_s - \rho_f)\; g\, D_{50}} \tag{4.10}$$

where g is the acceleration due to gravity, τ_{uw} is the Reynolds shear stresses for $i = 1$ and $j = 3$,

$$\tau_{ij} = -\rho_f\, R_{ij}(t) \tag{4.11}$$

and ρ_s and ρ_f are the sediment and fluid density.

4.3.2 Sonar

A custom-designed sonar system capable of performing fast three-dimensional surveys of the sand bed during an experiment was installed in the tunnel (Figure 4.5b). An L-shaped Imagenex 881L Digital Multi-Frequency Profiling Sonar, produced by Imagenex Technology Corp., Canada, was installed on a Velmex B4800TS motorized rotatory table with Velmex VXM controller, produced by Velmex Inc., USA. A mechanical system which allowed the combination of both the Imagenex pencil beam sonar and the Velmex Bislide positioning system was built by the Civil and Environmental Engineering Machine Shop at the University of Illinois at Urbana Champaign (Pedocchi, 2009). In addition, Pedocchi and Oberg[1] developed software to control the motion and acquisition of the backscatter data (Pedocchi, 2009). The combination of the pencil beam sonar and the positioning system with the mechanical system and system software allowed the sonar to be rotated over two axes: i) a horizontal axis that allows the sonar to cover a fan-shaped region contained in a vertical plane where the bed can be surveyed, and ii) a vertical axis that, by rotating along this axis, allows several crossing lines to be acquired to give a complete survey of the bed.

The spatial resolution of the system is controlled by: a) the angle between the ultrasound beam and the sediment bed; b) the opening of the ultrasound beam; c) the angular resolution given by the angular steps of both positioning systems, and d) the distance from the sonar to the bed. The combined system has a 2 mm radial resolution along the ultrasound beam and a 0.3° minimum angular step over the horizontal axis. In addition, to prevent acoustic returns coming from the tunnel walls, the opening angle of the fan was adjusted to between 70° and 100°.

Two-dimensional bed surveys

The single beam sonar was set in the longitudinal direction along the center of the tunnel to measure 'continuous' longitudinal profiles during the experiments. These longitudinal

[1]Nils Oberg, Software Engineer, UIUC. noberg@illinois.edu

sonar data were obtained every 3 s to measure the bed morphology and its spatio-temporal development. In order to eliminate errors due to suspended sediment, several profiles at different phases of the oscillation were averaged. This process averaged out the suspended sediment, leaving just the bed elevation as a function of time (Pedocchi, 2009; Pedocchi and García, 2012).

From this data set three critical observations can be made:

- *'Synthetic stratification'* is an semi-empirical model achieved by superimposing the successive longitudinal profiles of the bedforms with a vertical spacing set by a given aggradation rate (Figure 4.8a). This synthetic stratification methodology was initially implemented by Corea (1978) and continues to be employed by many researchers (e.g., Corea, 1978, 1981; Southard et al., 1990; Dumas et al., 2005; Dumas and Arnott, 2006; Pedocchi, 2009). Of course, it is unlikely that such stratification would be exactly the same as if the bed had actually aggraded; however, it is an intuitive tool to quantify the aggradation of the bed.

- *'Bed evolution'* can be achieved by measuring bedform properties such as wavelength, height (Figure 4.8b), bed elevation (Figure 4.8c) as a function of time.

- *'Bedload transport per unit width'* q_s is determined by

$$q_s = \beta_{bf} \, (1 - \lambda_p) \, \overline{C_{bf}} \, \eta \tag{4.12}$$

(Simons et al., 1965), where λ_p is the bed porosity ($\lambda_p \approx 0.3$, Table 4.2), β_{bf} is the bedform shape factor defined as the ratio between the bedform cross-sectional area A_{bf} and $\eta \, \lambda$ (Rubin and Hunter, 1982)

$$\beta_{bf} = \frac{A_{bf}}{\eta \, \lambda} \tag{4.13}$$

and $\overline{C_{bf}}$ is the mean bedform celerity. The bedform porosity λ_p was estimated for

three experiments (Table 4.2) by measuring the difference between the dry and wet weight of sand collected from an end-of-experiment bedform, instantaneously after the flume water was drained but whilst the bedform was still wet. The bedform porosity, λ_p, for all three cases was close to 0.3, and this value was assumed to be true for all experiments.

The mean bedform celerity $\overline{C_{bf}}$ was computed by time-averaging the instantaneous bedform migration velocity $C_{bf}(t)$ for $t > t_e$

$$\overline{C_{bf}} = \sum_{t>t_e} C_{bf}(t). \tag{4.14}$$

$C_{bf}(t)$ was recorded by tracking the crest displacement (e.g., Coleman, 1969; Dinehart, 2002) $\Delta x = x_2 - x_1$ over the time interval $\Delta t = t_2 - t_1$ (Figure 4.8:d). The results of Q_s, A_{bf} and $\overline{C_{bf}}$ are shown in Table 4.3.

Table 4.2: Bedform Porosity Measurements

#	Init. Cond.	T (s)	U_o ($m\,s^{-1}$)	U_u ($m\,s^{-1}$)	η_e (mm)	λ_e (m)	λ_p
15	00	05	0.20	0.30	27.6	0.27	0.29 ± 0.1
35	00	06	0.25	0.40	68.3	0.65	0.32 ± 0.1
55	00	-	-	0.50	18.1	0.21	0.28 ± 0.1

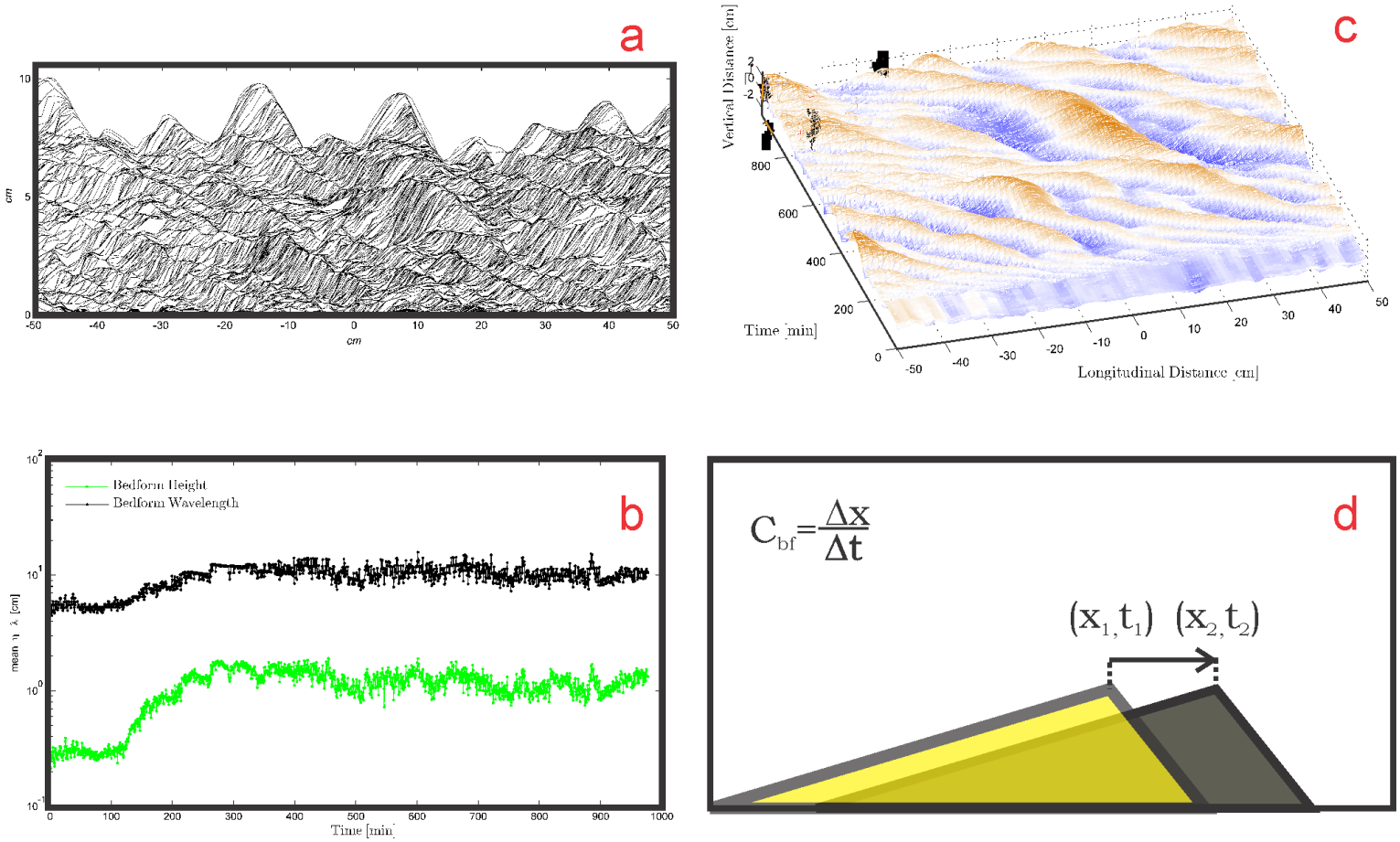

Figure 4.8: Different results generated with the two-dimensional bed elevation surveys; (a) Synthetic stratification, (b) Bedform height and wavelength as a function of time, (c) Evolution of the bed elevation profiles as a function of time. (d) Sketch showing how the bedform migration velocity was computed, where C_{bf} is the bedform celerity, $\Delta x = x_2 - x_1$ and $\Delta t = t_2 - t_1$.

Table 4.3: Summary of flow parameters and bedform development characteristics for experiments.

#[a]	T (s)	U_o ($m\,s^{-1}$)	U_u ($m\,s^{-1}$)	${\eta_e}^b$ (mm)	${\lambda_e}^b$ (m)	${A_{bf}}^c$ $\times 10^3$ (m^3)	${\beta_{bf}}^d$	${\overline{C_{bf}}}^e$ ($mm\,s^{-1}$)	${q_s}^f$ ($cm^2\,s^{-1}$)	${t_e}^g$ (hr)	${t_f}^h$ (hr)	Bedform[i] Type
1	4	0.25	0.00	34.8	0.22	3.63	0.48	0.128	14.94	2.21	5.07	SR
2	4	0.25	0.10	20.5	0.15	2.45	0.79	0.250	28.33	2.22	13.30	QAR
3	4	0.25	0.20	21.1	0.18	2.37	0.62	0.364	33.54	2.81	18.00	AR
4	4	0.25	0.30	26.9	0.23	3.74	0.62	0.413	47.90	1.10	12.50	ARR
5	4	0.25	0.40	35.6	0.51	5.36	0.30	0.221	16.27	9.45	42.20	SR
8	5	0.20	0.00	35.3	0.21	3.72	0.50	0.140	17.19	4.15	37.70	SR
11	5	0.20	0.10	36.4	0.15	2.98	0.53	0.199	27.04	3.80	18.10	QAR
12	5	0.20	0.20	27.3	0.22	2.46	0.42	0.360	28.75	2.60	20.20	QAR
15	5	0.20	0.30	27.6	0.27	3.09	0.41	0.880	70.41	0.73	9.70	ARR
16	5	0.20	0.40	30.3	0.60	9.92	0.55	1.350	156.30	0.58	7.30	ARD
17	5	0.20	0.50	44.6	0.88	17.60	0.45	1.500	210.00	0.30	2.30	ARD
18	5	0.40	0.00	22.0	0.20	2.36	0.53	0.340	27.74	0.67	15.20	SR
19	5	0.40	0.10	23.0	0.17	2.24	0.58	0.730	67.81	0.49	7.50	QAR
20	5	0.40	0.20	20.7	0.21	2.34	0.53	1.360	104.39	0.79	6.20	QARR
21	5	0.40	0.30	61.3	0.58	21.16	0.60	1.300	333.59	0.41	1.65	QARR
22	5	0.40	0.40	98.3	1.02	58.58	0.58	1.870	751.09	0.17	2.20	ARD
25	5	0.50	0.40	153.0	1.23	143.02	0.76	1.500	1220.93	0.50	2.20	ARD
27	6	0.10	0.50	35.5	0.49	5.60	0.32	1.490	119.29	0.93	3.80	CR
30	6	0.25	0.00	32.1	0.20	3.24	0.51	0.140	16.07	4.23	14.49	SR
31	6	0.25	0.05	26.6	0.18	3.70	0.78	0.147	21.36	1.97	17.04	SR
32	6	0.25	0.10	17.2	0.19	2.25	0.70	0.335	28.23	4.27	5.69	QAR
33	6	0.25	0.20	17.6	0.17	1.37	0.45	0.671	37.13	1.53	9.74	QAR
34	6	0.25	0.30	23.3	0.25	3.14	0.54	1.100	97.56	1.14	12.71	ARR
35	6	0.25	0.40	68.3	0.65	26.95	0.61	1.263	366.53	1.31	5.90	ARD
36	6	0.25	0.50	123.0	1.30	115.24	0.72	1.500	930.75	0.31	1.23	ARD
42	6	0.50	0.00	32.3	0.28	5.69	0.62	0.630	88.33	0.55	2.13	SR
55	-	-	0.50	18.1	0.21	2.99	0.77	1.200	117.10	0.82	3.28	CR

[a] Experiment number.
[b] Equilibrium height (η_e) and equilibrium wavelength (λ_e).
[c] Bedform cross-sectional area.
[d] Bedform shape factor (Equation 4.13).
[e] Mean bedform celerity (Equation 4.14).
[f] Bedload transport per unit width (Equation 4.12)
[g] Time until flow-bedform equilibrium.
[h] Duration of experiment.
[i] S-R = Symmetric Ripples, SR-R = Symmetric Rounded Ripples, S-D = Symmetric Dunes, SR-D = Symmetric Rounded Dunes, A-R = Asymmetric Ripples, AR-R = Asymmetric Rounded Ripples, QA-R = Quasi-Asymmetric Ripples, QAR-R = Quasi-Asymmetric Rounded Ripples, A-D = Asymmetric Dunes, AR-D = Asymmetric Rounded Dunes, USPB = Upper Stage Plane Bed and CR = Current Ripples.

Three-dimensional bed surveys

Following the same operation as the two-dimensional bed surveys, the single beam sonar was rotated over the vertical axis to obtain a complete 360° survey. The minimum angular step over the vertical axis (controlled by the rotatory table) was set to 1 deg. In addition, the angular position around the vertical axis was varied between −100° and +100°, with the zero aligned with the centerline of the tunnel. The digital acquisition of the bed morphology allows a detailed analysis of the bed geometry (e.g., wavelength, height, three dimensionality) for each individual flow (Figure 4.9). The complete 360° survey took around seven to ten minutes; hence, the flow was stopped in different stages for the measurement to be conducted. Previous work has shown that equilibrium bedform geometry for a given flow is independent of the initial configuration (Doucette and O'Donoghue, 2006; Perillo et al., 2009). Hence, it can be assumed that stopping the flow to take these measurements did not affect the final stage of the bed morphology as long as the flow was run long enough to reach equilibrium (Doucette and O'Donoghue, 2006; Perillo et al., 2009).

Errors associated with the sonar measurements were computed as the addition of the square-root of the standard deviations (e.g., σ_η) and the instrument error (σ_i)

$$\Delta\eta = \sqrt{\sigma_\eta^2 + \sigma_i^2} \tag{4.15}$$

Equation 4.15 takes into account two main sources of discrepancy. The standard deviations (e.g., σ_η) account for the natural variation of the physical phenomenon introduced by the constant motion of the bedforms and their three-dimensionality, and the second term is associated with the measurement errors from the equipment, which are mainly attributed to the vertical instrument resolution (± 2 mm).

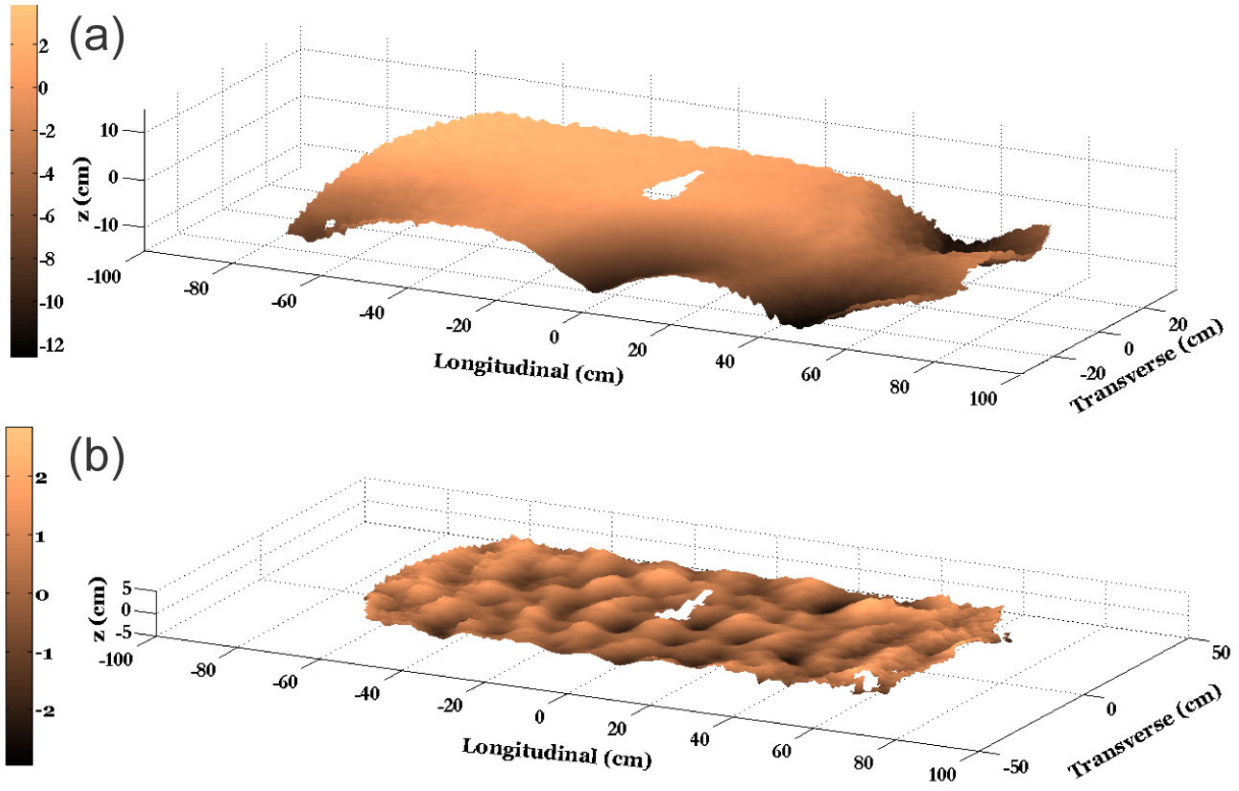

Figure 4.9: Three-dimensional bed elevation surveys for a) Oscillatory Condition: $U_o = 0.40\ m\,s^{-1}$ and $T = 5$ s. Unidirectional Condition: $U_u = 0.50\ m\,s^{-1}$. b) Oscillatory Condition: $U_o = 0.25\ m\,s^{-1}$ and $T = 4$ s. Unidirectional Condition: $U_u = 0.30\ m\,s^{-1}$. The hole in the data at the center, corresponds to the blind region below the sonar head. Color Bar is cm.

4.3.3 Ultrasonic Doppler Velocity Profiler

The Ultrasonic Doppler Velocity Profiler (UDVP) produced by Met-Flow SA consists of a UDVP-Duo system that was controlled by a computer connected via Ethernet and a set of three UDVP transducers. UDVP had been used successfully used to quantitative flow field in a wide range of studies (e.g., Takeda, 1991; Takeda et al., 1994; Best et al., 2001b,a,c; Best and Kostaschuk, 2002; Pedocchi and García, 2012. Similar to the ADV, the UDVP relies on the use of pulsed sound - in this case in the range of ultrasound (emitting frequency = 1 MHz) - to measure both velocity and suspended sediment profiles. As the pulse propagates in the water column, the UDVP transducer receives the echoes returning from the naturally-buoyant particulars (needed in the absence of sediment) or sediment in

suspension along the acoustic path. The scattered sound signal is detected by the receivers and used to compute the Doppler phase shift, from which the flow velocity in the radial or beam direction is calculated by:

$$u_r = \frac{F_D}{2}\frac{c}{F} \tag{4.16}$$

where F_D is the measured Doppler shift, F is the emitted ultrasound frequency (1 MHz) and c is the sound speed of the transmitting medium. From the measurements of F_D and the delayed time (δt) between the emission and reception of ultrasonic signal

$$\delta t = \frac{2\,r}{c} \tag{4.17}$$

the UDVP computes the components of the particle velocities inside the measuring volumes

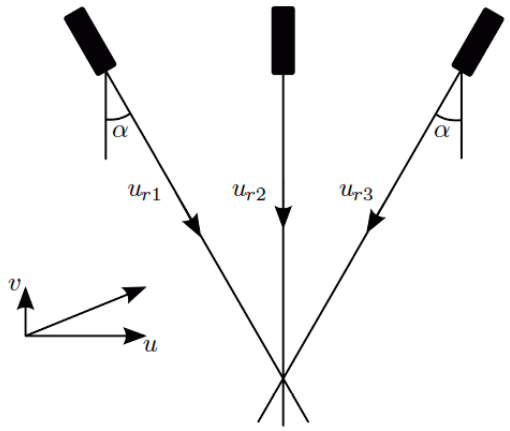

Figure 4.10: UDVP Beam Configuration. The ultrasound beams from the three transducers cross at 5 cm above the flat sediment bed. Where $\alpha = 30°$. From Pedocchi (2009)

at a distance r from the transducer along the sound axis. Following the same methodology proposed by Pedocchi (2009), three UDVP sensors were installed (Figure 4.10) in order to obtain the mean streamwise and vertical fluid velocities $(\overline{u}, \overline{w})$

$$\overline{u} = \frac{\overline{u_{r1}} - \overline{u_{r3}}}{2\,\sin\alpha} \tag{4.18}$$

$$\overline{v} = -\frac{\overline{u_{r1}} + \overline{u_{r3}}}{2\,\cos\alpha} \tag{4.19}$$

and the mean turbulent fluctuations $(\overline{u'}^2, \overline{w'}^2, \overline{u'\,w'})$

$$\overline{u'}^2 = \frac{\overline{u_{r1}'^2} + \overline{u_{r3}'^2} - 2\,\overline{u_{r2}'^2}\,\cos^2\alpha}{2\,\sin^2\alpha} \tag{4.20}$$

$$\overline{w'}^2 = \overline{u_{r2}'^2} \tag{4.21}$$

$$\overline{u'w'} = \frac{\overline{u_{r3}'^2} - \overline{u_{r1}'^2}}{2\,\sin^2\alpha} \tag{4.22}$$

where u_{r1}, u_{r2} and u_{r3} are the instantaneous radial velocities measured by each of the three sensors and $\alpha = 30°$ (Figure 4.10). A sampling volume with a diameter of about 60 mm was achieved with a half-angle divergence of 3.4° for the 1 MHz UDVP transducer (Met-Flow, 2002). The uncertainties introduced by selecting $\alpha = 30°$ on the Reynolds stresses are acceptable (Tropea, 1983). However, errors associated by the returned sound by particles contained inside a finite sampling volume and uncertainties in the computation of the Doppler shift are present (Lhermitte and Lemmin, 1994; Voulgaris and Trowbridge, 1998). In addition, the accuracy of the measurements close to the bed was reduced since the ultrasound beam forms an angle with the vertical. The resulting inclined measuring volume was about 3 cm along the vertical direction.

The strength of the backscattered signal can be used to estimate the sediment concentration. The echo pressure, p, scattered by sediment particles in the water column is:

$$p = \frac{a_s\,f_s\,p_0\,r_0\,D(\theta)^2}{2\,r^2}\exp\left[\omega\,t - 2\,r(k - i\,\alpha_a)\right] \tag{4.23}$$

where a_s is the equivalent particle radius, f_s is the form function that describes the scattering properties of the particle, p_0 is the reference pressure at r_0, $D(\theta)$ is the sensor directivity that is a function of the angle with the transducer axis θ, r is the distance from the sensor

and α_a is the sum of the sediment attenuation (α_s)

$$\alpha_s = \frac{1}{r} \int_0^r \xi \, M(r) \, \mathrm{d}r \tag{4.24}$$

and the water attenuation (α_w), where M(r) is the concentration profile and ξ is the sediment attenuation constant. It can be proved that the pressure wave is governed by the Rayleigh probability distribution as long as there are enough scatterers (Bendat and Piersol, 2000). In addition, if N particles are assumed to be randomly distributed in a measuring volume V, if α_s is relatively small and r is much larger than the sound wavelength the probability distribution of the pressure wave can be represented by the voltage intensity $\langle V^2 \rangle$(Thorne et al., 2002) reported by the UDVP as

$$\left\langle V^2 \right\rangle = \frac{K_s \, K_t}{r \, \psi} \, M \, e^{-4 \, \alpha_a \, r} \tag{4.25}$$

where K_s is a function of the scattering properties of the suspended sediment and K_t is a constant for the ultrasound system and ψ accounts for the departure of the backscattered signal from the spherical spreading in the near field. In order to obtain a relationship between the backscattered signal and the sediment concentration for each experiment (Figure 4.11b), suspended sediment samples were extracted at two different depths by a peristaltic pump. These two suspension samples were used to calibrate the relationship of the voltage intensity $\langle V^2 \rangle$ with the suspended sediment concentration, and then used in Equation 4.25 as the calibration curve for the rest of the profile. Once the calibration was done, the backscatter intensity data was used to calculate the suspended sediment concentration as a function of time at the same time the velocity profile was measured. Measurements by any ultrasound backscatter instrument introduce a number of uncertainties. However, if sufficient temporal averaging is done (e.g., Lemmin and Rolland, 1997 suggest 32 instantaneous samples for oscillatory flows) reliable estimations of the suspended sediment concentration can be ob-

tained. On other other hand, the advantage of the UDVP as compared to other types of sensor is that it provides a non-intrusive methodology to acquire two-dimensional velocity measurements and, at the same time, allows estimation of the sediment concentration. Such

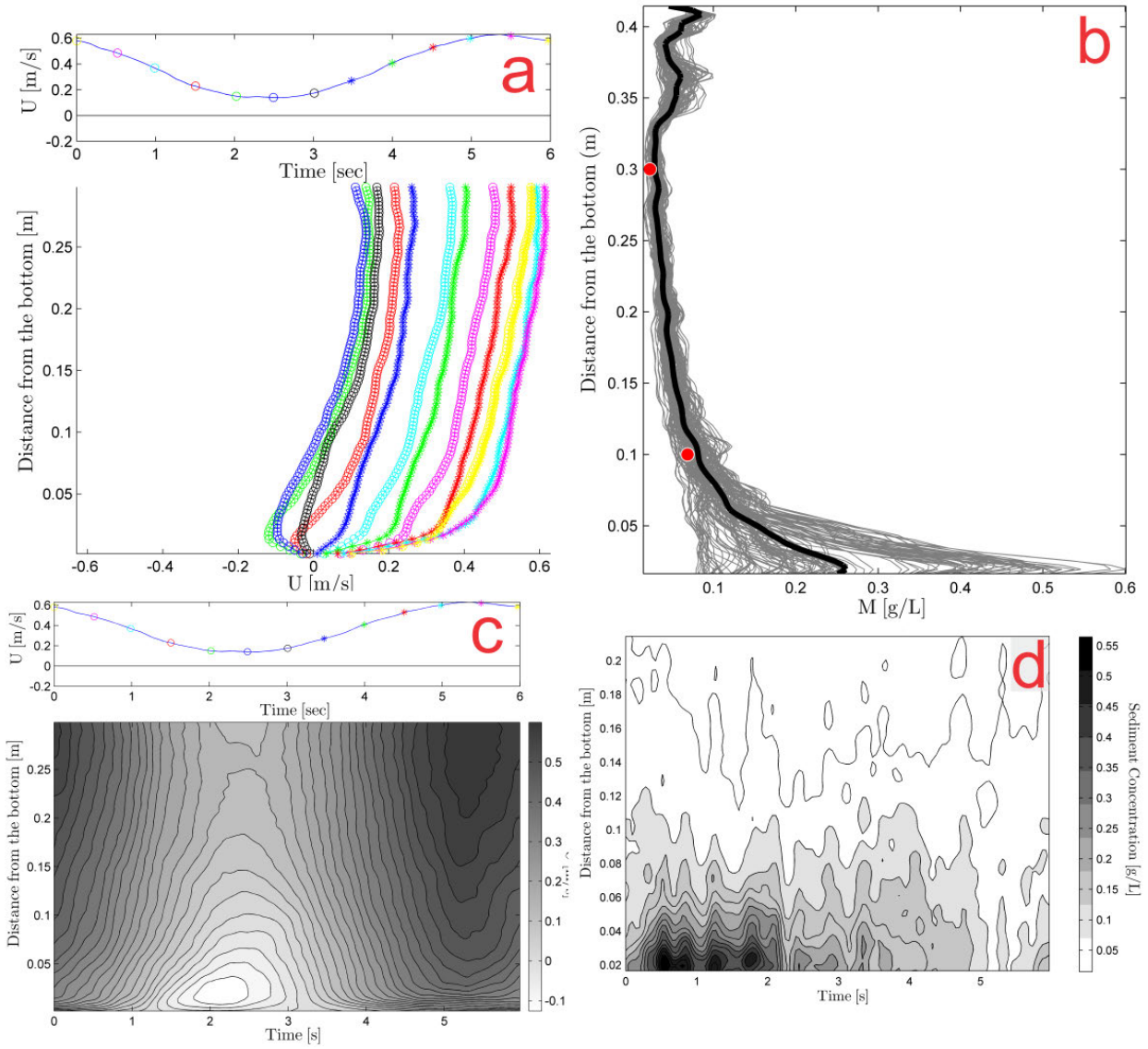

Figure 4.11: Oscillatory Condition: $U_o = 0.25$ ms^{-1}and $T = 6$ s. Unidirectional Condition: $U_u = 0.30$ ms^{-1}. a) Streamwise velocity profiles along the oscillation cycle. b) Inverted suspended sediment concentration profiles for different phases along the oscillation cycle. The bold line corresponds to the mean concentration profile over the cycle that is adjusted to the measured concentration values, indicated by the two dots. c) Contours of streamwise velocity profiles along the oscillation cycle. d) Contours of suspended sediment concentration profiles along the oscillation cycle.

a data set is key to characterize suspended sediment transport and its relation with the flow velocity. In addition, the nature of the experiments conducted in this study did not require the addition of any artificial seeding in order to use the UVDP.

Velocity, Shear Stress and Sediment Concentration Computations

Velocity profiles were obtained using the UDVP installed in the LOWST using a sampling frequency that satisfied Equations 4.2 and 4.3. The maximum Shields number θ was obtained by

$$\theta = \frac{\tau}{(\rho_s - \rho_f)\ g\, D_{50}} \tag{4.26}$$

where the shear stress τ was computed by

$$\tau = -\rho_f\, u_*^2 \tag{4.27}$$

where the shear velocity u_* was obtained by fitting a logarithmic profile to the velocity profile (Figure 4.12c; Nezu and Nakagawa, 1993; Kemp and Simons, 1982)

$$u = \frac{u_*}{\kappa} \ln \frac{z}{z_o} \tag{4.28}$$

All the fits had a R^2 larger than 0.99. The u_*, z_o/D_{50}, τ and maximum value of the Shields number (Equation 4.26) are reported in Table 4.4. Computed values of u_* are compared with the widely used models of Grant and Madsen (1979) (GM79) and Soulsby (1997) (S97). Both models were able to predict the shear velocity with more than $\sim 93\%$ accuracy (Figure 4.13), yet S97 does a slightly better job with almost a 99% precision. Although the fitting of the logarithmic profile to the velocity profile provided good results to obtain the maximum value of the Shields number, it was very difficult to use this technique to compute the shear stress and z_o throughout the oscillatory cycle. The computations were made difficult due to the absence of a clear logarithmic zone during some of the oscillation faces and the change of

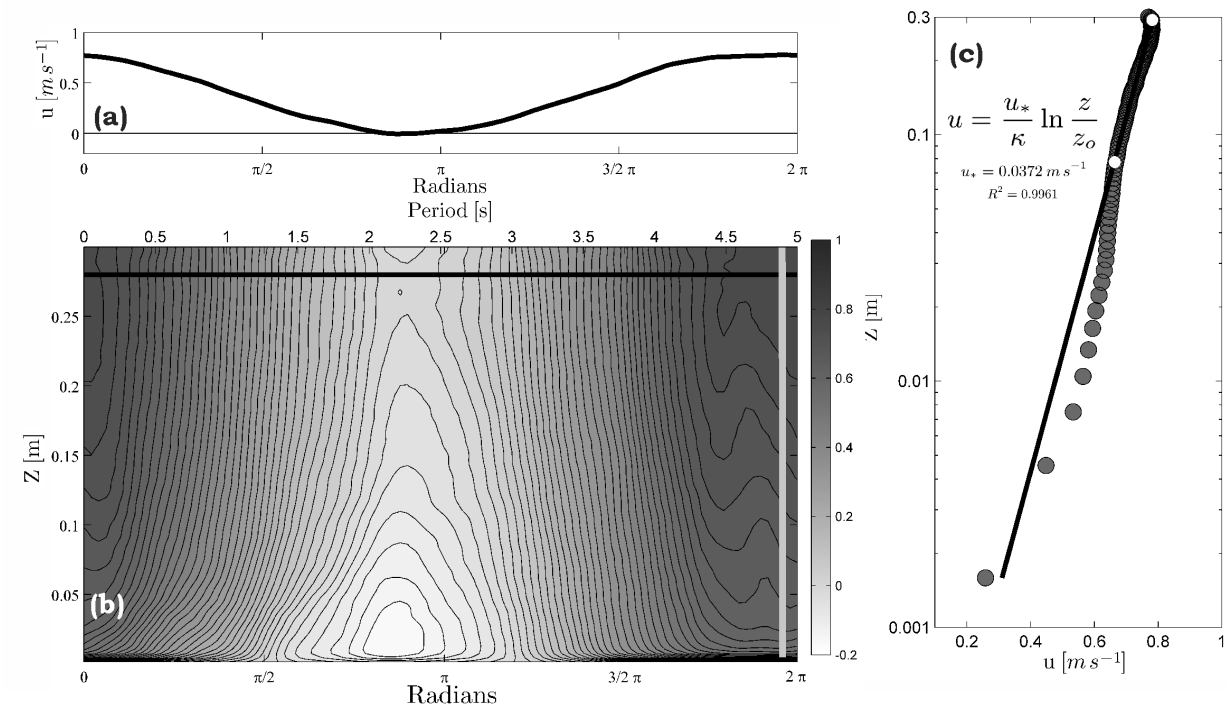

Figure 4.12: UDVP data from experiment 11. Oscillatory Condition: $U_o = 0.40\,m\,s^{-1}$ and $T = 5$ s. Unidirectional Condition: $U_u = 0.40\,m\,s^{-1}$. a) Streamwise phase-averaged velocity along the oscillation cycle at $z = 0.28$ m. These outer flow values are those used to define U_o and U_u . b) Contours of streamwise phase-averaged velocity profiles along the oscillation cycle. The solid black line corresponds to $z = 0.28$ m (plotted in a) and the solid gray line corresponds to $T = 4.896$ s where the maximum shear stress occurred (plotted in c). The gray-scale bar units are $m\,s^{-1}$. c) Logarithmic fit for the velocity profile. White dots indicate the limits of the fitting data.

accuracy of the bottom 5% of the velocity profile data due to changes in sediment suspension in the oscillation.

The depth-averaged unidirectional velocity was computed by integrating over the depth on the time-averaged velocity profile

$$U_H = \frac{1}{H} \int_0^H \overline{u(t,z)}\, dz \tag{4.29}$$

where $H = 0.3$ m and $\overline{u(t,z)}$ is computed with Equation 4.6 for each value of z. In addition, in order to characterize the near-bed concentrations and flow velocity, the near-bed

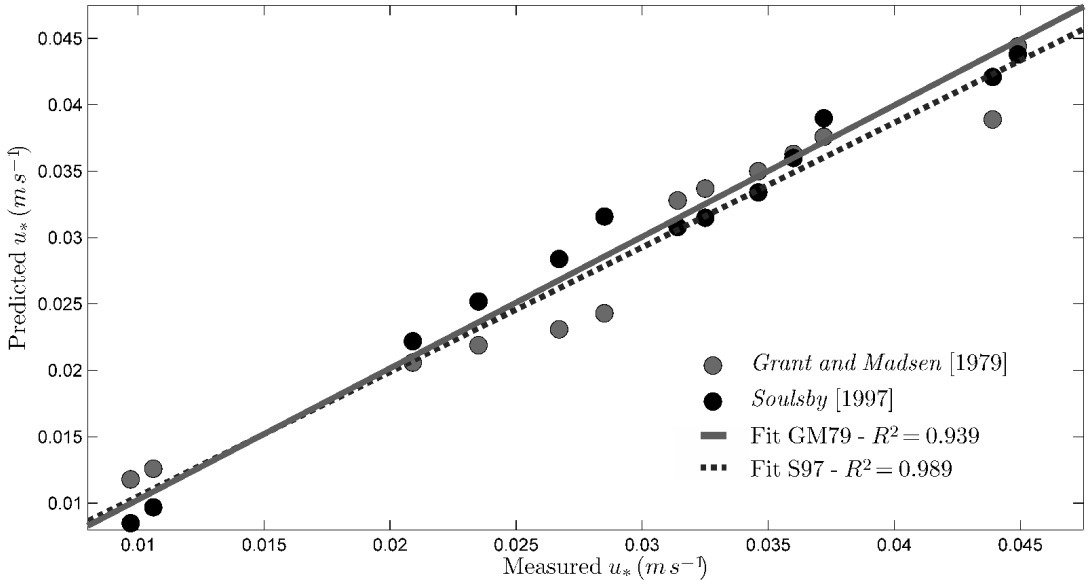

Figure 4.13: Comparison between the measured shear stress with that predicted using the methods of Grant and Madsen (1979) and Soulsby (1997).

depth-averaged combined flow velocity Uh_{wc} was computed as

$$Uh_{wc} = U_H + \tilde{U}_H \tag{4.30}$$

where U_H is computed using Equation 4.29, and $\tilde{U}_H$

$$\tilde{U}_H = \max \tilde{u}_H(t) = \frac{1}{H} \int_0^H \tilde{u}(z,t)\, dz \tag{4.31}$$

The mean sediment concentration, C_x, is computed by a double-averaging process. First, a temporal-average through the wave-cycle:

$$\overline{C(z)} = \frac{1}{N} \sum_j^N C(t,z) \tag{4.32}$$

and then a depth-average over the bottom x m of the flow:

$$C_x = \frac{1}{H} \int_0^H \overline{C(z)}\, dz \tag{4.33}$$

4.3.4 Digital camera

A Canon EOS 7D single-lens reflex (SLR) digital camera with a Canon EF 35mm f/2 wide angle lens was mounted on one of the circular ports located on the top of the tunnel (Figure 4.1). The 18.0 Megapixel digital camera was used to record high-definition and high relative speed (1920×1080 at 30 fps and 1280/720 at 60 fps) videos for planform visualization of the bed evolution. The calibrations between pixel distance and metric distance were achieved by taking a picture of a centimetric spaced target that was then compared to the size of a pixel with the scale in the target. The calibration resulted in 1 pixel being approximately equivalent to 270 μm, which is $1.07\,D_{50}$. In addition, a Logitech Webcam Pro 9000 with a video capture resolution of 1600×1200 pixels was connected to a computer to record the bed evolution from the central side window. These images have been used solely for visualization purposes.

Table 4.4: Summary of flow parameters and computed u_*, z_o/D_{50}, τ and maximum value of the Shields number.

T (s)	U_o ($m\,s^{-1}$)	d_o[a] (m)	U_u ($m\,s^{-1}$)	D_*	U_H[b] ($m\,s^{-1}$)	$u_{*,GM79}$[c] ($m\,s^{-1}$)	$u_{*,S97}$[d] ($m\,s^{-1}$)	u_* ($m\,s^{-1}$)	τ (Pa)	θ_{max}[e]	θ_{uv}[f]	z_o/D_{50}	Temp (°C)	Duration (hr)
05	0.20	0.32	0.00	6.36	0.00	0.0118	0.0085	0.0097	0.093	0.023	0.021	1.82	21.0	37.66
05	0.20	0.32	0.10	5.66	0.07	0.0126	0.0097	0.0106	0.113	0.028		7.77	14.0	18.07
05	0.20	0.32	0.20	5.56	0.15	0.0206	0.0222	0.0209	0.437	0.108		7.03	13.0	20.22
05	0.20	0.32	0.30	5.36	0.25	0.0219	0.0252	0.0235	0.551	0.136	0.153	1.42	11.0	09.68
05	0.20	0.32	0.40	6.11	0.35	0.0231	0.0284	0.0267	0.714	0.177		2.41	18.5	07.35
05	0.20	0.32	0.50	6.36	0.45	0.0243	0.0316	0.0285	0.811	0.200	0.228	1.74	21.0	02.32
05	0.40	0.64	0.00	5.56	0.00	0.0328	0.0308	0.0314	0.985	0.244		1.07	13.0	15.21
05	0.40	0.64	0.10	5.86	0.07	0.0337	0.0315	0.0325	1.055	0.261	0.307	1.18	16.0	07.54
05	0.40	0.64	0.20	5.86	0.15	0.0350	0.0334	0.0346	1.199	0.296		1.39	16.0	06.22
05	0.40	0.64	0.30	6.06	0.22	0.0363	0.0360	0.0360	1.297	0.321		2.02	18.0	01.66
05	0.40	0.64	0.40	6.11	0.33	0.0376	0.0390	0.0372	1.380	0.341		1.49	18.5	02.19
05	0.40	0.64	0.50	5.86	0.44	0.0389	0.0421	0.0439	1.927	0.477	0.404	0.75	16.0	01.39
05	0.50	0.80	0.40	5.56	0.34	0.0444	0.0438	0.0449	2.012	0.498	0.462	1.68	13.0	02.18

[a] Maximum Orbital Diameter, $d_o = (U_o\,T)/\pi$
[b] Depth averaged unidirectional velocity. UDVP data, computed with equation 4.29.
[c] Predicted value based on Grant and Madsen (1979).
[d] Predicted value based on Soulsby (1997).
[e] Maximum value through the oscillation cycle. UDVP data, computed with equation 4.26.
[f] Maximum value through the oscillation cycle. ADV data, computed with equation 4.10.

Chapter 5

Combined Flow Phase Diagram

5.1 Introduction

Subaqueous bedforms are ubiquitous in most sedimentary environments (e.g., deltas, rivers, lagoons, deep and shallow marine) and, depending on the setting, the bedforms or bed features can be generated by currents (unidirectional flows), waves (oscillatory flows) or a combination of both (combined flows). Much laboratory, field and theoretical work has been conducted over several centuries trying to understand bedform genesis, equilibrium, shapes and strata (e.g., Du Buat, 1786; Blasius, 1910; Kennedy, 1969; Harms et al., 1975; Allen, 1983; Southard, 1991; Baas, 1994; Kleinhans, 2001; Doucette and O'Donoghue, 2006; Reesink and Bridge, 2009). However, due to the complexity of the system, there are many aspects that are still barely understood (e.g., scaling relationships, preservation potential, Southard, 1991). This poor understanding of the basic characteristics of bedforms is especially severe for combined flow conditions. Some work has been conducted under combined flows at a range of relatively short oscillation periods and low unidirectional flow velocities (Inman and Bowen, 1963; Harms, 1969; Brevik and Bjørn, 1979; Brevik, 1980; Arnott and Southard, 1990; Southard et al., 1990; Yokokawa, 1995; Dumas et al., 2005; Sekiguchi and Yokokawa, 2008; Perillo et al., 2009). Despite these early attempts, there are still a broad range of combined flow bedforms that have never been investigated (Southard, 1991). Nevertheless, stratigraphers have used this limited set of information as the main tool for paleoenvironmental reconstruction when combined flow bedforms are present in the field (e.g., Basilici et al., 2012; Myrow and Southard, 1991; Myrow et al., 2002). Therefore, to address this gap

in our knowledge of combined flow bedforms, fifty-five experiments were conducted using the LOWST. These experiments permitted production of a set of tools that will allow researchers to better understand and predict environments using bedform geometries, especially those formed made by combined flows.

5.2 Terminology

There is no standard terminology to describe pure oscillatory and combined flow bedforms. Thus, it is essential for any bedform study to clearly define the bedform nomenclature that will be used. An ideal nomenclature or classification scheme should address the characteristic changes in bedform structure or geometry (e.g., planform, height, wavelength) and functionality (e.g., type of flow) for all the potential bed morphologies. Despite the fact that both the structure and functionality of bedforms are strictly related to one another (SFD "trinity"), the information necessary to fully characterize each of the SFD "trinity"products are different and generally not reported (e.g. Dumas et al., 2005). Therefore, based on the data available on combined flow bedforms, and the lack of a consistent nomenclature on oscillatory and unidirectional flows, a new nomenclature is proposed to produce a geometrical-process-based bedform classification. The detailed discussion of the proposed classification can be found in Section 3.5.

5.3 Experimental Data

Fifty-five experiments were conducted in the LOWST, both with and without an initially flattened bed. These experiments are divided into four sets, three of them are organized based on the period of oscillation chosen (T = 4, 5 and 6 s) and the additional set included only the pure unidirectional conditions. The period and maximum orbital velocity for the oscillatory and combined flow conditions were selected in order to conform with the criterion

of Miche (1951)

$$\frac{H_b}{h} = 0.142 \frac{L}{h} \tanh\left(\frac{2\pi h}{L}\right) \tag{5.1}$$

and Airy theory (Komar, 1976)

$$\frac{H}{h}\left(\frac{L}{h}\right)^2 < 32\pi^{2/3} \tag{5.2}$$

$$\frac{H}{h}\left[\frac{L}{h}\tanh\left(\frac{2\pi h}{L}\right)\right]^{-1} < 0.0625 \tag{5.3}$$

A graphical representation of Equations 5.1-5.3 and the experimental data can be found in Figure 5.1.

5.3.1 Experiments 1-7 (Period = 4 sec)

Bedform initiation and development in a 250 μm sandy bed was studied under combined flow conditions with an oscillation period (T) of 4 seconds (Table 5.1). The oscillatory component was set constant to two maximum orbital velocities (U_o): 0.25 and 0.3 $m\,s^{-1}$, while the unidirectional component (U_u) was varied in 0.1 $m\,s^{-1}$ increments from 0 to 0.4 $m\,s^{-1}$ for the case of $U_o = 0.25\,m\,s^{-1}$. The data set includes an additional experiment with a maximum orbital velocity and unidirectional velocity of 0.25 and 0.4 $m\,s^{-1}$ respectively (experiment 06). For this additional experiment, the bed did not develop from a flat bed but from the flow conditions of experiment 05. Run times ranged from 1 to 42 hr, with water temperatures ranging between 18 to 25 °C (Table 5.1).

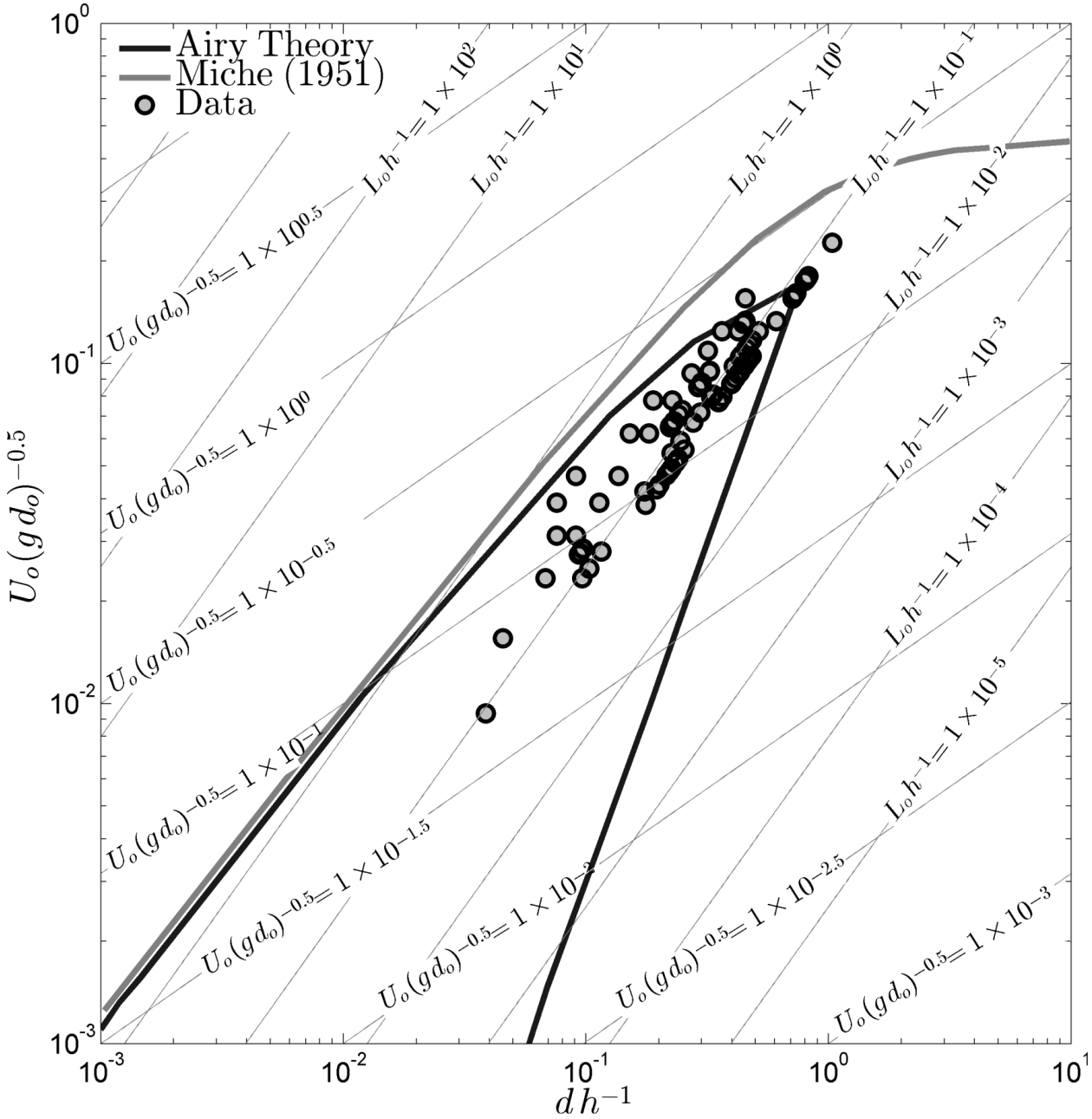

Figure 5.1: Experimental data of the present study plotted versus the criterion of Miche (1951) and Airy valid zone. The experimental data lies right on the valid zone represented by Equations 5.1-5.3.

Table 5.1: Summary of flow parameters and bedform characteristics with $T = 4$ s.

#[a]	Init.[b] Cond.	T (s)	U_o ($m\,s^{-1}$)	d_o (m)	U_u ($m\,s^{-1}$)	λ (m)	η (mm)	λ/d_o	Temp (°C)	Eq. Time[c] (hr)	Duration[d] (hr)
01	00	04	0.25	0.32	0.0	0.22	34.8	0.68	18.0	2.20	05.2
02	00	04	0.25	0.32	0.1	0.15	20.5	0.48	18.5	0.22	13.3
03	00	04	0.25	0.32	0.2	0.18	21.1	0.57	17.5	2.91	18.0
04	00	04	0.25	0.32	0.3	0.23	26.9	0.71	19.0	1.23	12.5
05	00	04	0.25	0.32	0.4	0.51	35.6	1.60	20.0	0.15	02.0
06	04	04	0.25	0.32	0.4	0.52	36.0	1.63	21.5	-	01.1
07	00	04	0.30	0.38	0.0	0.20	31.0	0.52	25.0	9.45	42.2

#[a]	Init.[b] Cond.	T (s)	U_o ($m\,s^{-1}$)	U_u ($m\,s^{-1}$)	BI[e]	BSI[e]	BRI[e]	2D/3D[f]	A/S[g]	nR/R[h]	Bedform[i] Type
01	00	04	0.25	0.0	06.3	0.96	0.40	2D	S	nR	SR
02	00	04	0.25	0.10	07.4	1.39	0.45	2.5D	S	nR	QAR$^{\phi}$
03	00	04	0.25	0.2	08.6	1.53	0.54	2.5D	A	nR	AR$^{\varsigma}$
04	00	04	0.25	0.3	08.4	1.66	0.61	3D	A	R	ARR$^{\varsigma}$
05	00	04	0.25	0.4	14.3	2.36	0.72	3D	A	R	ARD$^{\varsigma}$
06	04	04	0.25	0.4	14.4	2.14	0.71	3D	A	R	ARD$^{\varsigma}$
07	00	04	0.30	0.0	06.5	1.04	0.41	3D	S	nR	SR

[a] Experiment number: s at the end of the name indicate that smaller bedforms were observed superimposed on the larger ones.

[b] Initial condition of the sediment bed at the beginning of the experiment: 00 indicates flat bed, other numbers indicate the number of the experiment run before.

[c] Time until flow-bedform equilibrium.

[d] Experiment duration. [e] $BI = \lambda_\eta\,\eta^{-1}$, $BSI = \lambda_s\,\lambda_l^{-1}$ and $BRI = \lambda_{0.5\,s}\,\lambda_s^{-1}$, equation 3.32.

[f] 2D indicates two-dimensional bedforms, 2.5D indicates the presence of two-dimensional, and three-dimensional or wavy bedforms and 3D indicates three-dimensional bedforms. The superscript [1] indicates that the width of the flume was not large enough for bedforms to fully develop their planform geometry.

[g] A stands for asymmetric ($BSI > 2$) and S for symmetric ($BSI < 2$)

[h] nR stands for not-rounded ($BRI < 0.6$) and R stands for rounded ($BRI > 0.6$).

[i] SR = Symmetric Ripples, AR = Asymmetric Ripples, ARR = Asymmetric Rounded Ripples, QAR = Quasi-Asymmetric Ripples and ARD = Asymmetric Rounded Dunes. $^{\phi}$ = Wave-Dominated Combined Flows and $^{\varsigma}$ = Current-Dominated Combined Flows.

5.3.2 Experiments 8-25 (Period = 5 sec)

Experiments under combined flow conditions with an oscillation period (T) of 5 seconds (Tables 5.2 and 5.3) were conducted with durations ranging from 1 to 38 hours, with water temperatures ranging between 11 and 21°C. The unidirectional component (U_u) was varied

and superimposed over two maximum orbital velocities ($U_o = 0.2$ and $0.4\ m\,s^{-1}$) in $0.1\ m\,s^{-1}$ increments from 0 to $0.5\ m\,s^{-1}$. The only experiment that does not follow this description is Experiment 25 that has a maximum orbital velocity of $0.5\ m\,s^{-1}$ and a unidirectional velocity of $0.4\ m\,s^{-1}$.

Table 5.2: Summary of flow parameters and bedform characteristics with $T = 5$ s.

#[a]	Init.[b] Cond.	T (s)	U_o ($m\,s^{-1}$)	d_o (m)	U_u ($m\,s^{-1}$)	λ (m)	η (mm)	λ/d_o	Temp (°C)	Eq. Time[c] (hr)	Duration[d] (hr)
08	00	05	0.20	0.32	0.00	0.21	35.30	0.67	21.0	03.3	37.7
09	13	05	0.20	0.32	0.00	0.19	33.10	0.58	13.0	-	08.8
10	11	05	0.20	0.32	0.00	0.16	23.60	0.51	14.0	-	28.6
11	00	05	0.20	0.32	0.10	0.15	36.40	0.46	14.0	03.8	18.1

#[a]	Init.[b] Cond.	T (s)	U_o ($m\,s^{-1}$)	U_u ($m\,s^{-1}$)	BI[e]	BSI[e]	BRI[e]	2D/3D[f]	A/S[g]	nR/R[h]	Bedform[i] Type
08	00	05	0.20	0.00	6.01	0.97	0.36	2D	S	nR	SR
09	13	05	0.20	0.00	5.59	1.00	0.39	3D	S	nR	SR
10	11	05	0.20	0.00	6.86	0.98	0.42	3D	S	nR	SR
11	00	05	0.20	0.10	4.01	1.17	0.52	3D	S	nR	QAR$^{\phi}$

[a] Experiment number: s at the end of the name indicate that smaller bedforms were observed superimposed on the larger ones.

[b] Initial condition of the sediment bed at the beginning of the experiment: 00 indicates flat bed, other numbers indicate the number of the experiment run before.

[c] Time until flow-bedform equilibrium.

[d] Experiment duration.

[e] $BI = \lambda_\eta\,\eta^{-1}$, $BSI = \lambda_s\,\lambda_l^{-1}$ and $BRI = \lambda_{0.5\,s}\,\lambda_s^{-1}$, equation 3.32.

[f] 2D indicates two-dimensional bedforms, 2.5D indicates the presence of two-dimensional and three-dimensional or wavy bedforms and 3D indicates three-dimensional bedforms. The superscript [1] indicates that the width of the flume was not big enough for bedforms to fully develop their planform geometry.

[g] A stands for asymmetric ($BSI > 2$) and S for symmetric ($BSI < 2$)

[h] nR stands for not-rounded ($BRI < 0.6$) and R stands for rounded ($BRI > 0.6$).

[i] SR = Symmetric Ripples, AR = Asymmetric Ripples, ARR = Asymmetric Rounded Ripples, QAR = Quasi-Asymmetric Ripples, QARR = Quasi-Asymmetric Rounded Ripples, ARD = Asymmetric Rounded Dunes and USPB = Upper Stage Plane Bed. $^{\phi}$ = Wave-Dominated Combined Flows and $^{\varsigma}$ = Current-Dominated Combined Flows.

Table 5.3: Summary of flow parameters and bedform characteristics with $T = 5$ s (cont'd).

#[a]	Init.[b] Cond.	T (s)	U_o ($m\,s^{-1}$)	d_o (m)	U_u ($m\,s^{-1}$)	λ (m)	η (mm)	λ/d_o	Temp (°C)	Eq. Time[c] (hr)	Duration[d] (hr)
12	00	05	0.20	0.32	0.20	0.22	27.30	0.68	13.0	02.6	20.2
13	01	05	0.20	0.32	0.20	0.20	30.00	0.63	18.5	-	08.3
14	09	05	0.20	0.32	0.20	0.21	29.30	0.66	18.5	-	05.2
15	00	05	0.20	0.32	0.30	0.27	27.60	0.85	11.0	01.5	09.7
15s	00	05	0.20	0.32	0.30	0.12	14.60	0.38	11.0	-	09.7
16	00	05	0.20	0.32	0.40	0.60	30.30	1.89	18.5	00.6	07.3
16S	00	05	0.20	0.32	0.40	0.24	20.10	0.76	18.5	-	07.3
17	00	05	0.20	0.32	0.50	0.88	44.60	2.78	21.0	00.3	02.3
17s	00	05	0.20	0.32	0.50	0.27	21.20	0.84	21.0	-	02.3
18	00	05	0.40	0.64	0.00	0.24	22.00	0.38	13.0	00.6	15.2
19	00	05	0.40	0.64	0.10	0.22	23.00	0.35	16.0	00.4	07.5
19s	00	05	0.40	0.64	0.10	0.13	10.60	0.21	16.0	-	07.5
20	00	05	0.40	0.64	0.20	0.21	20.70	0.33	16.0	00.8	06.2
21	00	05	0.40	0.64	0.30	0.42	61.30	0.66	18.0	00.4	01.7
21s	00	05	0.40	0.64	0.30	0.17	16.30	0.27	18.0	-	01.7
22	00	05	0.40	0.64	0.40	1.02	98.30	1.60	18.5	00.2	02.2
23	16	05	0.40	0.64	0.40	1.05	102.30	1.65	17.0	-	00.8
24	00	05	0.40	0.64	0.50	-	-	-	16.0	-	01.4
25	00	05	0.50	0.80	0.40	1.23	153.00	1.55	13.0	00.5	02.2

#[a]	Init.[b] Cond.	T (s)	U_o ($m\,s^{-1}$)	U_u ($m\,s^{-1}$)	BI[e]	BSI[e]	BRI[e]	2D/3D[f]	A/S[g]	nR/R[h]	Bedform[i] Type
12	00	05	0.20	0.20	7.91	1.34	0.54	3D	S	nR	QAR$^{\varsigma}$
13	01	05	0.20	0.20	6.73	1.32	0.53	3D	S	nR	QAR$^{\varsigma}$
14	09	05	0.20	0.20	7.13	1.28	0.55	3D	S	nR	QAR$^{\varsigma}$
15	00	05	0.20	0.30	9.75	1.96	0.61	3D	A	R	ARR$^{\varsigma}$
15s	00	05	0.20	0.30	8.36	1.70	-	3D	A	nR	AR$^{\varsigma}$
16	00	05	0.20	0.40	19.83	2.29	0.78	3D	A	R	ARD$^{\varsigma}$
16S	00	05	0.20	0.40	12.04	1.63	-	3D	A	nR	AR$^{\varsigma}$
17	00	05	0.20	0.50	19.82	3.20	0.88	3D	A	R	ARD$^{\varsigma}$
17s	00	05	0.20	0.50	12.59	2.3	-	3D	A	nR	AR$^{\varsigma}$
18	00	05	0.40	0.00	10.86	1.11	0.43	3D	S	nR	SR
19	00	05	0.40	0.10	9.65	1.31	0.32	3D	S	nR	QAR$^{\phi}$
19s	00	05	0.40	0.10	12.36	1.2	-	3D	S	nR	SR
20	00	05	0.40	0.20	10.14	1.31	0.68	3D	S	R	QARR$^{\phi}$
21	00	05	0.40	0.30	6.88	1.22	0.73	3D	S	R	QARR$^{\varsigma}$
21s	00	05	0.40	0.30	10.55	1.2	-	3D	S	nR	SR
22	00	05	0.40	0.40	10.39	4.20	0.89	2D[1]	A	R	ARD$^{\varsigma}$
23	16	05	0.40	0.40	10.29	4.16	0.92	2D[1]	A	R	ARD$^{\varsigma}$
24	00	05	0.40	0.50	-	-	-	-	-	-	USPB
25	00	05	0.50	0.40	8.05	3.10	0.63	2D[1]	A	R	ARD$^{\varsigma}$

[a,b,c,d,e,f,g,h,i] See Table 5.4

5.3.3 Experiments 26-47 (Period = 6 sec)

A wide range of combined flow conditions with an oscillation period (T) of 6 seconds (Tables 5.4 to 5.6) were conducted with maximum orbital velocities (U_o) between 0.1 and 1.0 $m\,s^{-1}$ and unidirectional velocities between 0.0 and 0.5 $m\,s^{-1}$. Times ranged from approximately 0.5 to 43 hours with water temperatures ranging between 18 to 24°C (Tables 5.4 to 5.6).

Table 5.4: Summary of flow parameters and bedform characteristics with $T = 6$ s.

#[a]	Init.[b] Cond.	T (s)	U_o ($m\,s^{-1}$)	d_o (m)	U_u ($m\,s^{-1}$)	λ (m)	η (mm)	λ/d_o	Temp (°C)	Eq. Time[c] (hr)	Duration[d] (hr)
26c	41	06	0.10	0.19	0.20	0.22	23.20	1.15	24.0	-	28.4
26c	41	06	0.10	0.19	0.20	0.15	12.10	0.76	24.0	-	28.4
27	00	06	0.10	0.19	0.50	0.49	35.50	2.56	19.0	0.74	03.9
27s	00	06	0.10	0.19	0.50	0.21	15.10	1.11	19.0	0.74	03.9
28	28	06	0.15	0.29	0.40	0.56	37.90	1.97	20.0	-	07.7
28s	28	06	0.15	0.29	0.40	0.21	18.80	0.73	20.0	-	07.7

#[a]	Init.[b] Cond.	T (s)	U_o ($m\,s^{-1}$)	U_u ($m\,s^{-1}$)	BI[e]	BSI[e]	BRI[e]	2D/3D[f]	A/S[g]	nR/R[h]	Bedform[i] Type
26c	41	06	0.10	0.20	09.5	1.97	0.53	3D	A	nR	AR
26c	41	06	0.10	0.20	12.02	1.78	0.51	3D	A	nR	AR
27	00	06	0.10	0.50	13.77	1.72	0.52	3D	A	nR	CR$^{\varsigma}$
27s	00	06	0.10	0.50	13.99	1.60	0.51	3D	A	nR	CR
28	28	06	0.15	0.40	14.87	3.26	0.58	3D	A	nR	AD
28s	28	06	0.15	0.40	11.17	2.30	0.46	3D	A	nR	AR

[a] Experiment number: s at the end of the name indicate that smaller bedforms were observed superimposed on the larger ones.

[b] Initial condition of the sediment bed at the beginning of the experiment: 00 indicates flat bed, other numbers indicate the number of the experiment run before.

[c] Time until flow-bedform equilibrium.

[d] Experiment duration.

[e] $BI = \lambda_\eta\,\eta^{-1}$, $BSI = \lambda_s\,\lambda_l^{-1}$ and $BRI = \lambda_{0.5\,s}\,\lambda_s^{-1}$, equation 3.32.

[f] 2D indicates two-dimensional bedforms, 2.5D indicates the presence of two-dimensional and three-dimensional or wavy bedforms and 3D indicates three-dimensional bedforms. The superscript [1] indicates that the width of the flume was not big enough for bedforms to fully develop their planform geometry.

[g] A stands for asymmetric ($BSI > 2$) and S for symmetric ($BSI < 2$)

[h] nR stands for not-rounded ($BRI < 0.6$) and R stands for rounded ($BRI > 0.6$).

[i] SR = Symmetric Ripples, SRR = Symmetric Rounded Ripples, SD = Symmetric Dunes, SRD = Symmetric Rounded Dunes, AR = Asymmetric Ripples, ARR = Asymmetric Rounded Ripples, QAR = Quasi-Asymmetric Ripples, QARR = Quasi-Asymmetric Rounded Ripples, AD = Asymmetric Dunes, ARD = Asymmetric Rounded Dunes, USPB = Upper Stage Plane Bed and CR = Current Ripples. $^{\phi}$ = Wave-Dominated Combined Flows and $^{\varsigma}$ = Current-Dominated Combined Flows.

Table 5.5: Summary of flow parameters and bedform characteristics with $T = 6$ s (cont'd).

#[a]	Init.[b] Cond.	T (s)	U_o ($m\,s^{-1}$)	d_o (m)	U_u ($m\,s^{-1}$)	λ (m)	η (mm)	λ/d_o	Temp (°C)	Eq. Time[c] (hr)	Duration[d] (hr)
29	39	06	0.20	0.38	0.00	0.25	42.00	0.66	20.0	-	16.0
30	00	06	0.25	0.48	0.00	0.20	32.10	0.42	20.5	2.83	15.5
31c	00	06	0.25	0.48	0.05	0.18	26.60	0.38	20.0	2.57	17.7
31c	00	06	0.25	0.48	0.05	0.14	17.36	0.29	20.0	2.57	17.7
32	00	06	0.25	0.48	0.10	0.19	17.20	0.39	19.0	1.09	11.3
33	00	06	0.25	0.48	0.20	0.17	17.60	0.36	18.0	1.39	10.6
34	00	06	0.25	0.48	0.30	0.25	23.30	0.52	21.0	1.09	06.9
35	00	06	0.25	0.48	0.40	0.65	68.30	1.36	19.5	1.13	06.2
36	00	06	0.25	0.48	0.50	1.30	123.00	2.72	22.0	0.31	01.2
37	16	06	0.30	0.57	0.00	0.22	39.40	0.38	19.0	-	42.8
37s	16	06	0.30	0.57	0.00	0.14	17.00	0.24	19.0	-	42.8
38	40	06	0.30	0.57	0.10	0.17	18.45	0.30	20.0	-	09.5
39	42	06	0.30	0.57	0.20	0.30	38.80	0.53	20.0	-	08.4
39s	42	06	0.30	0.57	0.20	0.16	14.50	0.28	20.0	-	08.4
40	44	06	0.40	0.76	0.20	0.32	48.60	0.42	19.0	-	05.0
40s	44	06	0.40	0.76	0.20	0.17	13.70	0.23	19.0	-	05.0
41	45	06	0.40	0.76	0.30	0.74	84.16	0.97	20.0	-	03.4
42	00	06	0.50	0.95	0.00	0.28	32.30	0.29	21.0	0.72	06.4
43	29	06	0.50	0.95	0.30	0.56	31.00	0.58	23.5	-	01.2

#[a]	Init.[b] Cond.	T (s)	U_o ($m\,s^{-1}$)	U_u ($m\,s^{-1}$)	BI[e]	BSI[e]	BRI[e]	2D/3D[f]	A/S[g]	nR/R[h]	Bedform[i] Type
29	39	06	0.20	0.00	6.02	1.04	0.37	2D	S	nR	SR
30	00	06	0.25	0.00	6.23	1.08	0.42	2D	S	nR	SR
31c	00	06	0.25	0.05	6.77	1.37	0.43	2.5D	S	nR	SR$^{\phi}$
31c	00	06	0.25	0.05	8.02	1.20	0.39	2.5D	S	nR	SR$^{\phi}$
32	00	06	0.25	0.10	10.86	1.44	0.40	3D	S	nR	QAR$^{\phi}$
33	00	06	0.25	0.20	9.84	1.45	0.45	3D	S	nR	QAR$^{\varsigma}$
34	00	06	0.25	0.30	10.64	2.79	0.72	3D	A	R	ARR$^{\varsigma}$
35	00	06	0.25	0.40	9.52	3.15	0.64	3D	A	R	ARD$^{\varsigma}$
36	00	06	0.25	0.50	10.57	3.69	0.82	3D	A	R	ARD$^{\varsigma}$
37	16	06	0.30	0.00	5.57	1.15	0.45	2.5D	S	nR	SR
37s	16	06	0.30	0.00	7.96	1.02	0.42	2.5D	S	nR	SR
38	40	06	0.30	0.10	9.34	1.37	0.44	3D	S	nR	QAR
39	42	06	0.30	0.20	7.84	1.46	0.51	3D	S	nR	QAR
39s	42	06	0.30	0.20	11.14	1.53	0.55	3D	A	nR	AR
40	44	06	0.40	0.20	6.63	1.63	0.63	3D	A	R	ARR
40s	44	06	0.40	0.20	12.74	1.63	0.56	3D	A	nR	AR
41	45	06	0.40	0.30	8.80	2.17	0.72	3D[1]	A	R	ARD
42	00	06	0.50	0.00	8.67	1.14	0.41	3D	S	nR	SR
43	29	06	0.50	0.30	17.96	3.33	0.71	3D	A	R	ARD

[a,b,c,d,e,f,g,h,i] See Table 5.4

Table 5.6: Summary of flow parameters and bedform characteristics with $T = 6$ s (cont'd).

#[a]	Init.[b] Cond.	T (s)	U_o ($m\,s^{-1}$)	d_o (m)	U_u ($m\,s^{-1}$)	λ (m)	η (mm)	λ/d_o	Temp (°C)	Eq. Time[c] (hr)	Duration[d] (hr)
43s	29	06	0.50	0.95	0.30	0.18	14.00	0.19	23.5	-	01.2
44	00	06	0.60	1.15	0.40	-	-	-	20.0	-	00.4
45c	00	06	0.70	1.34	0.00	0.71	50.08	0.53	18.0	0.23	21.0
45c	00	06	0.70	1.34	0.00	0.36	19.80	0.27	18.0	0.23	21.0
46	29	06	0.80	1.53	0.20	0.73	71.00	0.48	20.0	-	00.5
47	00	06	1.00	1.91	0.50	-	-	-	23.0	-	00.4

#[a]	Init.[b] Cond.	T (s)	U_o ($m\,s^{-1}$)	U_u ($m\,s^{-1}$)	BI[e]	BSI[e]	BRI[e]	2D/3D[f]	A/S[g]	nR/R[h]	Bedform[i] Type
43s	29	06	0.50	0.30	12.64	2.10	0.55	3D	A	nR	AR
44	00	06	0.60	0.40	-	-	-	-	-	-	USPB
45c	00	06	0.70	0.00	14.18	0.91	0.38	3D	S	nR	SD
45c	00	06	0.70	0.00	18.19	1.12	0.42	3D	S	nR	SR
46	29	06	0.80	0.20	10.28	1.20	0.50	3D	S	nR	SD
47	00	06	1.00	0.50	-	-	-	-	-	-	USPB

[a,b,c,d,e,f,g,h,i] See Table 5.4

5.3.4 Experiments 48-55 (Unidirectional Flows)

A limited number of pure unidirectional flow conditions were investigated (Table 5.7). Sediment entrainment occurred for flow velocities larger than 0.3 $m\,s^{-1}$, and hence there were not any bedforms in experiments 48 to 53 (Table 5.7).

Table 5.7: Summary of flow parameters and bedform characteristics pure unidirectional flows.

#[a]	Init.[b] Cond.	T (s)	U_o ($m\,s^{-1}$)	d_o (m)	U_u ($m\,s^{-1}$)	λ (m)	η (mm)	λ/d_o	Temp (°C)	Eq. Time[c] (hr)	Duration[d] (hr)
48	00	-	-	-	0.05	-	-	-	16.00	-	8.0
49	00	-	-	-	0.10	-	-	-	17.00	-	6.0
50	00	-	-	-	0.15	-	-	-	18.00	-	0.5
51	00	-	-	-	0.20	-	-	-	18.00	-	3.3
52	00	-	-	-	0.30	-	-	-	18.50	-	5.0
53	52	-	-	-	0.40	-	-	-	18.50	-	4.6
54	00	-	-	-	0.40	0.20	17.6	-	17.00	9.4	18.0
55	00	-	-	-	0.50	0.21	18.1	-	18.50	0.8	3.3

#[a]	Init.[b] Cond.	T (s)	U_o ($m\,s^{-1}$)	U_u ($m\,s^{-1}$)	BI[e]	BSI[e]	BRI[e]	2D/3D[f]	A/S[g]	nR/R[h]	Bedform[i] Type
48	00	-	-	0.05	-	-	-	-	-	-	NM
49	00	-	-	0.10	-	-	-	-	-	-	NM
50	00	-	-	0.15	-	-	-	-	-	-	NM
51	00	-	-	0.20	-	-	-	-	-	-	NM
52	00	-	-	0.30	-	-	-	-	-	-	NM
53	52	-	-	0.40	-	-	-	-	-	-	CR
54	00	-	-	0.40	11.36	2.21	0.51	3D	A	nR	CR
55	00	-	-	0.50	11.84	2.36	0.49	3D	A	nR	CR

[a] Experiment number

[b] Initial condition of the sediment bed at the beginning of the experiment: 00 indicates flat bed, other numbers indicate the number of the experiment run before.

[c] Time until flow-bedform equilibrium.

[d] Experiment duration. [e] $BI = \lambda_\eta\,\eta^{-1}$, $BSI = \lambda_s\,\lambda_l^{-1}$ and $BRI = \lambda_{0.5\,s}\,\lambda_s^{-1}$, equation 3.32.

[f] 2D indicates two-dimensional bedforms, 2.5D indicates the presence of two-dimensional and three-dimensional or wavy bedforms and 3D indicates three-dimensional bedforms. The superscript [1] indicates that the width of the flume was not big enough for bedforms to fully develop their planform geometry.

[g] A stands for asymmetric ($BSI > 2$) and S for symmetric ($BSI < 2$)

[h] nR stands for not-rounded ($BRI < 0.6$) and R stands for rounded ($BRI > 0.6$).

[i] NM = No Motion and CR = Current Ripples.

5.4 Phase Diagrams

As discussed in chapter 3, phase diagrams are graphs that show the regimes of existence of one or more stable bed states. Before plotting different phase diagrams, it is important to discuss the relevant variables that characterize the system.

5.4.1 Relevant Variables

For the case of a system with co-existing waves and currents in the absence of any bed topography, a complete representation can be achieved by selecting:

- the oscillation period (T), the maximum orbital speed (U_o), the wave amplitude (A) and the wave orbital diameter (d_0) for the oscillatory component.
- the water depth (h) and the mean velocity (U_u) for the unidirectional component.
- the angle (γ) between the waves and the current to quantify the wave-current interaction.
- the mean grain size (D_{50}) and the sediment density (ρ_s) to quantify the sediment.
- the fluid viscosity (ν) and the fluid density (ρ) to quantify the fluid flow.

In addition to these variables, the acceleration due to gravity (g) is needed to fully characterize the system. This yields seven variables for the flow and five for the sediment and fluid. Further analysis of the physics of wave-current interactions allows choice of the most relevant variables that will characterize the system. As mentioned before, in this particular study the waves and currents are co-linear, and therefore $\gamma = 0°$. Furthermore, if the water oscillation is assumed sinusoidal, the difference between the wave amplitude and the wave orbital diameter is a factor of 2,

$$d_0 = 2\,A = \frac{U_o\,T}{\pi} \tag{5.4}$$

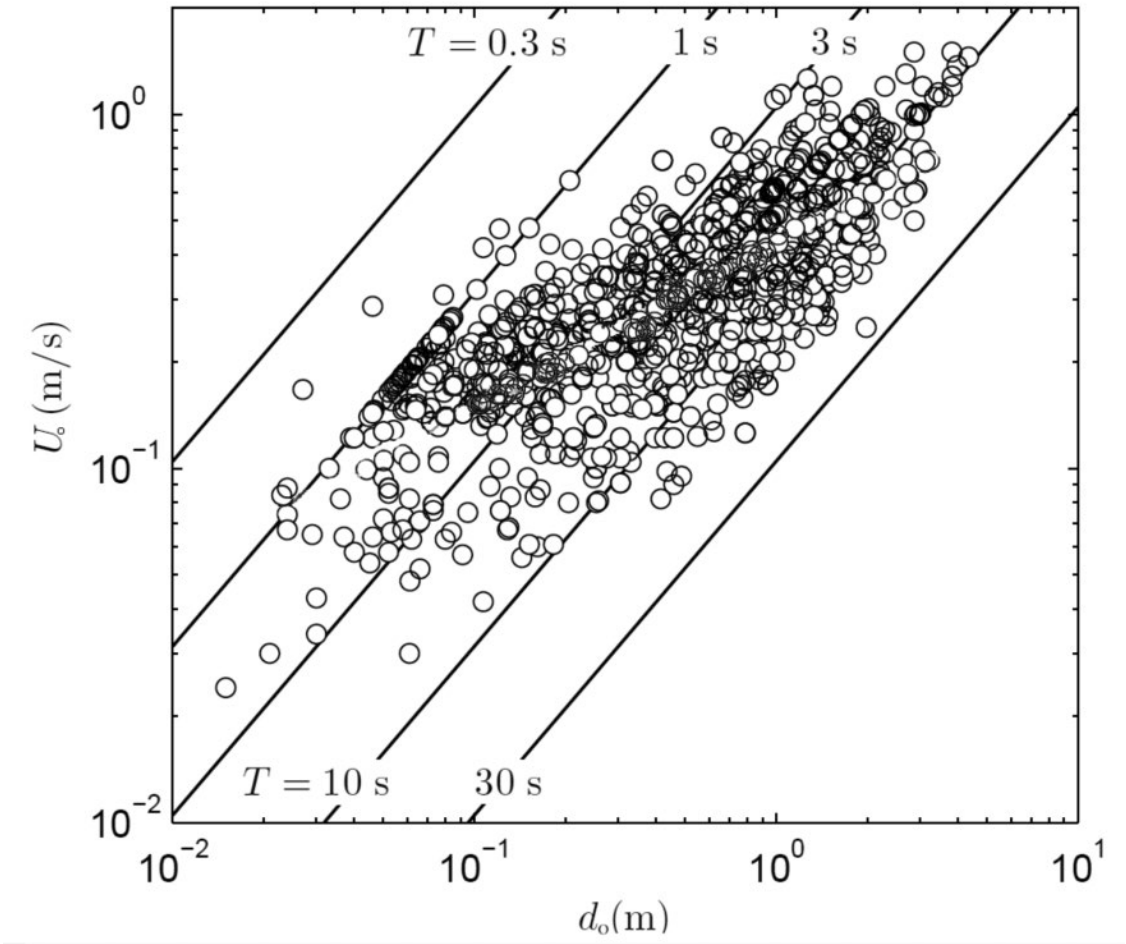

Figure 5.2: The wave orbital diameter, d_o, plotted against the maximum orbital velocity, U_o. Lines of constant period, T, are also plotted. Although the variables should be independent of eachother, the data suggests the opposite. Modified from Pedocchi and García (2009b).

Therefore, in order to characterize the oscillatory flow, only two of the three variables (d_0, T, U_o) are needed, since the third can be computed using equation 5.4. However, recent studies by Pedocchi and García (2009b) have suggested that there is no true independence between these three characteristic variables (d_0, T and U_o; Figure 5.2). Figure 5.2 shows that there is a correlation between the variables, where short excursions tend to take place with weak oscillatory velocities and short periods and long excursions over longer periods and stronger velocities. However, the same short or long excursions do not happen over long or short periods since the velocity necessary to achieve such values do not occur in natural environments. Therefore, it is very important to address this dependence, when using d_0, T

or U_o, to obtain relationships that characterize oscillatory and combined flows. Nevertheless, keeping in mind this dependence, two of the variables are used here to characterize the oscillatory component of the combined flow, reducing the relevant variables from twelve to nine. In addition, in combined flow as in oscillatory flows, the flow depth does not play a significant role and is assumed to be shallow enough that the waves and sea-bed interact (Pedocchi, 2009). Including this simplification, the number of variables is then reduced from nine to eight

- the oscillation period (T), the maximum orbital speed (U_o) or the wave orbital diameter (d_0) for the oscillatory component.
- the mean velocity (U_u) for the unidirectional component.
- the mean grain size (D_{50}) and the sediment density (ρ_s) to quantify the sediment.
- the fluid viscosity (ν) and the fluid density (ρ) to quantify the fluid flow.
- acceleration due to gravity g.

In order to reduce the system to a manageable set of variables, two possible solutions are proposed in the literature: fixed parameters or dimensionless quantities.

5.4.2 Fixed Parameters: Dimensional Phase Diagram

Fixed parameters have often been used by geologists to generate phase diagrams with a number of fixed variables (e.g., Arnott and Southard, 1990; Dumas et al., 2005). Such simplification allows the use of standard variables on the axes, making it intuitively easier to relate with natural conditions, but more restrictive. From the previous section (section 5.4.1), eight variables were stated as needed to characterize the system. These variables can be reduced to a more manageable quantity if there is more information about the particular system. The bedforms studied in this chapter were generated under an acceleration due

to gravity of $\approx 9.8\,m\,s^{-2}$, and the range of water temperatures occurring in shallow-marine environments is not great enough to have significant variations in the fluid viscosity ($\nu \approx 1 \times 10^{-6}\,m^2\,s^{-1}$) and density ($\rho \approx 1000\,kg\,m^{-3}$). In addition, despite the presence of many types of grains, in general the density of the grains can be assumed to be $\rho_s \approx 2650\ kg\,m^{-3}$, which is the density of quartz. Therefore, the system can now be described by four variables, the oscillation period (T), the maximum orbital velocity (U_o), the mean unidirectional velocity (U_u) and the mean grain size (D_{50}).

Following the approach described above, the existence field for various combined-flow bedforms is plotted on a phase space of oscillatory velocity versus unidirectional velocity with a fixed grain size ($D_{50} = 0.25$ mm) and a fixed period of $T = 4$ (Table 5.1, Figure 5.3), 5 (Tables 5.2 & 5.3, Figure 5.4a) and 6 s (Tables 5.4 to 5.6, Figure 5.4b). In the range of flows studied, the equilibrium stages of the bed observed were *no motion (NM), 2D symmetric ripples (2D SR), 3D symmetric ripples (3D SR), 3D symmetric dunes (SD), 3D asymmetric ripples (AR), 3D quasi-asymmetric ripples (QAR), 3D asymmetric dunes (AD), 3D current ripples (CR), 3D current dunes (CD)* and *upper-stage plane bed (USPB)*. The partitioning of the phase space for each of the bed states was decided and traced as equidistant lines from experimental points located on adjacent states (Figures 5.3 and 5.4). However, for some scenarios (e.g., Experiment 34 or Experiment 44) the middle line did not represent a realistic case since one of the experimental points showed a significant proximity to the transition zone, and thus the limit was shifted to the proximity of such a value. In addition, the transitions were described as gradual or sharp based on the continuous or abrupt change of the bedform characteristics as they change bed state. The transition limits presented in Figures 5.3 and 5.4 are an attempt to identify regions with distinctive bed geometry and are not meant to imply that the transition occurs precisely along the plotted line. In order to define the 'absolute' location and the physical reason of any of these transitions a large effort should be made in a very localized zone to delimit the transition, but this was outside the scope of this project. Nevertheless, the differences between the bedforms from the different

regions are real and substantial, and the transition line provides a good first approximation of what should be the true limits of the bed states.

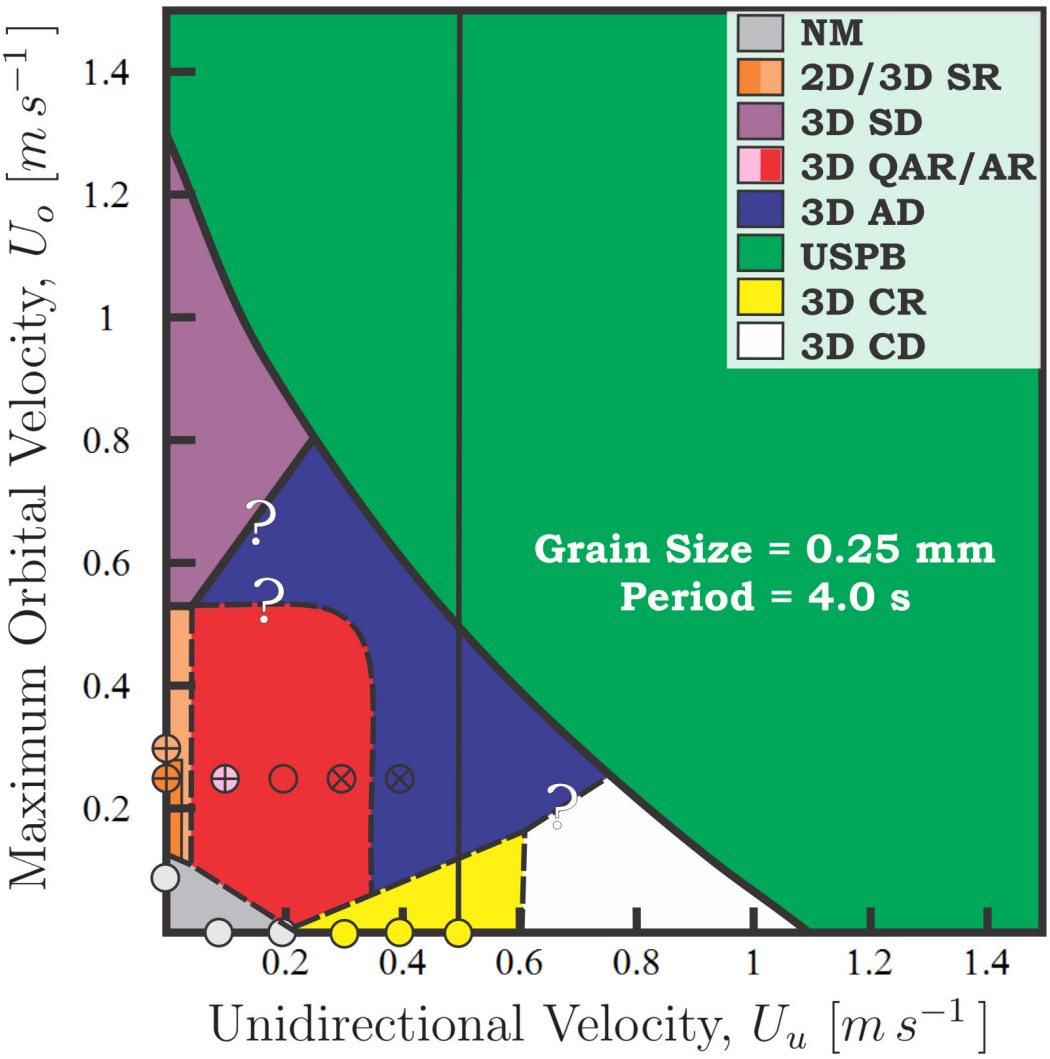

Figure 5.3: Dimensional phase diagram for combined-flow bed-phase stability fields in a plot of U_0 vs U_u with grain sizes $D_{50} = 0.25$ mm and period $T = 4$ s. + and × signs represent symmetrical and rounded bedforms, all other bedforms are asymmetric and non-rounded. The vertical dark line represents the limits of the experimental data. NM = No Motion, SR = Symmetric Ripples, SD = Symmetric Dunes, AR = Asymmetric Ripples, QAR = Quasi-Asymmetric Ripples, AD = Asymmetric Dunes, USPB = Upper Stage Plane Bed, CR = Current Ripples and CD = Current Dunes. Dashed line represents a gradual transition among different bed states, whereas a solid line denotes a sharp transition. Transition lines with question marks indicate that there is no knowledge about the nature of the transition.

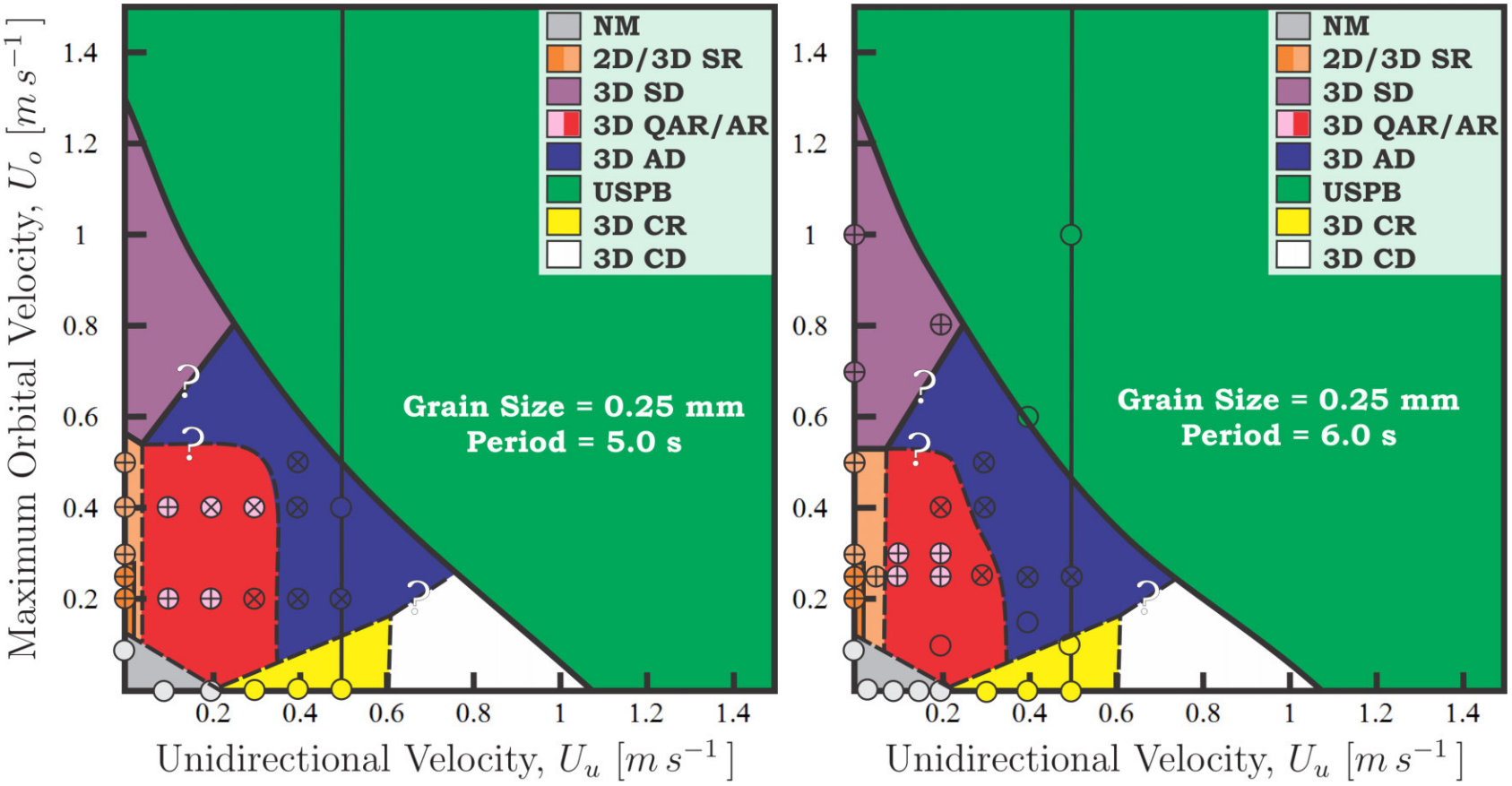

(a) Oscillation period $T = 5$ s.

(b) Oscillation period $T = 6$ s.

Figure 5.4: Dimensional phase diagram for combined-flow bed-phase stability fields in a plot of U_0 vs U_u with grain sizes $D_{50} = 0.25$ mm. $+$ and $\times$ signs represent symmetrical and rounded bedforms, all other bedforms are asymmetric and non-rounded. The vertical-dark line represents the limits of the experimental data. NM = No Motion, SR = Symmetric Ripples, SD = Symmetric Dunes, AR = Asymmetric Ripples, QAR = Quasi-Asymmetric Ripples, AD = Asymmetric Dunes, USPB = Upper Stage Plane Bed, CR = Current Ripples and CD = Current Dunes. Dashed line represents a gradual transition among different bed states, whereas a solid line denotes a sharp transition. Transition lines with question marks indicate that there is no knowledge about the nature of the transition.

The transitions of bed phases observed in the three diagrams (Figures 5.3 and 5.4) show remarkable similarities, which shows that a small change in oscillatory period (from 4 to 5 or 6) does not change the bed configuration dramatically. A combined dimensional phase diagram for all periods (T = 4, 5 and 6 s) is plotted in Figure 5.5. The small differences in the phase boundaries are associated with the relative narrow range of periods. The transitions along the U_u axis (x-axis in Figure 5.3 and 5.4) are well known and follow the same trend observed in many pure unidirectional flow studies (eg., Southard, 1991): no movement (NM), current ripples (CR), current dunes (CD) and upper-stage plane bed (USPB). Likewise, the sequence of bed configurations seen in the U_o axis (y-axis in Figures 5.3 and 5.4) follows the trend of pure oscillatory flow bedforms (eg., Pedocchi and García, 2009c): no motion (NM), 2D symmetrical ripples (2D SR), 3D symmetrical ripples (3D SR), symmetrical dunes (3D SD, previously named large 3D ripples or hummocks) and upper-stage plane bed (USPB, previously named plane bed). In the interior of the graph, the bed configuration is mainly dominated by 3D quasi-asymmetric and asymmetric ripples and 3D asymmetric dunes (Figures 5.3 and 5.4). Figures 5.3 and 5.4 show a very small domain where two-dimensional ripples can be generated; however, such conditions are very common in fair weather conditions in most shallow-marine and lacustrine environments (e.g., Komar, 1976), and relicts of these bedforms are commonly found in many outcrops (e.g., Komar, 1974).

On the other hand, despite the fact that bedforms exhibit different characteristics for different flow conditions, there is a range of flows where the differences in the characteristics of the bed are insignificant. These areas where the different flow conditions produce similar bedforms are called bedform phases and are described in detail below.

No Motion (NM)

No motion (NM) is characterized by a plane bed with an absence of sediment movement. A minimal number of experiments under pure oscillatory and pure unidirectional flows were conducted in order to determine the minimum velocity needed to entrain sediment. In

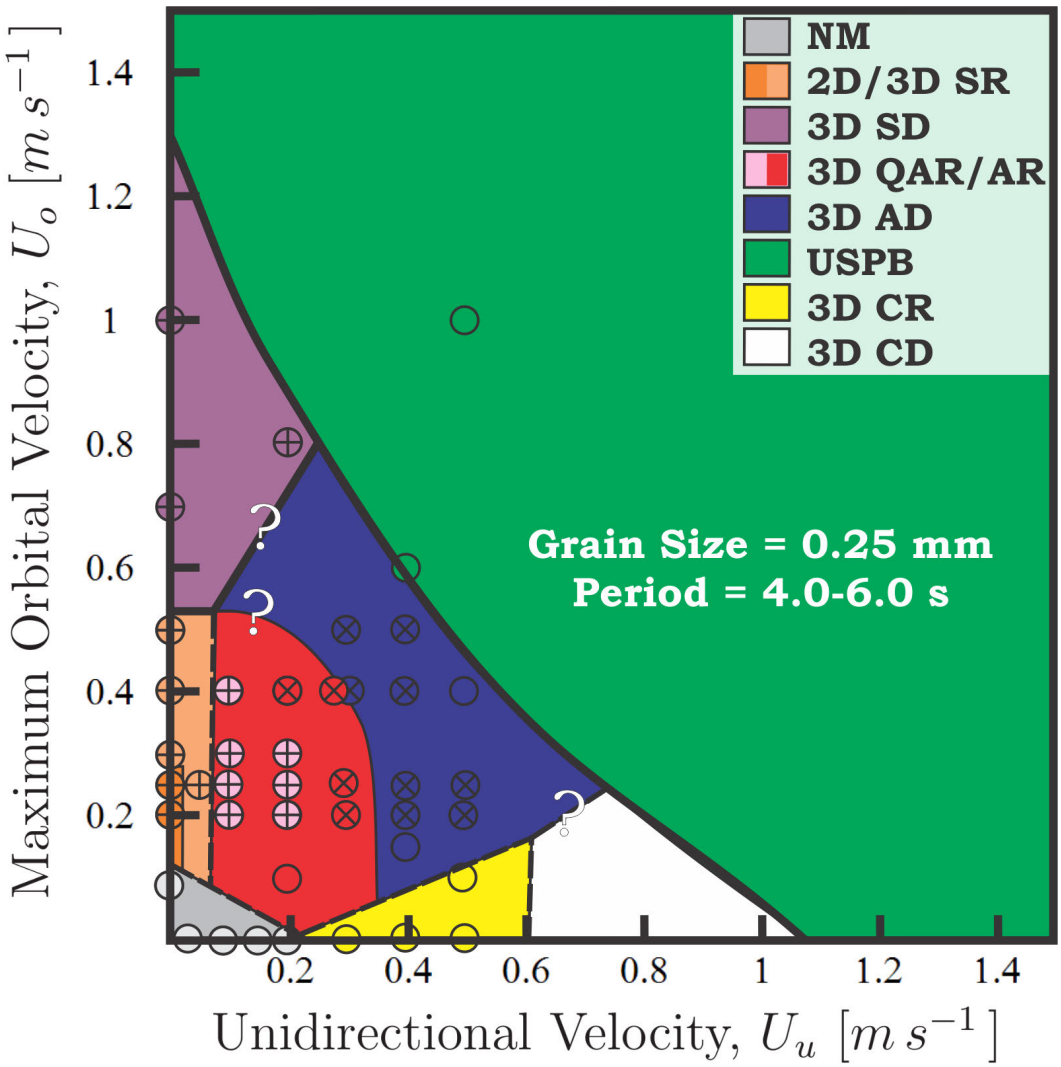

Figure 5.5: Dimensional phase diagram for combined-flow bed-phase stability fields in a plot of U_0 vs U_u with grain sizes D_{50} = 0.25 mm and periods T = 4, 5 and 6 s. + and × signs represent symmetrical and rounded bedforms, all other bedforms are asymmetric and non-rounded. The vertical dark line represents the limits of the experimental data. NM = No Motion, SR = Symmetric Ripples, SD = Symmetric Dunes, AR = Asymmetric Ripples, QAR = Quasi-Asymmetric Ripples, AD = Asymmetric Dunes, USPB = Upper Stage Plane Bed, CR = Current Ripples and CD = Current Dunes. Dashed line represents a gradual transition among different bed states, whereas a solid line denotes a sharp transition. Transition lines with question marks indicate that there is no knowledge about the nature of the transition.

addition, no study was performed to determine what combination of combined flow velocities could mobilize the sediment. Therefore, the stability field proposed for NM is drawn as a straight line between the entrainment value for pure oscillatory and pure unidirectional flows. Despite the lack of data supporting the exact shape of the curve, the NM field is generally

consistent with other studies of initiation of motion under unidirectional (e.g. Shields, 1936), oscillatory (e.g. Pedocchi, 2009) and combined (e.g. Li and Amos, 1999a) flows.

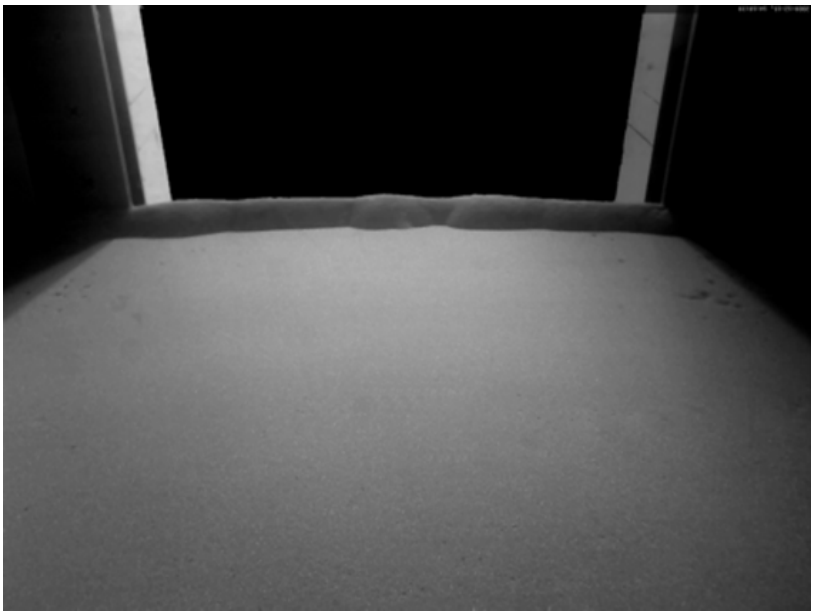

Figure 5.6: Bedform phase state: No Motion. Flow Conditions: Oscillatory Condition: *none*. Unidirectional Condition: $U_u = 0.10\, m\, s^{-1}$. The window on the back of the picture is 0.60 m wide.

2D Symmetric Ripples (2D SR)

2D symmetric ripples can be unambiguously characterized by well defined, regular bed configurations with straight and laterally continuous sharp crests oriented perpendicular to the flow (Figure 3.26). These two-dimensional bedforms have a very clear symmetrical cross-sectional shape ($BSR = 1$, Figure 5.7). The stability field for 2D SR lies just above the threshold of motion, with relatively weak oscillatory velocities ($U_o \lesssim 0.3\ m\, s^{-1}$) and non-existent unidirectional flows ($U_u \lesssim 0.01\ m\, s^{-1}$; Figures 5.3-5.4). For any increment in both the unidirectional and oscillatory velocities, the bed transitioned gradually to a three-dimensional planform geometry (Figures 5.3-5.4). The mean equilibrium bedform wavelength was $\overline{\lambda_\eta} = 0.23 \pm 0.02$ m and the mean equilibrium height was $\overline{\eta} = 37 \pm 4$ mm. In addition, the mean bedform indices for 2D SR were $\overline{BI} = 6.12 \pm 0.09$, $\overline{BSI} = 1.01 \pm 0.05$ and

$\overline{BRI} = 0.38 \pm 0.02$. Due to the clear cross-sectional symmetry, there was no large difference between the lee and stoss side angle, $\overline{\alpha_l} = 20 \pm 2°$ and $\overline{\alpha_s} = 19 \pm 2°$.

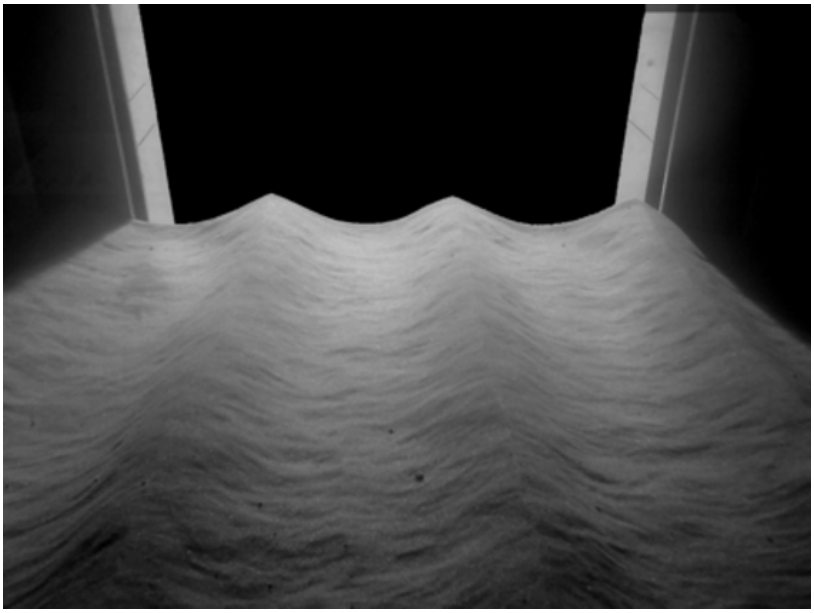

Figure 5.7: Bedform phase state: 2D Symmetric Ripples. Flow Conditions: Oscillatory Condition: $U_o = 0.25\, m\, s^{-1}$ and $T = 4$ s. Unidirectional Condition: $U_u = 0.00\, m\, s^{-1}$. The window on the back of the picture is 0.60 m wide.

3D Symmetric Ripples (3D SR)

Three-dimensional symmetrical ripples are the immediate bed-state forming after any velocity increment over the 2D SR bed configuration (Figures 5.3-5.4). These ripples have very similar characteristics to the 2D SR, with the exception of a three-dimensional planform geometry (Figure 5.8). Previous studies of oscillatory and combined flows have proven that for a given grain size and oscillation period, larger oscillatory velocities (U_o) generate three-dimensional bedforms (Figure 3.16; Southard, 1991; Pedocchi, 2009). Furthermore, Arnott and Southard (1990) observed that increments of the unidirectional component of combined flows also produced three-dimensionality. At equilibrium, the mean bedform wavelength was $\overline{\lambda_\eta} = 0.21 \pm 0.04$ m and mean height $\overline{\eta} = 31 \pm 6$ mm. In addition, the mean bedform indices for 3D SR were $\overline{BI} = 7 \pm 2$, $\overline{BSI} = 1.1 \pm 0.1$ and $\overline{BRI} = 0.42 \pm 0.02$. Similar to the

two-dimensional symmetric ripples, there was little difference between the lee and stoss side angles, $\overline{\alpha_l} = 16 \pm 5°$ and $\overline{\alpha_s} = 16 \pm 4°$.

Figure 5.8: Bedform phase state: 3D Symmetric Ripples. Flow Conditions: Oscillatory Condition: $U_o = 0.50\,m\,s^{-1}$ and $T = 6$ s. Unidirectional Condition: $U_u = 0.00\,m\,s^{-1}$. The window on the back of the picture is 0.60 m wide.

3D Symmetric Dunes (3D SD)

Combined flow dunes, previously named large ripples (Dumas et al., 2005), were classified as bedforms that have wavelengths larger than 0.5 m. Previous studies under combined flows (e.g., Arnott and Southard, 1990; Dumas et al., 2005), defined larger ripples as bedforms with wavelength larger or equal than 1 m, since no bedforms were recorded with wavelengths between 0.3 and 0.99 m. This was not the case in the present study, where a gradual size transition was observed as the velocity was increased (for more details, see section 8.3.1). In the case of 3D symmetrical dunes, the stability field was found at larger oscillatory velocities below USPB conditions (Figure 5.3-5.4). These three-dimensional, symmetric, bedforms exhibited the same characteristics as 3D SR with the exception that the bedforms were larger (Figure 5.9). Mean wavelength and height were $\overline{\lambda_\eta} = 0.72 \pm 0.01$ m and $\overline{\eta} = 60 \pm 1$ mm

respectively. Mean bedform indices were $\overline{BI} = 11 \pm 4$, $\overline{BSI} = 1.1 \pm 0.2$ and $\overline{BRI} = 0.44 \pm 0.08$. Similar to the other symmetric bed configuration, the lee and stoss side angles were very similar, $\overline{\alpha_l} = 18 \pm 3°$ and $\overline{\alpha_s} = 17 \pm 2°$.

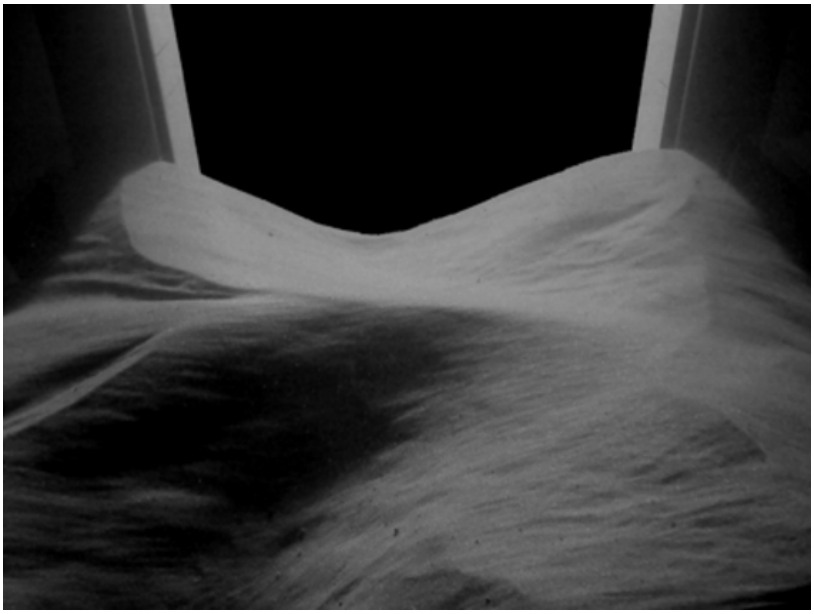

Figure 5.9: Bedform phase state: 3D Symmetric Dunes. Flow Conditions: Oscillatory Condition: $U_o = 0.80\, m\, s^{-1}$ and $T = 6$ s. Unidirectional Condition: $U_u = 0.20\, m\, s^{-1}$. The window on the back of the picture is 0.60 m wide.

3D Asymmetric Ripples (3D AR)

Three-dimensional asymmetric ripples are bedforms that are characterized by a 3D asymmetric ($BSI \gtrsim 1.5$) form with a relatively wide range of sizes and shapes (Figure 5.10). 3D AR have a mean wavelength of $\overline{\lambda_\eta} = 0.22 \pm 0.07$ m but values ranged from 0.14 to 0.42 m. Similar to the wavelength, the height of the 3D AR shows some variability, the mean height was $\overline{\eta} = 25 \pm 9$ mm with values ranging from 16 to 50 mm. The lee and stoss side angle were $\overline{\alpha_l} = 21 \pm 4°$ and $\overline{\alpha_s} = 11 \pm 3°$ respectively. The stability field of three-dimensional asymmetric ripples exists for $0.15 \lesssim U_o \lesssim 0.5\ m\, s^{-1}$ and $0.08 \lesssim U_u \lesssim 0.35\ m\, s^{-1}$ (Figure 5.3-5.4).

3D AR were first described by Dumas et al. (2005) who named them asymmetrical small

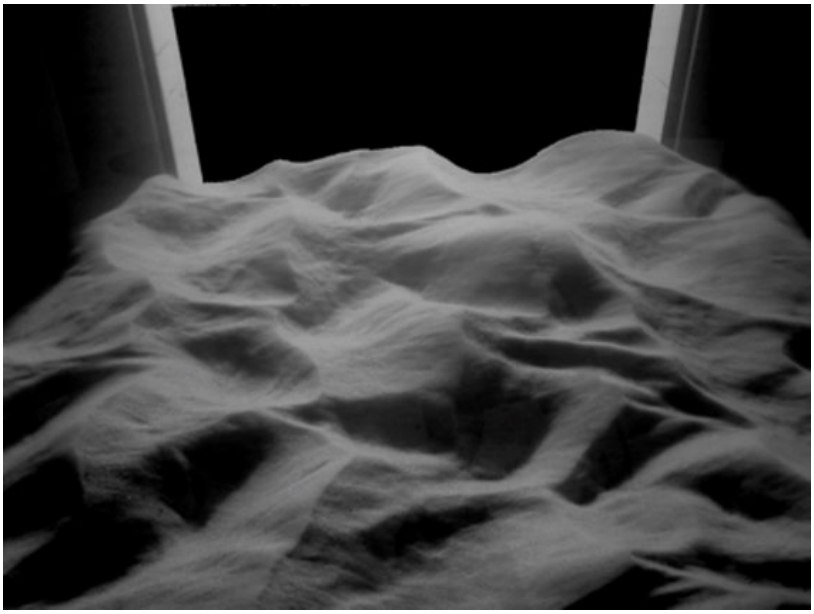

Figure 5.10: Bedform phase state: 3D Asymmetric Ripples. Flow Conditions: Oscillatory Condition: $U_o = 0.30\,m\,s^{-1}$ and $T = 6$ s. Unidirectional Condition: $U_u = 0.20\,m\,s^{-1}$. The window on the back of the picture is 0.60 m wide.

ripples (ASR) as a moderately asymmetric bedform ($BSI \sim 1.5$) with a rounded profile ($BRI \sim 0.6$). However, this description does not address all of the geometric variability that characterizes this complex bed morphology. In addition to the variability of bedform sizes, 3D AR have a gradual change in asymmetry and roundness as the unidirectional flow is increased (Figure 5.11). 3D AR are then a key bed configuration to illustrate the effects of unidirectional flow on the bed morphology at relatively low orbital velocities ($U_o \lesssim 0.5$ $m\,s^{-1}$). When the unidirectional component of a combined flow is very small ($U_u \approx 0\ m\,s^{-1}$), the bed configuration at equilibrium is a 2D and symmetric bedform (2D SR, Figure 5.3-5.4). However, if the unidirectional is slightly increased ($U_u \lesssim 0.08\ m\,s^{-1}$), the bed configuration becomes 3D while still preserving the symmetric cross-sectional geometry (2D SR to 3D SR). The transition between symmetrical ripples to asymmetrical ripples occurs gradually as the unidirectional flow is increased for a given oscillatory flow (Figure 5.11a). This transition can be divided in three stages: symmetric ($BSI \approx 1$, light-orange in Figure 5.11a-b), quasi-asymmetric ($BSI \approx 1.3 - 1.5$, pink in Figure 5.11a-b) and fully asymmetric ($BSI > 1.5$,

red, blue and yellow in Figure 5.11a-b) ripples. A simple linear regression analysis showed that the relationship between BSI and U_u is

$$BSI = 4.40\,U_u + 1.0 \tag{5.5}$$

Despite the relative good R-squared fit ($R^2 = 0.68$ and p-value = 0.036, Appendix B.1) of Equation (5.5) to the experimental data, the fitted function does not predict the clear dispersion present in the data, shown by the the large majority of the values outside the 95% confidence interval of the fitted equation (gray-shaded area in Figure 5.11a). However, Equation (5.5) can be used to predict the overall effects of the unidirectional component of the combined flow on the cross-sectional bedform geometry: the transition to a fully asymmetric morphology ($BSI = 1.5$) occurs at $U_u \approx 0.11\,m\,s^{-1}$ and for $U_u = 0\,m\,s^{-1} \rightarrow BSI = 1$, which implies a fully symmetric bedform, these results match the experimental observations. It is important to note that the ASR described by Dumas et al. (2005) could be redefined as quasi-asymmetric ripples, since the BSI was equal or slightly less than 1.5, a value that was selected as the transitional value for the symmetric-asymmetric transition (section 5.2). The use of the term quasi-asymmetric bedform is employed instead of the 'moderately' asymmetric term applied by Dumas et al. (2005). In addition to the 2D to 3D and the symmetric to asymmetric transition, this bedform becomes more rounded as the unidirectional flow increases (see section 8.3.3). However, this transition is more gradual

$$BRI = 0.64\,U_u + 0.42 \tag{5.6}$$

Similar to Equation (5.5), Equation (5.6) provides a good predictive power, despite the large experimental dispersion ($R^2 = 0.62$, p-value = 0.042 and large majority of values outside the 95% confidence interval; gray-shaded area in Figure 5.11c). The general trend shows that $BRI \approx 0.4$ for $U_u = 0\,m\,s^{-1}$ and non-rounded to rounded transition at $U_u = 0.28\,m\,s^{-1}$.

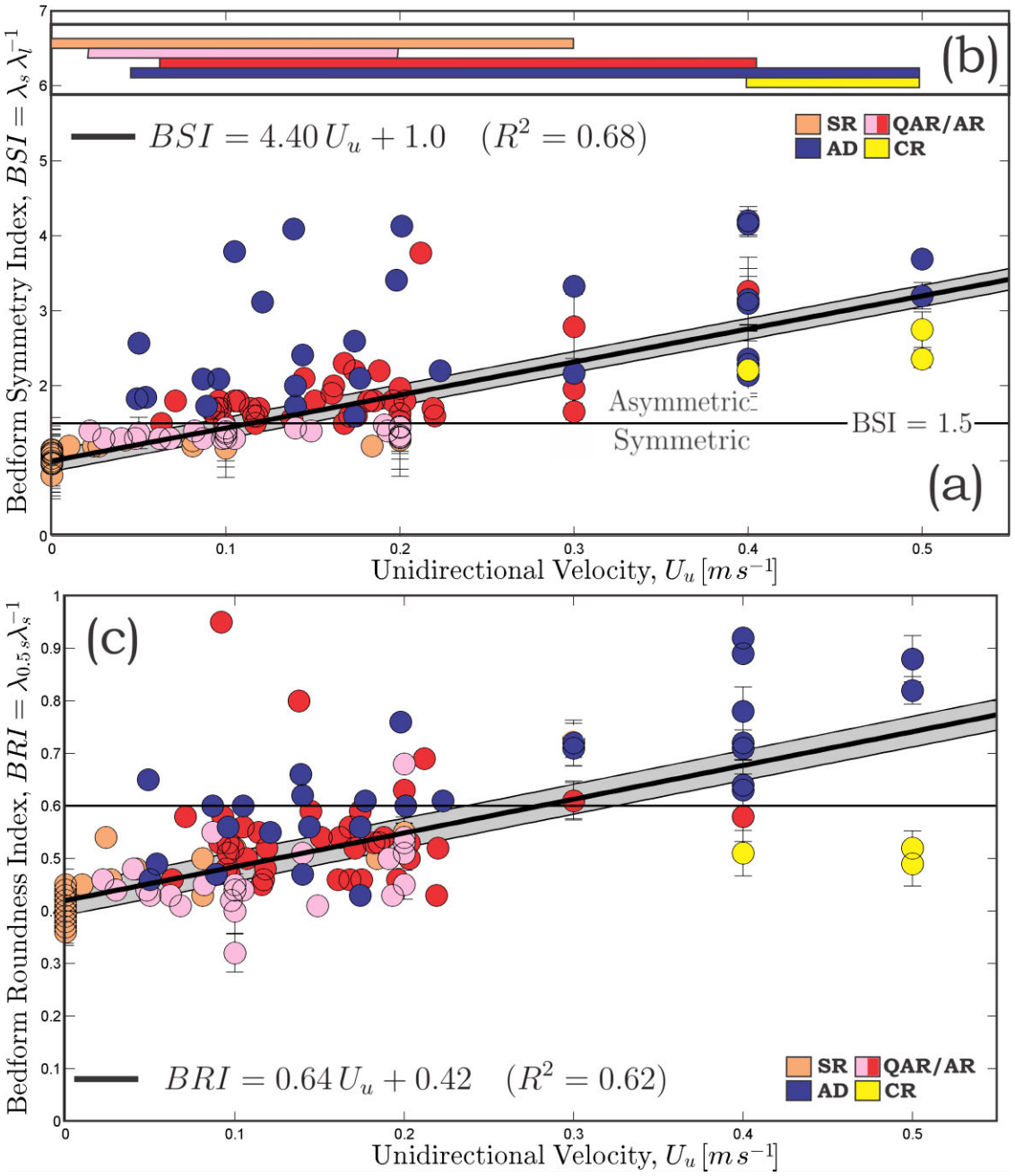

Figure 5.11: (a) Bedform symmetry index as a function of the unidirectional component of the flow velocity. (b) Graphical scheme that represents the range of unidirectional velocities for different type of bed states. (c) Bedform roundness index as a function of the unidirectional component of the flow velocity. The gray-shaded area represents the 95% confidence interval of the fitted functions (Equations 5.5 and 5.6). SR = Symmetric Ripples (light-orange), AR = Asymmetric Ripples (red), QAR = Quasi-asymmetric Ripples (pink), AD = Asymmetric Dunes (blue), and CR = Current Ripples (yellow). Experimental data from Dumas et al. (2005) and the present study. Error bars are ploted for the experimental data of this study and they are mainly associated with the range of variability of the index (standar deviation).

3D Asymmetric Dunes (3D AD)

Three-dimensional asymmetric dunes exhibit the same characteristics to 3D AR with the exception that the bedforms are larger (AD size = 350% AR size), fully asymmetric ($BSI > 1.5$, Figure 5.11a) and generally rounded ($BRI > 0.6$, Figure 5.11c). The three dimensionality of these bedforms was difficult to assess since in most cases the width of the flume was smaller than the bedform wavelength ($W/\lambda_\eta < 1$). This is a problem because the presence of the wall may limit the space available for the bedforms to fully develop and, hence stay as 2D or 2.5D features when the equilibrium stage might have a three-dimensional planform geometry (Southard et al., 1990). However, for some cases (e.g., Figure 5.12) the bed exhibited a three-dimensional planform geometry despite the fact that the W/λ_η ratio was smaller than one.

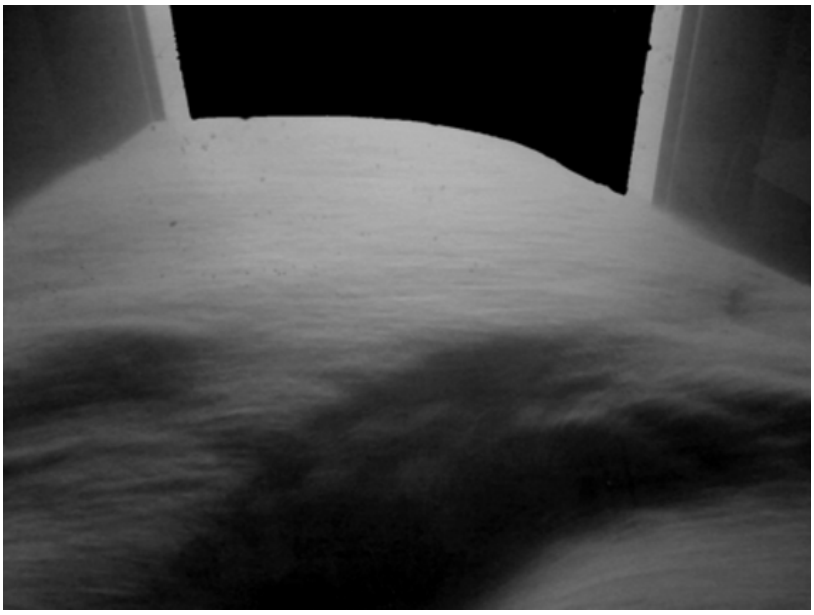

Figure 5.12: Bedform phase state: 3D Asymmetric Dunes. Flow Conditions: Oscillatory Condition: $U_o = 0.25\, m\, s^{-1}$ and $T = 6$ s. Unidirectional Condition: $U_u = 0.50\, m\, s^{-1}$. The window on the back of the picture is 0.60 m wide.

3D A-D occurred gradually as the flow velocity was increased. The stability field of three-dimensional asymmetric dunes exists for a wide range of combined flow conditions ($0.1 \lesssim U_o \lesssim 0.8\ m\, s^{-1}$ and $0.15 \lesssim U_u \lesssim 0.7\ m\, s^{-1}$, Figure 5.3-5.4). Mean wavelength and

height were $\overline{\lambda_\eta} = 0.8 \pm 0.2$ m and $\overline{\eta} = 74 \pm 39$ mm respectively. The relatively large variation for the mean wavelength and height are 0.51 to 1.30 m in wavelength and 3.1 to 15 mm in height. The mean bedform indices do not show such a high dispersion as the wavelength and height, and $\overline{BI} = 12 \pm 3$, $\overline{BSI} = 3.1 \pm 0.7$ and $\overline{BRI} = 0.7 \pm 0.1$. Similar to the other asymmetric bed configuration, the lee and stoss side angle were $\overline{\alpha_l} = 22 \pm 5°$ and $\overline{\alpha_s} = 11 \pm 4°$.

Upper-stage Plane Bed (USPB)

An upper-stage plane bed is characterized by a flat bed generated by intense sediment movement (Figure 5.13). The term USPB is used instead of Plane Bed in a attempt to merge the unidirectional nomenclature with that of oscillatory and combined flows. Similar to pure unidirectional (section 3.2.4) and oscillatory (section 3.3.5) flows, this bed configuration is generated under very high bed shear stress and sediment-transport rates. This stable configuration is characterized by a highly mobile active sediment transport layer of the order of 10 mm in thickness and a suspended sediment layer which is confined to only a few centimeters above the bed.

3D Current Ripples (3D CR)

A small number of experiments were conducted in order to characterize current ripples since a large amount of information can be found in the literature (e.g., Allen, 1962; Baird, 1962; Richards, 1980; Baas, 1994; Raudkivi, 1997). However, it was of interest to investigate at what unidirectional and oscillatory flow conditions they emerged. As expected, current ripples form under very weak to non-existent oscillatory flows ($U_o < 0.15\ m\,s^{-1}$) and relatively strong unidirectional flows ($U_u > 0.2\ m\,s^{-1}$). Current ripples were characterized by a fully three-dimensional and asymmetric morphology (Figure 5.14). There was a large dispersion in the wavelength and height values, even at stable equilibrium. Mean wavelength and height were $\overline{\lambda_\eta} = 0.35 \pm 0.03$ m and $\overline{\eta} = 15 \pm 5$ mm, respectively.

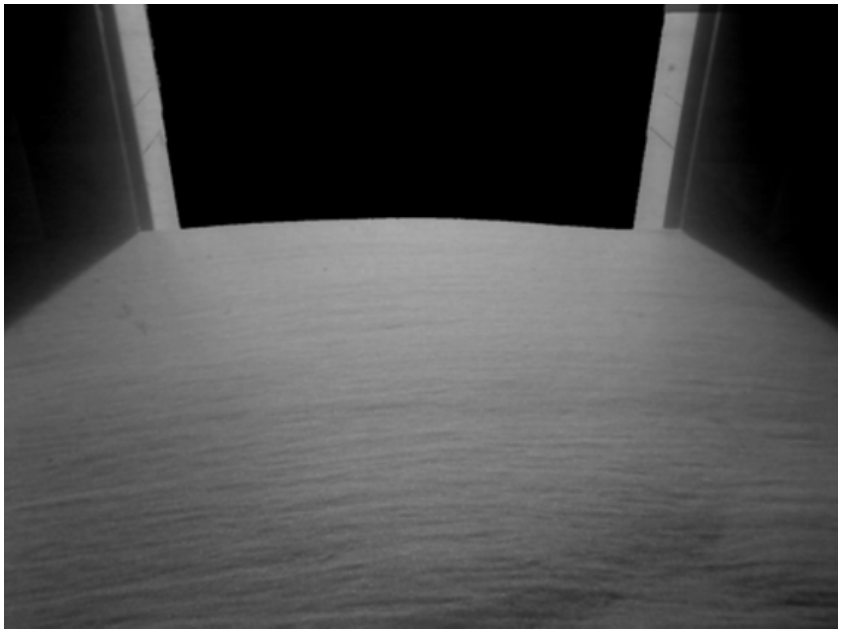

Figure 5.13: Bedform phase state: Upper-stage Plane Bed. Flow Conditions: Oscillatory Condition: $U_o = 0.40\,m\,s^{-1}$ and $T = 5$ s. Unidirectional Condition: $U_u = 0.50\,m\,s^{-1}$. The window on the back of the picture is 0.60 m wide.

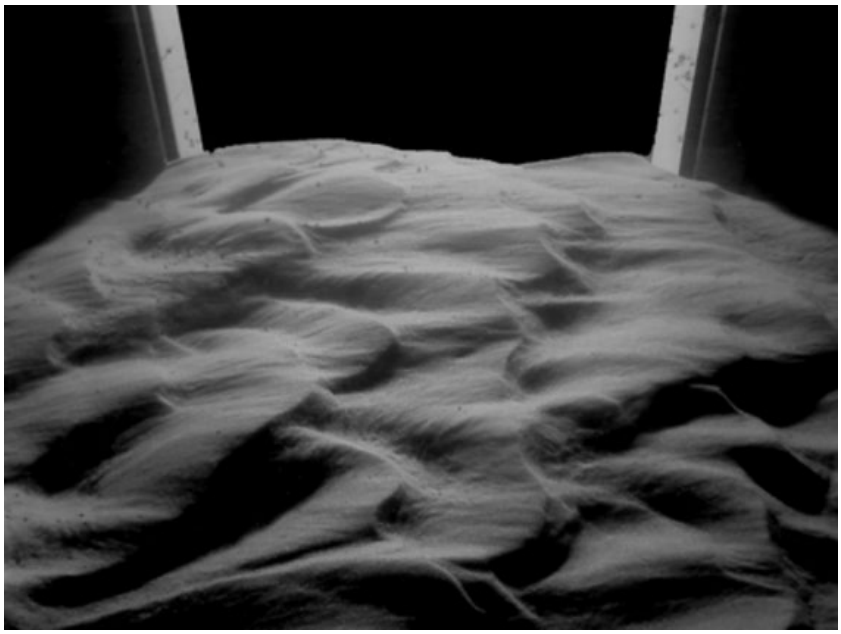

Figure 5.14: Bedform phase state: 3D Current Ripples. Flow Conditions: Oscillatory Condition: *none*. Unidirectional Condition: $U_u = 0.50\,m\,s^{-1}$. The window on the back of the picture is 0.60 m wide.

3D Current Dunes (3D CD)

3D Current Dunes were not observed for the range of flow conditions that can be run in the LOWST with a grain size of $D_{50} = 0.25$ mm (see section 4.1). It is assumed that at larger unidirectional flow velocities, the current ripple to current dune transition would occur.

Phase Diagram Comparison

Several studies have conducted experimental work under combined flows with fixed oscillation period, T, and grain size, D_{50}, with variable orbital velocity, U_o, and unidirectional velocity, U_u (Arnott and Southard, 1990; Southard et al., 1990; Yokokawa, 1995; Dumas et al., 2005; Sekiguchi and Yokokawa, 2008). One of the most cited studies is the laboratory data set from Arnott and Southard (1990), where the unidirectional velocity ranges from 0 to 0.26 $m\,s^{-1}$ and the oscillatory component varies from 0 to 0.8 $m\,s^{-1}$. The oscillation period was 8.5 s and the D_{50} was 90 μm. Dumas et al. (2005) investigated the same range of unidirectional conditions as Arnott and Southard (1990) (less than 0.25 $m\,s^{-1}$), but increased the oscillatory velocity to 1.25 $m\,s^{-1}$. Two different grain sizes (110 and 170 μm) and two wave periods (9.4 and 7 s) were used to quantify the effect of grain size and oscillation period (Figure 5.15). The equilibrium stages of the bed were similar to those found by Arnott and Southard (1990), with the principal difference being that Dumas et al. (2005) made the distinction between symmetrical and asymmetrical ripples. These two studies, as well as Sekiguchi and Yokokawa (2008), had targeted the bed morphologies generated in relatively fine sediments ($D_{50} < 200$ μm) and low unidirectional flow velocities ($U_u < 0.40\ m\,s^{-1}$). The overall bed states from these studies are *no motion, symmetric small ripples, symmetric large ripples, asymmetric small ripples, 3D asymmetric large ripples* and *plane bed*.

In general, the results of Arnott and Southard (1990), Yokokawa (1995), Dumas et al. (2005) and Sekiguchi and Yokokawa (2008) and the results presented herein are consistent, except for several differences in terminology; the small ripples, large ripples and plane bed of previous researchers equate to ripples, dunes and upper-stage plane bed respectively in

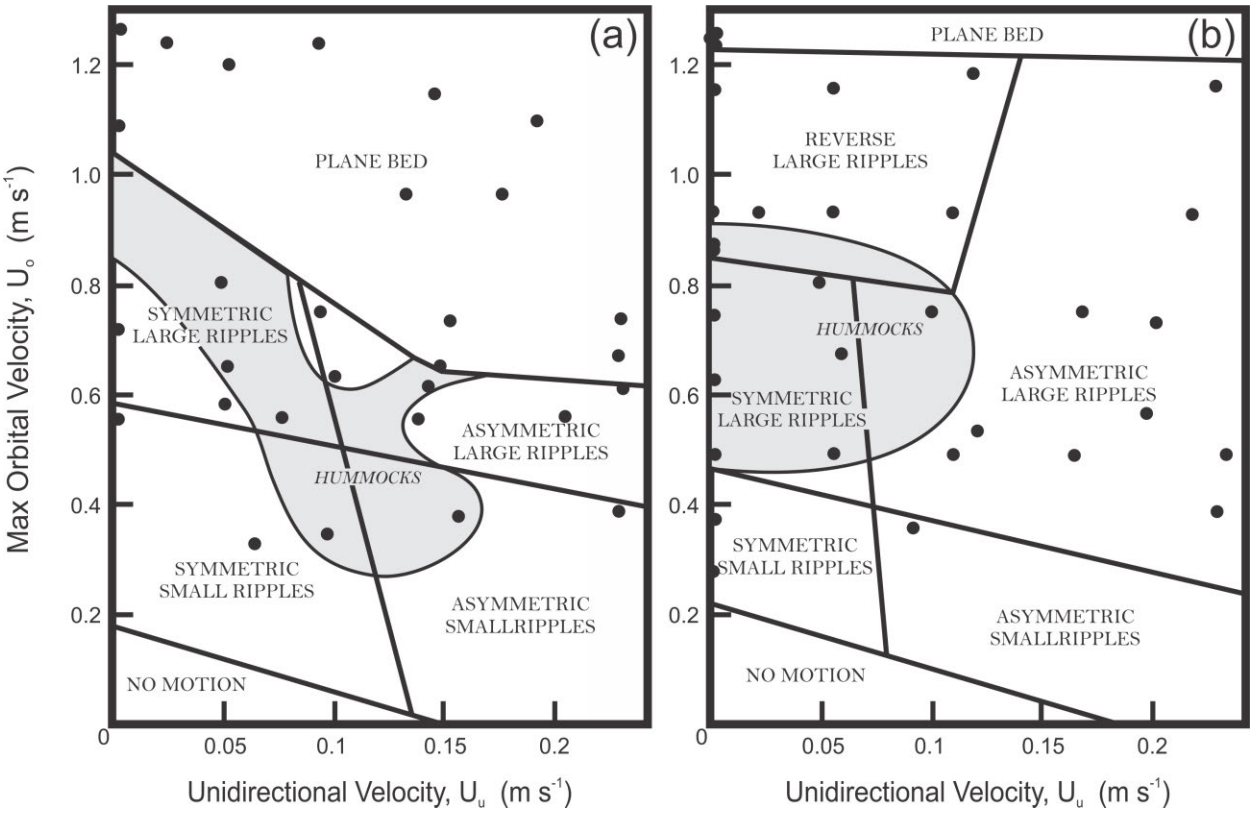

Figure 5.15: Combined flow bedform diagram after Dumas et al. (2005). (a) Phase diagram 1 - $D_{50} = 110\,\mu$m and $T = 9.4\ s$. (b) Phase diagram 3 - $D_{50} = 170\ \mu$m and $T = 9.4\ s$. For phase description see section 3.4.

the nomenclature of this thesis (section 5.2). Despite these similarities, there are some remarkable differences. First, the present study considers the addition of the planform geometry as vital to properly classify the bedforms (i.e., 2D or 3D). Hence, an individual zone where two-dimensional symmetric ripples are stable is generated. Second, the boundary between the small-scale and large-scale ripples of previous studies is horizontal across the whole phase space, but it was found that there is a transition between ripples (small-ripples) and dunes (large-ripples) for higher unidirectional flow velocities. Third, because the LOWST facility allowed conditions under which current ripples were generated under combined flows, the phase boundary between combined flow bedforms and current ripples is experimentally constrained instead of estimated. Fourth, the present study was able to distinguish between fully asymmetric ripples (AR; $BSI > 1.5$) and quasi-asymmetric rip-

ples (QAR; $1.3 < BSI < 1.5$). The experimental work of Dumas et al. (2005) was also not able to generate such differences since the unidirectional to oscillatory shear stress was not asymmetric enough to see the fully asymmetric bedforms (section 8.3.2). Finally, although there was not enough data to fully define a bed state, rounded ($BRI > 0.6$) bedforms have been demarcated to fully understand this geometrical transition.

Based on these new insights, a new generalized phase diagram is proposed and plotted on a phase space of oscillatory velocity versus unidirectional velocity (Figure 5.16a). Such a diagram should be evaluated with a fixed grain size and a fixed period, but in order to illustrate the differences of variable grain size and period, all the available data has been plotted. Figure 5.16b presents the same figure without the data symbols. Figure 5.16a clearly shows that such a diagram is not perfect, displaying a large variability between the experimental data and the bed states proposed, and such variability should be expected. Finer sediments are mobilized at lower velocities than coarser sediments, and at the same time oscillation period has a large effect on the bed morphology (e.g., as the period becomes larger, $T \rightarrow \infty$, the bedforms become similar to one generated under unidirectional flows). It is important to note that for some cases the relative position of each of these bed phases will remain the same (e.g., low velocities 2D SR, then with increased velocity a transition to 3D SR), yet the precise boundary between each of these bedform states will vary depending on which parameter is changed. Furthermore, these changes in boundaries can lead to the disappearance of stable bedforms, as occurs for current ripples ($D_{50} > 0.7$ mm) or current dunes ($D_{50} < 0.12$ mm).

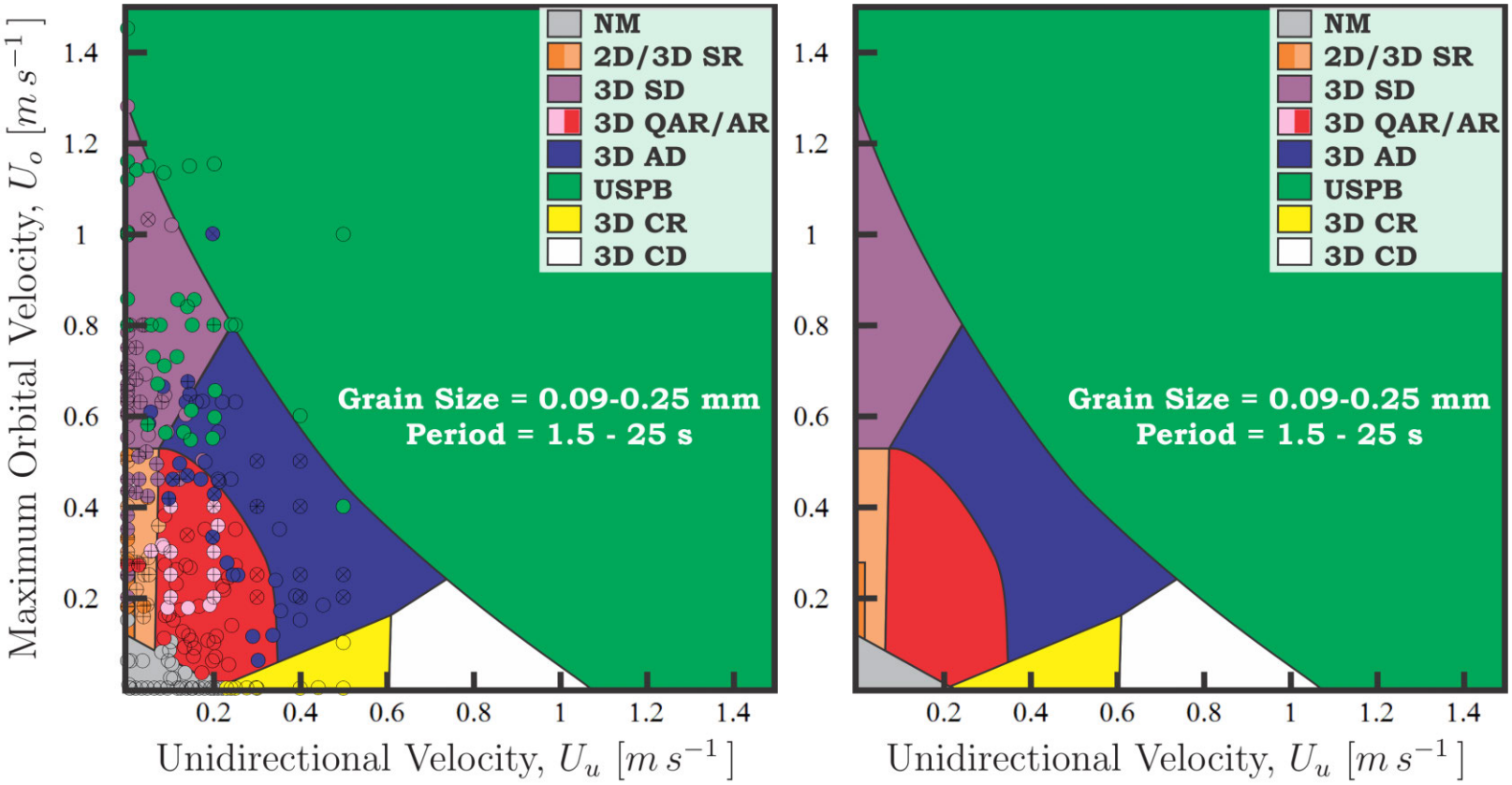

(a) Data from Arnott and Southard (1990); Yokokawa (1995); Amos et al. (1988); Dumas et al. (2005); Sekiguchi and Yokokawa (2008); Pedocchi (2009) and Tables 5.1-5.7. Sample size = 264.

(b) Schematic dimensional phase diagram.

Figure 5.16: Dimensional phase diagram for combined flows. Relationships of combined-flow bed-phases stability fields in a plot of U_o vs U_u with grain sizes D_{50} between of 0.09-0.25 mm and periods T between 1.5-25 s. All the data was collected from flume experiments. + and * signs represent symmetrical bedforms and two-dimensional planform geometries, all other bedforms are asymmetric and three-dimensional.

5.4.3 Dimensionless Quantities: Dimensionless Phase Diagram

There is still no general agreement on which dimensional variables are relevant for the determination of the bed configuration under any type of flow, and this is especially true for the case of combined flows. A dimensionless analysis was performed in order to find the relevant variables in order to explain the bed morphologies for combined flows and to reconstruct the bedforms under pure oscillatory and pure unidirectional flows as particular cases (i.e. pure oscillatory flows are a combined flow with zero unidirectional velocity). By using the Buckingham Pi Theorem, seven dimensionless parameters, Π_ζ, associated with the sedimentological variable ζ can be obtained:

$$\Pi_\zeta = f\left(\frac{U_u^2}{g\,R\,D_{50}}, \frac{U_o^2}{g\,R\,D_{50}}, \frac{T\nu}{D_{50}^2}, \frac{g^{1/3}\,R^{1/3}}{\nu^{2/3}}D_{50}, \frac{\rho_s}{\rho}, \frac{U_u}{\sqrt{g\,h}}, \frac{h}{D_{50}}\right) \tag{5.7}$$

The ratio of the sediment and water density ρ_s/ρ is generally given as the submerged specific density $R = \rho_s/\rho - 1$, (García, 2008), and for natural siliciclastic sands this can be assumed to possess a constant value of $R \approx 1.65$ (Vanoni, 2006). Furthermore, as discussed in section 5.4.1, h by itself is not a relevant variable for the present problem, so h/D_{50} and $U_u/\sqrt{g\,h}$ can be neglected. Hence, Equation 5.7 can be reduced to

$$\Pi_\zeta = f\left(\psi_w, \psi_c, T_*, D_*\right) \tag{5.8}$$

where

$$\begin{aligned} \psi_o &= \frac{U_o^2}{g\,R\,D_{50}} \qquad \psi_u = \frac{U_u^2}{g\,R\,D_{50}} \\ T_* &= \frac{T\nu}{D_{50}^2} \qquad D_* = \left(\frac{g\,R}{\nu^2}\right)^{1/3} D_{50} \end{aligned} \tag{5.9}$$

Hence, similar to section 5.4.2, an existence field for combined-flow bedforms is produced and plotted, but now in a dimensionless phase space using Equation 5.8 (Figure 5.17). Figure 5.17 shows the stability field for all the bed states classified herein: *no motion (NM), 2D symmetric ripples (SR), 3D symmetric ripples (SR), 3D symmetric dunes (SR), 3D asym-*

metric ripples (AR), 3D quasi-asymmetric ripples (QAR), 3D asymmetric dunes (AD), 3D current ripples (CR), 3D current dunes (CD) and *upper-stage plane bed (USPB)*. A detailed description of each of the bed stages has been given in section 5.4.2. The relative location and distribution of the different bed stages in the dimensionless phase space (Figure 5.17) remains unchanged from the locations displayed on the dimensional diagram (Figure 5.16). Therefore, similar to the defined transitions in Section 5.4.2, the transitions for Figure 5.17 are also an attempt to identify regions with distinctive bed geometry and are not meant to imply that the transition occurs precisely along the plotted line. However, in order to characterize the phase boundaries between stable configurations, instead of tracing equidistant lines between bed states, a set of functions were found to describe the limits between bed states;

1 - Initiation of Motion

$$(\psi_u + 1.41)^2 + (\psi_o + 43.08)^2 = 46.10^2 \tag{5.10}$$

2 - Oscillatory Ripples to Oscillatory Dunes

$$\psi_o - 0.009\,\psi_u^3 + 0.35\,\psi_u^2 - 0.38\,\psi_u = 77.02 \qquad \text{for} \quad \psi_u < 3.8 \tag{5.11}$$

3 - Combined Flow Ripples to Combined Flow Dunes

$$\psi_o - 0.009\,\psi_u^3 + 0.35\,\psi_u^2 - 0.38\,\psi_u = 77.02 \qquad \text{for} \quad \psi_u < 25 \tag{5.12}$$

4 - Symmetric Bedforms to Asymmetric Bedforms

$$7.05\,\psi_u^2 - 1.53\,\psi_u = 23.3 - \psi_o \qquad \text{for} \quad 2 < \psi_u < 6 \tag{5.13}$$

5 - Upper-Stage Plane Bed

$$\begin{aligned} &(\psi_u - 548.44)^2 + (\psi_o - 322.00)^2 = 554.54^2 \qquad \text{for} \quad \psi_u < 90 \\ &\textit{Interpretative} \text{ (Figure 5.17)} \qquad \psi_u > 90 \end{aligned} \tag{5.14}$$

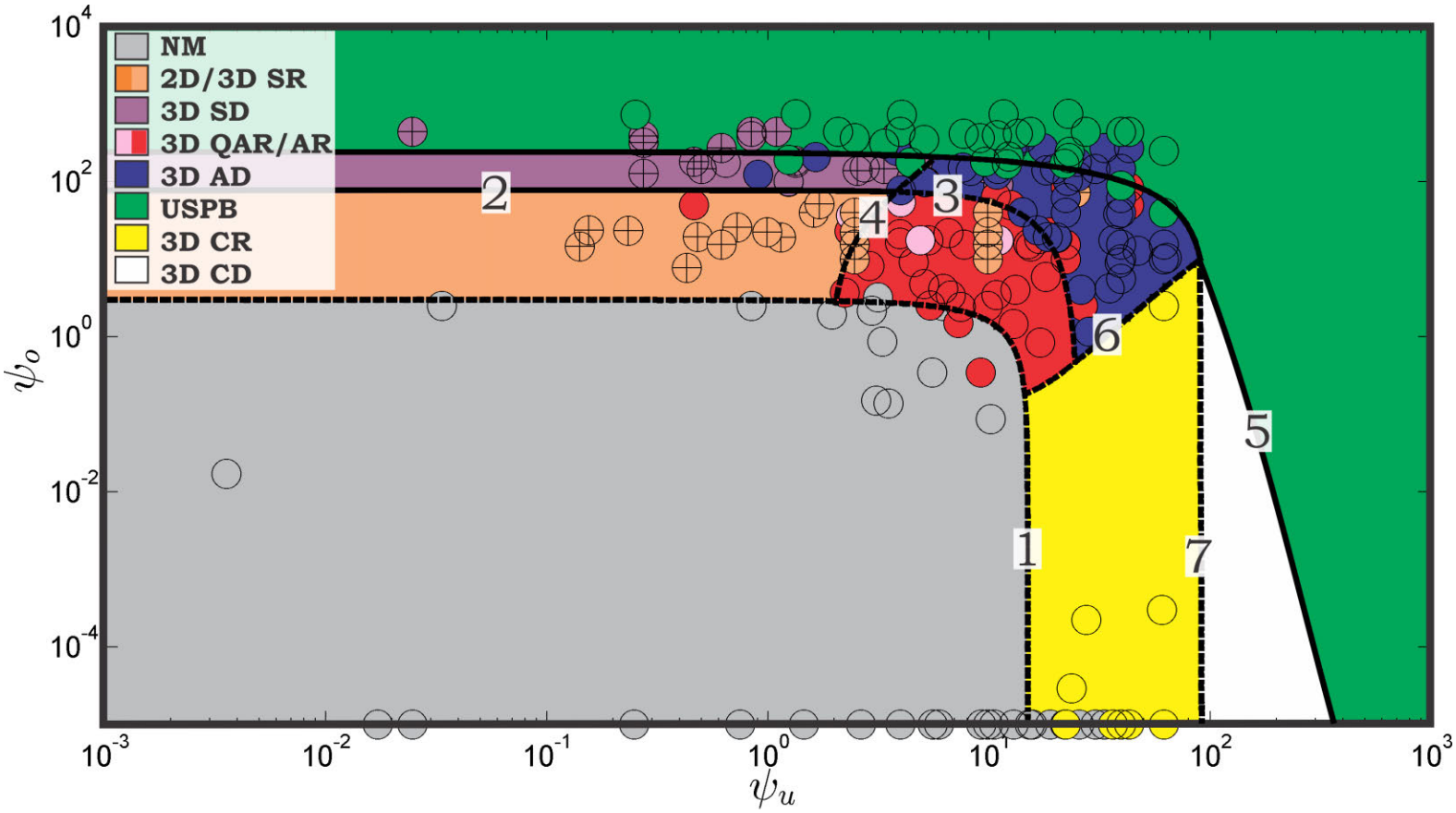

Figure 5.17: Dimensionless phase diagram for combined-flow bed-phase stability fields in a plot of ψ_u vs ψ_o. + and × signs represent symmetrical and rounded bedforms, all other bedforms are asymmetric and non-rounded. The vertical-dark line represents the limits of the experimental data. Data from Arnott and Southard (1990); Yokokawa (1995); Amos et al. (1988); Dumas et al. (2005); Sekiguchi and Yokokawa (2008); Pedocchi (2009) and Tables 5.1-5.7. Dashed line represents a gradual transition among different bed states, whereas a solid line denotes a sharp one. Numbers 1 to 7 denoted the different transition curves, see text for details (Equations 5.10 to 5.16). NM = No Motion, SR = Symmetric Ripples, SD = Symmetric Dunes, AR = Asymmetric Ripples, QAR = Quasi-Asymmetric Ripples, AD = Asymmetric Dunes, USPB = Upper Stage Plane Bed, CR = Current Ripples and CD = Current Dunes. Sample size = 264.

6 - Combined Flow Bedforms to Current Bedforms

$$\psi_o - 0.0015\,\psi_u^2 - 0.03\,\psi_u = 0.3143 \qquad \text{for} \quad 14 < \psi_u < 90 \tag{5.15}$$

7 - Current Ripples to Current Dunes

$$\psi_u = 90 \tag{5.16}$$

These set of equations are consistent with previous work under pure unidirectional and oscillatory flows. For the CR-CD transition, Equation 5.12 predicts $\psi_u(\psi_o = 0) \sim 99 \rightarrow U_u \sim 0.59\,m\,s^{-1}$, which is very similar to $U_u \sim 0.58\,m\,s^{-1}$ from the work of Southard and Boguchwal (1990). In addition, Equation 5.14 predicts $\psi_u(\psi_o = 0) \sim 300 \rightarrow U_u \sim 1.10\,m\,s^{-1}$ for the CD-USPB transition, whereas Southard and Boguchwal (1990) propose $U_u \sim 0.96\,m\,s^{-1}$. Furthermore, Dingler and Inman (1976) proposed a threshold condition to plane bed at $\psi_o = 240$ for pure oscillatory flows, the same value is predicted by Equation 5.14 ($\psi_u \rightarrow 0, \psi_o = 239.9$).

In order to compare the present work with dimensionless diagrams proposed in other studies, it is necessary to utilize them in another set of variables.

$$\Pi_\zeta = f\left(\theta_o, \theta_u, D_*, T_*\right) \tag{5.17}$$

where

$$\begin{aligned} \theta_o &= \frac{\rho_f\, u_{*,o}^2}{(\rho_s - \rho_f)\; g\, D_{50}} \\ \theta_u &= \frac{\rho_f\, u_{*,u}^2}{(\rho_s - \rho_f)\; g\, D_{50}} \end{aligned} \tag{5.18}$$

where

$$\begin{aligned} u_{*,o}^2 &= f_o\, U_o^2 \\ u_{*,u}^2 &= f_u\, U_u^2 \end{aligned} \tag{5.19}$$

where f_o and f_u are the wave and current friction coefficient respectively (see Chapter 2).

Hence, Equation 5.17 can be related back to Equation 5.9 using Equation 5.19

$$\begin{aligned} \theta_o &= f_o\,\psi_o \\ \theta_u &= f_u\,\psi_u \end{aligned} \tag{5.20}$$

The use of a dimensionless shear stress to plot the combined flow phase-diagram was first proposed by Amos et al. (1988), and was followed by further studies with new data that was used to adjust boundaries or bed state types (Amos et al., 1996, 1999). Kleinhans (2005) presented a literature review of phase diagrams for unidirectional, oscillatory and combined flows, showing that for combined flows the diagram originally proposed by Amos et al. (1988) can be used to capture the initiation of motion and transition to upper-stage plane beds. The use of shear stress as a variable depends strictly on the accuracy of the friction coefficient used, and although the friction coefficient might do a good job estimating the shear stress, it is a source of uncertainty that can be avoided by using the formulation proposed in the present study (Equation 5.9). Nevertheless, if the right friction coefficients are used Figure 5.17 can be represented by the shear stress instead of the mobility number (Figure 5.18). Figure 5.18 shows a combined flow phase diagram in a θ_u vs θ_o phase space with the phase boundaries proposed by Kleinhans (2005). The experimental data was plotted using the unstratified, three-layer eddy viscosity friction factors of Madsen and Grant (1976). The phase boundaries proposed by Kleinhans (2005) were estimated based on a similar data set, but using the friction factors of van Rijn (1984a) for the unidirectional component and Soulsby (1997) for the oscillatory flow. The phase boundaries proposed by Kleinhans (2005) do a fair job predicting the experimental data, however the most notorious mismatch is the lack of prediction for the symmetrical dunes (purple in Figure 5.18) and the underestimation of the stability field of current bedforms (yellow and white in Figure 5.18). Therefore, the present study states that the mobility number should be used instead of the Shields number, since it provides a better representation of the system.

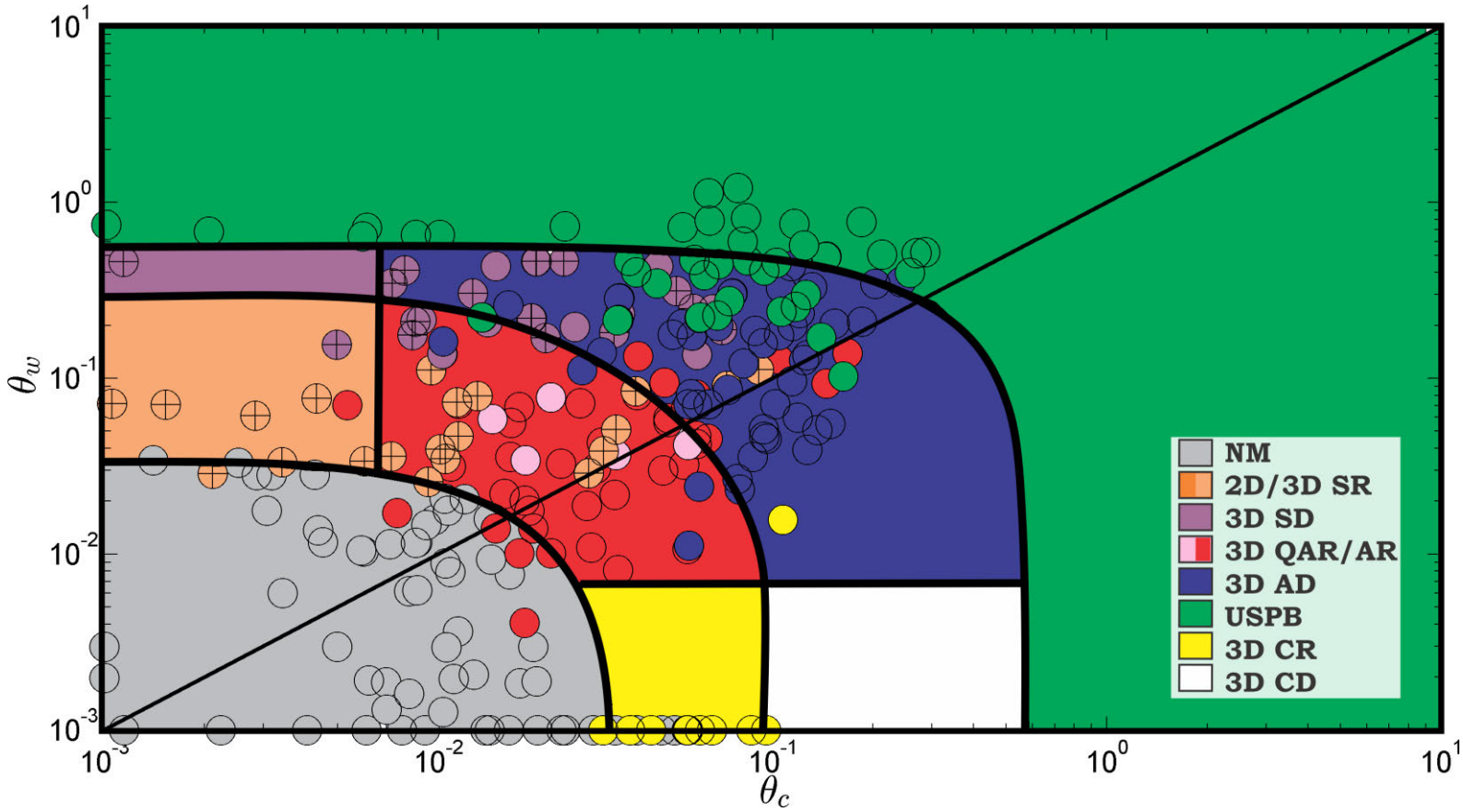

Figure 5.18: Dimensionless phase diagram for combined-flow bed-phase stability fields in a plot of θ_u vs θ_o. + and × signs represent symmetrical and rounded bedforms, all other bedforms are asymmetric and non-rounded. Data from Arnott and Southard (1990); Yokokawa (1995); Li and Amos (1999b,a); Amos et al. (1988); Dumas et al. (2005); Sekiguchi and Yokokawa (2008); Pedocchi (2009) and Tables 5.1-5.7. The different phase boundaries are those proposed by Kleinhans (2005). NM = No Motion, SR = Symmetric Ripples, SD = Symmetric Dunes, AR = Asymmetric Ripples, QAR = Quasi-Asymmetric Ripples, AD = Asymmetric Dunes, USPB = Upper Stage Plane Bed, CR = Current Ripples and CD = Current Dunes. Sample size = 304.

5.5 Conclusions

The stable bedform configuration under a diverse range of unidirectional, oscillatory and combined flow conditions was studied and divided into *no motion (NM), 2D symmetric ripples (SR), 3D symmetric ripples (SR), 3D symmetric dunes (SR), 3D asymmetric ripples (AR), 3D quasi-asymmetric ripples (QAR), 3D asymmetric dunes (AD), 3D current ripples (CR), 3D current dunes (CD)* and *upper-stage plane bed (USPB)*. Each of these stages was described, characterized and reproduced in a dimensional and dimensionless phase diagram. The present study proposed a new nomenclature to name combined flow bedforms; bed states previously named small ripples, large ripples and plane bed are now refer as ripples, dunes and upper-stage plane bed respectively. In addition, the introduction of the planform and cross-sectional geometries as properties to classify bedforms leads to the definition of stable phase space for two-dimensional symmetrical ripples and three-dimensional quasi-asymmetrical ripples. Moreover, the experimental data collected under unidirectional flows larger than 0.30 $m\,s^{-1}$ allows expansion of the current understanding of the bed configuration within the *Terra Incognita* zone, where the phase boundary between combined flow bedforms and current ripples was experimentally constrained. On the other hand, based on dimensionless analysis, the oscillatory and unidirectional mobility numbers were used to represent the dimensionless phase diagram under combined flows. This set of dimensionless numbers provides a better representation than previous studies that use a friction factor to compute the Shields number.

Chapter 6

Bedform Initiation

6.1 Introduction

The hydrodynamics and morphodynamics involved in the initiation of motion and transport of different sediment sizes, and the resulting geometric shapes (i.e., bedforms) generated by both bedload and near-bed suspended-load sediment transport, has sparked intrigue amongst researchers from different disciplinary fields over centuries (Du Buat, 1786; Deacon, 1894; Blasius, 1910). This fascination has led to a large number of studies on unidirectional (e.g. Shields, 1936), oscillatory (e.g. Komar and Miller, 1975) and, more recently, combined flows (e.g. Li and Amos, 1999a). Although there is a good understanding of the hydrodynamic conditions that will lead to the development of bedforms (e.g. Raudkivi, 1963; Gyr and Schmid, 1997; Coleman and Nikora, 2011), there still exists a large knowledge gap regarding the specific mechanisms that transform a featureless bed to one with bedforms. The limited amount of research that has explored the intricate details involved in bedform genesis under unidirectional (e.g. Liu, 1957; Gyr and Schmid, 1997; Venditti et al., 2005a), and oscillatory (e.g. Darwin, 1884; Bagnold, 1946; Lofquist, 1978; Allen, 1979) flows has not yet fully detailed the major driving mechanisms within this process, thus leaving much debate over exactly how a flat sediment-laden bed transitions into an irregular morphologic surface populated with ubiquitous bedforms through time. The competing ideas or models are the following: (i) linear stability theory and perturbations upon a flat bed (Kennedy and Falcon, 1965; Richards, 1980), (ii) instabilities within the flow (Folk, 1976) or bed (Liu, 1957) and (iii) development and propagation of bed defects (Raudkivi, 1963; Williams and Kemp, 1971).

Despite its widespread use to predict the initial wavelength of bed morphologies, linear stability theory cannot be addressed experimentally like the other two models, and hence will not be tested in this chapter. Consequently, a simple set of experiments were conducted that were aimed to quantitatively explore the initiation of ripples under unidirectional, oscillatory and combined flow conditions. These sets of experiments investigated the development of the bed when the initial bed configuration for each experiment had a small negative defect (Figure 6.1), providing a nucleus for the initiation of ripples in the test section.

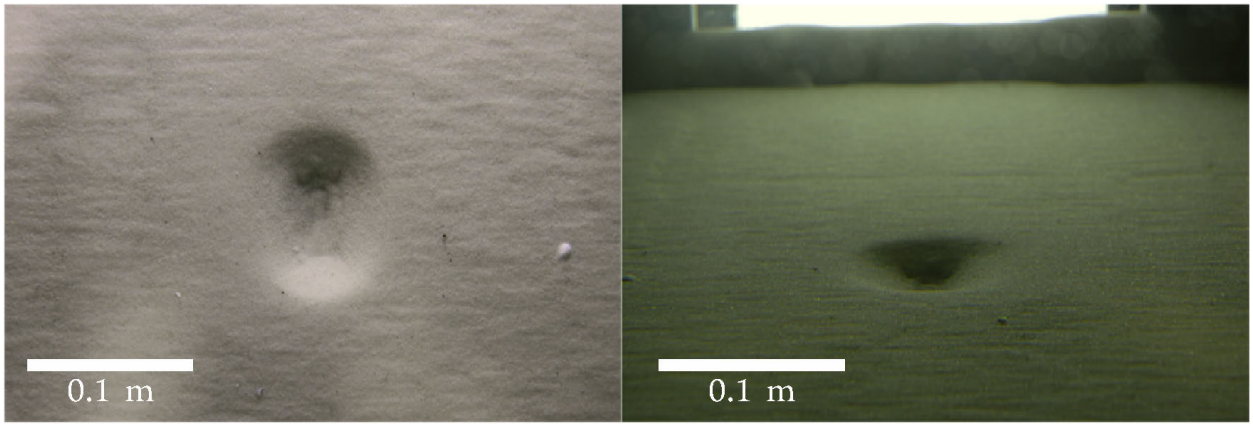

Figure 6.1: Initial bed configuration with a small negative defect. Unidirectional flow is from right to left.

6.2 Experimental Procedures

Bedform initiation and development in flat bed conditions were studied under pure unidirectional, pure oscillatory and combined flow conditions with artificially generated defects (Table 6.1). The average initial defect was made by compacting the flat bed generating a negative defect with a length $\approx$ 0.08 m, a width $\approx$ 0.1 m and height $\approx$ 0.03 m. Four sets of experiments were conducted: (1) pure oscillatory conditions, which consisted of four oscillation periods, T = 5, 10, 15 and 20 s, at a fixed oscillatory velocity, $U_o = 0.30\ ms^{-1}$; (2) wave-dominated combined flows that conserved the flow conditions of experiment (1) but with the superimposition of a unidirectional current (U_u) of 0.10 ms^{-1}; (3) current-dominated

Table 6.1: Summary of experiments performed to study bedform initiation with artificially generated defects.

Set	Exp	T (s)	U_o ($m\,s^{-1}$)	U_u ($m\,s^{-1}$)	D_*	U_H [a] ($m\,s^{-1}$)	$u_{*,M94}$ [b] ($m\,s^{-1}$)	$u_{*,S97}$ [c] ($m\,s^{-1}$)	u_* ($m\,s^{-1}$)	$\theta_{max}^{(+)d}$	$\theta_{max}^{(-)e}$	SSSI[f]	Temp (°C)	Duration (min)
01	01	05	0.30	0.00	6.06	0.00	0.026	0.025	0.021	0.105	-0.113	1.07	18.0	46.83
01	02	10	0.30	0.00	6.06	0.00	0.023	0.021	0.021	0.108	-0.102	1.06	18.0	34.23
01	03	15	0.30	0.00	6.08	0.00	0.022	0.019	0.020	0.101	-0.106	1.05	18.5	34.33
01	04	20	0.30	0.00	6.16	0.00	0.021	0.017	0.018	0.084	-0.092	1.09	19.0	15.98
02	01	05	0.30	0.10	6.11	0.09	0.027	0.026	0.022	0.122	-0.078	1.56	18.5	46.72
02	02	10	0.30	0.10	6.16	0.09	0.024	0.022	0.022	0.115	-0.068	1.68	19.0	21.40
02	03	15	0.30	0.10	6.08	0.09	0.023	0.020	0.022	0.114	-0.085	1.33	18.0	46.30
02	04	20	0.30	0.10	6.06	0.09	0.022	0.018	0.021	0.109	-0.083	1.32	18.0	41.37
03	01	15	0.30	0.00	6.08	0.00	0.022	0.019	0.020	0.101	-0.106	1.05	18.0	34.33
03	02	15	0.30	0.10	6.08	0.09	0.023	0.020	0.022	0.114	-0.085	1.33	18.5	46.30
03	03	15	0.30	0.20	6.11	0.18	0.024	0.022	0.024	0.148	-0.033	4.47	18.5	46.35
04	01	—	—	0.10	5.76	0.07	—	—	0.003	$0.002^{g,+}$	—	—	15.0	12.00
04	02	—	—	0.20	5.76	0.16	—	—	0.006	$0.008^{g,+}$	—	—	15.0	12.00
04	03	—	—	0.30	5.76	0.24	—	—	0.013	0.043^{g}	—	—	15.0	48.00

[a]Depth averaged unidirectional velocity. UDVP data, computed with Equation 4.29.
[b]Predicted value based on Grant and Madsen (1979).
[c]Predicted value based on Soulsby (1997).
[d]Maximum value through the oscillation cycle. UDVP data, computed with Equation 4.26.
[e]Minimum value through the oscillation cycle. UDVP data, computed with Equation 4.26.
[f]SSSI = Shear Stress Symmetry Index
[g]Time-averaged values. [+] Below critical threshold for sediment transport.

combined flows that used a wave period of $T = 15$ s, an oscillatory velocity $U_o = 0.30\ ms^{-1}$ and three unidirectional flow velocities of $U_u = 0$, 0.10 and 0.20 ms^{-1}, and (4) pure unidirectional conditions which consisted of three unidirectional velocities $U_u = 0.10$, 0.20 and 0.30 ms^{-1}. Experiments are referred to as S#E#, where the first value corresponds with the experimental set and the second with the experimental number (Table 6.1). For example, S1E3 refers to experiment 3 of set 1 with $T = 15$ s, $U_o = 0.30\ ms^{-1}$ and $U_u = 0\ ms^{-1}$.

Different from all other experiments in this thesis, the bedform initiation experiments were not conducted until bed equilibrium, and once the bed was fully covered with bedforms the experiments were stopped (Table 6.1). The goal of these initiation experiments was not to analyze the development or final equilibrium of the bedforms, but to capture the first stages of bedform generation under defect propagation. For each experiment, time-lapse photographs were taken from above the test section (Section 4.3.4). The time-lapse photographs were manually analyzed by measuring the perimeter of the defect as it developed in time (Figure 6.2). Human errors associated with the selection of the defect edge were estimated by measuring the same picture several times during different days. The difference between the measurements (15 measurements from 4 different pictures) were always less than 1% of the measured value. From these measurements, the geometrical center was computed, and from it the downstream (λ_{DS}) and upstream (λ_{US}) distance to the edge of the defect (Figure 6.2). The geometrical center and active defect area were computed using the MATLAB®(R2012a) algorithm *polygeom.m* (Sommer, 2008). In addition, during the experiments, velocity profiles were measured with an Ultrasonic Doppler Velocity Profiler (UDVP, Section 4.3.3). Following the same methodology as Section 4.3.3, the Shields number was computed for the maximum and minimum shear stress throughout the wave cycle (Table 6.1).

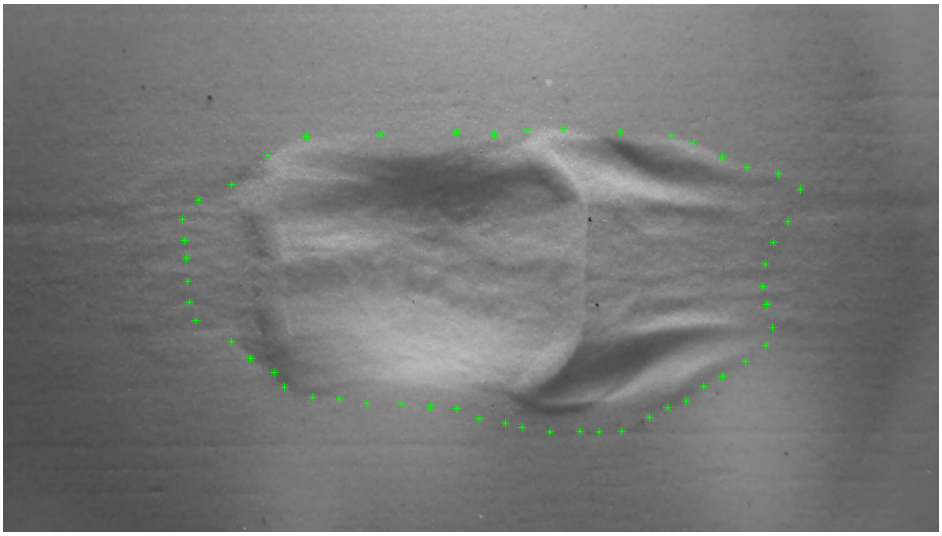

Figure 6.2: Defect perimeter at time = 57 seconds into experiment S3E1. Flow condition; $U_o = 0.3\,m\ s^{-1}$, $T = 15$ s and $U_u = 0.10\,m\ s^{-1}$. Green dots are the manually-measured defect perimeter and the blue lines are the distance from the geometrical center to the edge of the defect. Area of view ≈ 0.34 m long and ≈ 0.23 m wide.

6.3 Bedform Genesis

A characteristic geometric pattern was observed in all the experiments independent of the flow conditions (i.e., different periods and flow velocities; Figure 6.3). This geometric pattern is generated from the propagation by erosion of the edge of the original defect, and development of a crest and twin scour pits or 'horns' (Figure 6.4). These geometrical features were previously described also under bedform initiation with artificially-generated defects under unidirectional (Southard and Dingler, 1971; Venditti et al., 2005a) and oscillatory (Bagnold, 1946) flows. Hence, it can be concluded that this geometrical signature is independent of the type of flow. However, the main distinction between flows is the propagation direction of the initial feature. For the case of unidirectional and combined flows (Figure 6.4), the two-lobed horns initially propagated downstream, whereas for oscillatory flows, the migration was either downstream or upstream. Figure 6.4 shows the evolution of the defect propagation under combined flow conditions (S02E01), 33 s after the initiation of the experiment where a clear downstream propagation took place (i.e., red-shaded area is much larger than

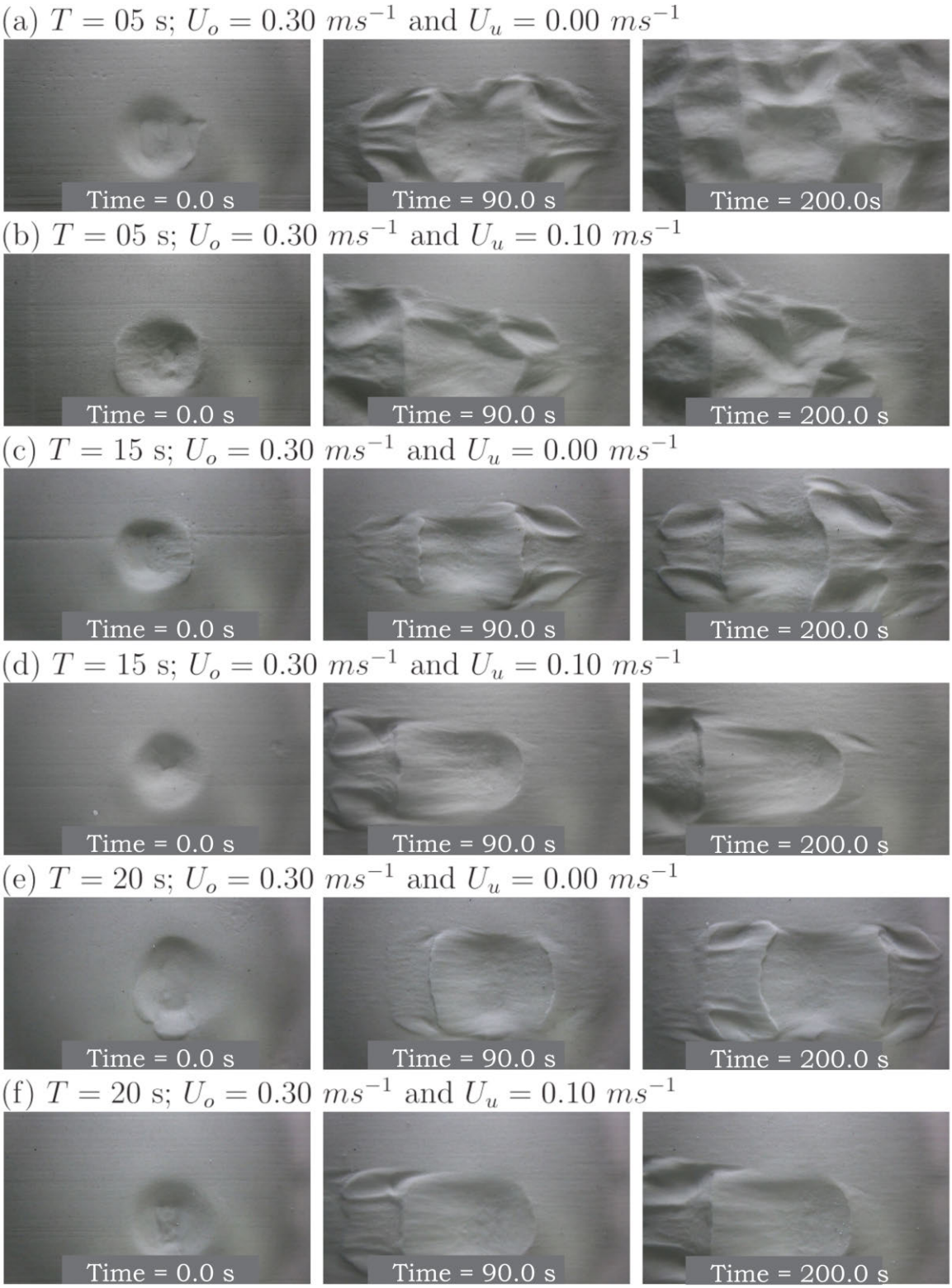

Figure 6.3: Bedform initiation under different flows by defect initiation mechanisms, where T = period, U_o = maximum oscillatory velocity and U_u = mean free-flow unidirectional velocity. Unidirectional flow is from right to left. The area of view for each individual image is ≈ 0.34 m long and ≈ 0.23 m wide.

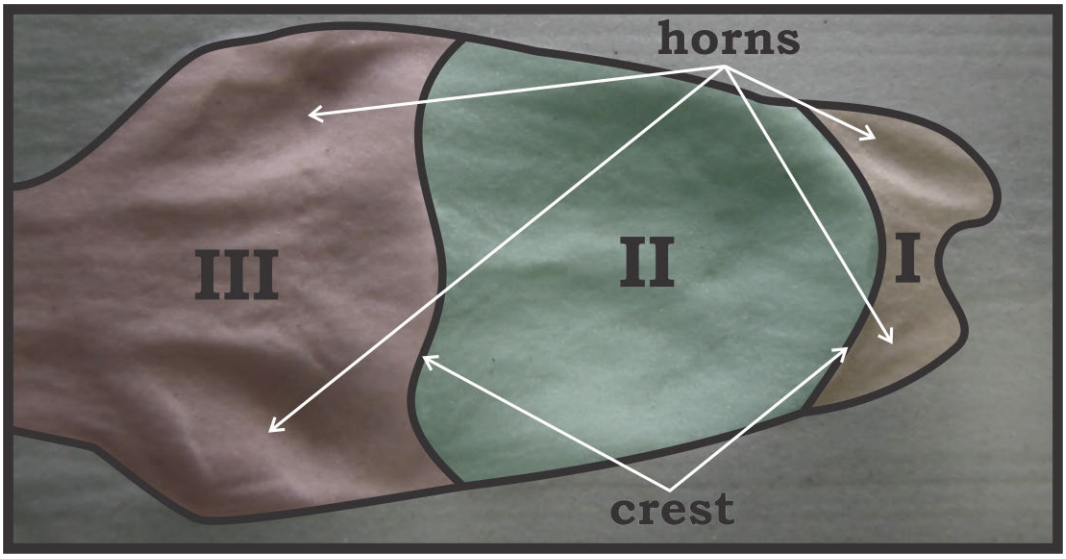

Figure 6.4: Downstream (III) and upstream (I) twin scour pits or 'horns' resulting from the bedform genesis mechanisms with an artificially generated defect (II) in a combined flow experiment (S02E01, Time = 33 s). It is important to note the relatively large asymmetry of bedform propagation; the downstream propagation (red-shaded area) is much larger than the upstream one (golden-shaded area). Unidirectional flow is from right to left. Area of view is ≈ 0.20 m long and ≈ 0.15 m wide.

the golden-shaded one). The reason why the shape is the same lies in the same fluid-flow processes occurring at the edge of the defect. Despite the fact that no flow data was measured over the defect, it can be deduced by looking at the recorded movies (video Ch06 - 01*:T05O30U00_Genesis.avi* from Appendix A.1.1), that the flow separates from the defect edge, generating a zone of high instantaneous bed shear stresses large enough to move the sediment, mainly as bedload. As sediment gets transported both downstream and laterally, the two-lobed horns form in the bed. Over time, the newly-formed feature becomes the new edge of the defect generating flow separation, which causes scour and development of a new feature; this process is repeated to form a train of defects in the direction of propagation. Unfortunately, due to the natural limitation of the facility, the area of view captured with the camera was relatively small (≈ 0.34 m long and ≈ 0.23 m wide) to record the overall evolution of the defect as it further moved in the propagation direction. However, from side-view observations, it was found that the initial wavelength and height of the defects

increased over time and distance (Figure 6.5), similar to results under unidirectional flows (Southard and Dingler, 1971; Venditti et al., 2005a). In addition, the geometrical signature of these structures remained the same as the initial features despite their development and growth (Figure 6.5), until the bed became fully developed and then interaction among the horns gave rise to a bed full of bedforms (video Ch06 - 01*:T05O30U00_Genesis.wmv* from Appendix A.1.1). Once this stage was reached, the experiment was stopped, the bed was flattened and a new condition was run.

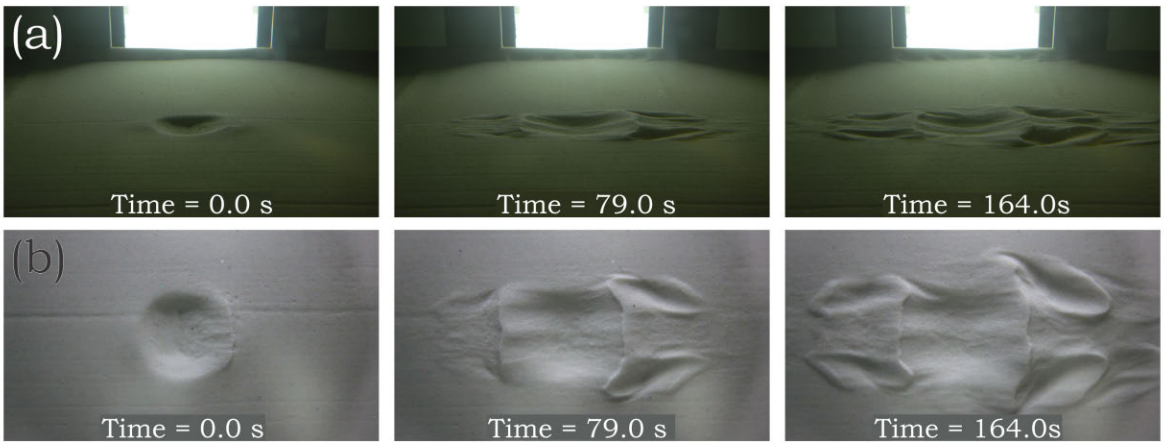

Figure 6.5: Side (a) and top (b) view of bedform initiation in S1E3 ($T = 15$ s; $U_o = 0.30\ ms^{-1}$ and $U_u = 0.00\ ms^{-1}$). Unidirectional flow is from right to left. For scaling, the window on the back of the picture in (a) is 0.60 m wide and the area of view in (b) is ≈ 0.34 m long and ≈ 0.23 m wide.

6.4 Propagation Direction

Measurements from the geometrical center of the defect to the downstream (λ_{DS}) and upstream (λ_{US}) edges were computed from time-lapse photographs for all flows. For the case of the first set of experiments (S1, pure oscillatory flows), the two-lobed horns were generated to each side of the defect within the first wave cycles (less than 10 cycles), independent of the oscillation period (Figure 6.6). Furthermore, the development of the edges was symmetric as was the propagation of the consequent defects (Figure 6.7a). This symmetry can be

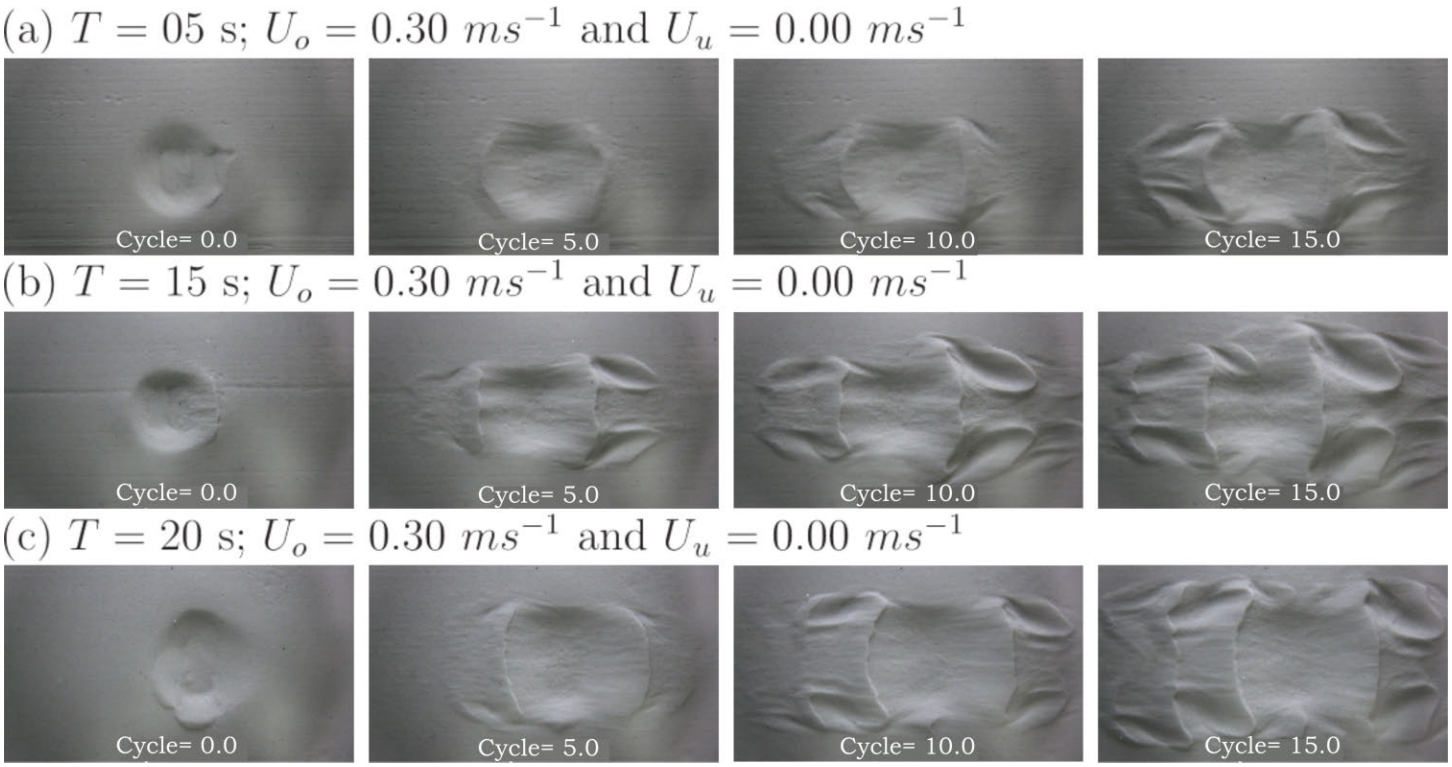

Figure 6.6: Bedform initiation under pure oscillatory flows by defect initiation, where T = period, U_o = maximum oscillatory velocity, U_u = mean free-flow unidirectional velocity and Cycle = Time/Period. Area of view for each individual image is ≈ 0.34 m long and ≈ 0.23 m wide. Note the relative symmetry of the two-lobed horns on each side of the defect.

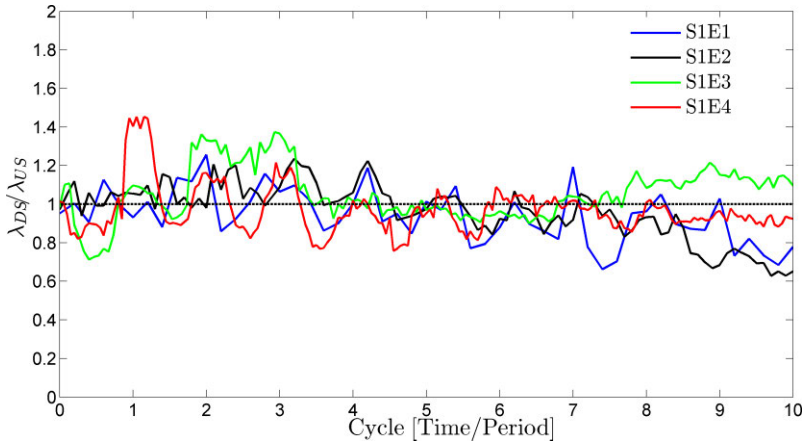

(a) Defect development under pure oscillatory flow (S1).

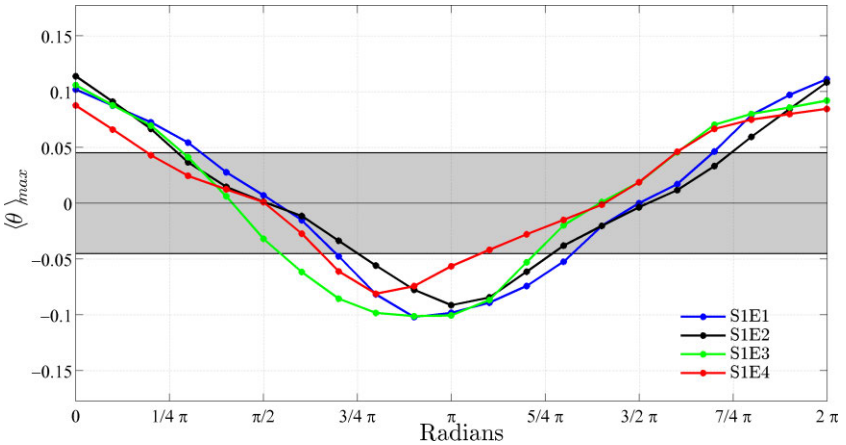

(b) Maximum phase-averaged Shields number throughout the wave cycle (S1). The shaded area represents shear stresses that are below the critical shear stress necessary to mobilize 0.25 mm diameter sediment (Brownlie, 1981).

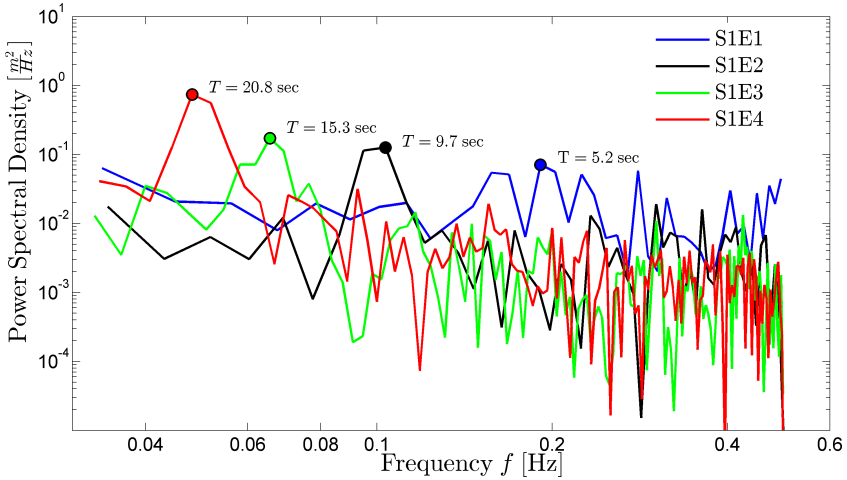

(c) Spectral Analysis of $\lambda_{DS}/\lambda_{US}$ (S1).

Figure 6.7: Bedform development under pure oscillatory flows (S1).

observed in the overall trend of the ratio between the downstream and upstream growth ($\lambda_{DS}/\lambda_{US} \approx 1$, Figure 6.7a). However, as was expected, this symmetric growth was not uniform throughout the oscillation period. It was observed that the defects had predominant downstream migration (i.e., $\lambda_{DS}/\lambda_{US} > 1$, Figure 6.7a) followed by upstream migration (i.e., $\lambda_{DS}/\lambda_{US} < 1$, Figure 6.7a), which averages-out through the wave cycle (i.e., $\lambda_{DS}/\lambda_{US} \approx 1$, Figure 6.7a). Such differential transport is associated with peaks in shear stress in both the upstream and downstream direction (Figure 6.7b). For the four pure oscillatory flow experiments (S1), the peak shear stress had the necessary energy to mobilize the 0.25 mm sediment (values outside the shaded area in Figure 6.7b). Moreover, the symmetric growth of the defect ($\lambda_{DS}/\lambda_{US} \approx 1$, Figure 6.7a) is linked to the symmetric shear applied in both upstream and downstream directions (Figure 6.7b). The downstream and upstream migration stages in the defect development are controlled by the changes in shear stress directions (i.e., change in sign; Figure 6.7b), and hence due to the changes in migration direction, there must be a clear time scale in the growth patterns associated with the wave period. Thus, the important time scale must be the oscillatory period and it can easily be recovered by conducting a spectral analysis of the ratio $\lambda_{DS}/\lambda_{US}$ (Figure 6.7c), which shows a periodicity that correlates within 1% of the period.

For the case of the second set of experiments (S2, wave-dominated combined flows), two-lobed horns were generated to each side of the defect within the first cycles with a predominant growth towards the downstream side (Figure 6.8), independent of the oscillatory period. This asymmetry during the formation of the bedforms persisted over time, resulting in completely asymmetric defect propagation with a net transport downstream ($\lambda_{DS}/\lambda_{US} > 1$, Figure 6.9a). Spectral analysis of the ratio $\lambda_{DS}/\lambda_{US}$ for these wave-dominated combined flows (Figure 6.9b) shows that there is a clear period-driven peak for the short periods (T = 5 and 10 s) but a flat spectrum for the longer periods (T = 15 and 20 s). The absence of a growth-frequency in the spectrum can be associated with purely unidirectional flows, where the transport is driven by random packets of turbulence that do not have a characteristic

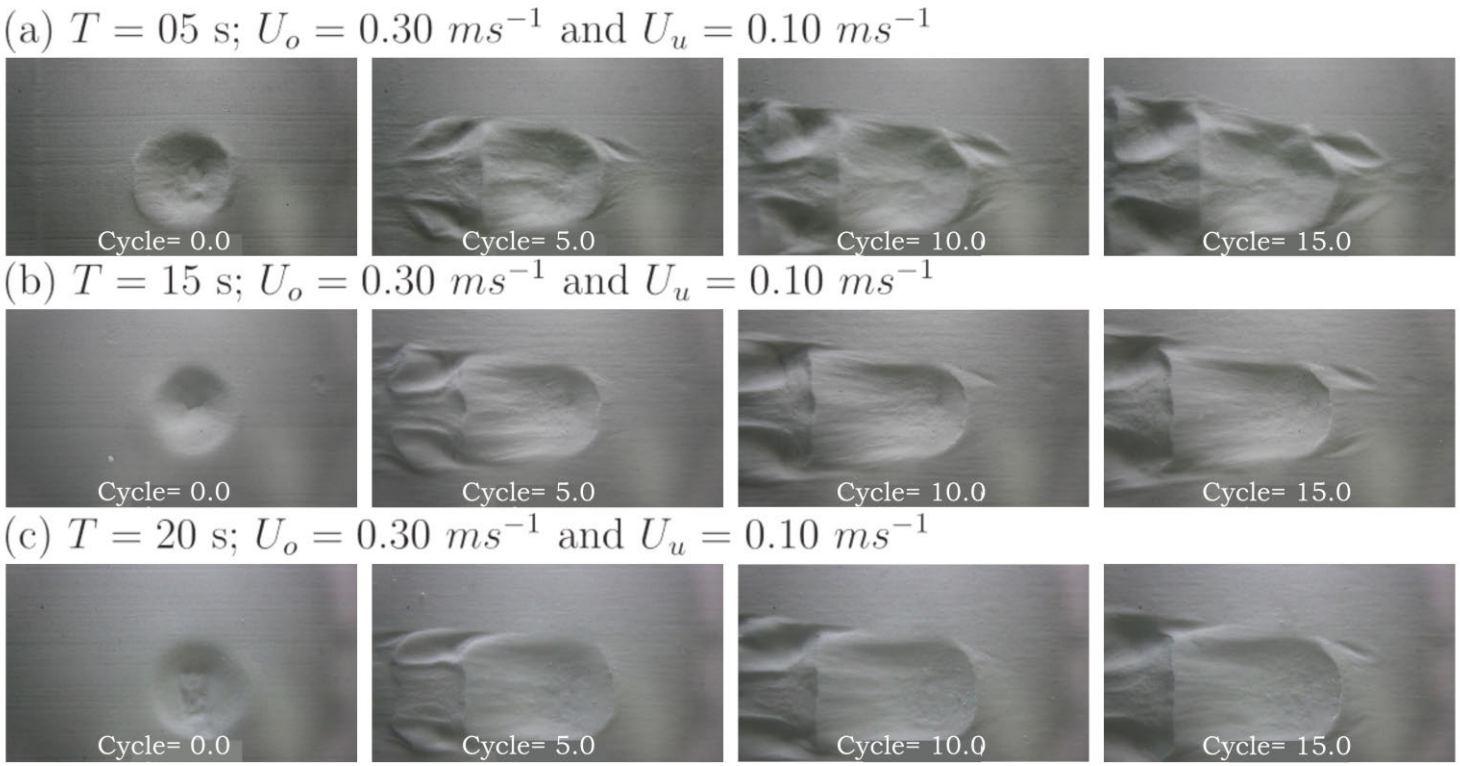

Figure 6.8: Bedform initiation under wave-dominated combined flows by defect initiation mechanisms, where T = period, U_o = maximum oscillatory velocity, U_u = mean free-flow unidirectional velocity and Cycle = Time/Period. Unidirectional flow is from right to left. Area of view for each individual image is ≈ 0.34 m long and ≈ 0.23 m wide. Note the asymmetric generation of the two-lobed horns on each side of the defect.

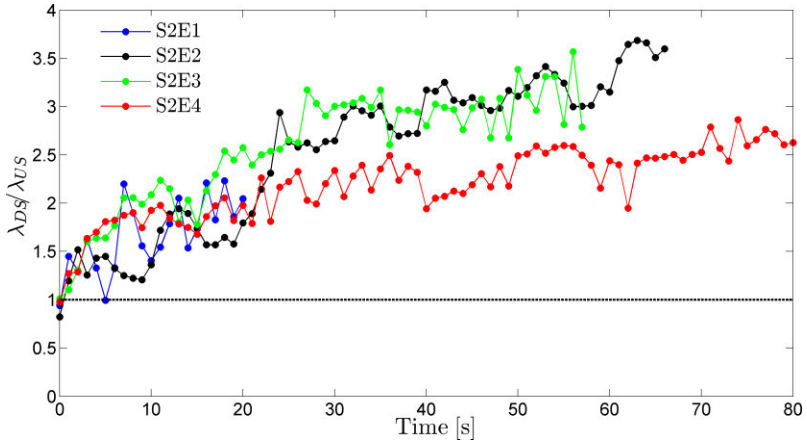

(a) Defect development under wave-dominated combined flows (S2).

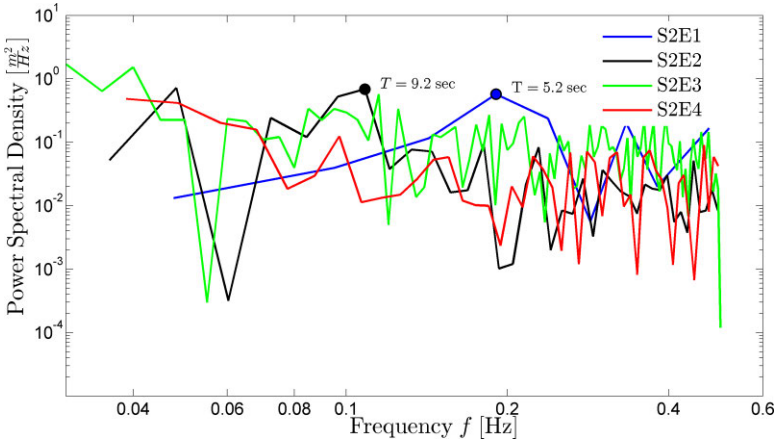

(b) Spectral Analysis of $\lambda_{DS}/\lambda_{US}$ (S2).

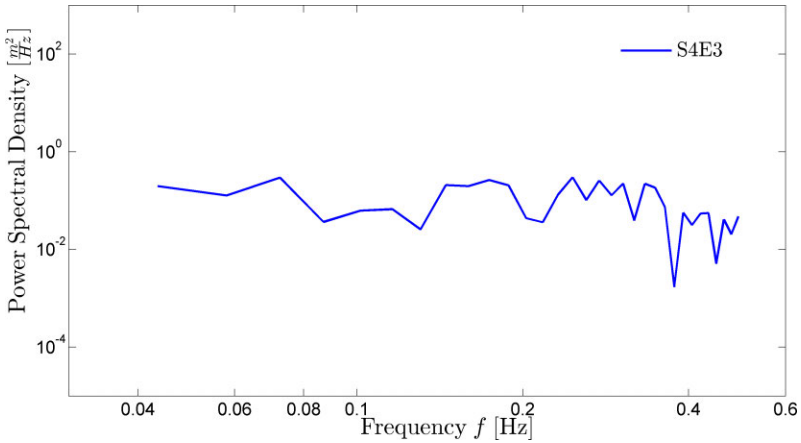

(c) Spectral Analysis of $\lambda_{DS}/\lambda_{US}$ for pure unidirectional flow (S4E3).

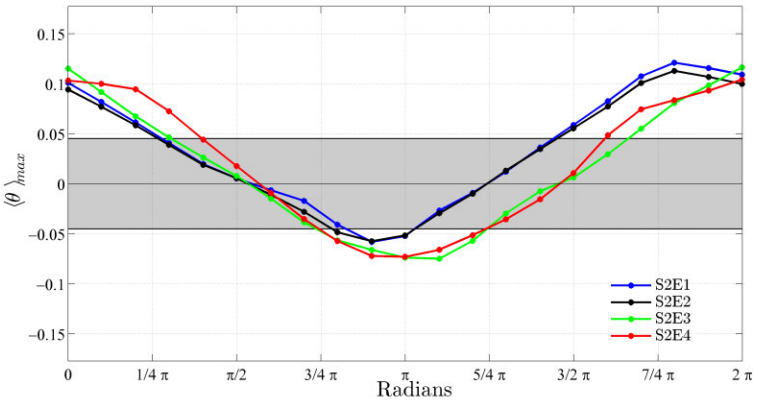

(d) Maximum phase-averaged Shields number throughout the wave cycle (S2). Shaded area represents shear stresses that are below the critical shear stress necessary to mobilize the 0.25 mm sediment (Brownlie, 1981).

Figure 6.9: Bedform development for wave-dominated combined flows (S2) and pure unidirectional flows (S4E3).

time scale (Figure 6.9c). The fact that there is a flat spectrum for the longer periods conforms with the experimental results shown in Chapter 5, where the effect of the unidirectional flows becomes stronger as the period becomes longer. This behavior cannot be explained based on the phase-averaged shear stresses (Figure 6.9d), since the instantaneous unidirectionally-driven shear stresses average-out in the computation of the phase-averaged shear stresses. However, the asymmetry seen in Figure 6.9d for all periods is responsible for the similar asymmetry in growth of the defects (Figure 6.9a) for all periods, despite the absence of periodic fluctuations for the longer periods. In other words, the development process for all oscillatory periods is the same for wave-dominated combined flows (same overall trend, Figure 6.9a), although for longer periods the growth of the defects does not exhibit period-related fluctuations.

For the case of the third set of experiments (S3, current-dominated combined flows), two-lobed horns were generated on each side of the defect within the first oscillation cycles in experiments S3E1 (pure oscillatory; Figure 6.10a) and S3E2 (wave-dominated combined flow; Figure 6.10b). However, there was no development of two-lobed horns on the upstream side of the defect during S3E3 (current-dominated combined flow; Figure 6.10c). The main difference between the S3 experiments is the increase of the unidirectional component of flow from 0 to 0.2 ms^{-1}, keeping the period (15 s) and the oscillatory velocity (0.3 ms^{-1}) constant. Increasing the unidirectional flow changed both the initiation geometries and the propagation trends, resulting in symmetric (S3E1), slightly asymmetric (S3E2) and completely asymmetric (S3E3) defect propagation (Figure 6.11a). Figure 6.11a shows how the downstream (closed dots) and upstream (open dots) distance, measured from the geometrical center of the defect, evolved throughout the experiment. For the case of S3E1 (only waves; Figure 6.10a), the downstream and upstream distance are similar over time, showing a similar growth-path in opposite directions. This result is the same as the trends exhibited for all periods for the pure oscillatory experiments (S1). In the case of the second experiment (S3E2, wave-dominated combined flow; Figure 6.10b), both edges of the defect propagate

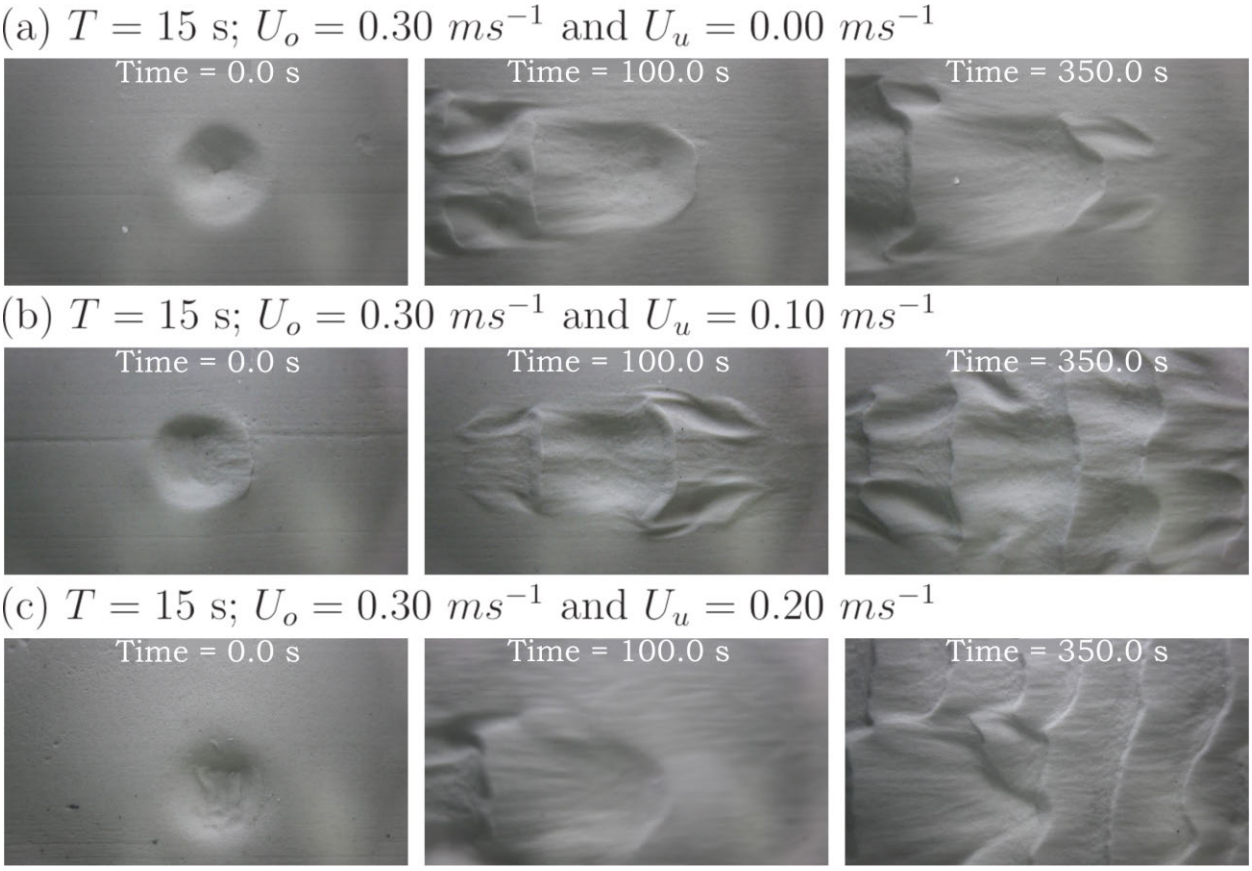

Figure 6.10: Bedform initiation under different combined flows by defect initiation, where T = period, U_o = maximum oscillatory velocity, U_u = mean free-flow unidirectional velocity and Cycle = Time/Period. Unidirectional flow is from right to left. Area of view for each individual image is ≈ 0.34 m long and ≈ 0.23 m wide. Note the asymmetric generation of the two-lobed horns on each side of the defect.

away from the center, but the downstream edge of the defect moved ≈ 5 times faster than the upstream edge, with the upstream edge still moving away from the defect center. Once again, this asymmetric growth has similar mechanisms like the second set of experiments (S2). However, for experiment S3E3 (current-dominated combined flow; Figure 6.10c), both the upstream and downstream edge of the defect propagated in the same downstream direction (Figure 6.11a), which is reflected in the decreasing length (i.e., closer to the center of the defect) of the upstream edge with time (green line with open dots, Figure 6.11a). The reason why the upstream edge was not able to propagate upstream is associated with the evolution of the shear stresses in the combined flow boundary layer (Figure 6.11b). All the

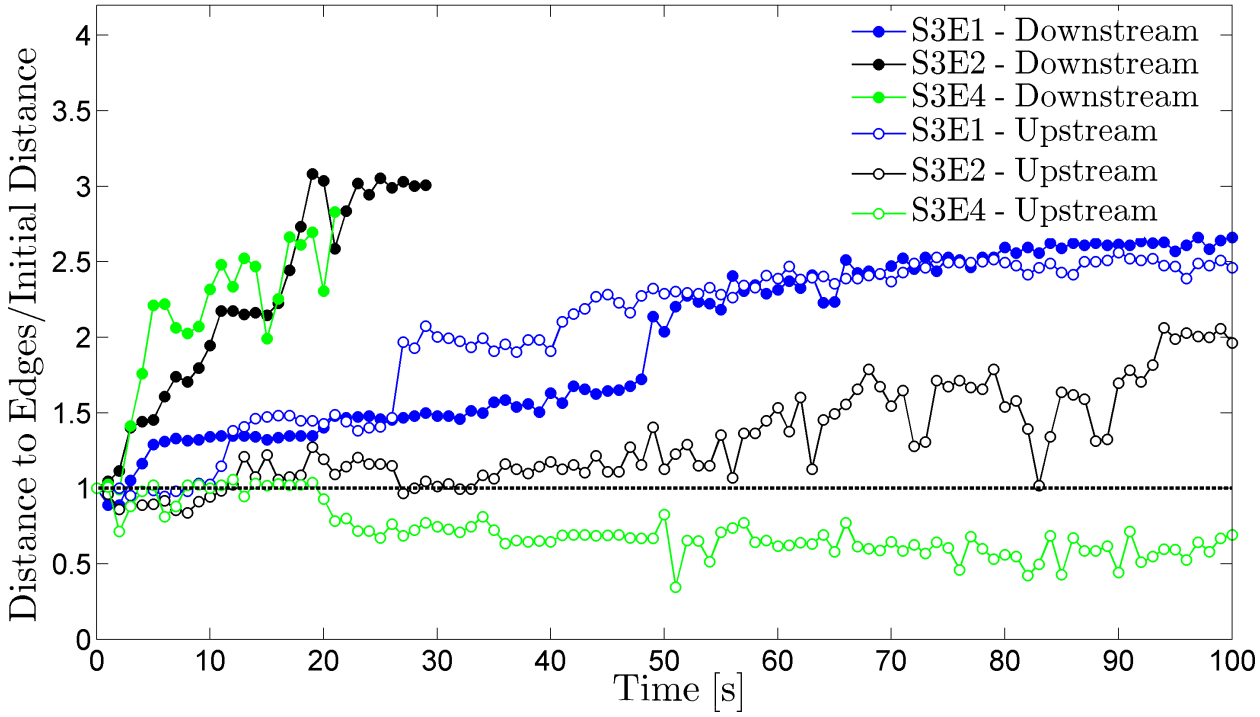

(a) Defect development under current-dominated combined flows (S3). Downstream (closed dots) and upstream (open dots) distances are dimensionalized by the initial defect length.

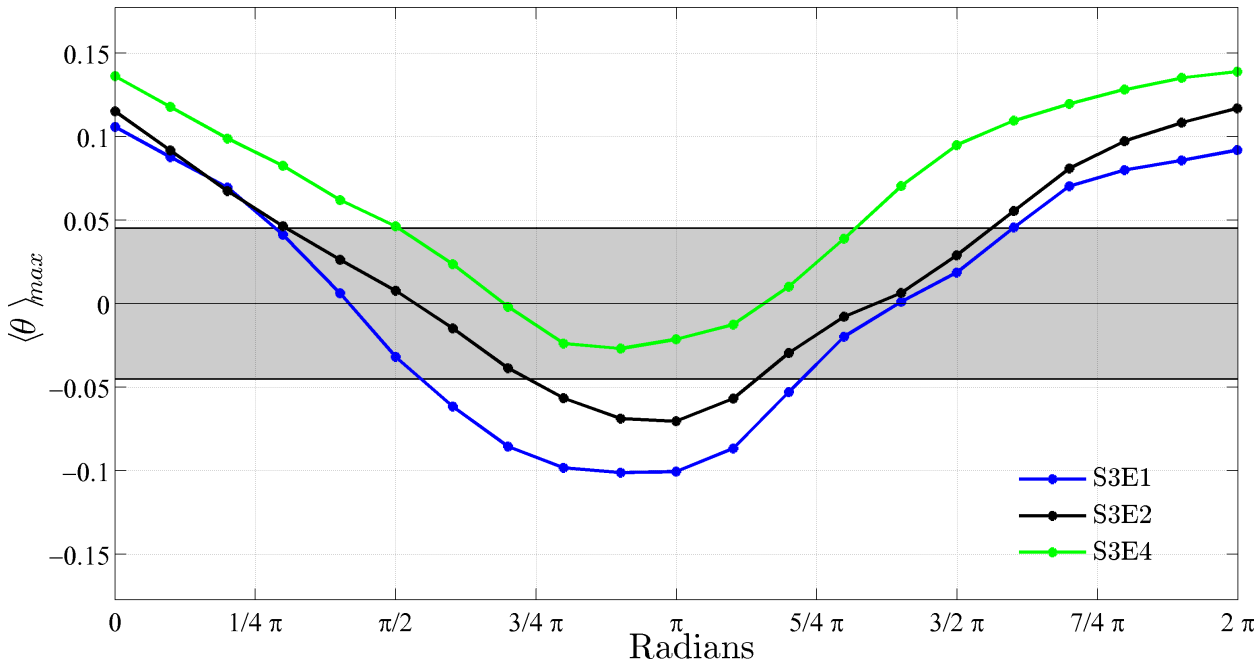

(b) Maximum phase-averaged Shields number throughout the wave cycle (S3). The shaded area represents shear stresses that are below the critical shear stress necessary to mobilize the 0.25 mm sediment (Brownlie, 1981).

Figure 6.11: Bedform development under current-dominated combined flows (S3).

experiments in S3 have flow reversals (negative values in Figure 6.11b), however, for experiment S3E3 the shear stresses generated in the flow reversal were not strong enough to mobilize the sediment (Figure 6.11b). Thus, there is no net transport in the upstream direction. In addition, the FFT of the defect growth fluctuations showed that there is a clear period-driven peak for the pure oscillatory case (S3E1), but a flat spectrum for combined flow cases (S3E2 and S3E3; Figure 6.12). These result is the same phenomenon that occurred for the S2 experiments, where the absence of a spectral peak was associated with the presence of a unidirectional component associated with a relatively long oscillation period ($T = 15$ s).

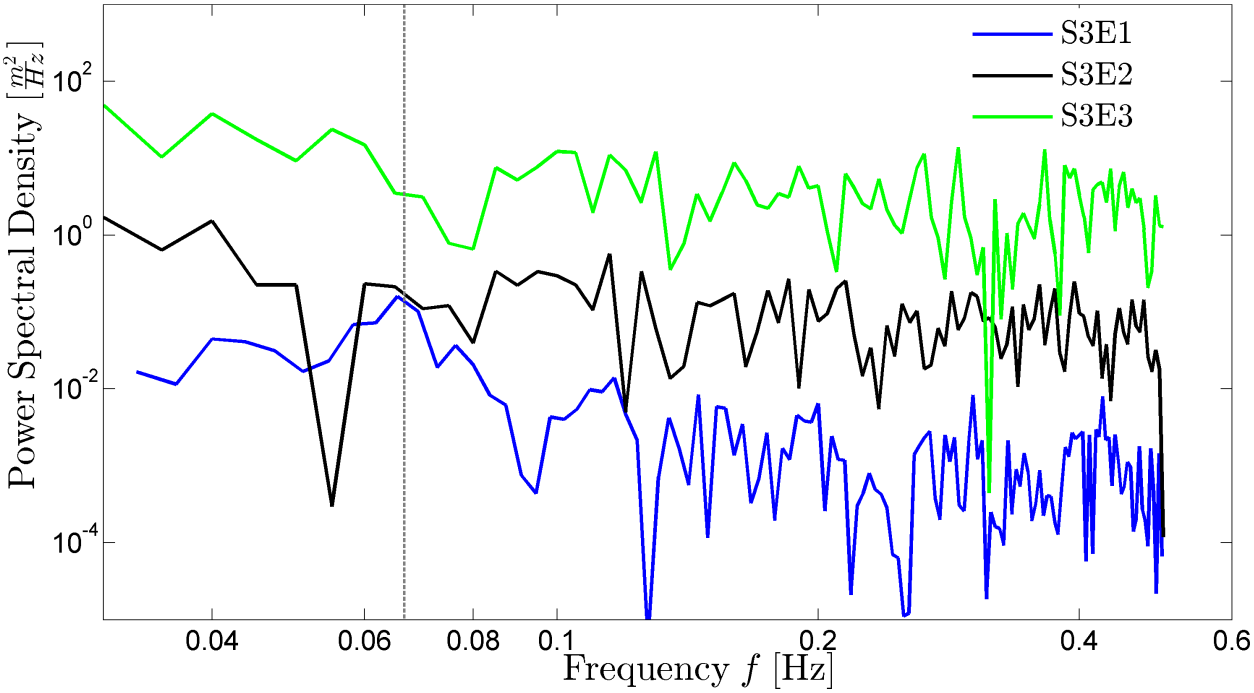

Figure 6.12: Spectral Analysis of $\lambda_{DS}/\lambda_{US}$ (S3). The dashed line demarcates where the $T = 15$ s peak should be if present.

6.5 Prediction of Propagation Rate

The average development rate as a function of time, α, was computed by fitting a polynomial function of order one to the ratio between the downstream and upstream growth for

pure oscillatory (S1; Figure 6.7a), wave-dominated combined flows (S2; Figure 6.9a) and current-dominated combined flows (S3; Figure 6.11a). The polynomial function was

$$\frac{\lambda_{DS}}{\lambda_{US}}(t) = \alpha\, t + \beta \tag{6.1}$$

where t is time measured in minutes and $\beta = \lambda_{DS,0}/\lambda_{US,0} \approx 1$ is the ratio of the downstream and upstream distances from the center of the defect to the edges at time = 0 (Table 6.2). For the pure oscillatory flows, the average slope was $\alpha = 0.13 \times 10^{-2}$ [1/min], for the wave-dominated combined flows it was $\alpha = 3.56 \times 10^{-2}$ [1/min] and for the case of the current-dominated combined flow it was $\alpha = 7.47 \times 10^{-2}$ [1/min]. The mean R^2 from all the fits was 0.68 with a standard deviation of 0.1 and an averaged p-value of 0.04 (Appendix B.2), and each of the fits was able to capture the overall trend of the growth (e.g., Figure 6.13). From the discussion in Section 6.3, it is clear that the change of α is a function of the peak

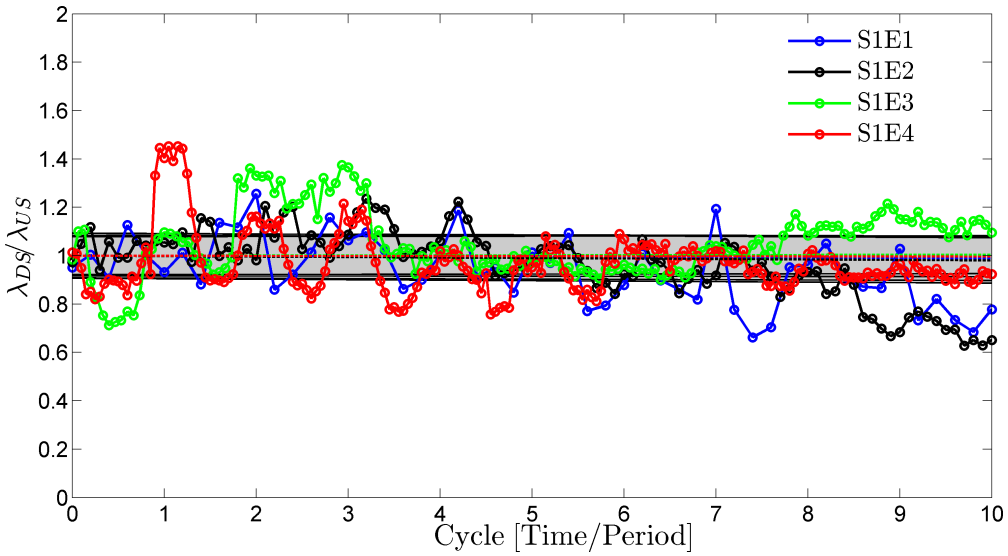

Figure 6.13: Defect development under pure oscillatory flow (S1). Dotted line is the fit of Equation 6.1, where the gray-shaded area represents the 95% confidence interval of the fitted function. Mean $R^2 = 0.68$.

upstream and downstream shear stresses. Therefore, the ratio of the maximum downstream shear stress ($\theta_{max}^{(+)}$) and the maximum upstream shear stress ($\theta_{max}^{(-)}$) through the wave cycle was used to characterize the shear stress dependence via the Shear Stress Symmetry Index

($SSSI = \theta_{max}^{(+)}/\theta_{max}^{(-)} \geq 1$). Thus, based on the experimental data available, a power law is proposed to predict the development rate for oscillatory and combined flows:

$$\alpha = \gamma \ (SSSI - 1)^{\phi} \tag{6.2}$$

where $\gamma = 0.035$ and $\phi = 0.6$ with an $R^2 = 0.82$ and p-value of 0.04 (Figure 6.14). The interpretation of Equation 6.2 is straightforward and follows the results of Section 6.3, when the ratio between the maximum downstream shear stress and the maximum upstream shear stress is one (i.e., $SSSI = 1$ represents a pure oscillatory flow), α is zero, leading to a symmetric growth. On the other hand, if $SSSI > 1$ there is an asymmetry in the shear stress which is reflected in an asymmetric development quantified by Equation 6.2.

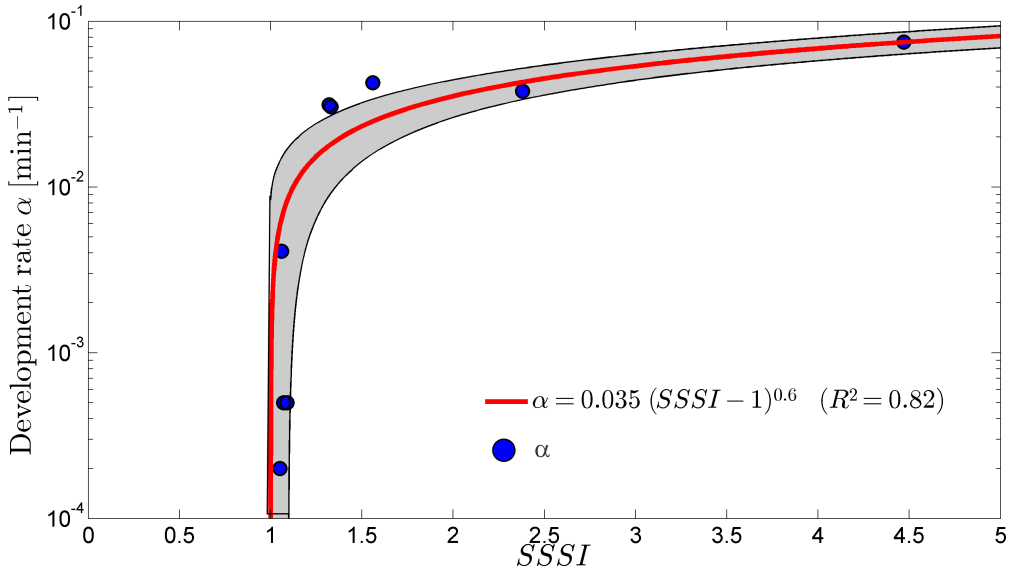

Figure 6.14: Power law of the defect development rate as a function of the shear stress symmetry index.

6.6 Conclusions

This chapter presents new experimental data on bedform initiation under oscillatory and combined flows in order to gain a quantitative insight into bedform genesis over artificially-

Pure Oscillatory Flows	S01E01	S01E02	S01E03	S01E04
$\theta_{max}^{(+)}$	0.105	0.108	0.101	0.084
$\theta_{max}^{(-)}$	-0.113	-0.102	-0.106	-0.092
SSSI	1.07	1.06	1.05	1.09
$\alpha \times 10^{-2} \quad [s^{-1}]$	0.05	0.41	0.02	0.05
Wave-Dominated Combined Flows	S02E01	S02E02	S02E03	S02E04
$\theta_{max}^{(+)}$	0.122	0.115	0.114	0.109
$\theta_{max}^{(-)}$	-0.078	-0.068	-0.085	-0.083
SSSI	1.56	1.68	1.33	1.32
$\alpha \times 10^{-2} \quad [s^{-1}]$	4.26	3.79	3.04	3.14
Current-Dominated Combined Flows	S03E01	S03E02	S03E03	
$\theta_{max}^{(+)}$	0.101	0.114	0.148	
$\theta_{max}^{(-)}$	-0.106	-0.085	-0.033	
SSSI	1.05	1.33	4.47	
$\alpha \times 10^{-2} \quad [s^{-1}]$	0.02	3.04	7.47	

Table 6.2: Summary of shear stress and average defect development rate.

generated defects. These results show that combined flows share the same bedform initiation processes as unidirectional and oscillatory flows. This result was reflected in the same geometric pattern (i.e., two lobed horns) regardless of the flow conditions. In addition, as expected, the development of the defects shows a strong relationship with the direction and magnitude of the shear stress throughout the oscillation. If the condition had a symmetric shear stress, the defects grew and propagated symmetrically, whereas if the shear stress was asymmetric, the defects grew and propagated with a predominant downstream direction. Furthermore, for the case of current-dominated combined flow (S3E3), the maximum upstream shear stress was not large enough to entrain sediment in the upstream direction, resulting in solely downstream migration transport.

Chapter 7

Bedform Development under Unidirectional, Oscillatory and Combined Flows

7.1 Introduction

Over the past few decades, there have been several studies analyzing the development of bedforms under unidirectional and oscillatory flows (e.g., Oost and Baas, 1994; Baas, 1999; Faraci and Foti, 2002; Doucette and O'Donoghue, 2006). These studies have provided a better understanding of temporally-varying bedforms, with especial emphasis on the importance of initial conditions and the time required for bed-flow equilibrium. These studies can be used to understand the spatial and temporal variations of bedform size (e.g., wavelength or height) and geometrical shape (e.g., Bedform Symmetry Index or Bedform Roundness Index) for a given bed state (Harms et al., 1975; Allen, 1982; Anthony, 2009). However, our comprehension of the development of bedforms under combined flows is still far from complete. Hence, a set of experiments presented herein were made under a range of combined flow conditions to gain insights on the equilibrium time for different bed states, temporal changes of bedform height and wavelength, and their relationships with combined flow velocities and sediment transport. In addition, a more limited set of pure unidirectional and pure oscillatory flow experiments were performed to compare the results with previous studies.

7.2 Experimental Data

Bedform development in a 250 μm diameter sand bed was studied under pure oscillatory and combined flow conditions with oscillation periods (T) of 4, 5 and 6 seconds (Table 7.1). The

maximum orbital velocity (U_o) was varied from 0.10 to 0.70 $m\,s^{-1}$, while the unidirectional component (U_u) was varied from 0 to 0.50 $m\,s^{-1}$. The two pure unidirectional experiments had unidirectional velocities (U_u) of 0.40 and 0.50 $m\,s^{-1}$. Experiments started from a smooth flat bed and were consistently run until equilibrium conditions were obtained. These equilibrium conditions were established following the methodology of Prins and de Vries (1971), Gee (1974) and Baas (1993), where the development was estimated by

$$\eta_t(t) = \eta_e \left(1 - e^{-c_\eta\, t}\right) \tag{7.1}$$

$$\lambda_t(t) = \lambda_e \left(1 - e^{-c_\lambda\, t}\right) \tag{7.2}$$

where t is time in minutes, and c_η and c_λ are the bedform height and wavelength adaptation constants. The subscripts indicate the actual (t) and equilibrium (e) values of height and wavelength. It is important to note that Equations 7.1 and 7.2 only consider *temporal* variations of the bedform characteristics. Therefore, a spatial average is also used to determine the mean height and wavelength for a particular time, t,

$$\begin{aligned} \eta_t(t) &= \tfrac{1}{N} \textstyle\sum_{i=1}^{N} \eta_i(x,t) \\ \lambda_t(t) &= \tfrac{1}{N} \textstyle\sum_{i=1}^{N} \lambda_i(x,t) \end{aligned} \tag{7.3}$$

where N is the number of bedforms present in the 1 m center-span of the tunnel surveyed by the sonar. It is important to note that the η and λ data sets include multiple measurements of the same bedform as it migrates in the sampled area. However, since the bedforms evolve over time, that bedform does not contribute to the same height or wavelength value every time, and hence no oversampling is occurring. A non-linear least squares fit, using a least absolute residual method, was used to find the best solution for Equations 7.1 and 7.2 to fit the spatially-averaged height and wavelength data. From these solutions, the values of $[\eta_e, c_\eta]$ and $[\lambda_e, c_\lambda]$ were obtained.

The equilibrium time t_e is defined as the time when the actual height (η_t) and wavelength

Table 7.1: Summary of flow and bedform development characteristics. The table is divided into pure unidirectional, pure oscillatory and combined flow experiments.

#[a]	T (s)	U_o (ms^{-1})	U_u (ms^{-1})	η_e[b] (mm)	c_η[a] (hr^{-1})	$R^2(\eta)^a$	λ_e (m)	c_λ[b] (hr^{-1})	$R^2(\lambda)^b$	q_s[c] ($cm^2\,s^{-1}$)	t_e[d] (hr)	t_t[e] (hr)	Bedform[f] Type
Pure Unidirectional Flows													
54	-	-	0.40	17.6	1.36	0.72	0.20	3.69	0.76	71.6	9.36	18.00	CR
55	-	-	0.50	18.1	2.09	0.63	0.21	2.82	0.78	117.1	0.82	3.28	CR
Pure Oscillatory Flows													
1*	4	0.25	0.00	34.8	0.99	0.95	0.22	0.87	0.96	14.9	2.21	5.07	SR
8*	5	0.20	0.00	35.3	0.82	0.97	0.21	0.65	0.98	17.2	4.15	37.70	SR
18	5	0.40	0.00	22.0	2.79	0.62	0.20	3.48	0.53	27.7	0.67	15.20	SR
30*	6	0.25	0.00	32.1	0.45	0.94	0.20	0.48	0.97	16.1	4.23	14.49	SR
42	6	0.50	0.00	32.3	3.67	0.45	0.28	3.94	0.45	88.3	0.55	2.13	SR
Combined Flows													
2	4	0.25	0.10	20.5	0.75	0.60	0.15	1.01	0.56	28.3	2.22	13.30	QAR
3	4	0.25	0.20	21.1	0.89	0.65	0.18	0.47	0.82	33.5	2.81	18.00	AR
4	4	0.25	0.30	26.9	2.02	0.40	0.23	1.80	0.56	47.9	1.10	12.50	ARR
5	4	0.25	0.40	35.6	1.34	0.45	0.51	6.90	0.45	16.3	0.88	2.00	ARD
11	5	0.20	0.10	36.4	0.69	0.66	0.15	0.24	0.46	27.0	3.80	18.10	QAR
12	5	0.20	0.20	27.3	2.10	0.87	0.22	1.24	0.91	28.8	2.60	20.20	QAR
15	5	0.20	0.30	27.6	2.68	0.63	0.27	2.72	0.48	70.4	0.73	9.70	ARR
16	5	0.20	0.40	30.3	2.20	0.50	0.60	0.98	0.45	156.3	0.58	7.30	ARD
17	5	0.20	0.50	44.6	0.06	0.85	0.88	0.06	0.85	210.0	0.30	2.30	ARD
19	5	0.40	0.10	23.0	4.30	0.43	0.17	3.17	0.35	67.8	0.49	7.50	QAR
20	5	0.40	0.20	20.7	2.65	0.53	0.21	2.48	0.59	104.4	0.79	6.20	QARR
21	5	0.40	0.30	61.3	0.93	0.92	0.58	0.77	0.93	333.6	0.41	1.65	QARR
22	5	0.40	0.40	98.3	0.98	0.89	1.02	0.93	0.79	751.1	0.17	2.20	ARD
25	5	0.50	0.40	153.0	0.06	0.47	1.23	0.96	0.47	1220.9	0.50	2.20	ARD
27	6	0.10	0.50	35.5	6.10	0.97	0.49	0.86	0.96	119.3	0.93	3.80	CR
31	6	0.25	0.05	26.6	0.70	0.63	0.18	2.50	0.39	21.4	1.97	17.04	SR
32	6	0.25	0.10	17.2	0.55	0.92	0.19	0.37	0.91	28.2	4.27	5.69	QAR
33	6	0.25	0.20	17.6	1.47	0.63	0.17	0.89	0.76	37.1	1.53	9.74	QAR
34	6	0.25	0.30	23.3	2.15	0.62	0.25	1.42	0.51	97.6	1.14	12.71	ARR
35	6	0.25	0.40	68.3	1.78	0.34	0.65	1.52	0.42	366.5	1.31	5.90	ARD
36	6	0.25	0.50	123.0	3.36	0.78	1.30	1.61	0.69	930.8	0.31	1.23	ARD

[a]Experiment Number: * indicates that the stable planform geometry is 2D, otherwise it is 3D.

[b]Values obtained by fitting Equation 7.1 and Equation 7.2 to the experimental data. $R^2(\eta)$ and $R^2(\lambda)$ are the square of the sample correlation coefficient for Equation 7.1 and Equation 7.2 respectively.

[c] Bedload transport per unit width (Section 4.3.2).

[d] Time until flow-bedform equilibrium obtained from Equation 7.7

[e] Duration of Experiment. [f]SR = Symmetric Ripples, AR = Asymmetric Ripples, ARR = Asymmetric Rounded Ripples, QAR = Quasi-Asymmetric Ripples, QARR = Quasi-Asymmetric Rounded Ripples, AD = Asymmetric Dunes, ARD = Asymmetric Rounded Dunes and CR = Current Ripples.

(λ_t) reach 90% of their equilibrium height (η_e) and wavelength (λ_e)

$$\begin{aligned} \eta_t &= 0.9\,\eta_e \\ \lambda_t &= 0.9\,\lambda_e. \end{aligned} \tag{7.4}$$

Therefore, by applying Equation 7.4 to Equations 7.1 and 7.2, the equilibrium time for the height was computed as

$$t_e\left(\eta\right) = -\frac{\ln 0.1}{c_\eta} \tag{7.5}$$

and for wavelength

$$t_e\left(\lambda\right) = -\frac{\ln 0.1}{c_\lambda} \tag{7.6}$$

The final equilibrium time was computed as the average of Equations 7.5 and 7.6

$$t_e = 0.5\,\left[t_e\left(\eta\right) + t_e\left(\lambda\right)\right]. \tag{7.7}$$

Table 7.1 shows the equilibrium time (t_e), equilibrium height (η_e) and equilibrium wavelength (λ_e), as well as the adaptation constants for the height (c_η) and wavelength (c_λ).

7.3 Bedform development as a function of flow conditions

The evolution of bedforms from an initial flat bed was studied for different types of flow conditions: pure unidirectional (Section 7.3.1), pure oscillatory (Section 7.3.2) and combined flows (Section 7.3.3).

7.3.1 Pure Unidirectional Flows

The development of pure unidirectional flow bedforms over a 0.25 mm diameter sand bed exhibits the same general trend to that described by Baas (1993) with 0.095 and 0.238

mm diameter sand grains. The evolution of the bed showed a characteristic asymptotic growth (e.g., Sutherland and Hwang, 1965; Baas, 1994, 1999; Coleman et al., 2003) seen in Figure 7.1. Once the overall equilibrium stage was reached (Equation 7.4), the wavelength and height fluctuated around their equilibrium values as long as the flow conditions remain unchanged (i.e., to the right of the vertical line in Figure 7.1). This development behavior was found for both unidirectional experiments, in which their final equilibrium state was 3D current ripples (Table 7.1). The development of the unidirectional bedforms was successfully estimated by Equations 7.1 and 7.2 (e.g., red lines in Figure 7.1). Baas (1994, 1999) also reports successful results of Equations 7.1 and 7.2, the strength of the prediction of these equations can be seen by the relatively high R^2 values obtained from the fits (Table 7.1). The mean R^2 value for all fits was 0.72 (Table 7.1) with a averaged p-value of 0.03 (Appendix B), Baas (1993) experiments had a mean $R^2 = 0.70$). The fact that the p-value$<$ 0.05 allows rejection of the null hypothesis, which makes the regression statistically significant. In addition, Figure 7.1 shows the 95% confidence intervals in the gray-shaded area, which denotes that the fit produces a reliable estimate of the development history of the bedform.

Similar to Baas (1994), four major stages of bedform development were distinguished during the unidirectional flow experiments (Figure 7.2): (1) incipient bedforms, (2) growing bedforms, (3) stabilizing bedforms, and (4) fully-developed bedforms:

Stage 1 - Incipient Bedforms

Stage 1 starts with the initiation of the bed morphologies from an initially flat bed, until the first signs of bedform growth (Figure 7.2). Once the threshold for sediment entrainment is exceeded, a series of small incipient bedforms started to propagate from flow-generated defects. For the case of unidirectional flows, the bed deformation started as longitudinal streaks (Figure 7.3b) that rapidly transformed into very small, three-dimensional, bedforms (Figure 7.3c) that then merged into straight and sinuous small bedform trains (Figure 7.3d).

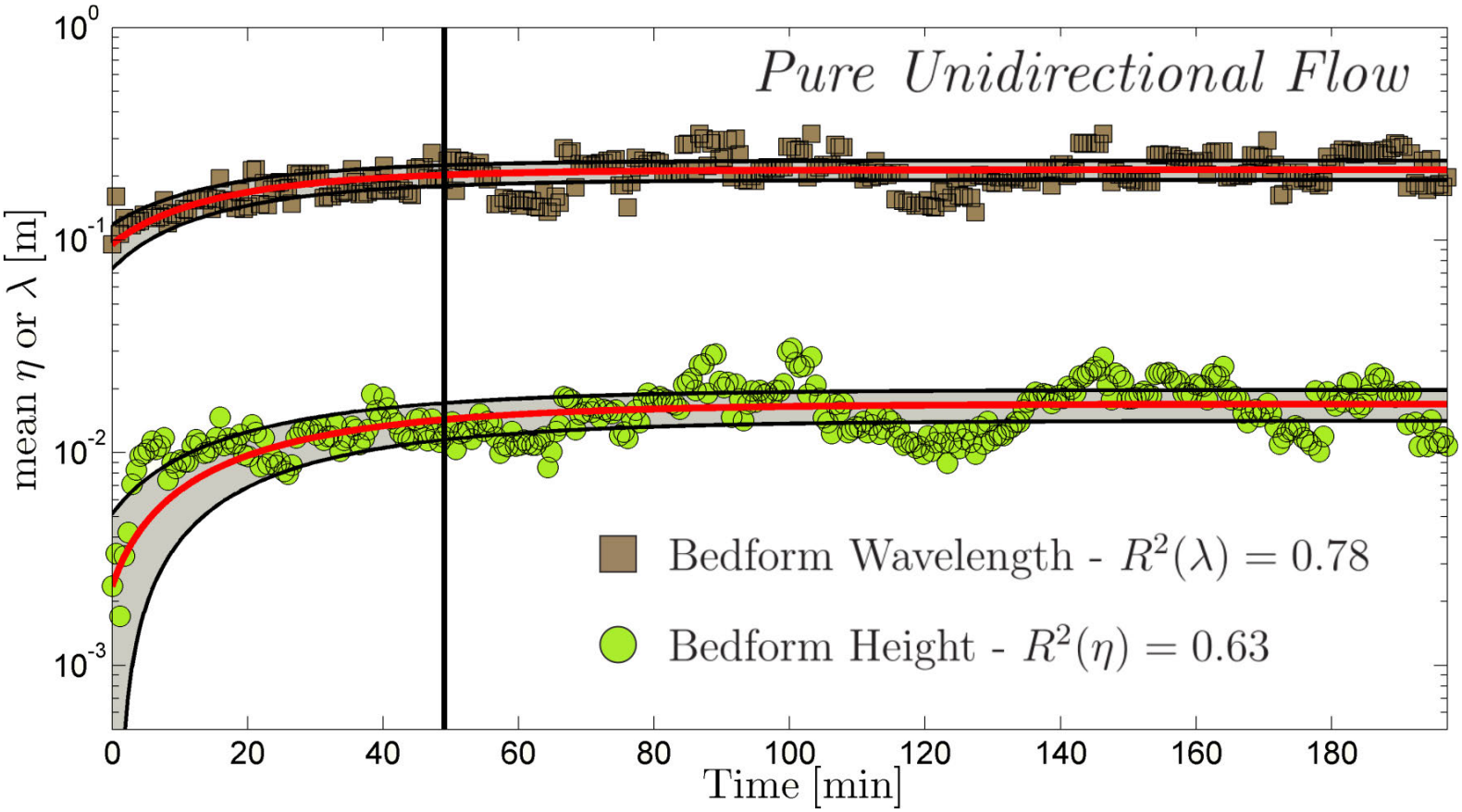

Figure 7.1: Development of bedform wavelength and height on an initially flat bed for pure unidirectional flow (Experiment 55, $t_e = 0.82$ hr). The equilibrium time t_e is denoted by the vertical line. $R^2(\lambda)$ and $R^2(\eta)$ are the correlation coefficients for the bedform wavelength and bedform height, respectively, obtained by fitting Equations 7.1 and 7.2. The gray-shaded area represents the 95% confidence interval of the fitted function. Bed morphology at equilibrium = three-dimensional current ripple (3D CR). Note the gently 'sinusoidal oscillation' of the bedform height data for $t > 80$ min and its negligible influence on the wavelength data.

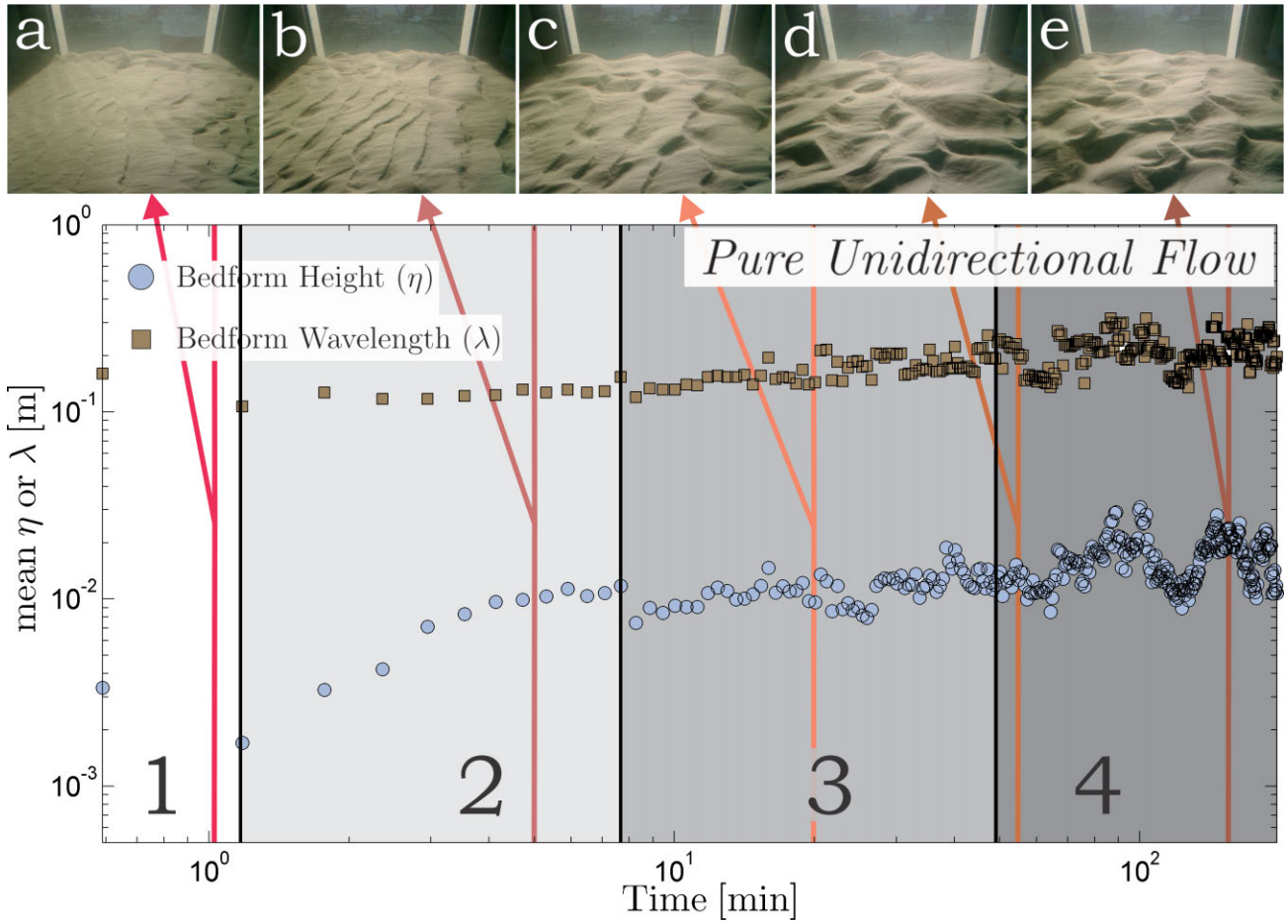

Figure 7.2: Spatially-averaged bedform height and wavelength plotted against time for a three-dimensional asymmetric current-ripple (Experiment 55). The numbers at the base of the diagram indicate development stages: (1) incipient ripples (white box), (2) growing bedforms (light-gray box), (3) stabilizing bedforms (gray box), and (4) fully-developed bedforms (dark-gray box). The vertical line dividing boxes 3 and 4 marks the equilibrium time at $t_e = 44.4$ min. Both axes have a log-normal scale. A series of photos were taken at (a) $t = 1.5$ min, (b) $t = 5.0$ min, (c) $t = 20.4$ min, (d) $t = 50.7$ min and (e) $t = 139.9$ min; and are denoted by the different colored arrows. The window on the back of the picture is 0.60 m wide. Note how the three-dimensionally of the planform geometry grows from photos a-e.

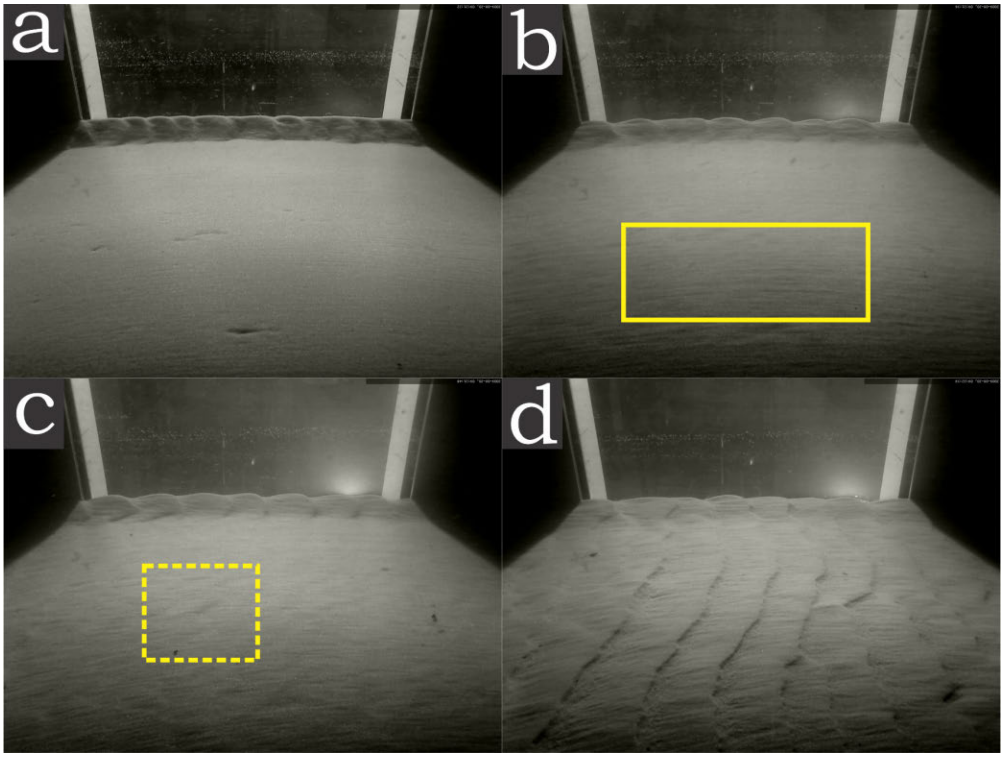

Figure 7.3: Incipient bedforms at the first stage of development for a three-dimensional asymmetric current-ripple (Experiment 55). The series of photos were taken at (a) $t = 1$ s, (b) $t = 14$ s, (c) $t = 52$ s, and (d) $t = 77$ s. The window on the back of the picture is 0.60 m wide. Note the bed deformation started as longitudinal streaks (solid-box in b), which rapidly transformed into straight and sinuous small bedform trains (c-d). In addition, the initial conditions of Stage 1 are characterized by 3D features (dashed box in c) which turned into 2D bedforms (d)

Stage 2 - Growing Bedforms

Once the bed was fully covered with bed features, the bedforms started to grow in size by a combination of sediment capturing and merging with nearby bedforms (Figure 7.2b). Sediment incorporation into the bedforms occurred as it was transported as bedload over the stoss side (saltation or surface creeping processes) and some of the sediment deposits in the lee side of the bedform. The growth occurring during this stage accounts for $\sim 85\%$ of the total bedform enlargement. This result is consistent with the experiments reported by Baas (1994) that show an overall growth of $\sim 75\%$.

Stage 3 - Stabilizing Bedforms

Stage 3 is defined as the temporal gap that occurs in the interval between the moment when the asymptotic growth ends and the time when the bed reaches equilibrium conditions (Figure 7.2). During this stage, the bedforms are in a transitional stage. On the one hand, the bed is not fully developed since the criteria defined in Equation 7.4 is not fulfilled and, in addition, there are still signs of net bedform growth (mainly by merging with nearby bedforms, Figure 7.4). On the other hand, the bed morphology exhibits all the 'visual' characteristics that fully developed bedforms display (e.g., planform geometry, shapes), but they are just smaller. This observation is consistent with that of Baas (1994).

The rate at which the bedforms grow during Stage 3 is significantly lower than Stage 2. The mean overall growth during Stage 3 was $\sim$ 10% of the overall growth. Baas (1994) reports that during the stabilizing bedform state, the mean height and wavelength values increased from 10 to 13 mm and from 100 to 116 mm, respectively, accounting for an estimated $\sim$ 14% of the total growth. The difference in growth between Stage 2 ($\sim$ 80% of the overall growth) and Stage 3 ($\sim$ 12% of the overall growth) denotes the main reason why there is a need to separate Stage 3 from Stage 2 (Figure 7.2).

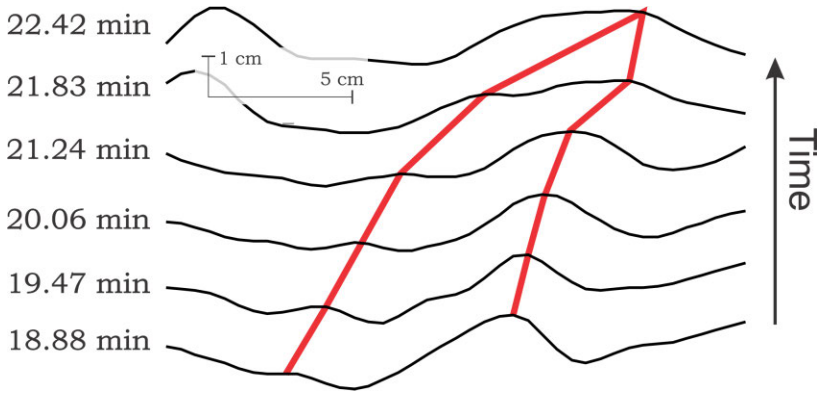

Figure 7.4: Amalgamation of two current ripples during the third stage of development (Experiment 55). Lines between bed surfaces indicate successive positions of the ripple crest on the bed. The number beside the bed surface refers to the development time in minutes since the initiation of the experiment. The red line correlates the same crest along its evolution as a function of time.

Stage 4 - Fully-developed Bedforms

Once the bed reaches a morphodynamic equilibrium (i.e., fully developed bedforms under the exact flow conditions acting on the bed), the average bedform height and wavelength will converge to singular values, ceasing to change with time. However, the height and wavelength of individual bedforms will continue to fluctuate around the equilibrium average values (Figure 7.1). The primary factors driving the observed fluctuations around the mean values are: (i) the dynamic evolution of bedforms over time and space (e.g., amalgamation, Figure 7.4) and (ii) the inherent three-dimensionality of the bed configuration. The experimental results conducted by Baas (1994) show that the dynamic evolution of bedforms introduces intrinsic scatter in the data. Additionally, the second cause of scatter (also reported by Baas, 1994) was the result of transverse changes in bedform geometry and size. The geometry of the equilibrium bedforms for both Experiments 54 and 55 are best described as linguoid and lunate ripples (Figure 7.2). For example, a linguoid or lunate ripple possesses its maximum height if measured in a cross-sectional plane through the center of the ripple and parallel to the mean flow direction, whereas the height measurements through other planes will record a smaller value. Hence, the transverse variability of these bedforms adds another source of dispersion and fluctuation on individual measurements that will result in fluctuations around the mean bedform height value. However, the 'error' associated with the transverse variability of bedforms in Experiments 54 and 55 may be considered identical to the 'error' reported from measurements conducted in field studies (e.g., cross-sectional cuts of bedform cross-strata in outcrops). Therefore due to this characteristic variability, and despite the good predictive power of Equations 7.1 and 7.2, the use of a unique value (η_e or λ_e) to describe all the range of geometries is insufficient for some conditions (e.g., values outside the 95% confident interval, Figure 7.1). This result has been discussed within the context of unidirectional bedforms, where a two-parameter gamma density function was employed instead of a single value to describe the distribution of bedforms under equilibrium conditions

(e.g., Paola and Borgman, 1991; Leclair and Bridge, 2001). Therefore, a Gaussian density function was applied to characterize the bedform size distributions:

$$\mathcal{P}(\eta(t > t_e); \mu_\eta, \sigma_\eta) = \frac{1}{\sqrt{2\,\pi}\sigma_\eta} exp\left\{ -\frac{(\eta - \mu_\eta)^2}{2\,\sigma_\eta^2} \right\} \tag{7.8}$$

$$\mathcal{P}(\lambda(t > t_e); \mu_\lambda, \sigma_\lambda) = \frac{1}{\sqrt{2\,\pi}\sigma_\lambda} exp\left\{ -\frac{(\lambda - \mu_\lambda)^2}{2\,\sigma_\lambda^2} \right\} \tag{7.9}$$

where μ is the mean (peak location) and σ is the standard deviation. Equations 7.8 and 7.9 assume a unimodal distribution; however, in some cases the distribution had a bimodal distribution. In that case, a homotopic mapping method was used to possess a continuous bimodal Gaussian density function:

$$\begin{aligned} \mathcal{P}(\eta(t > t_e); \mu_{\eta,\{1,2\}}, \sigma_{\eta,\{1,2\}}) = & \frac{\vartheta}{\sqrt{2\,\pi}\sigma_{\eta,1}} exp\left\{ -\frac{(\eta - \mu_{\eta,1})^2}{2\,\sigma_{\eta,1}^2} \right\} \\ & + \frac{1-\vartheta}{\sqrt{2\,\pi}\sigma_{\eta,2}} exp\left\{ -\frac{(\eta - \mu_{\eta,2})^2}{2\,\sigma_{\eta,2}^2} \right\} \end{aligned} \tag{7.10}$$

$$\begin{aligned} \mathcal{P}(\lambda(t > t_e); \mu_{\lambda,\{1,2\}}, \sigma_{\lambda,\{1,2\}}) = & \frac{\vartheta}{\sqrt{2\,\pi}\sigma_{\lambda,1}} exp\left\{ -\frac{(\lambda - \mu_{\lambda,1})^2}{2\,\sigma_{\lambda,1}^2} \right\} \\ & + \frac{1-\vartheta}{\sqrt{2\,\pi}\sigma_{\lambda,2}} exp\left\{ -\frac{(\lambda - \mu_{\lambda,2})^2}{2\,\sigma_{\lambda,2}^2} \right\} \end{aligned} \tag{7.11}$$

where μ_1 and μ_2 are the locations of the two peaks in the bimodal distribution, σ_1 and σ_2 are standard deviations of the μ_1 and μ_2 distributions and ϑ is the unit interval (e.g., Armstrong, 1983).

Figure 7.5 displays the histogram of the recorded heights (Figure 7.5a) and wavelengths (Figure 7.5b) for all equilibrium bedforms for a three-dimensional asymmetric current-ripple (Experiment 55). These measurements include all the observed bedforms for each time (the N bedforms from Equation 7.3) from the time $t = t_e$ to the end of the experiment (t_t, Table 7.1).

Both the distribution of bedform heights (Figure 7.5a) and wavelengths (Figure 7.5b) show signs of significant temporal variation of the spatially-averaged wavelength or height once the bed reached an equilibrium state (e.g., $\sigma_\eta/\mu_\eta \times 100 \sim 43.52\%$ and $\sigma_\lambda/\mu_\lambda \times 100 \sim 33.3\%$). Assuming a normal distribution for both the height and wavelength, it can be found that 71.8% of the variability in bedform height lies within one standard deviation (σ_η) while 97.5% lies within $2\sigma_\eta$; whereas for bedform wavelength, 71.3% lies within one σ_λ and 95.4% within $2\sigma_\lambda$. Moreover, 100% of the variability lies within $\sim 6\,\sigma$; $\Delta\eta(t > t_e) \approx 34$ mm $\approx 4.9\,\sigma_\eta$ and $\Delta\lambda(t > t_e) \approx 0.43$ m $\approx 5.9\,\sigma_\lambda$. In addition, the distribution of bedform heights for the particular case of Experiment 55 shows a bimodal distribution (Figure 7.5a). However, based on the developmental behavior exhibited in Figures 7.1 and 7.2, it is evident that the bimodal distribution in bedform height is not real, and this is a consequence of the bed morphology was not being measured long enough within the equilibrium stage. Therefore, the bimodal distribution does not capture the true morphological behavior of the bedforms in Experiment 55. This is due to the fact that once the bed reached equilibrium conditions ($t > t_e$, to the right of the vertical line in Figure 7.1), the bedforms exhibited a gentle variation in their height, going first larger to smaller and then to large again ('sinusoidal oscillation' of the bedform height data for $t > 80$ min in Figure 7.1), which then stabilizes at the equilibrium value (inside the 95% interval confidence denoted by the gray-shaded areas in Figure 7.1). During this readjustment, the bed is overpopulated with bedforms just below and above the true equilibrium value ($\eta_e = 18.1$ mm vs $\mu_{\eta,1} = 10.6$ mm and $\mu_{\eta,1} = 20.2$ mm), which suggests that to capture the true bedform height distribution (i.e. bedform distibution peak similar to η_e) a longer time series may be required. Similar errors occur in other finite time series such as instantaneous velocity measurements, where a particular record length may be sufficient to obtain a mean value (e.i. η_e or λ_e) but inadequate to estimate higher order moments (e.g., Soulsby, 1980).

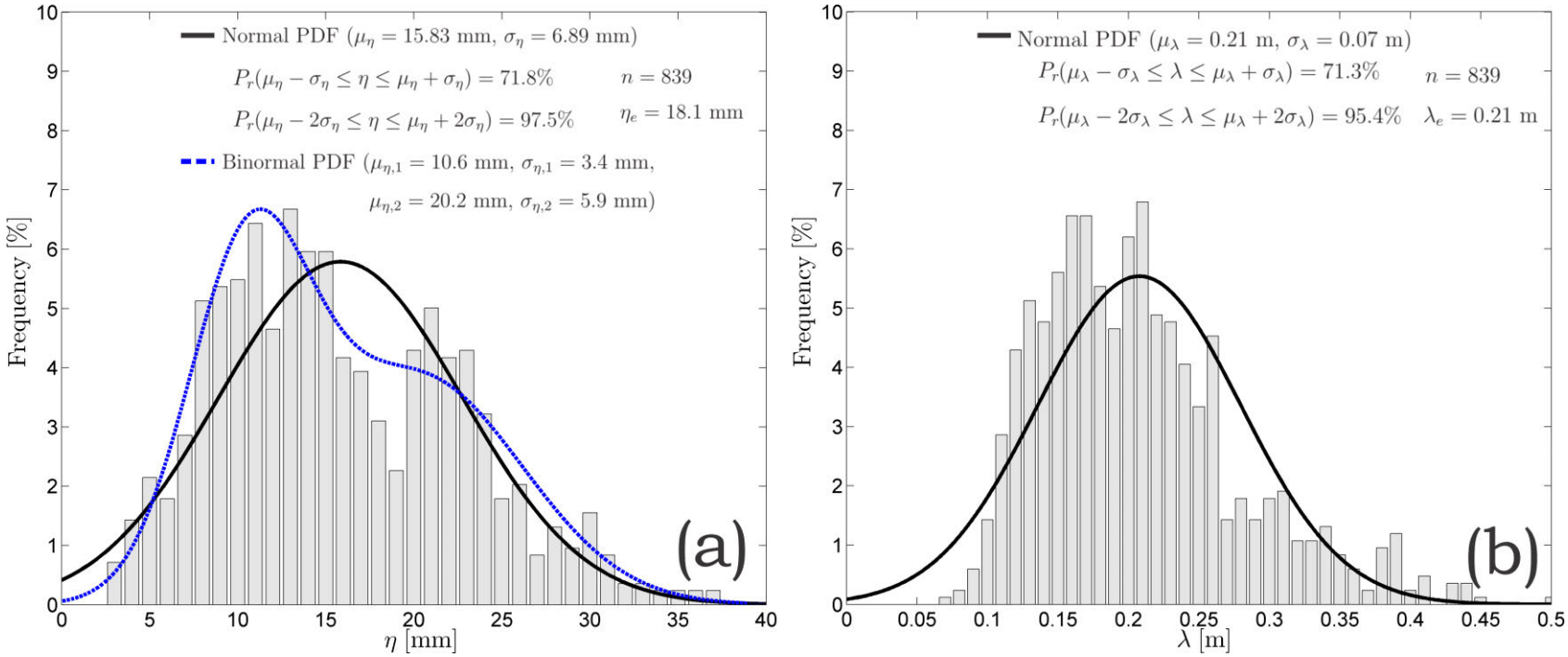

Figure 7.5: Histogram of a) bedform height and b) wavelength at equilibrium conditions ($t > t_e$) for a three-dimensional asymmetric current-ripple (Experiment 55). n is the number of measurements, P_r is the cumulative distribution function of the normal PDF (black line, Equations 7.8 and 7.9), η_e and λ_e are the equilibrium height and wavelength obtained by Equations 7.1 and 7.2. The unit interval for the bimodal distribution (blue line, Equations 7.10 and 7.11) was (a) $\vartheta = 0.458$.

7.3.2 Pure Oscillatory Flows

The development or growth of oscillatory bedforms exhibits the same general trend to that described by Lofquist (1978) and that previously discussed herein for unidirectional flows (section 7.3.1). Furthermore, the development of bedform height and wavelength showed the same characteristic asymptotic growth for all types of pure oscillatory flow bedforms (see Chapter 5) regardless of their final stable planform geometry (i.e., 2D = continuous and straight creastlines and 3D = discontinuous and curved creastlines). Therefore, Equations 7.1 and 7.2 were used to characterize bedform development from an initially flat bed to two characteristic bed configurations: (i) 2D symmetrical ripples (Experiment 30, Figure 7.6) and (ii) 3D symmetrical ripples (Experiment 18, Figure 7.7). These fits (red lines) and their 95% confidence intervals (gray-shaded area) are plotted in Figures 7.6 and 7.7. The mean R^2 value obtained by the fits for all the pure oscillatory bedform datasets was 0.78 (Table 7.1) with an averaged p-value of 0.02 (Appendix B), which is, in general, a better overall fit than the mean R^2 value for unidirectional flows bedforms (0.72, Table 7.1; The experiments of Baas (1993) had a mean $R^2 = 0.70$). The better performance of Equations 7.1-7.2 to predict the overall development of the pure oscillatory bedforms is mainly driven by the high R^2 obtained for the two-dimensional bed configurations. The mean R^2 value obtained for all the 2D oscillatory bed morphologies (Experiments 1, 8 and 30; Table 7.1) was 0.9 with an averaged p-value of 0.008 (Appendix B), whereas for the 3D oscillatory bedforms the R^2 values ranged from 0.45 to 0.62 with an averaged p-value of 0.02. Equations 7.1 and 7.2 provide a better representation of the 2D bed morphologies due to the low variability (only 18.3% of the data lie outside of the 95% confident intervals) that occurs once the bed reaches equilibrium conditions (i.e., to the right of the vertical line in Figure 7.6). However, for the case of three-dimensional bedforms, the scatter was much larger, with almost 50% of the data lying outside of the 95% confidence intervals. The variability of the three-dimensional bedforms can be explained by the dynamic migration, separation and amalgamation of the

bed features, a situation that is absent in the two-dimensional case (Figure 7.8).

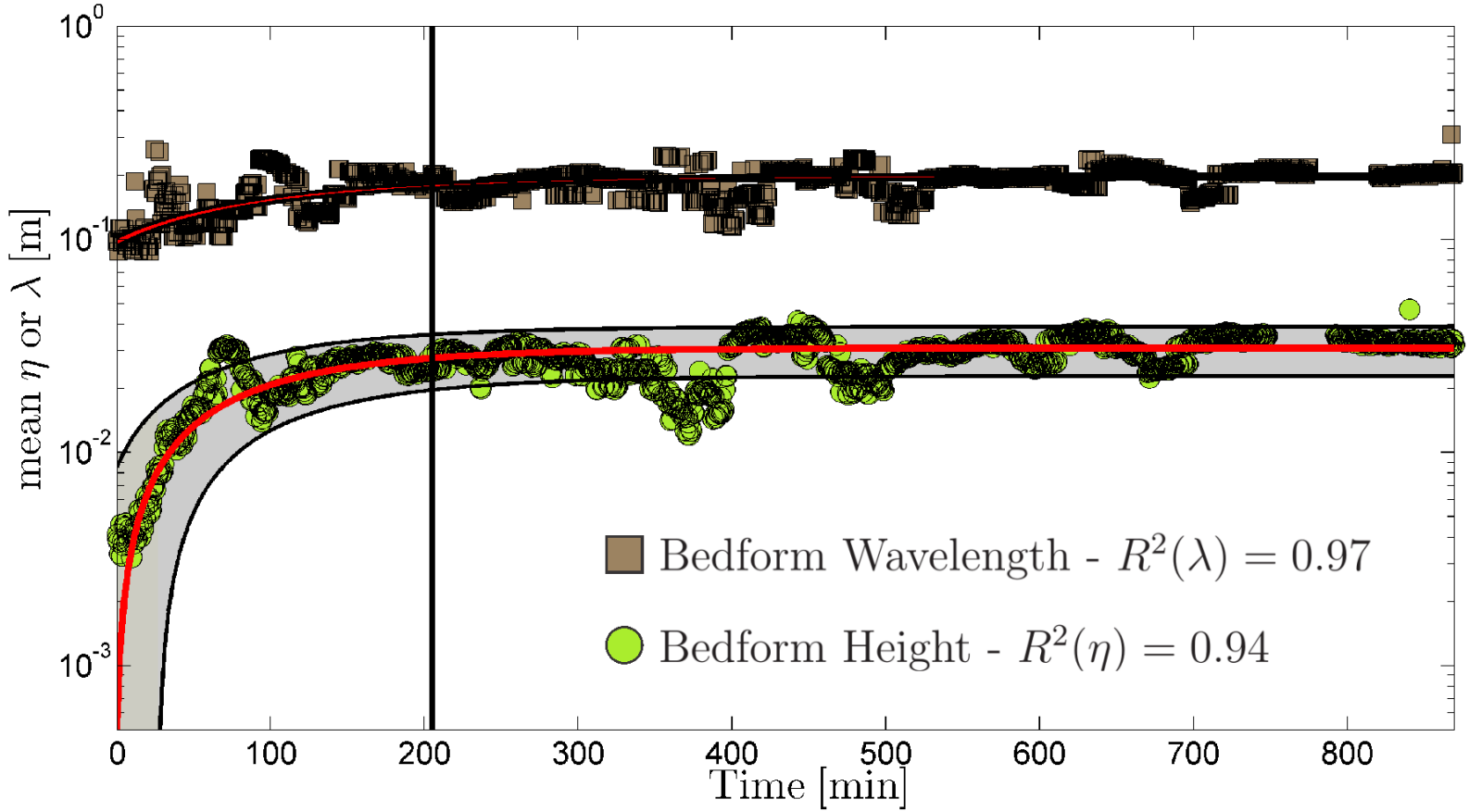

Figure 7.6: Development of bedform wavelength and height on an initially flat bed for pure oscillatory flow (Experiment 30, $t_e = 4.23$ hr). The equilibrium time, t_e, is denoted by the vertical line. $R^2(\lambda)$ and $R^2(\eta)$ are the correlation coefficients for the bedform wavelength and bedform height, respectively, obtained by fitting Equations 7.1 and 7.2. The gray-shaded area represents the 95% confidence interval of the fitted function. Bed morphology at equilibrium = Two-dimensional Symmetrical Ripple (2D SR).

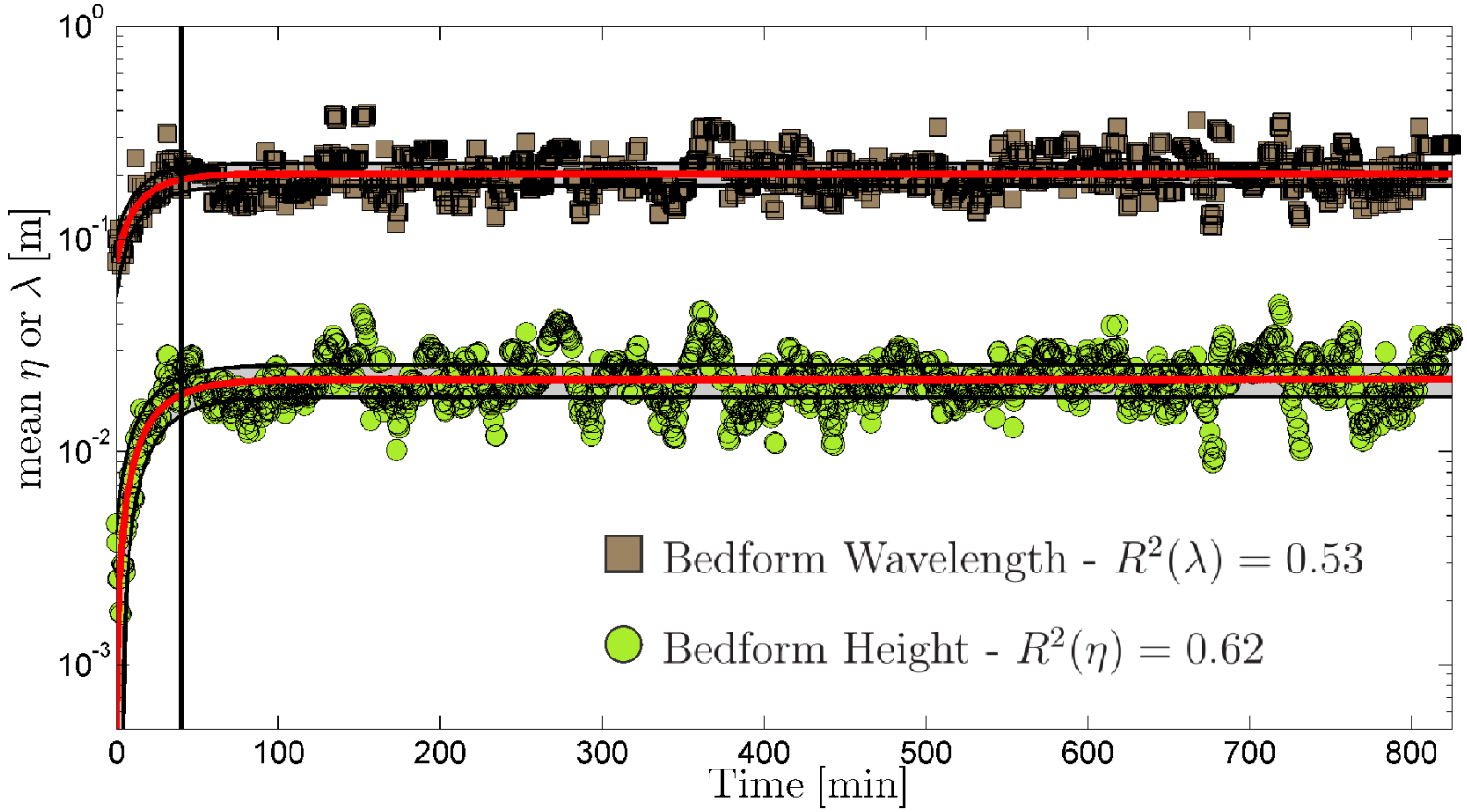

Figure 7.7: Development of bedform wavelength and height on an initially flat bed for pure oscillatory flow (Experiment 18, $t_e = 0.67$ hr). The equilibrium time, t_e, is denoted by the vertical line. $R^2(\lambda)$ and $R^2(\eta)$ are the correlation coefficients for the bedform wavelength and bedform height, respectively, obtained by fitting Equations 7.1 and 7.2. The gray-shaded area represents the 95% confidence interval of the fitted function. Bed morphology at equilibrium = Three-dimensional Symmetrical Ripple (3D SR).

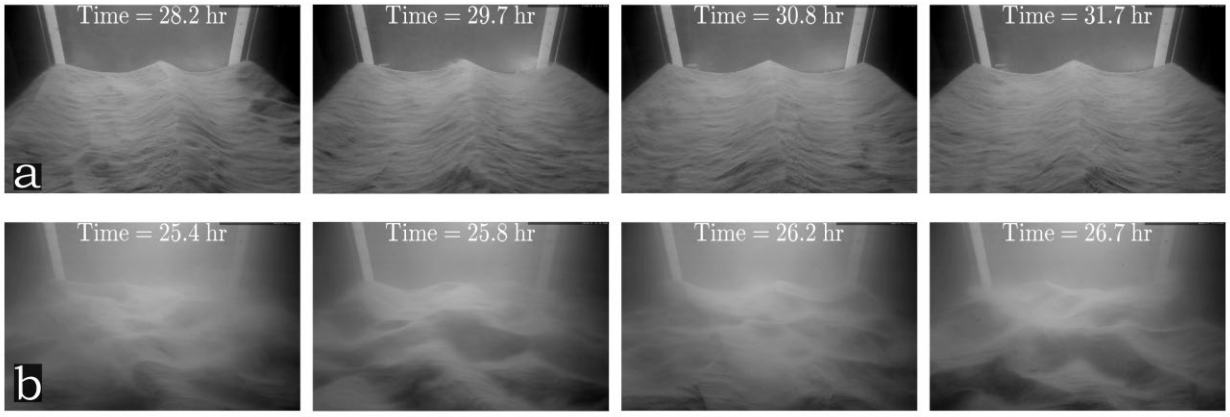

Figure 7.8: Stable (a) or dynamic (b) equilibrium conditions for pure oscillatory bedforms. The window on the back of the picture is 0.60 m wide. (a) Sequence of photographs showing the absence of change during the equilibrium stages of Experiment 30 along a 3.5 hrs of bed-flow equilibrium conditions. (b) Sequence of photographs showing the diversity of bedforms and an active movable bed (Experiment 18).

The development stages under pure oscillatory flows are the same as those described for unidirectional bedforms (Section 7.3.1; Figures 7.9 and 7.10): (1) incipient bedforms, (2) growing bedforms, (3) stabilizing bedforms, and (4) fully-developed bedforms. However, the main difference between oscillatory and unidirectional flows lies in the morphological aspects of the bedforms.

Stage 1 - Incipient Bedforms

Like unidirectional flows, Stage 1 started with the initiation of sediment transport on an initially flat bed, until the first signs of bedform growth (Figures 7.9-7.10). A series of small incipient bedforms started to propagate from the walls (Figure 7.11) or the center of the flume (Figure 7.12) once sediment had been entrained. For the case of the experiments where the bedform initiation was controlled by the wall, the incipient bedforms did not reflect the true interactions between the flow and the bed, and hence such experiments are ignored for the discussion on this development stage. However, once the bed was fully covered with bed features (e.g., Figure 7.11f), the bed evolved in stages where its development reflected the true behavior of the phenomenon.

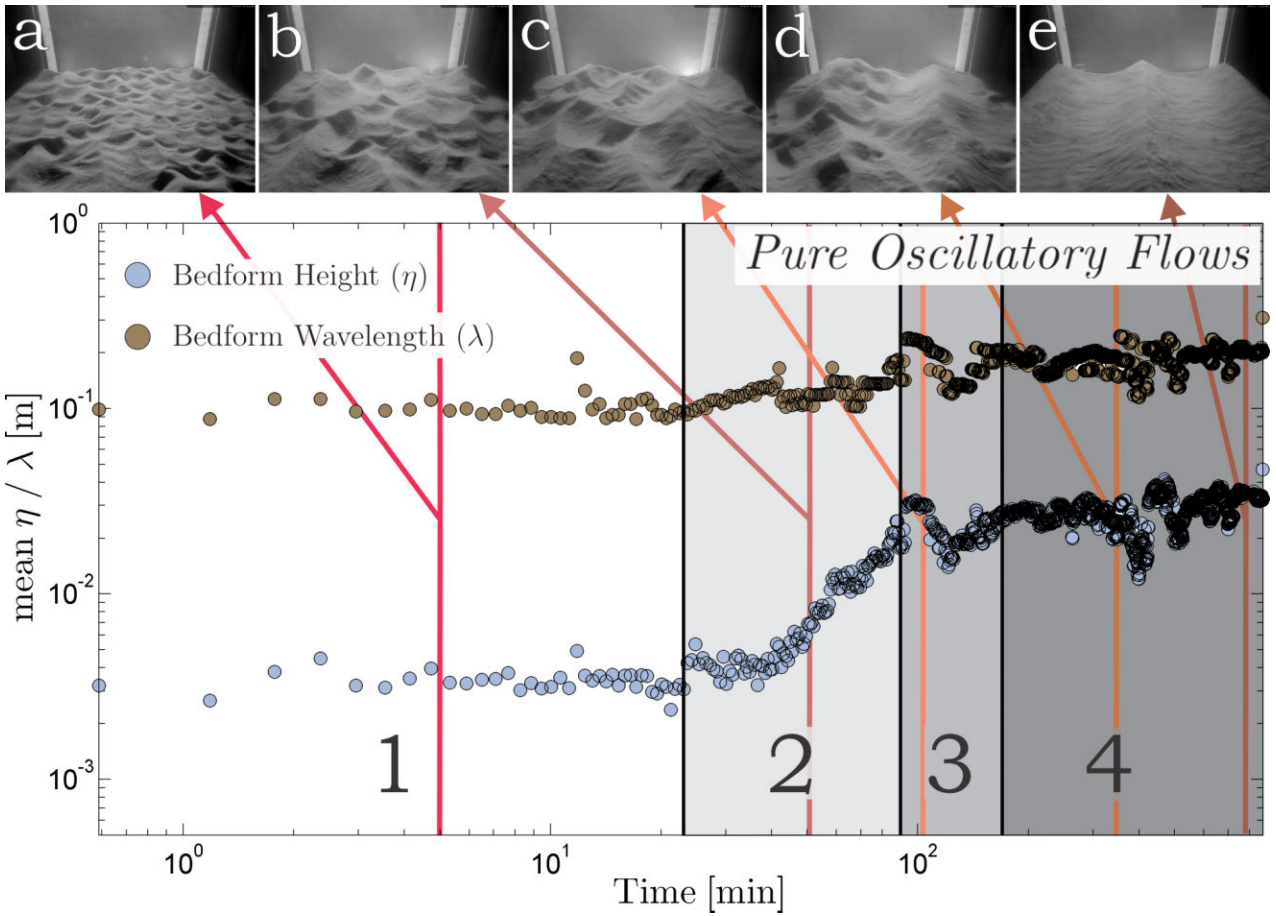

Figure 7.9: Spatially-averaged bedform height and wavelength plotted against time for a two-dimensional symmetric ripple (Experiment 30). The numbers at the base of the diagram indicate development stages: (1) incipient ripples (white box); (2) growing bedforms (light-gray box); (3) stabilizing bedforms (gray box); and (4) fully-developed bedforms (dark-gray box). The vertical line dividing boxes 3 and 4 marks the equilibrium time at $t_e = 255.6$ min. Both axes have a log-normal scale. A series of photos were taken at (a) $t = 4.9$ min, (b) $t = 51.2$ min, (c) $t = 107.4$ min, (d) $t = 410.1$ min and (e) $t = 810.2$ min; and are denoted by the different colored arrows. The window on the back of the picture is 0.60 m wide. Note that photographs (d) and (e) were both taken during Stage 4 where the wavelength and height were at equilibrium, yet the planform in (d) was not yet fully-developed.

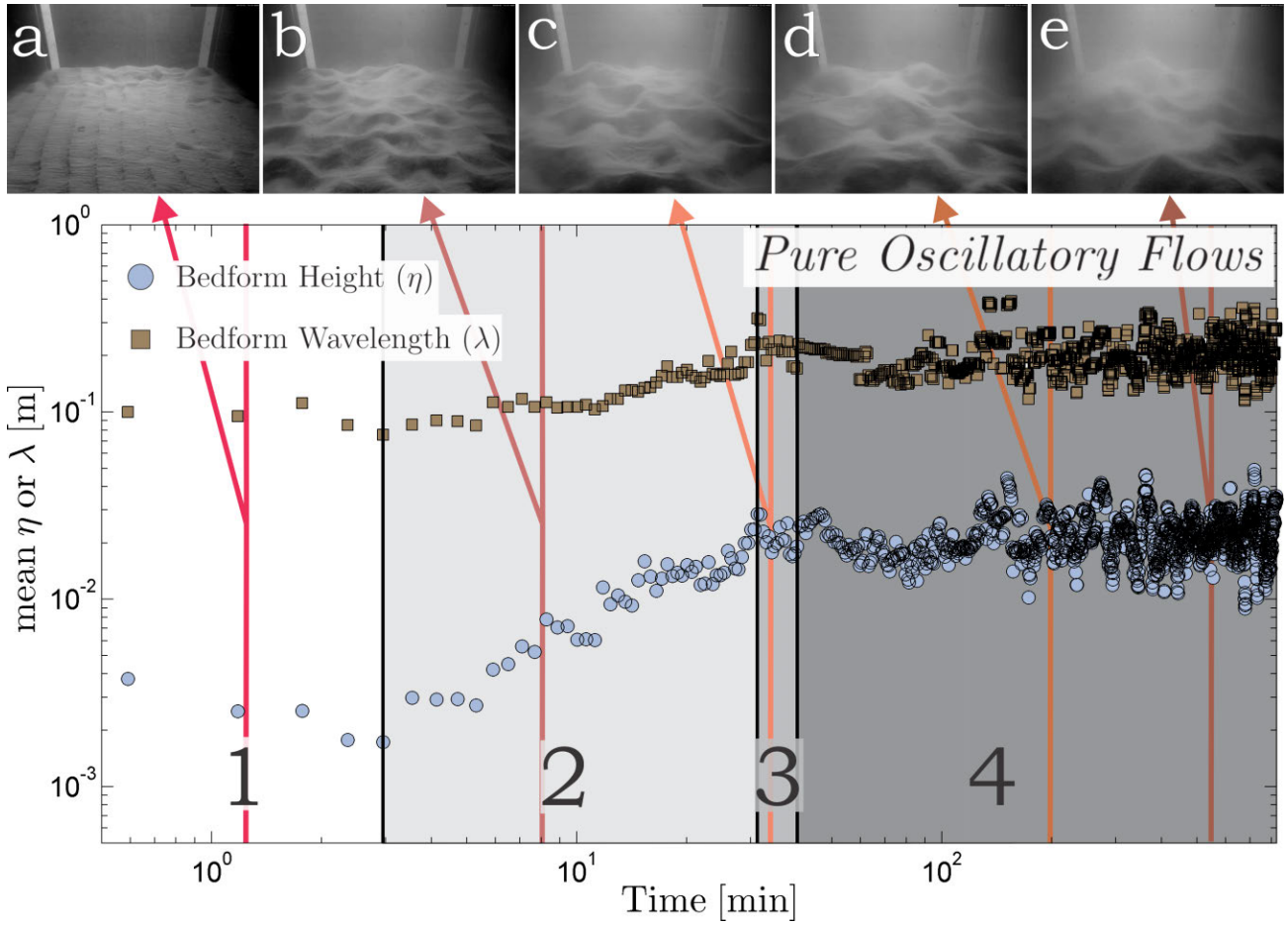

Figure 7.10: Spatially-averaged bedform height and wavelength plotted against time for a three-dimensional symmetric ripple (Experiment 18). The numbers at the base of the diagram indicate development stages: (1) incipient ripples (white box); (2) growing bedforms (light-gray box); (3) stabilizing bedforms (gray box); and (4) fully-developed bedforms (dark-gray box). The vertical line dividing boxes 3 and 4 marks the equilibrium time at $t_e = 44.4$ min. Both axes have a log-normal scale. A series of photos were taken at (a) $t = 1.25$ min, (b) $t = 8.15$ min, (c) $t = 34.5$ min, (d) $t = 199.4$ min and (e) $t = 548.4$ min; and are denoted by the different colored arrows. The window on the back of the picture is 0.60 m wide. Note how the picture becomes more blurred due to the increase in sediment suspension from a-e.

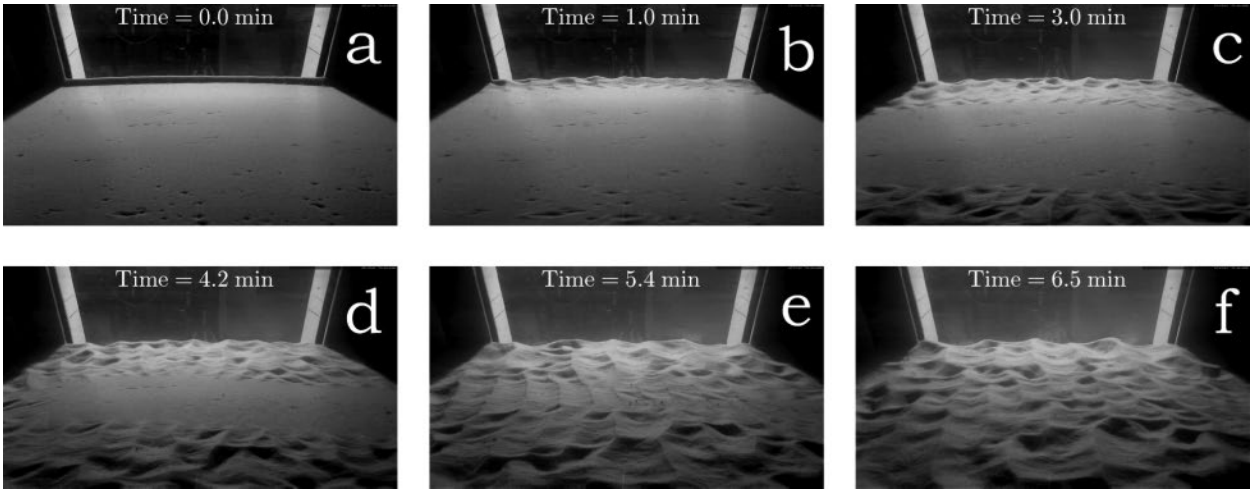

Figure 7.11: Incipient bedforms at the first stage of development for a two-dimensional symmetric oscillatory-ripple (Experiment 01). The window on the back of the picture is 0.60 m wide.

For the flow conditions where the bed morphology did not develop from wall-defects, the predominant morphological features during this early stage were two-dimensional rolling grain ripples. Rolling-grain ripples appeared on the initially plane bed within only a few wave cycles (3 wave cycles for the case of Experiment 18; Figure 7.12). These results are consistent with other studies under pure oscillatory flow, which describe rolling-grain ripples as the first bed state to generate from a flat bed (e.g., Bagnold, 1946; Lofquist, 1978; Pedocchi, 2009). These rolling-grain ripples exhibited their characteristic alternation of crestline direction from upstream to downstream during every cycle (Figure 7.12). In addition, unlike the classification proposed by Baas (1994), the planform geometry changed within this first stage. Figure 7.12 shows the development from a very short early three-dimensional stage (Figure 7.12:c-d) to a more stable two-dimensional set of rolling grain ripples.

Stage 2 - Growing Bedforms

No difference was found between unidirectional and oscillatory flow conditions regarding the mechanisms of bedform growth. The bedforms grew in size by a combination of sediment capturing and amalgamation with nearby bedforms (Figure 7.10b). However, during this

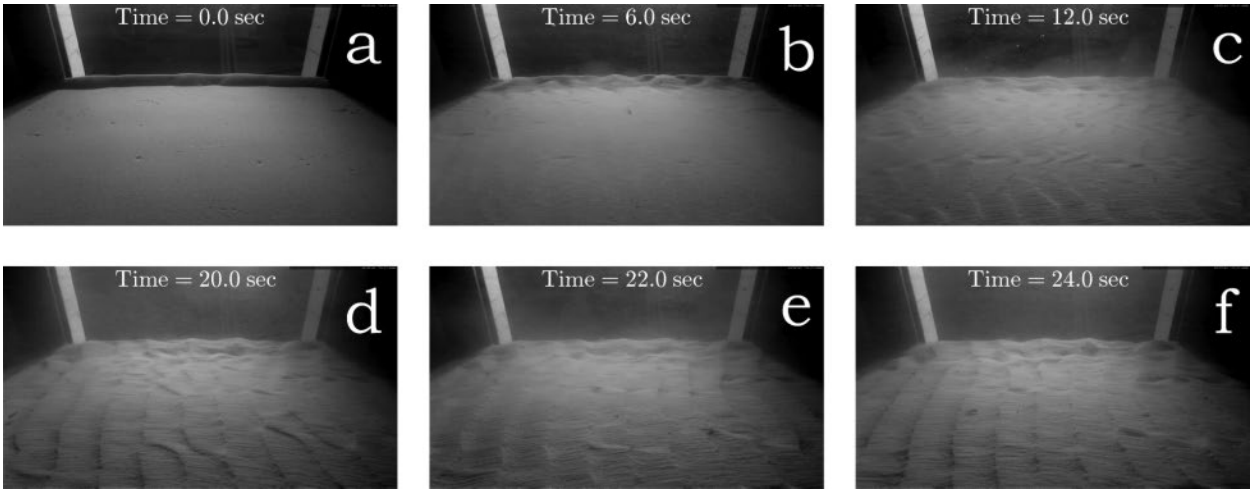

Figure 7.12: Incipient bedforms at the first stage of development for a three-dimensional symmetric oscillatory-ripple (Experiment 18). Note the change in direction from upstream to downstream oriented crestlines. The window on the back of the picture is 0.60 m wide.

stage, the bed configuration quickly transitioned from rolling grain ripples to small three-dimensional vortex ripples within a few minutes (Figure 7.13). Once this transition occurred, the bed remained populated with three-dimensional vortex ripples unless the stable configuration is two-dimensional, and hence the bed rearranged its planform geometry to become two-dimensional (Figures 7.9 and 7.10). The growth occurring during this stage accounted for $\sim 93\%$ of the total bedform enlargement. This result is consistent with the experiments reported under unidirectional flows ($\sim 85\%$; Section 7.3.1) and by Baas (1994) ($\sim 75\%$), which show that the large majority of overall growth occurs in this stage.

Stage 3 - Stabilizing Bedforms

Under oscillatory flow conditions, resembling those occurring under unidirectional flows (section 7.3.1), Stage 3 was also defined as the temporal gap that occurs in the interval between the moment when the asymptotic growth ends and the time when the bed reached equilibrium conditions (Figures 7.9 and 7.10). The rate at which oscillatory bedforms grew during Stage 3 is significantly lower than Stage 2, and less than that observed for unidirectional flows. The mean overall growth during Stage 3 was $\sim 5\%$ of the overall growth (Figures

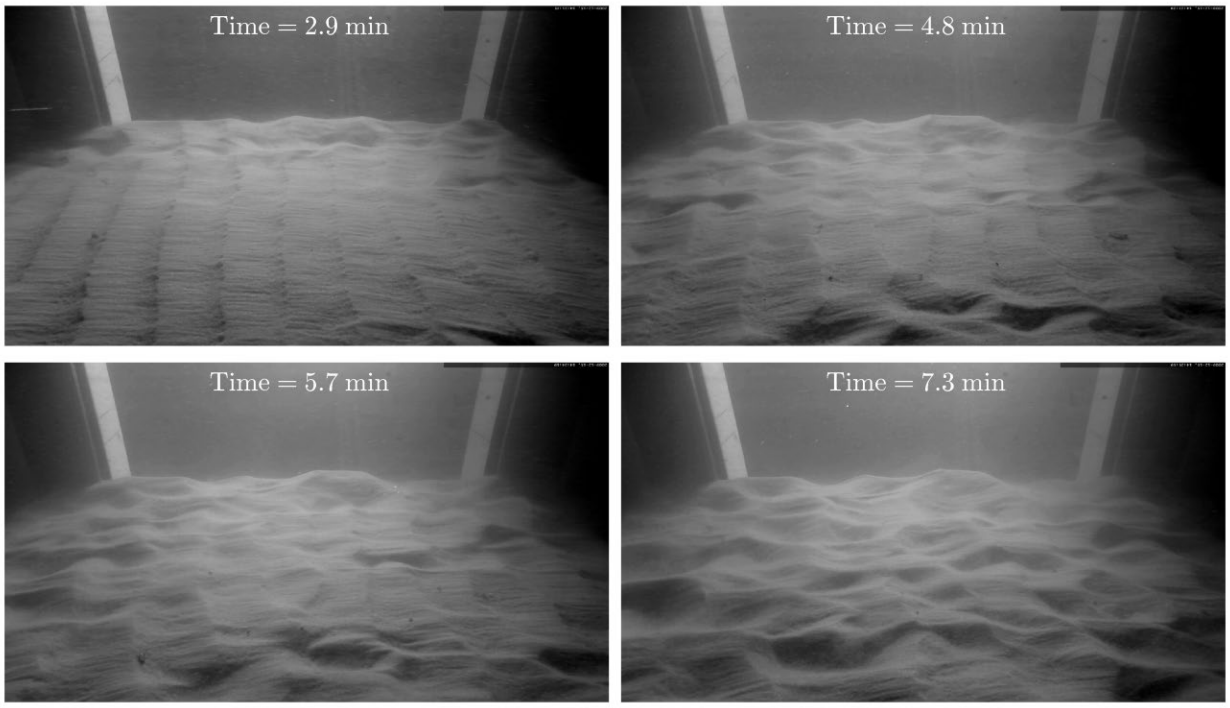

Figure 7.13: Development Stage 2 - Transition between rolling grain ripples to small three-dimensional vortex ripples (Experiment 18). The window on the back of the picture is 0.60 m wide.

7.6-7.10), about half of that observed for unidirectional flow bedforms (section 7.3.1). However, this result is consistent with the observations seen in Stage 2, in which there was a greater percentage growth under oscillatory than unidirectional flows ($\sim$ 93% vs $\sim$ 85%; Section 7.3.1).

Stage 4 - Fully-developed Bedforms

Unlike the unidirectional flow bed morphologies, oscillatory bedforms exhibited two different stable planform bed configurations: two-dimensional and three-dimensional (Chapter 5). In the previous development stages (Stages 1 to 3; Figure 7.9), there was no difference in the development history between bedforms that displayed a stable two-dimensional configuration or a three-dimensional configuration. However, for the case of the 'fully-developed' bedform stage, the fundamental change in the planform geometry (i.e. 2D vs 3D) showed significant

differences. It is important to note that the two-dimensional stable planform bed configurations occurred under oscillatory flow conditions that obeyed the empirical relationship of Pedocchi and García (2009b)

$$D_* = Re_p^{2/3} > 0.15\, Re_w^{1/3} \quad \Rightarrow \quad \frac{D_*}{Re_w^{1/3}} > 0.15 \tag{7.12}$$

where D_* is a dimensionless grain size

$$D_* = \left(\frac{g\,R}{\nu^2}\right)^{1/3} D_{50} \tag{7.13}$$

and Re_w is the wave Reynolds number

$$Re_w = \frac{U_o\,A}{\nu}. \tag{7.14}$$

Two-Dimensional bedforms

There are two main reasons why two-dimensional oscillatory bedforms are different or behave differently to three-dimensional bedforms during the fourth stage of development. One of these is the temporal lag in the development history of 2D oscillatory bedforms between the time required for these bedforms to reach equilibrium sizes (i.e., $\eta_t \sim 0.9\,\eta_e$ and $\lambda_t \sim 0.9\,\lambda_e$) and the time to reach equilibrium planform geometry (i.e., the time for the bed to be fully 2D; video Ch07 - 01*: T06O25U00_Develop.wmv* from Appendix A.1.2 and Table 7.2). For example, during the fourth development stage for Experiment 30 (dark-gray box; Figure 7.9), the bed reached size equilibrium after 253.8 min from the initiation of the experiment, although the bed did not achieve a fully two-dimensional planform configuration until 738.6 min (Table 7.2). Similarly, Figure 7.14 shows a sequence of photographs during the planform geometry equilibrium transition for Experiment 1, where the bed was at size equilibrium ($t > t_e = 132$min), but did not exhibit a fully two-dimensional planform configuration until 141 min (bottom two photographs in Figure 7.14).

Table 7.2: Summary of equilibrium times of size and planform geometry for the bedform experiments with stable two-dimensional planform geometries.

#	T (s)	U_o ($m\,s^{-1}$)	U_u ($m\,s^{-1}$)	η_e [a] (mm)	λ_e [a] (m)	D_* [b]	Re_w [c] $\times 10^4$	$\frac{D_*}{Re_w^{1/3}}$ [d]	q_s [e] ($cm^2\,s^{-1}$)	t_e [f] (hr)	t_{pg} [g] (hr)	t_t [h] (hr)	Bedform[i] Type
1	4	0.25	0.00	34.8	0.22	6.06	3.73	0.18	14.9	2.21	2.3	5.1	SR
8	5	0.20	0.00	35.3	0.21	6.36	3.21	0.20	17.2	4.15	20.6	37.7	SR
30	6	0.25	0.00	32.1	0.20	6.31	5.95	0.16	16.1	4.23	12.3	14.5	SR

[a] Values obtained by fitting Equation 7.1 and Equation 7.2 to the experimental data.
[b] Dimensionless grain size (Equation 7.13). [c] Wave Reynolds Number (Equation 7.14).
[d] Empirical relationship by Pedocchi and García (2009b) = 2D > 0.15 > 3D (Equation 7.12)
[e] Bedload transport per unit width (Section 4.3.2).
[f] Time until size equilibrium obtained from Equation 7.7.
[g] Time until planform geometry equilibrium.
[h] Duration of experiment. [f]SR = 2D Symmetric Ripples.

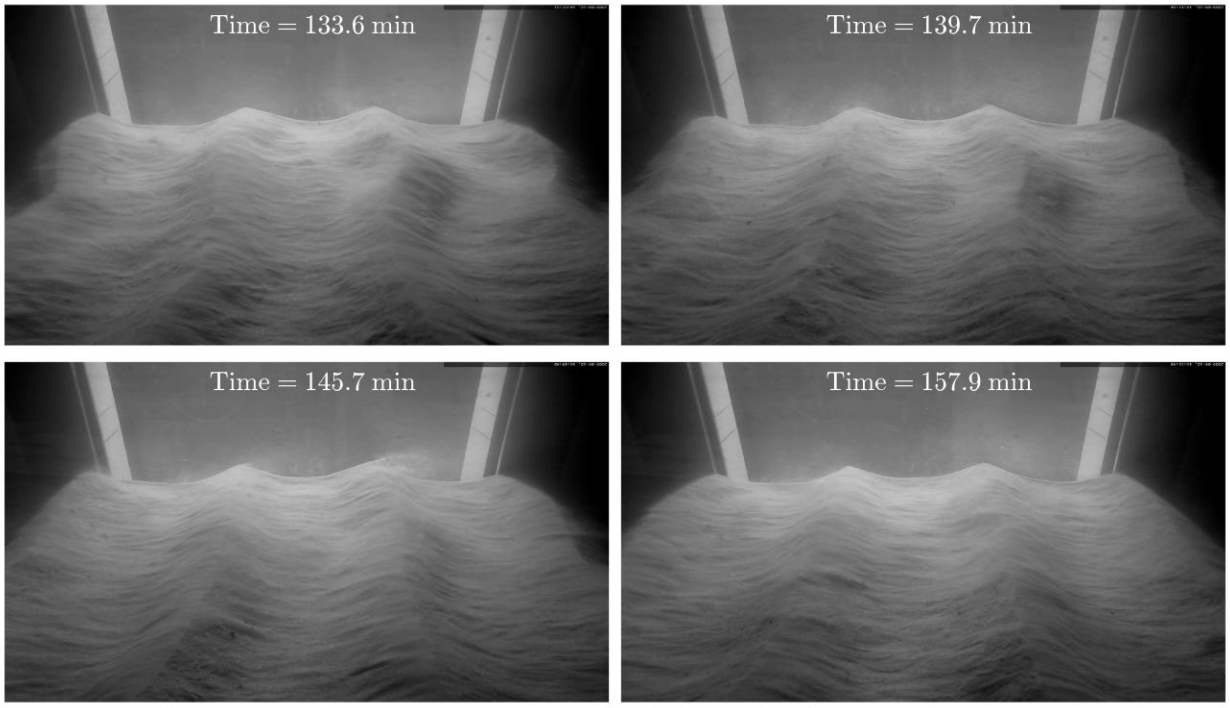

Figure 7.14: Transition between 2.5 to 2D oscillatory ripples during the fourth stage of development (Experiment 1). Flow-size equilibrium was obtain at $t_e \sim 132$ min, whereas the flow-planform geometry equilibrium was achieved $t_{pg} \sim 141$ min (Table 7.2). The window on the back of the picture is 0.60 m wide.

After detailed examination of the development curves (e.g., Figure 7.9) and the photographs taken from the side window (e.g., Figure 7.14), it was observed that by the time the bed reached size-equilibrium ($t = t_e$) the crest of the bedforms still possessed numerous defects (Figure 7.9c). This presence of defects prevents the bed from being fully two-dimensional, since lateral discontinuities in the crestline produce different flow velocities, which then induce differential sediment transport (e.g., Chapter 5, Venditti et al., 2005b). Thus, additional time is necessary in order to fully reshape the bed from the three-dimensional configuration (multiple defects on the bedform crest) to the final two-dimensional configuration (very few defects on the bedform crest; Figure 7.14).

Pedocchi and García (2009b) discuss that the stability of two-dimensional bedforms lies in the ratio between grain sizes D_* and wave Reynolds numbers Re_w (Equation 7.12). Equation 7.12 implies that the larger the grain size becomes (D_*) and/or the smaller the turbulence (Re_w) is, the more likely the bedform will be two-dimensional. This ratio can be understood in this manner; the larger the grain size (D_s), the least susceptible it will be to turbulent fluctuations (the flow is three-dimensional in nature; e.g., Carstensen et al., 2010) and the more responsive it will be to the mean pure-oscillatory flow (2D motion), thus becoming more two-dimensional. This grain size behavior is consistent with results by other researchers that two-dimensional bedforms are predominately formed in coarser sands (e.g., Southard, 1991; O'Donoghue and Clubb, 2001; O'Donoghue et al., 2006). However, the larger the grain size, the harder it is to move the sediment (i.e., higher shear stress), and thus the longer it will take to reshape the bedforms into a two-dimensional form. This result can even be seen within the limited datan available (Table 7.2). Equation 7.15 is a linear fit of the planform equilibrium time, t_{pg}, as a function of the dimensionless grain size D_*. Equation 7.15 implies that for larger D_* longer planform equilibrium times t_{pg} are required to reach a stable two-dimensional bed configuration

$$t_{pg} = 54\, D_* - 326 \tag{7.15}$$

(black line in Figure 7.15). However, it is important to state that Equation 7.15 is estimated using only 3 data points (Table 7.2), which are enough to perform a linear regression, yet not sufficient to capture the true behavior of the system. Therefore, Equation 7.15 should not be considered as the true relationship, but just as an overall guide that describes the observed trends between variables. Another indicator that Equation 7.15 is not the true formulation to encapture the relationship is the fact that it predicts negative values of t_{pg} for grain sizes smaller than $D_* < 6.03$, a result that lacks any physical grounding.

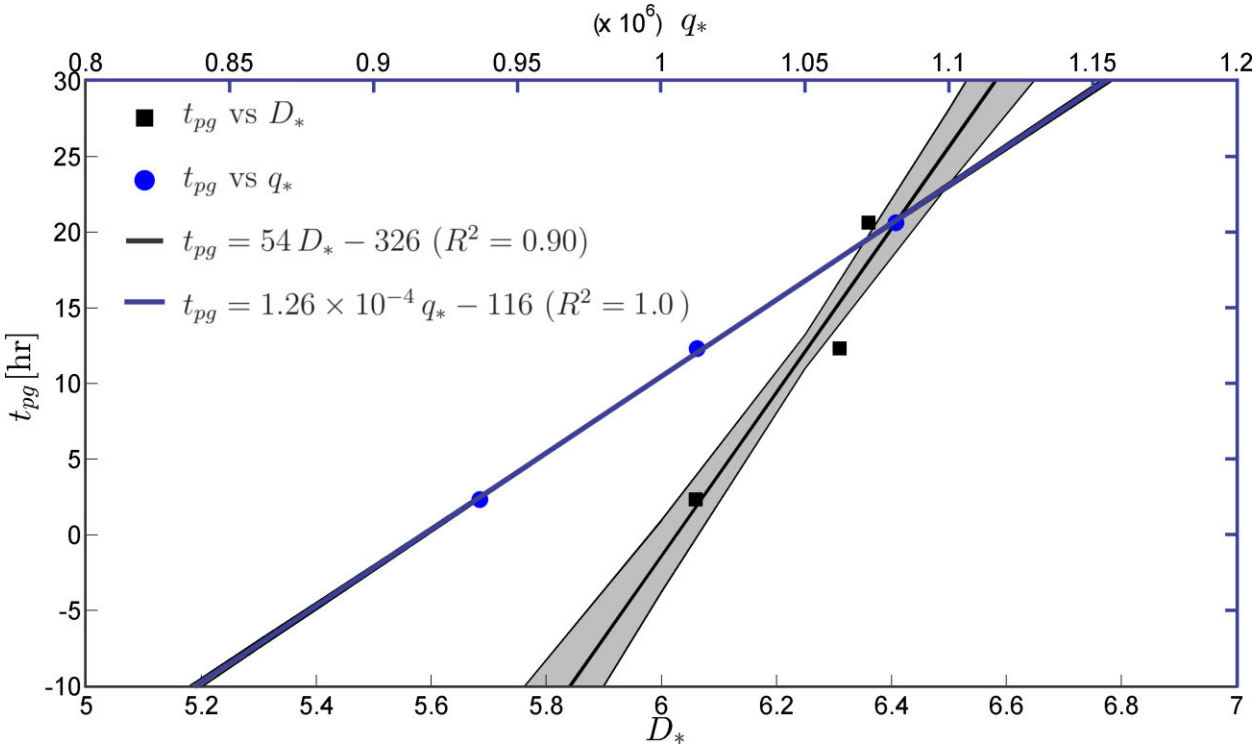

Figure 7.15: Planform equilibrium time (t_{pg}) as a function of the dimensionless grain size ($D_* = (g\,R/\nu^2)^{1/3}\;D_{50}$; black axis) and the dimensionless bedload sediment transport ($q_* = q_s/\sqrt{g\;R\;D_{50}}\;D_{50}$; blue axis). Solid line represent a potential (linear) relationship between the three data points available. R^2 values are the correlation coefficient obtained by fitting Equations 7.15 and 7.16. The gray-shaded area represents the 95% confidence interval of the fitted function.

Furthermore, following the same limited linear regression analysis, the time required to reach two-dimensional planform geometry can also be linked with the sediment transport by the dimensionless bedload sediment transport q_* (blue line in Figure 7.15). If the good

correlation between t_{pg} and q_* ($R^2 = 1.0$) implies causation, it can be inferred that for two-dimensional oscillatory bedforms (Equation 7.12), the greater the sediment transport, the longer it will take the bedforms to reach planform equilibrium conditions (Figure 7.15)

$$t_{pg} = 1.26 \times 10^{-4} q_* - 116. \tag{7.16}$$

The planform geometry equilibrium time should not be confused with the size equilibrium time t_e, which exhibits an inverse relationship; higher sediment transport equates to a smaller equilibrium time (Section 7.4). Yet, since the nature of sand transport is far from homogeneous along the bed, a relatively high transport rate will produce differential transport along the bed. Hence, relatively high sediment transport rates will populate the bedform crests with multiple defects (Figure 7.9c), and therefore additional time will be required to fully reshape the bed to the final two-dimensional configuration (very few defects on the bedform crest; Figure 7.14).

The second main reason for the differential behavior of two-dimensional oscillatory bedforms is that they exhibit very little variability once the bed reached size-equilibrium conditions, regardless of the planform geometry ($t \geq t_e$; right of the vertical line Figure 7.6). Figure 7.14 shows a sequence of photographs during size-equilibrium conditions ($t > t_e =$ 132min) for Experiment 1. Despite the difference in planform geometry through time, the overall wavelength and height remained the same along the nearly 30 min of duration portrayed in Figure 7.14. Figures 7.6 and 7.16 show the spatially-averaged wavelength and height as a function of time, where the very small temporal variations for equilibrium conditions ($t \geq t_e$; right of the vertical line) are reflected by the good coverage of the 95% confidence interval of the Equations 7.1 and 7.2 fits (gray-shaded area).

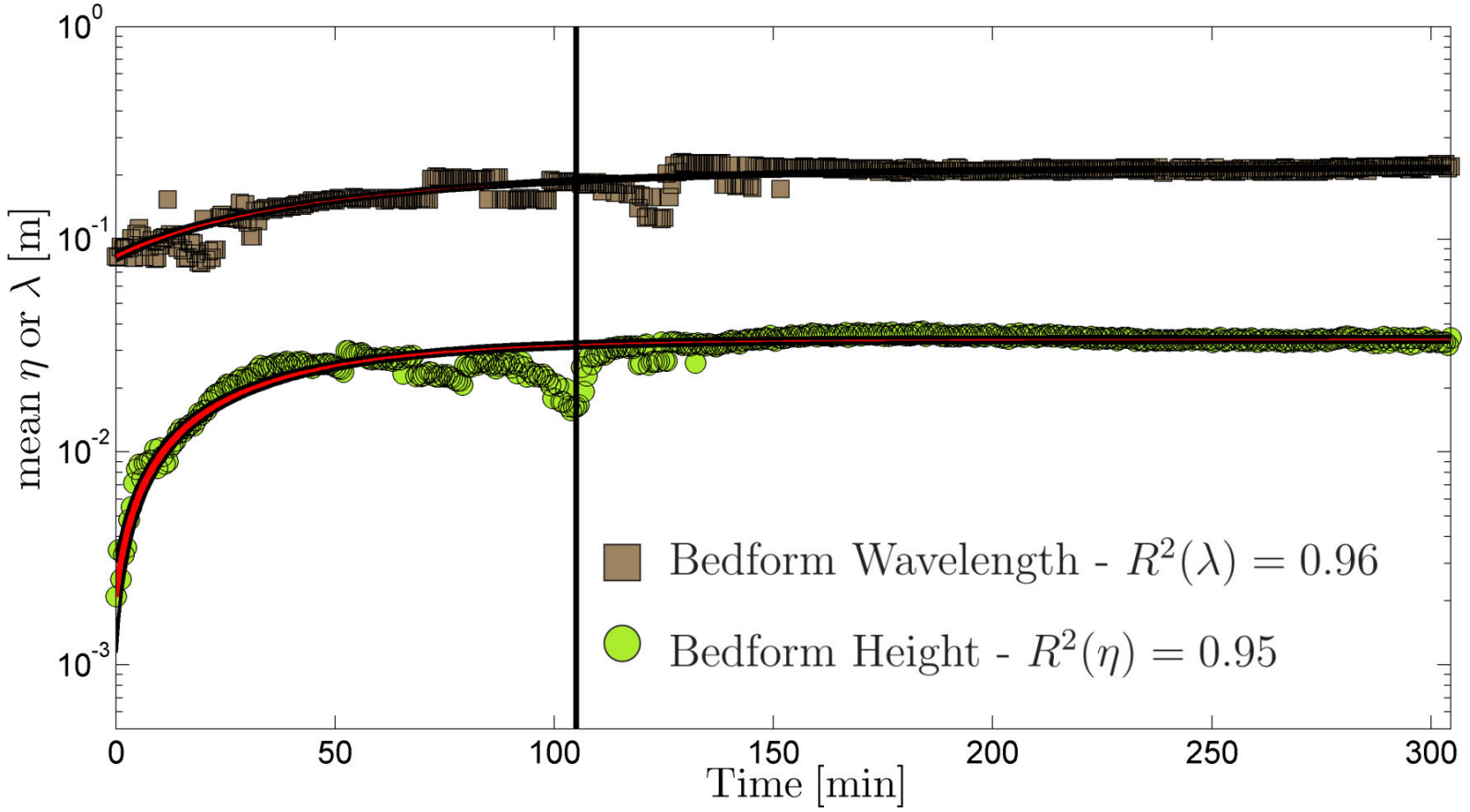

Figure 7.16: Development of bedform wavelength and height on an initially flat bed for pure oscillatory flow (Experiment 1 t_e = 2.21 hr). The equilibrium time, t_e, is denoted by the vertical line. $R^2(\lambda)$ and $R^2(\eta)$ are the correlation coefficients for the bedform wavelength and bedform height respectively obtained by fitting Equations 7.1 and 7.2. The gray-shaded area represents the 95% confidence interval of the fitted function. Bed morphology at equilibrium = Two-dimensional Symmetrical Ripple (2D SR).

Figure 7.17 displays the histogram of the recorded heights (Figure 7.17a) and wavelengths (Figure 7.17b) for all equilibrium bedforms for a two-dimensional symmetric oscillatory-ripple (Experiment 1). Both the distribution of bedform heights (Figure 7.17a) and wavelengths (Figure 7.17b) show very little signs of temporal variations of the spatially-averaged wavelength or height once the bed reached an equilibrium state (e.g., $\sigma_\eta/\mu_\eta \times 100 \sim 7.3\%$ and $\sigma_\lambda/\mu_\lambda \times 100 \sim 9.3\%$). Assuming a normal distribution for both the height and wavelength, it can be found that 80.9% of variability of bedform height lies within one standard deviation (σ_η), and 98.5% lies within $2\sigma_\eta$; whereas for bedform wavelength, 77.1% lies within one σ_λ and 97.1% within $2\sigma_\lambda$. Moreover, 100% of the variability lies within $\sim 7.5\,\sigma$; $\Delta\eta(t > t_e) \approx 15.0$ mm $\approx 5.6\,\sigma_\eta$ and $\Delta\lambda(t > t_e) \approx 0.22$ m $\approx 7.5\,\sigma_\lambda$.

The narrow spectrum of bed morphologies for two-dimensional oscillatory bedforms can be explained by the relatively fixed position of the bedforms once the bed reached equilibrium conditions (e.g., Figure 7.14). During the time interval between size equilibrium and planform equilibrium a few fluctuations (e.g., Figure 7.9) were recorded since the bed was still moving (e.g., Figure 7.14). However, this migration culminated when the bed reached a full two-dimensional planform geometry, where no further change in height and wavelength is recorded. The bedform wavelength and height present at the bed during this stage will persist until the flow conditions are changed, and then the bed will break the two-dimensionality to rearrange itself to a new equilibrium stage that is stable with the new flow condition. This behavior is a fundamental characteristic of two-dimensional oscillatory ripples, and is not seen in any other type of flow type or bedform.

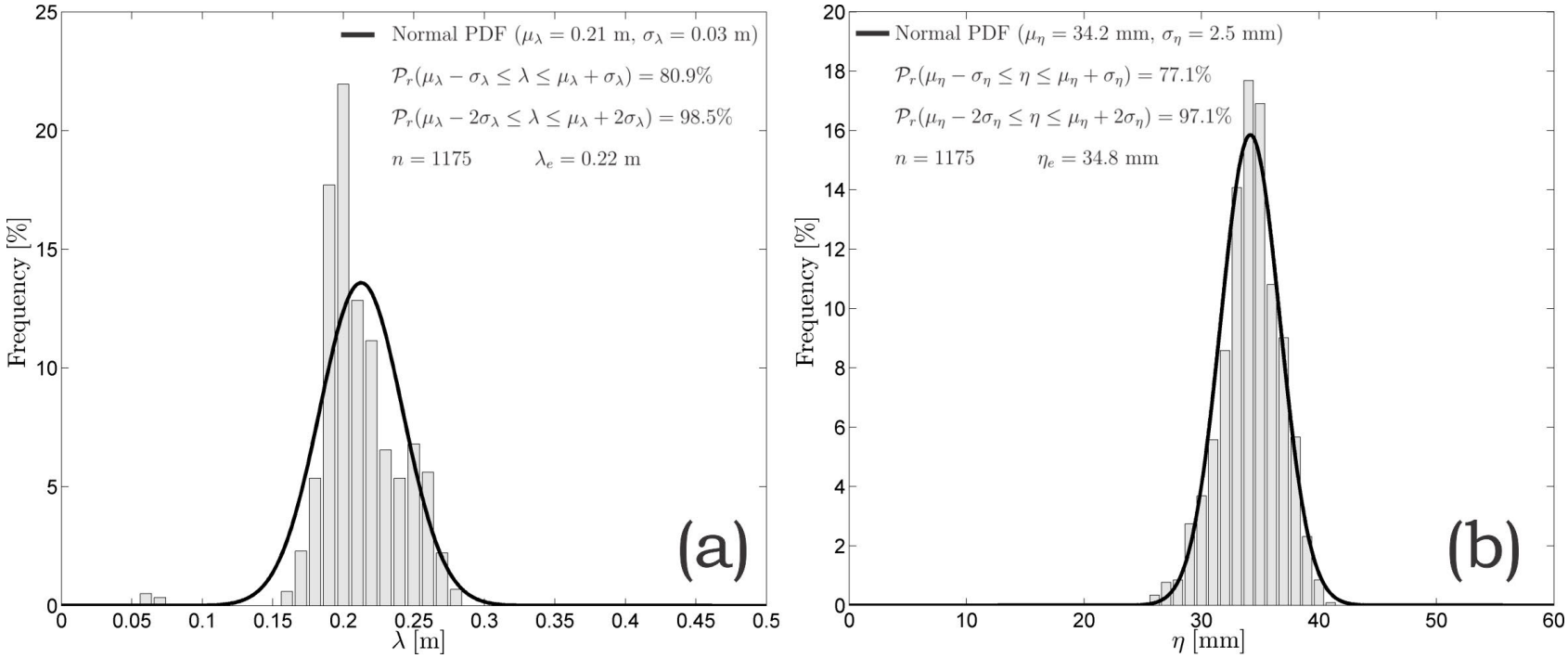

Figure 7.17: Histogram of bedform a) height and b) wavelength at equilibrium conditions ($t > t_e$) for two-dimensional symmetric oscillatory-ripples (Experiment 01). n is the number of measurements, P_r is the cumulative distribution function of the normal PDF (black line, Equations 7.8 and 7.9), and η_e and λ_e are the equilibrium height and wavelength obtained by Equations 7.1 and 7.2.

Three-Dimensional bedforms

The fourth stage of the development history of three-dimensional oscillatory bedforms behaved more like that of three-dimensional unidirectional bedforms than two-dimensional oscillatory bedforms. During this last development stage, the wavelengths and heights, for both three-dimensional oscillatory and unidirectional bedform, fluctuated around the equilibrium average values (e.g., Figure 7.7), therefore providing a wider spectrum of wavelengths and heights (Figure 7.18). Figure 7.18 shows the histogram of the measured heights (Figure 7.18a) and wavelengths (Figure 7.18b) for all equilibrium bedforms for experiment 18 (three-dimensional oscillatory ripple). Contrary to the two-dimensional oscillatory bedforms, both the distribution of bedform heights (Figure 7.18a) and wavelengths (Figure 7.18b) show significant variations of the spatially-averaged wavelength and height once the bed reached an equilibrium state (e.g., $\sigma_\eta/\mu_\eta \times 100 \sim 54.1\%$ and $\sigma_\lambda/\mu_\lambda \times 100 \sim 38.5\%$). Based on a normal distribution, 66.5% of the variability of bedform height lies within one standard deviation (σ_η), and 96.6% lies within $2\sigma_\eta$; whereas for bedform wavelength, 71.3% lies within one σ_λ and 96.6% within $2\sigma_\lambda$. Moreover, 100% of the variability lies within $\sim 6\,\sigma$; $\Delta\eta(t > t_e) \approx 51.0$ mm $\approx 4.3\,\sigma_\eta$ and $\Delta\lambda(t > t_e) \approx 0.45$ m $\approx 5.84\,\sigma_\lambda$.

The wider range of three-dimensional oscillatory bedform sizes ($\sim$ 45% from the mean values) compared with two-dimensional oscillatory bedforms ($\sim$ 8% from the mean values) can be explained by the dynamic behaviour of the bedforms over time and space once the bed reached equilibrium conditions (similar to that discussed for three-dimensional unidirectional bedforms, Section 7.3.1: Stage 4). During this fourth stage of development, the bedforms are constantly moving and generating new bed features that promoted the separation of the old forms or the merger between nearby features. As discussed in Stage 4 for unidirectional flows, this variability can be accounted for by the dynamic migration, separation and merging of the bedforms (Section 7.3.1: Stage 4).

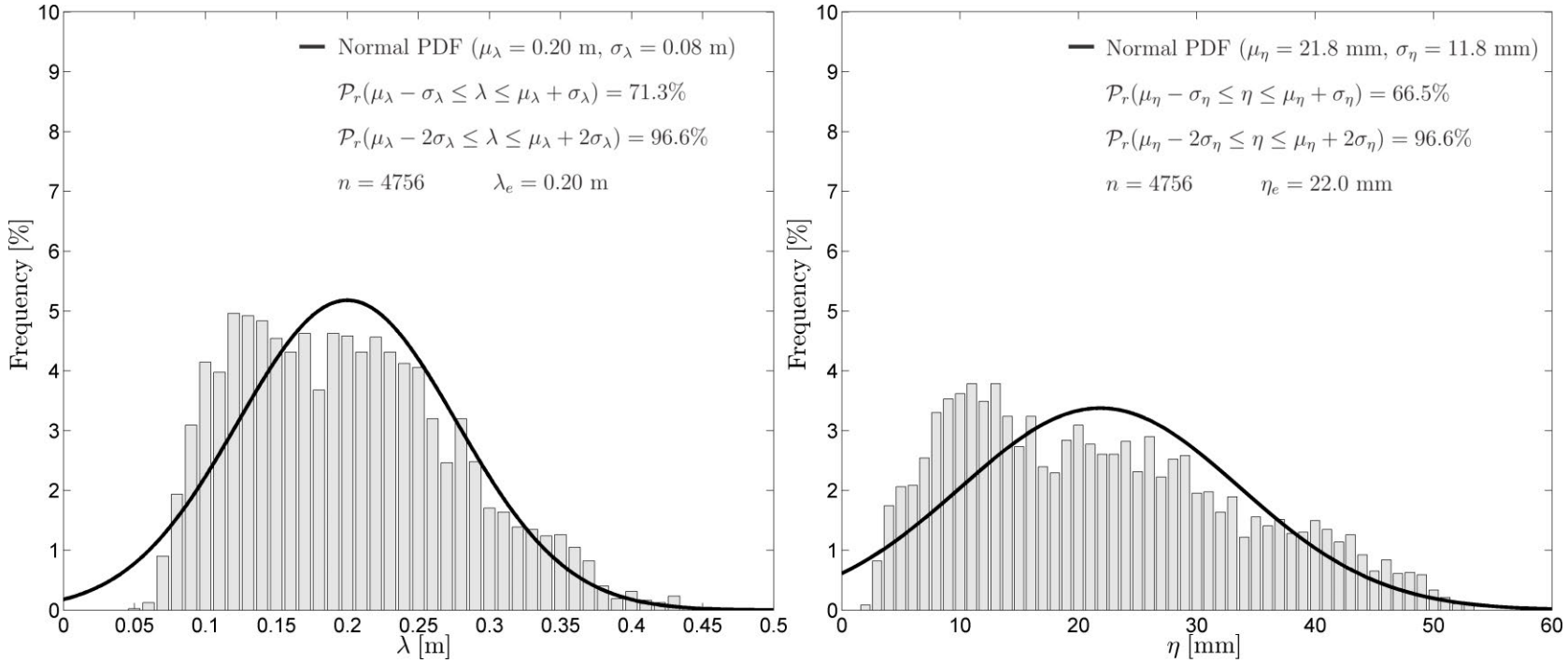

Figure 7.18: Histogram of bedform a) height and b) wavelength at equilibrium conditions ($t > t_e$) for three-dimensional symmetric oscillatory-ripples (Experiment 18). n is the number of measurements, P_r is the cumulative distribution function of the normal PDF (black line, Equations 7.8 and 7.9), and η_e and λ_e are the equilibrium height and wavelength obtained by Equations 7.1 and 7.2.

7.3.3 Combined Flows

Similar to the pure unidirectional and pure oscillatory fow bedforms, the general trend followed by the development or growth of the combined flow bedforms was characterized by the previously described (Sections 7.3.1 and 7.3.2) asymptotic exponential growth rate (Figures 7.19 to 7.22). This behavior was shared by all combined flows bedforms regardless of the final equilibrium stage; e.g., three-dimensional asymmetric ripple (Figure 7.19), three-dimensional quasi-asymmetric rounded ripple (Figure 7.20), three-dimensional quasi-asymmetric ripple (Figure 7.21) and three-dimensional asymmetric rounded dune (Figure 7.22). Hence, following the same methodology as the other flow conditions (Sections 7.3.1 and 7.3.2), Equations 7.1 and 7.2 were used to characterize the development from an initially flat bed of the four experiments listed above (Figures 7.19-7.22). The fits (red lines) and their 95% confidence intervals (gray-shaded areas) are plotted in each of the development curves (Figures 7.19-7.22). The mean R^2 value obtained by the fits of all the combined flow bedform data sets was 0.64 with a standard deviation of 0.21 (Table 7.1) and an averaged p-value of 0.03, a value that is a little below the mean R^2 for unidirectional flows bedforms of 0.72 (no standard deviation was computed since there are only two data points) or oscillatory flow bedforms of $R^2 = 0.78$ with a standard deviation of 0.24 (Table 7.1). The fact that the mean R^2 value is slightly lower for the combined flows does not imply that the predictive power of Equations 7.1 and 7.2 for the combined flow case is worse than the other flows, since if the variations of these means are taken into account (i.e., standard deviation) the results among the three overlap.

The development stages under combined flows are the same as those described for unidirectional (Section 7.3.1) and oscillatory (Section 7.3.2) bedforms. Figures 7.23 to 7.25 show the same development stages to those discussed for the other flow types: (1) incipient bedforms, (2) growing bedforms, (3) stabilizing bedforms, and (4) fully-developed bedforms.

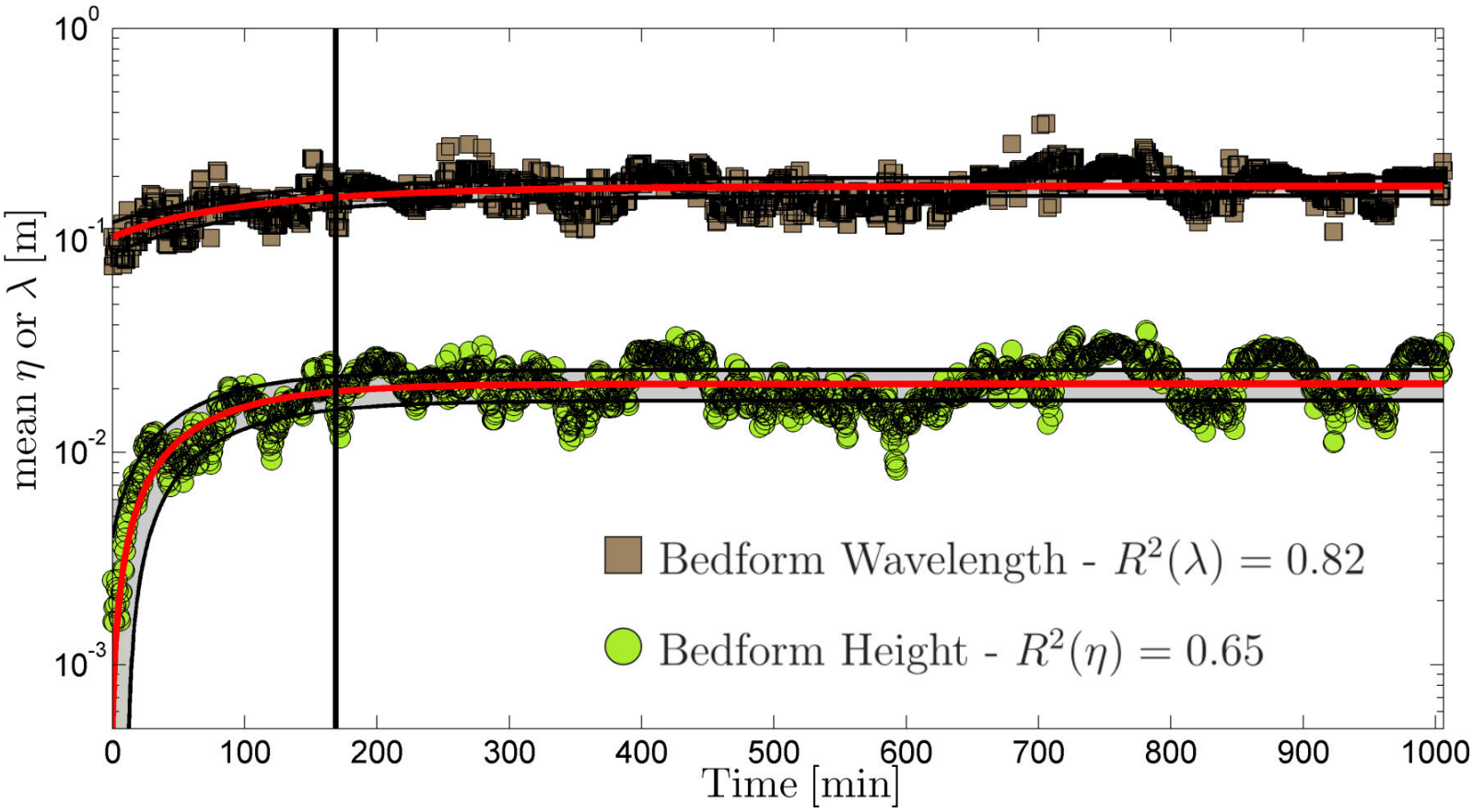

Figure 7.19: Development of bedform wavelength and height on an initially flat bed for combined flow (Experiment 03, $t_e = 2.81$ hr). The equilibrium time, t_e, is denoted by the vertical line. $R^2(\lambda)$ and $R^2(\eta)$ are the correlation coefficients for bedform wavelength and bedform height respectively obtained by fitting Equations 7.1 and 7.2. The gray-shaded area represents the 95% confidence interval of the fitted function. Bed morphology at equilibrium = Three-dimensional Asymmetric Ripple (3D AR).

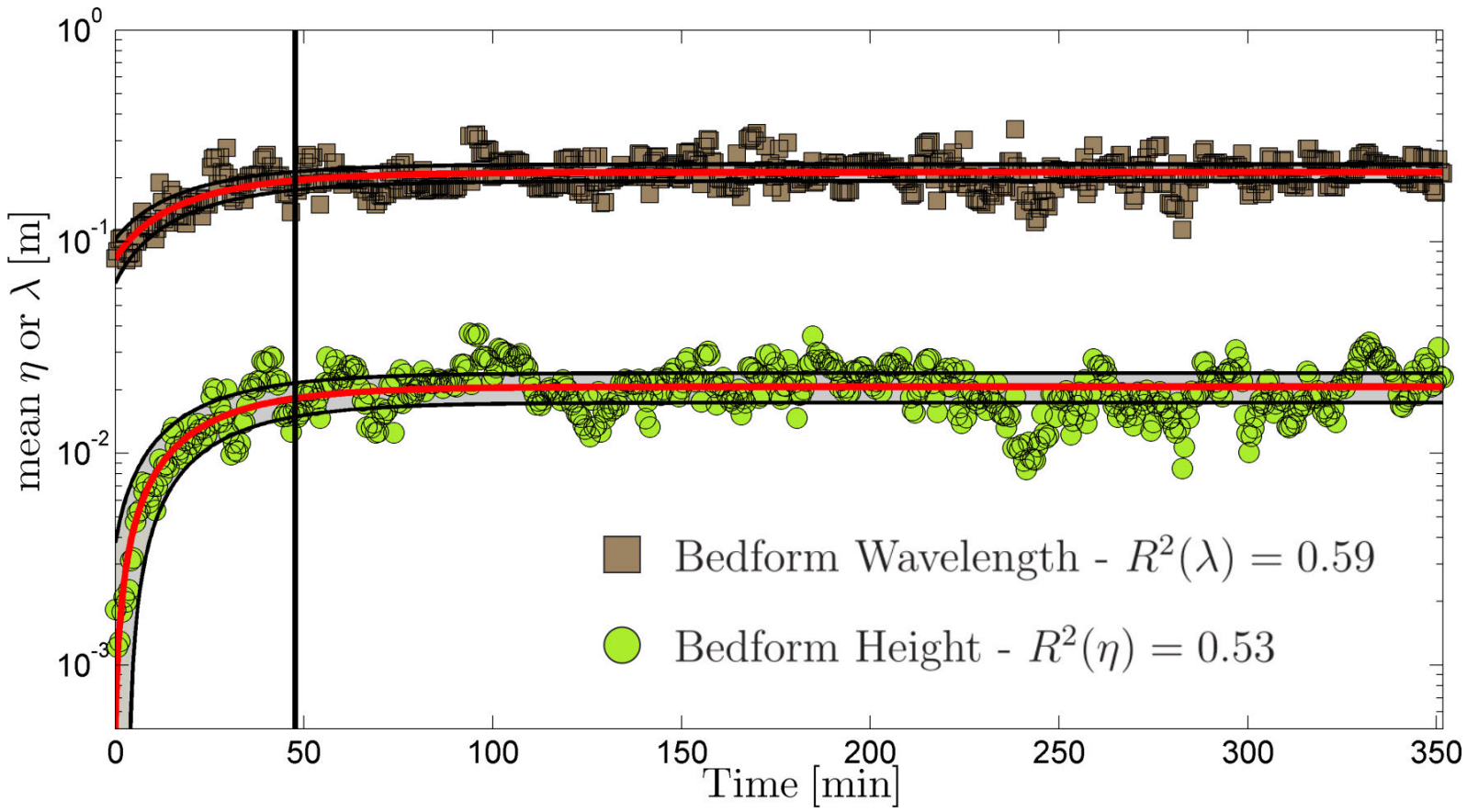

Figure 7.20: Development of bedform wavelength and height on an initially flat bed for combined flow (Experiment 20, $t_e = 0.79$ hr). The equilibrium time, t_e, is denoted by the vertical line. $R^2(\lambda)$ and $R^2(\eta)$ are the correlation coefficients for the bedform wavelength and bedform height respectively obtained by fitting Equations 7.1 and 7.2. The gray-shaded area represents the 95% confidence interval of the fitted function. Bed morphology at equilibrium = Three-dimensional Quasi-Asymmetric Rounded Ripple (3D QARR).

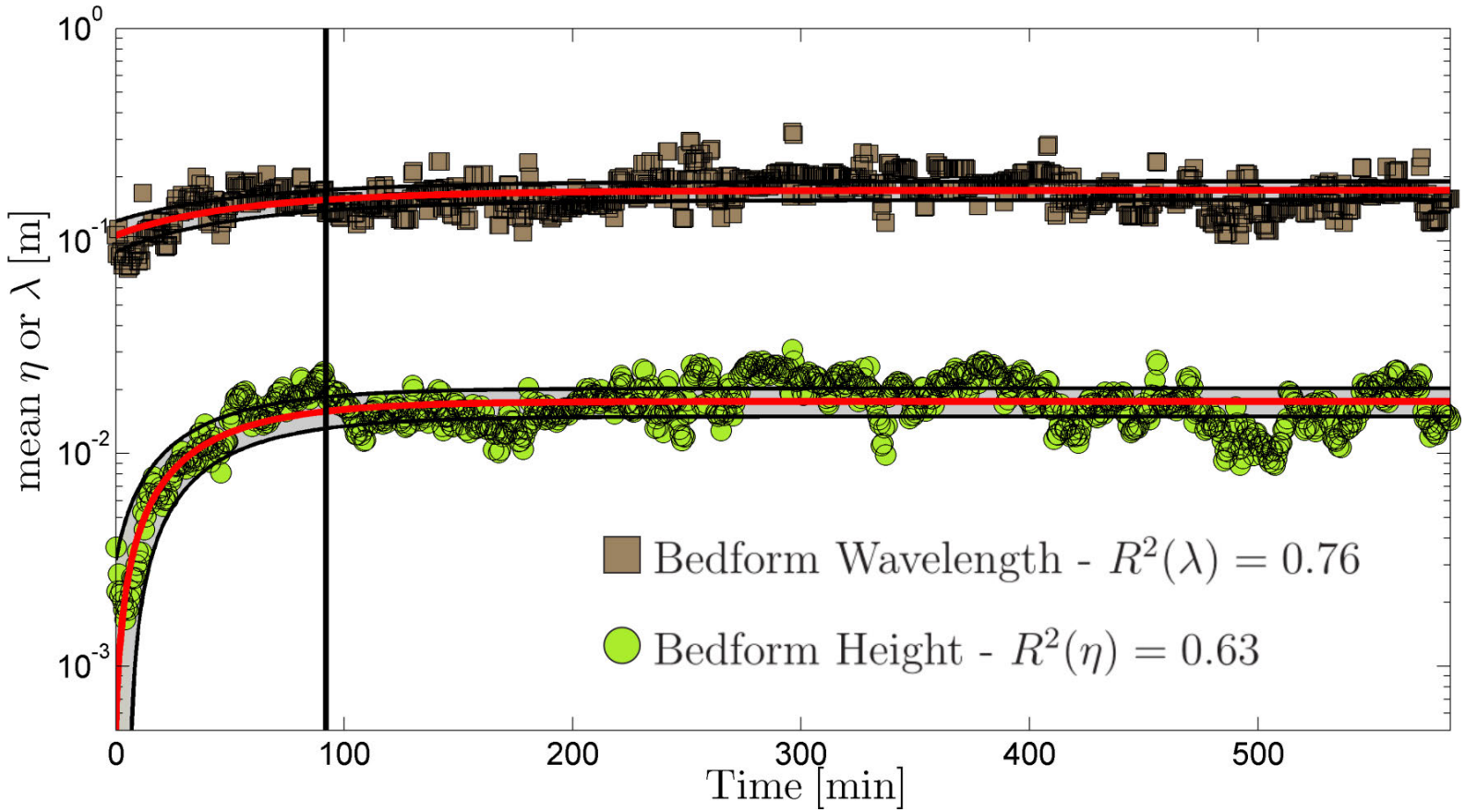

Figure 7.21: Development of bedform wavelength and height on an initially flat bed for combined flow (Experiment 33, $t_e = 1.53$ hr). The equilibrium time, t_e, is denoted by the vertical line. $R^2(\lambda)$ and $R^2(\eta)$ are the correlation coefficients for the bedform wavelength and bedform height respectively obtained by fitting Equations 7.1 and 7.2. The gray-shaded area represents the 95% confidence interval of the fitted function. Bed morphology at equilibrium = Three-dimensional Quasi-Asymmetric Ripple (3D QAR).

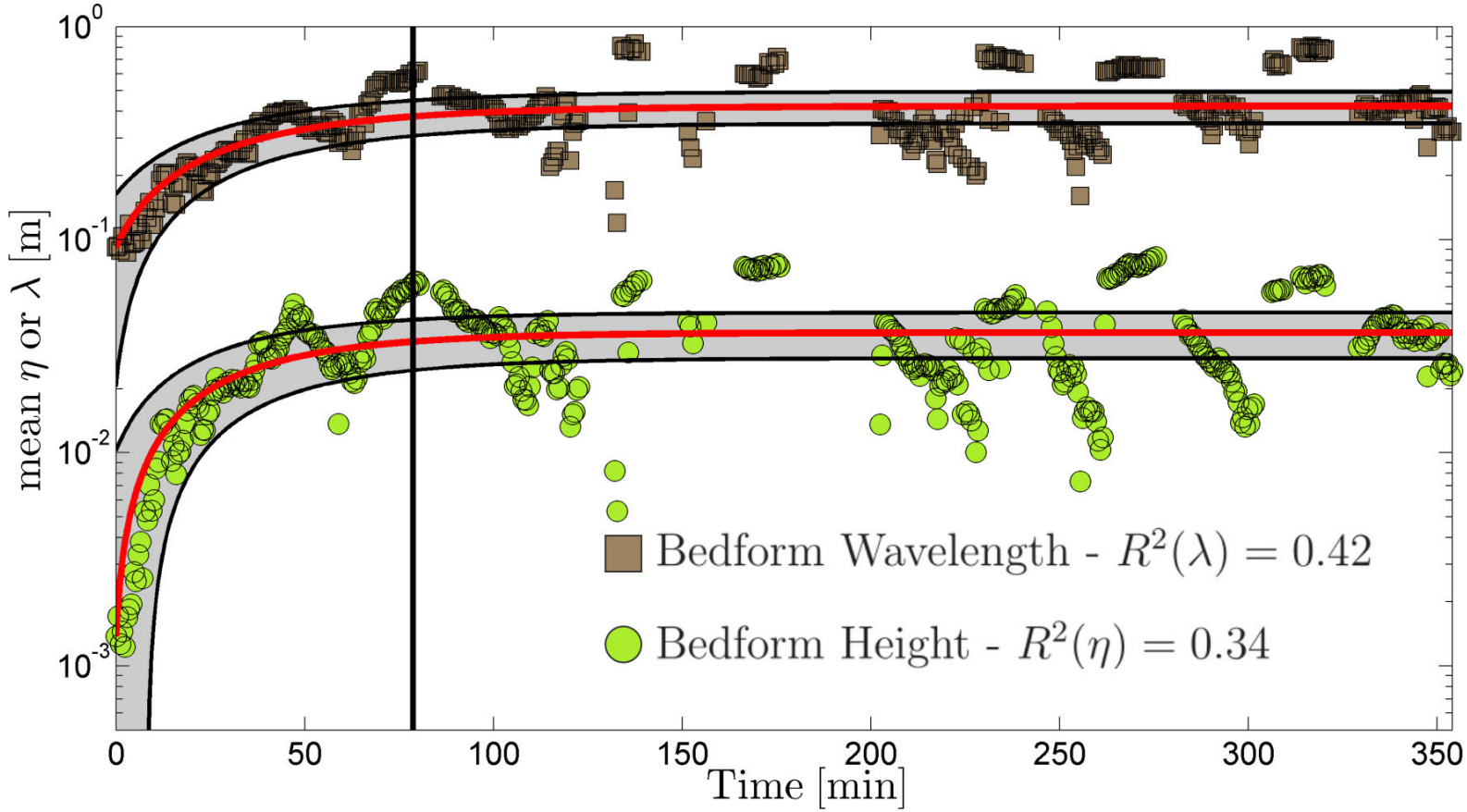

Figure 7.22: Development of bedform wavelength and height on an initially flat bed for combined flow (Experiment 35, $t_e = 1.31$ hr). The equilibrium time, t_e, is denoted by the vertical line. $R^2(\lambda)$ and $R^2(\eta)$ are the correlation coefficients for the bedform wavelength and bedform height respectively obtained by fitting Equations 7.1 and 7.2. The gray-shaded area represents the 95% confidence interval of the fitted function. Bed morphology at equilibrium = Three-dimensional Asymmetric Rounded Dune (3D ARD).

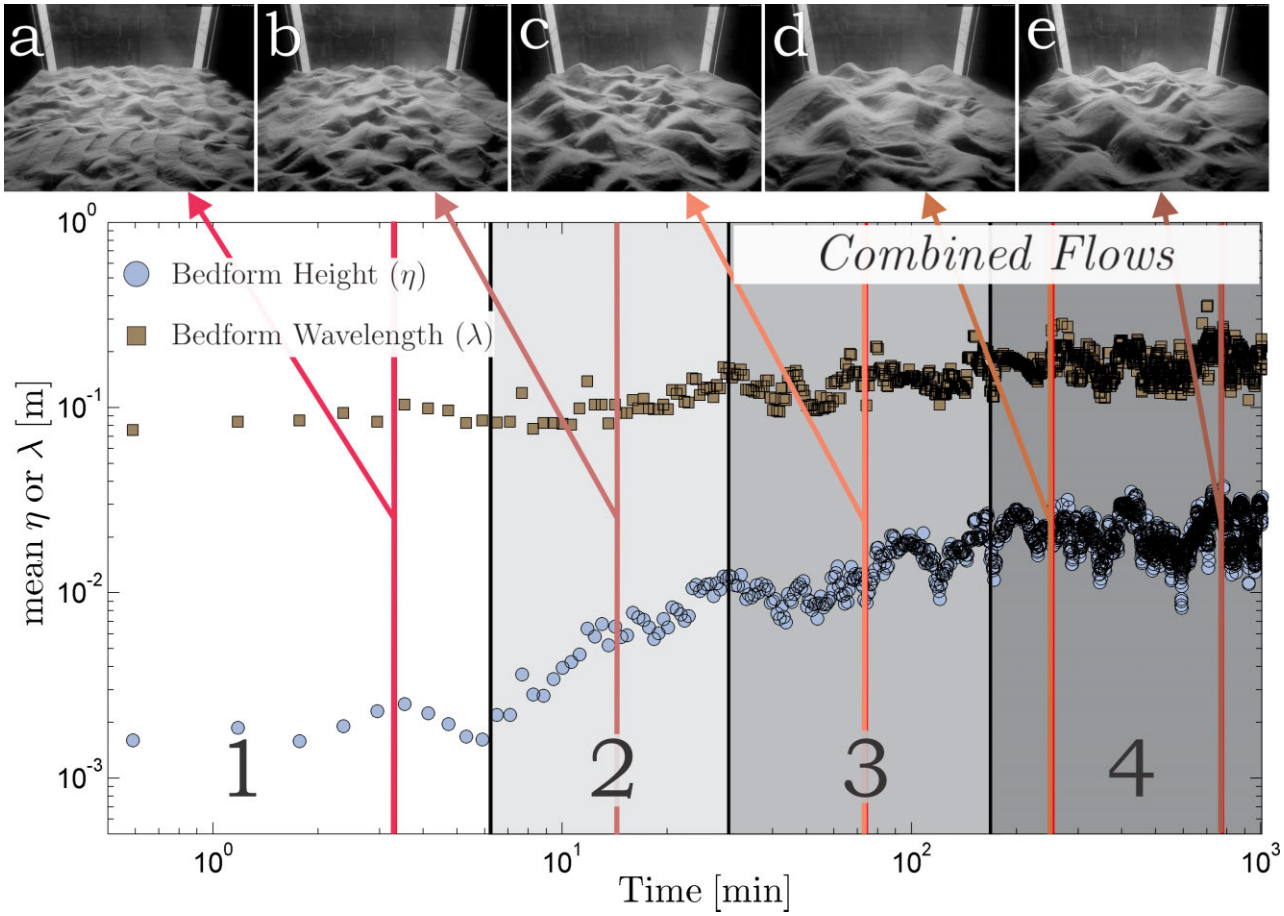

Figure 7.23: Spatially-averaged bedform height and wavelength plotted against time for three-dimensional asymmetric ripples (Experiment 03). The numbers at the base of the diagram indicate development stages: (1) incipient ripples (white box); (2) growing bedforms (light-gray box); (3) stabilizing bedforms (gray box); and (4) fully-developed bedforms (dark-gray box). The vertical line dividing boxes 3 and 4 marks the equilibrium time at $t_e = 168.6$ min. Both axes have a log-normal scale. A series of photos were taken at (a) $t = 3.33$ min, (b) $t = 14.31$ min, (c) $t = 74.36$ min, (d) $t = 254.77$ min and (e) $t = 777.08$ min and are denoted by the different colored arrows. The window on the back of the picture is 0.60 m wide.

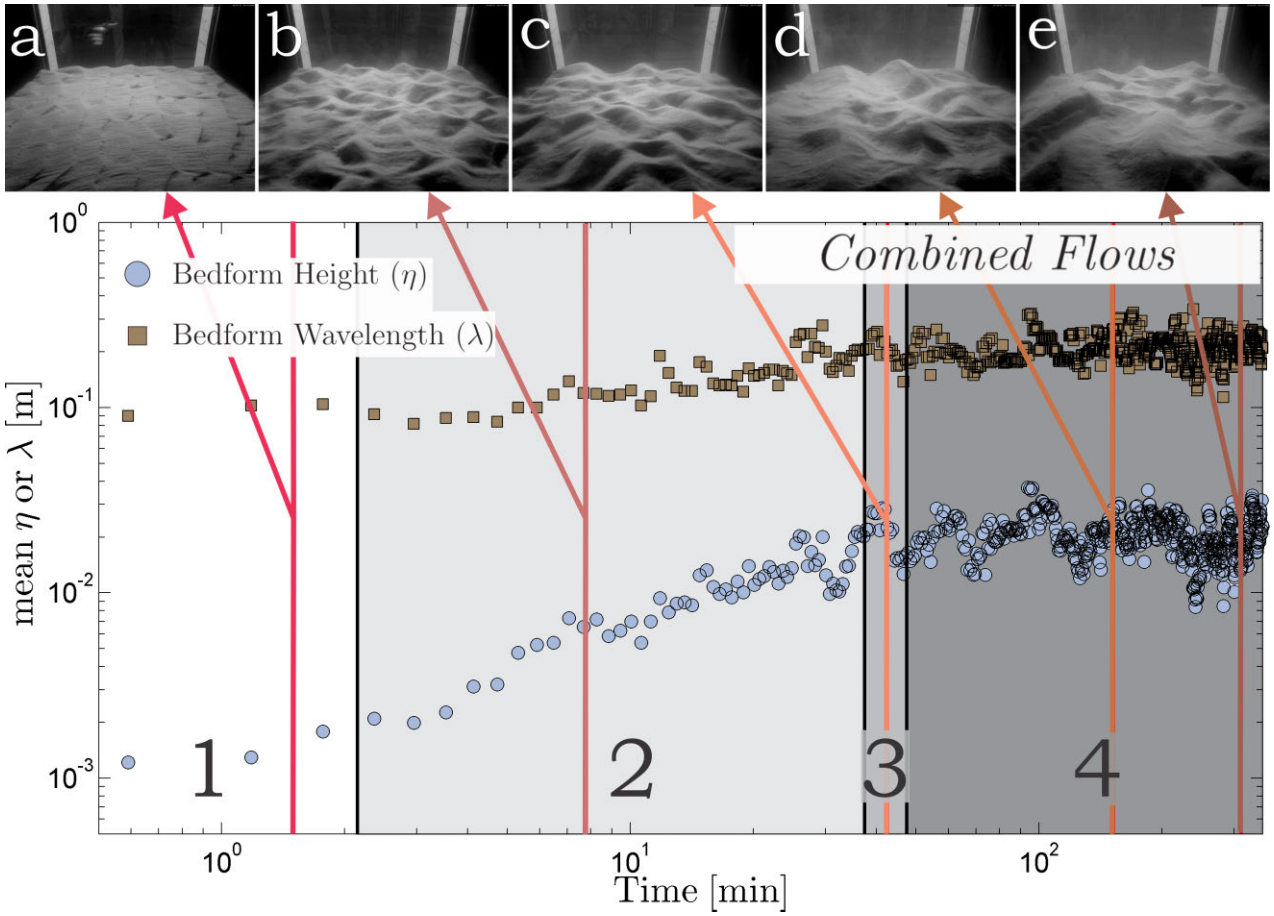

Figure 7.24: Spatially-averaged bedform height and wavelength plotted against time for three-dimensional quasi-asymmetric rounded ripple (Experiment 20). The numbers at the base of the diagram indicate development stages: (1) incipient ripples (white box); (2) growing bedforms (light-gray box); (3) stabilizing bedforms (gray box); and (4) fully-developed bedforms (dark-gray box). The vertical line dividing boxes 3 and 4 marks the equilibrium time at $t_e = 47.4$ min. Both axes have a log-normal scale. A series of photos were taken at (a) $t = 1.5$ min, (b) $t = 7.8$ min, (c) $t = 42.6$ min, (d) $t = 152.3$ min and (e) $t = 312.1$ min and are denoted by the different colored arrows. The window on the back of the picture is 0.60 m wide.

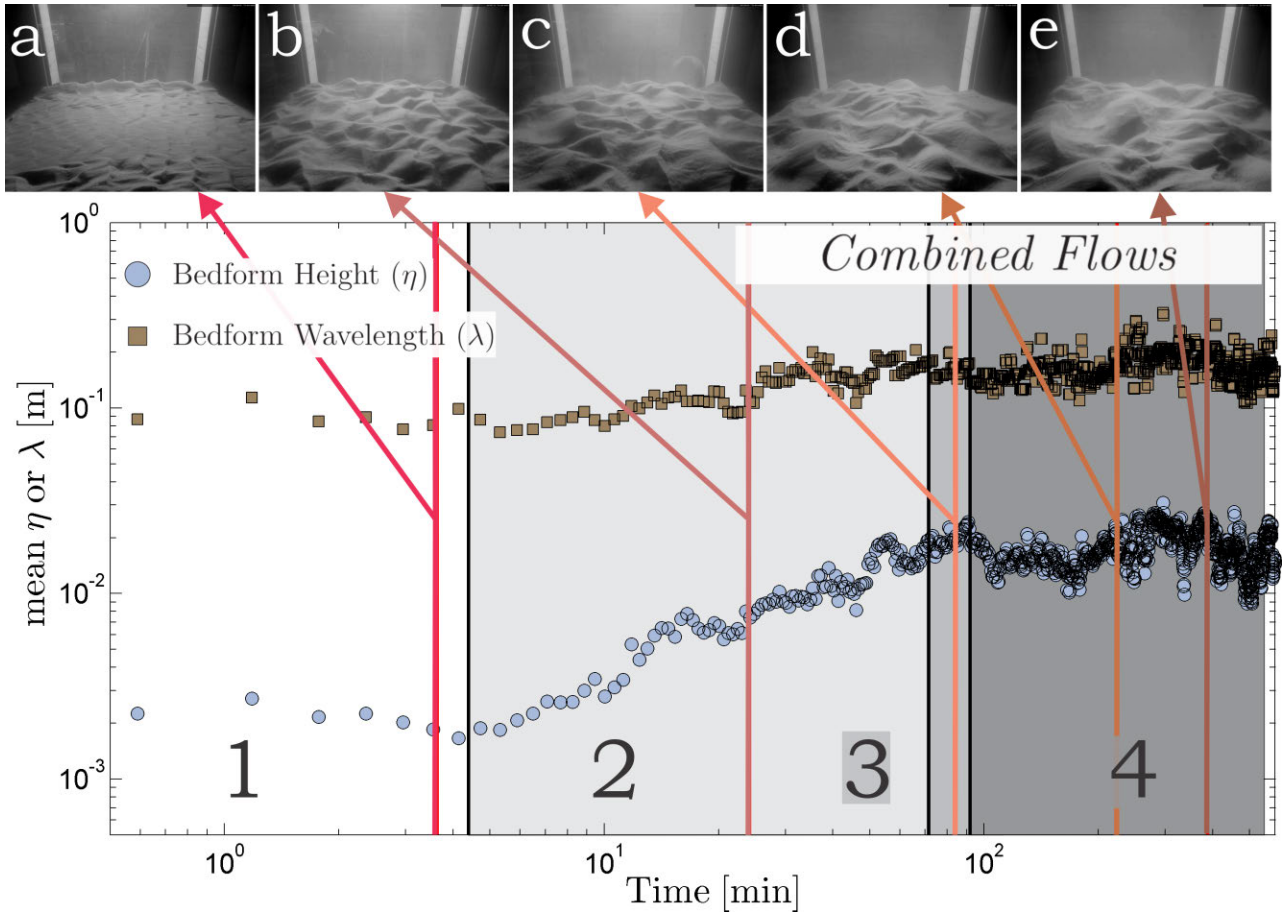

Figure 7.25: Spatially-averaged bedform height and wavelength plotted against time for three-dimensional quasi-asymmetric ripple (Experiment 33). The numbers at the base of the diagram indicate development stages: (1) incipient ripples (white box); (2) growing bedforms (light-gray box); (3) stabilizing bedforms (gray box); and (4) fully-developed bedforms (dark-gray box). The vertical line dividing boxes 3 and 4 marks the equilibrium time at $t_e = 91.8$ min. Both axes have a log-normal scale. A series of photos were taken at (a) $t = 3.6$ min, (b) $t = 24.1$ min, (c) $t = 84.05$ min, (d) $t = 224.0$ min and (e) $t = 388.4$ min and are denoted by the different colored arrows. The window on the back of the picture is 0.60 m wide.

Stage 1 - Incipient Bedforms

For the combined flow conditions where the bed morphology did not develop from wall-defects (i.e., Section 7.3.2), a clear distinction could be observed between the predominant morphological features present under wave (e.g., Figure 7.26) or current dominated (e.g., Figure 7.27; Chapter 5) combined flow conditions. For the case of wave-dominated combined flow bedforms (e.g., Figure 7.26), the incipient bedforms resembled those observed for pure oscillatory bedforms: rolling grain ripples (Figure 7.26, Section 7.3.2). However, for the case of current-dominated combined flows, the incipient bedforms behave as those described for the pure unidirectional case (Figure 7.3, Section 7.3.1). The diagnostic features used to differentiate the incipient bedforms generated under wave-dominated (WD) combined flow versus current-dominated (CD) combined flow was the presence (Figure 7.26) or absence (Figure 7.27) of crest reversal during the wave cycle. Moreover, during the first stages of bedform development under a wave-dominated combined flow (Figure 7.26), there is a clear back and forth movement of the crest direction or crest reversal (white arrows in Figure 7.26). In addition, it can be observed that a full crest reversal (e.g., from downstream-pointing to later downstream-pointing with an intermediate stage of upstream-pointing) occurs within one wave cycle (white-box, Figure 7.28). On the other hand, during the genesis of bedforms for current-dominated combined flows, the bedform crestline does not change direction (Figure 7.27).

The morphological difference between wave and current-dominated combined flow bedforms (i.e., presence and absence of crest reversal on the incipient bedforms along the wave cycle) is a clear representation of the interactions of the SFD "trinity"components (Chapter 1). The interaction between the fluid dynamics and the sediment grains produces temporal changes in the velocity profiles (Figures 7.29 and 7.30), which are reflected by the sediment transport, and thus in the way the bedforms develop for different combined flow conditions (Figures 7.26 and 7.27).

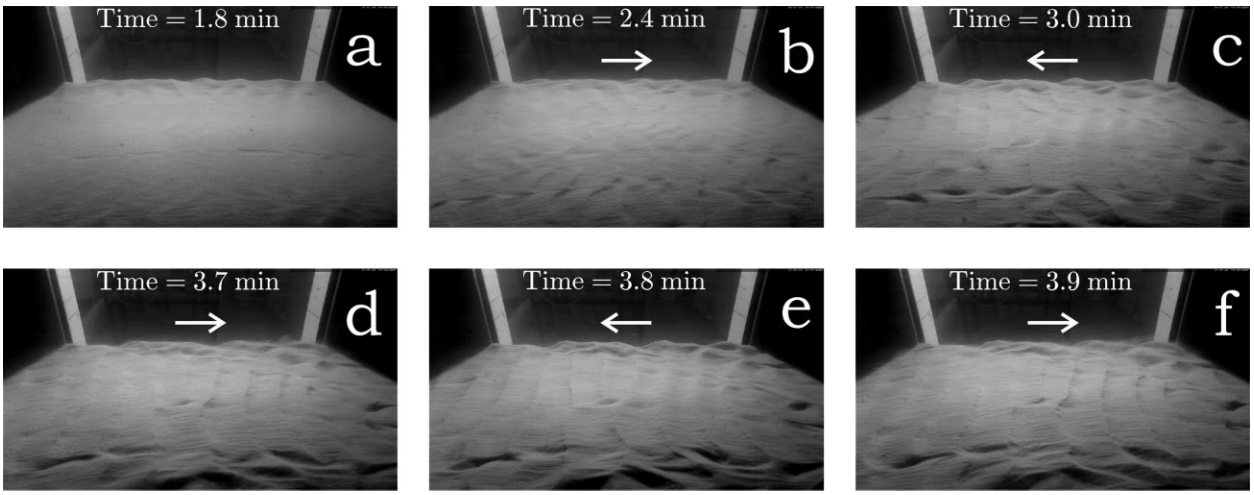

Figure 7.26: Incipient bedforms at the first stage of development for a three-dimensional quasi-asymmetric wave-dominated combined flow ripple (Experiment 19). The white arrows indicate the change of direction (upstream to downstream) of the crestline along the wave cycle. This process is shared with the rolling grain ripples generated at the first stage of pure oscillatory bedforms (Figure 7.10), but does not occur under the genesis of current-dominated combined flow bedforms (Figure 7.27). The window on the back of the picture is 0.60 m wide.

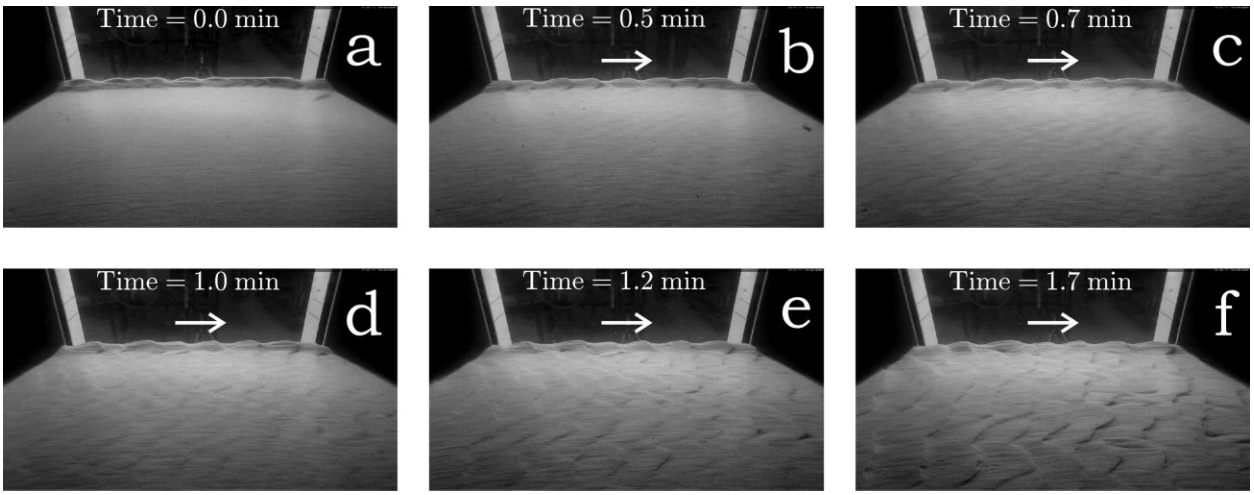

Figure 7.27: Incipient bedforms at the first stage of development for a three-dimensional asymmetric rounded current-dominated combined flow ripple (Experiment 4). The white arrows indicate the absence of directional change of the crestline along the wave cycle; the crest line always points downstream. This scenario is different than the wave (Figure 7.10) and wave-dominated bedforms (Figure 7.26) where the crest alternates in direction. The window on the back of the picture is 0.60 m wide.

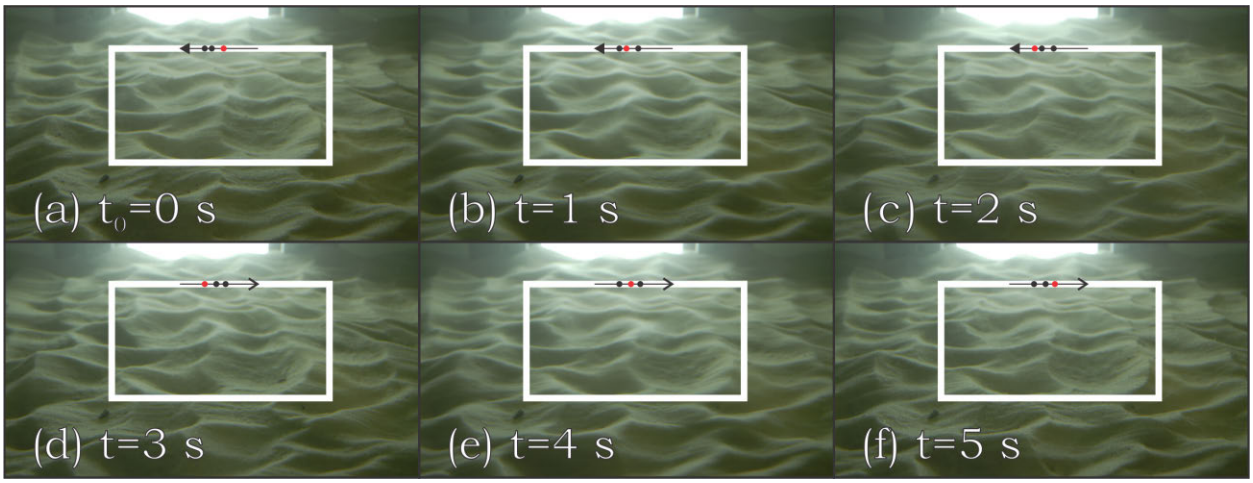

Figure 7.28: Crestal reversal occurring in the first stages of development of a wave-dominated combined flow bedform (Experiment 19). Photographs (a) to (c) show the crest evolution towards the upstream direction, whereas (d) to (f) are towards the downstream direction. On the top axis of the white-box, the arrow denotes the overall direction of the crest migration. In addition, within the arrow, three dots were plotted to illustrate where the average crestline is located, with the red dot corresponding to the active frame. The window on the back of the picture is 0.60 m wide.

Figures 7.29 and 7.30 show the streamwise phase-averaged (a) velocity profiles $u(z)$ and (b) a point measurement at $z = 0.28$ m along the oscillation cycle for wave-dominated combined flow (Figure 7.29) and current-dominated combined flow (Figure 7.30). Figure 7.29 and 7.30 represent a clear example of the intrinsic interactions of the wave and current boundary layers, which play a significant role in the dynamic of wave and current-dominated combined flows bedforms. For example, the maximum combined flow velocity for both, the wave (Figure 7.29) and current-dominated (Figure 7.30) combined flow conditions is roughly the same ($\sim 0.5\, m\, s^{-1}$). This similar maximum velocity produces a very similar velocity profile when the direction of the oscillatory velocity coincides with the unidirectional flow (phase $\sim 0°$ in Figure 7.29 and phase $\sim 240°$ Figure 7.30). However, for the case where the oscillatory velocity direction opposes the unidirectional flow, the velocity profiles look very different (phase $\sim 179°$ in Figure 7.29 and phase $\sim 61°$ Figure 7.30).

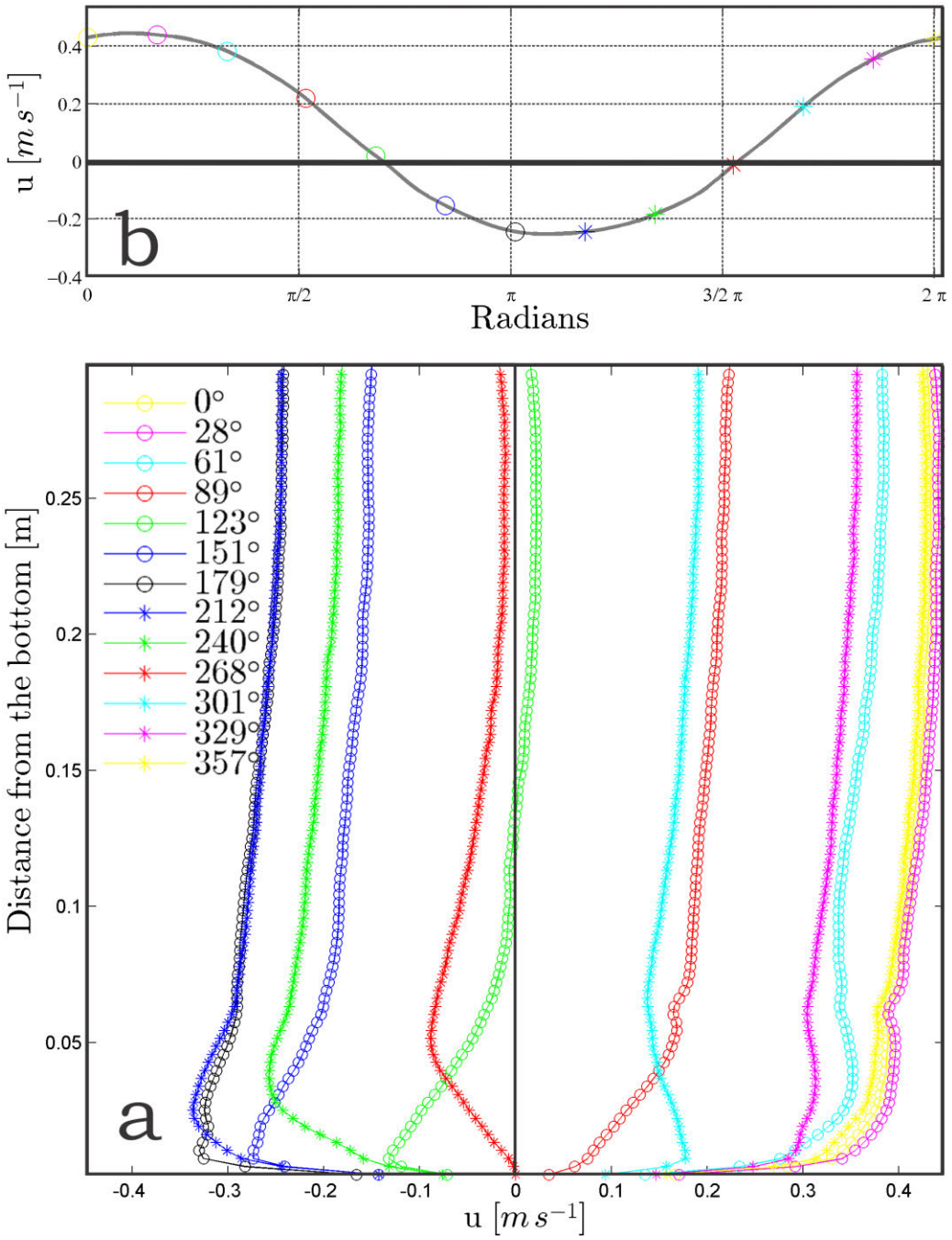

Figure 7.29: Velocity over a three-dimensional quasi-asymmetric, wave-dominated combined flow ripple (Experiment 19). Oscillatory Condition: $U_o = 0.40\,m\,s^{-1}$ and $T = 5$ s. Unidirectional Condition: $U_u = 0.10\,m\,s^{-1}$. (a) Streamwise phase-averaged velocity profile along the oscillation cycle. (b) Streamwise phase-averaged velocity along the oscillation cycle at $z = 0.28$ m. The symbols correspond to the velocity profiles plotted in (a).

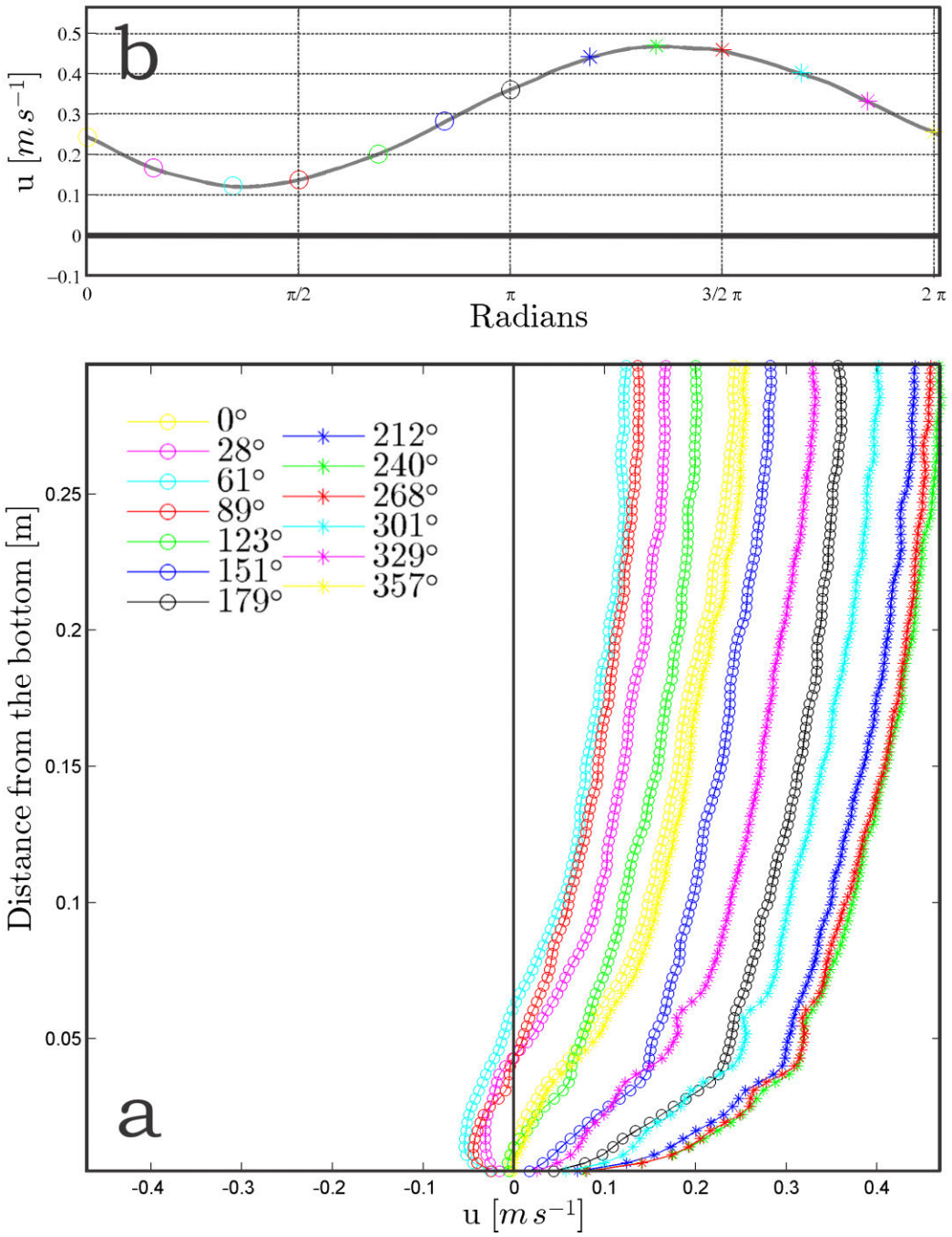

Figure 7.30: Velocity over a three-dimensional asymmetric rounded current-dominated combined flow ripple (Experiment 4). Oscillatory Condition: $U_o = 0.25\,m\,s^{-1}$ and $T = 4$ s. Unidirectional Condition: $U_u = 0.30\,m\,s^{-1}$. (a) Streamwise phase-averaged velocity profile along the oscillation cycle. (b) Streamwise phase-averaged velocity along the oscillation cycle at $z = 0.28$ m. The symbols correspond to the velocity profiles plotted in (a).

The differences between wave and current-dominated combined flows not only concern the mean or upper flow conditions, but also the dynamics occurring very close to the bed. Near the bed, there are two boundary layers - one due to oscillatory flow and the other due to unidirectional flow (Mathisen and Madsen, 1996a,b, 1999; Fredsøe et al., 1999). The boundary layer formed by the wave is relatively thin compared to that generated by the unidirectional flow, and thus the effects of the oscillatory conditions can be seen much more clearly near the bed (e.g., flow reversal for $z < 0.05\,m$, Figure 7.30) than in the upper parts of the flow (e.g., $u > 0$ for all wave phases for $z > 0.1\,m$, Figure 7.30). This explains why current-dominated combined flows can exhibit flow reversal ($z < 0.05\,m$, Figure 7.30), yet the magnitude of such velocities is insufficient to entrain sediment ($\theta_{max}^{(-)} = -0.01 < \theta_c = -0.04$; Equation 4.26.) in the upstream direction. On the other hand, for the case of the wave-dominated combined flow conditions (Figure 7.29), the unidirectional velocity is not strong enough to prevent the oscillatory velocity fully reversing ($z < 0.05\,m$, Figure 7.29). Hence, a net sediment transport in the upstream direction occurs, which can be clearly observed in the crest reversal phenomenon (Figure 7.26 and 7.28).

Stage 2 - Growing Bedforms

Similar to unidirectional and oscillatory flows, combined flow bedforms grow by a combination of sediment capturing and amalgamation with nearby bedforms (Figures 7.23b, 7.24b and 7.25b). The growth occurring during this stage accounts for $\sim 95\%$ of the total bedform enlargement. This result is consistent with the experiments reported under unidirectional flows ($\sim 85\%$; Section 7.3.1), oscillatory flows ($\sim 93\%$; Section 7.3.2) and by Baas (1994) ($\sim 75\%$), which shows that the large majority of the overall growth occurs in this stage.

Stage 3 - Stabilizing Bedforms

Identical to unidirectional (Section 7.3.1) and oscillatory flow (Section 7.3.2), the third stage in the development of combined flow bedforms was also defined as the temporal gap that

occurs in the interval between the moment when the asymptotic growth ends (Stage 2) and the time when the bed reached equilibrium conditions (Figures 7.23 to 7.25). The overall growth occurring during Stage 3 under combined flow is almost insignificant ($< 3\%$, Figures 7.23-7.25).

Stage 4 - Fully-developed Bedforms

The fourth stage of the development history of combined flow bedforms was very similar to those described under unidirectional (Section 7.3.1) and oscillatory flows that generate three-dimensional planform geometries (Section 7.3.2). For the three different types of flows (all flows except the one that generated two-dimensional oscillatory bedforms), the bedform wavelengths and heights fluctuated around the equilibrium average values (e.g., Figure 7.20 or Figure 7.22), providing a wide spectrum of wavelengths and heights (Figure 7.32 and 7.31). This spectrum can be seen in both the wave (Figure 7.31) and current-dominated bedforms (Figure 7.32). For the case of wave-dominated bedforms, the histogram of the measured heights (Figure 7.31a) and wavelengths (Figure 7.31b) is analyzed for all bedforms present in the sample volume during Stage 4 for experiment 20 (three-dimensional quasi-asymmetric rounded combined flow ripple). The three-dimensional nature of the bedform (see discussion in Section 7.3.1) is represented by the relative large range of sizes, $\sigma_\eta/\mu_\eta \times 100 \sim 47.9\%$ and $\sigma_\lambda/\mu_\lambda \times 100 \sim 33.9\%$. If the distribution of equilibrium bedforms is represented by a normal distribution, 69.1% of the variability of the bedform heights are within one standard deviation (σ_η), and 97.4% within $2\sigma_\eta$; whereas for bedform wavelength, 75.7% lies within one σ_λ and 96.2% within $2\sigma_\lambda$. In addition, 100% of the variability lies within $\sim 6\,\sigma$; $\Delta\eta(t > t_e) \approx$ 47.0 mm $\approx 4.8\,\sigma_\eta$ and $\Delta\lambda(t > t_e) \approx 0.43$ m $\approx 6.0\,\sigma_\lambda$. Similarly, the histograms of the heights (Figure 7.32a) and wavelengths (Figure 7.32b) for experiment 3 were processed in order to see the distribution for a current-dominated combined flow bedform. Current-dominated bedforms at equilibrium states show a relatively wide spectrum of sizes (e.g., $\sigma_\eta/\mu_\eta \times 100 \sim$ 45.2% and $\sigma_\lambda/\mu_\lambda \times 100 \sim 28.9\%$). Using the same methodology as for the other types of

bedforms, a normal distribution characterizes the dispersion of sizes; 65.5% of the variability of bedform height lies within one standard deviation (σ_η), and 97.1% lies within $2\sigma_\eta$; whereas for bedform wavelength, 62.5% lies within one σ_λ and 97.3% within $2\sigma_\lambda$. Moreover, 100% of the variability lies within $\sim 6\,\sigma$; $\Delta\eta(t > t_e) \approx 42.0$ mm $\approx 4.4\,\sigma_\eta$ and $\Delta\lambda(t > t_e) \approx 0.35$ m $\approx 6.5\,\sigma_\lambda$.

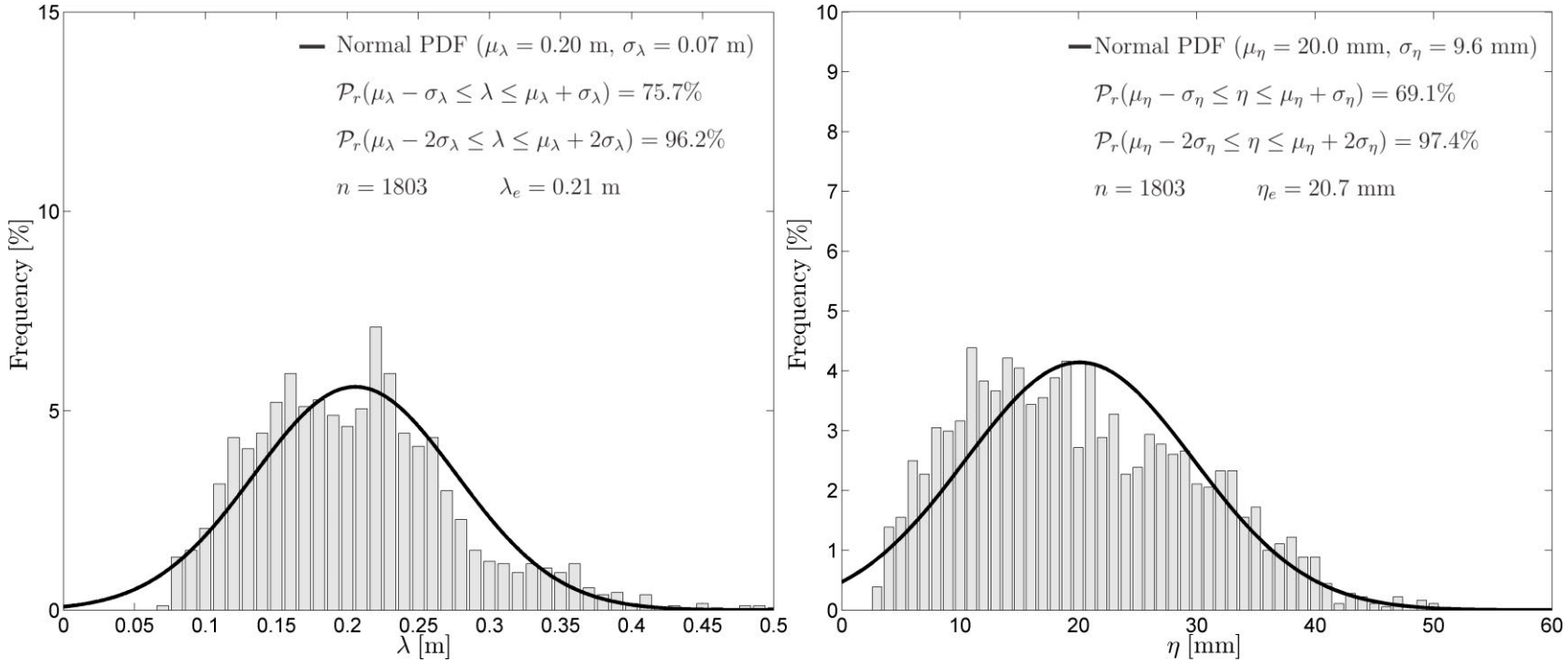

Figure 7.31: Histogram of bedform a) height and b) wavelength at equilibrium conditions ($t > t_e$) for a three-dimensional quasi-asymmetric rounded combined flow ripple (Experiment 20). n is the number of measurements, P_r is the cumulative distribution function of the normal PDF (black line, Equations 7.8 and 7.9), η_e and λ_e are the equilibrium height and wavelength obtained by Equations 7.1 and 7.2.

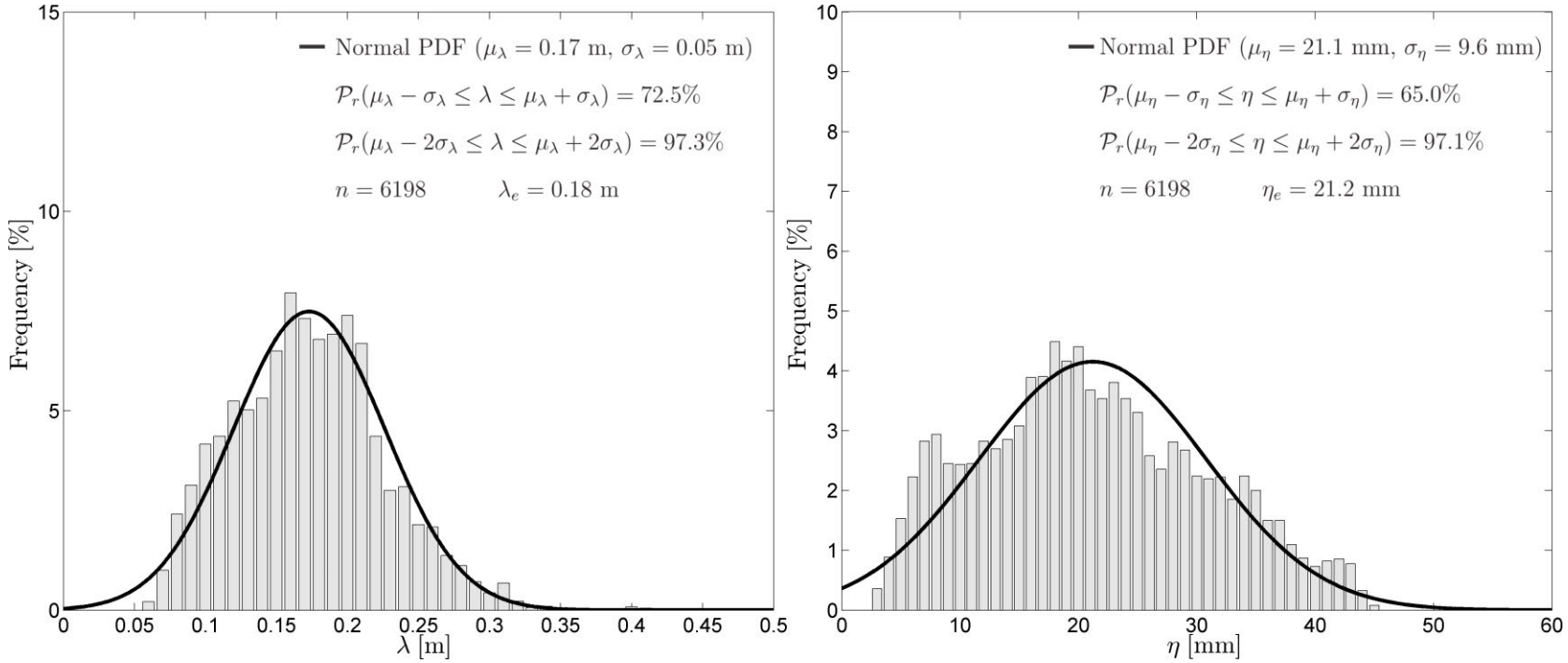

Figure 7.32: Histogram of bedform a) height and b) wavelength at equilibrium conditions ($t > t_e$) for a three-dimensional asymmetric current-dominated combined flow ripple (Experiment 3). n is the number of measurements, P_r is the cumulative distribution function of the normal PDF (black line, Equations 7.8 and 7.9), η_e and λ_e are the equilibrium height and wavelength obtained by Equations 7.1 and 7.2.

7.4 Equilibrium time as a function of the flow and sediment transport conditions

The empirical model proposed by Baas (1999) was used to predict the equilibrium time as a function of the flow conditions. This model uses an inverse power of the flow velocity to find the best-fit for the equilibrium time measured (Baas, 1999). However, Baas (1999) reported a individual fit for the time required for the height and wavelength to reach equilibrium conditions. Hence, Equation 7.7 was used to re-evaluate the experimental data from Baas (1999) ($D_{50} = 0.238$ mm) and obtain a unified bed state equilibrium time as a function of flow velocity

$$U_u = 0.2695\, t_e^{-0.333} + 0.274. \tag{7.17}$$

(see solid red line in Figure 7.33). In addition, since Equation 7.17 does not account for the oscillatory component of the combined flow, a peak combined flow velocity value was used instead of U_u. Therefore,

$$U_{cf} = 0.2185\, t_e^{-0.508} + 0.272. \tag{7.18}$$

(see solid blue line in Figure 7.33), where U_{cf} is the unidirectional velocity linearly added to the maximum orbital velocity

$$U_{cf} = U_u + U_o. \tag{7.19}$$

The fitting statistics of both Equations were similar, the R^2 for Equation 7.17 (Baas, 1999) was $R^2 = 0.55$ (p-value= 0.04), whereas for Equation 7.18 being $R^2 = 0.63$ (p-value= 0.03). Equation 7.18 provides a slightly better prediction (better R^2), but both equations are unable to predict the large scatter. This observation can be seen by the multiple points outside the gray-shaded area in Figure 7.33, which represents the 95% confidence interval for Equation 7.18. In addition, even though the mean absolute percentage deviation (MAPD column in Table 7.3) is relatively large, the true difference from the fitted coefficient is not

significant (Δ column in Table 7.3).

Table 7.3: Comparison between the coefficients of Baas (1999) and Equation 7.18 for the equilibrium time as a function of flow velocity. Equation Structure: $U = A\,t_e^B + C$

Coefficient	Units	Baas (1999)'s Equation (Equation 7.17)	Proposed Equation (Equation 7.18)	Δ^a	MAPD^b
A	$[m(s\,hr)^{-1}]$	0.2695	0.2185	0.05	20.9
B		-0.333	-0.508	0.2	41.6
C	$[ms^{-1}]$	0.274	0.272	0.002	0.7

[a]Absolute Difference
[b]Mean Absolute Percentage Deviation

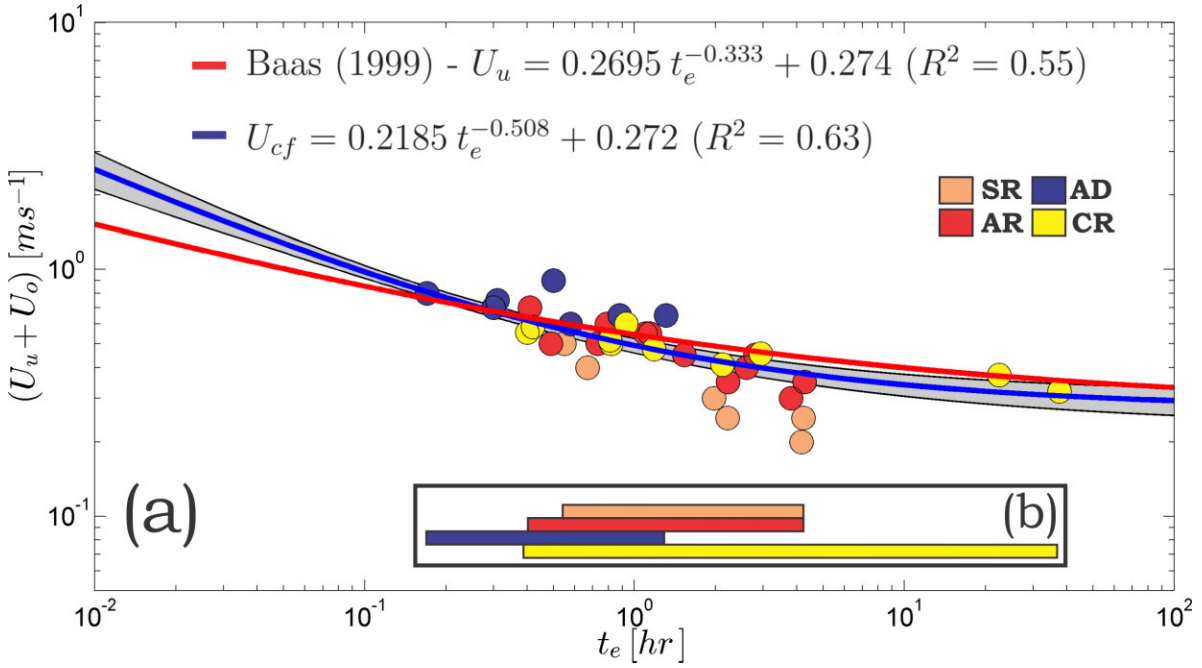

Figure 7.33: (a) Equilibrium time as a function of flow velocity. Current Ripple (CR, yellow) data was taken from Baas (1999) ($D_{50} = 0.238$ mm). The gray-shaded area represents the 95% confidence interval of the fitted function for the new proposed Equation (Equation 7.18). (b) Graphical scheme that represents the range of equilibrium times for different types of bed states. SR = Symmetric Ripples (light-orange), AR = Asymmetric Ripples (red), AD = Asymmetric Dunes (blue), and CR = Current Ripples (yellow).

Based on the distribution and relatively large overlap of the different equilibrium times for different bedforms (Figure 7.33b), it can be concluded that t_e is not a good variable to differentiate bed states. This result is consistent with the observations of Baas et al.

(1993). However, based on the overall distribution of time scales (Figure 7.33b), in general dunes required less time (only a few tens of minutes) to reach equilibrium conditions, whilst ripples generally require several hours. As expected by the size alone (dunes being larger than ripples), dunes would require more time to reach equilibrium than ripples. Yet, since the flow conditions for dunes mobilized significantly more sediment than ripples, dunes reach equilibrium faster. This result suggests that the sediment transport dynamics play a key role in defining the equilibrium time of the system. Moreover, the similarities between Equation 7.17 and Equation 7.18 can be explained since the time required for a bed to reach equilibrium is related to the amount of sediment transported, regardless of what type of flow is producing the transport. Therefore, a new formulation is required to better capture the physical process controlling the equilibrium time of the different bedforms. This new formulation must place more emphasis on the sediment transport characteristics, rather than the flow conditions in the upper flow (i.e., U_{cf} in Equation 7.18). Hence, using the methodology explained in Section 4.3.2, bedload was estimated for each experiment, and used to reformulate Equation 7.18 as

$$q^* = 4.89\, t_e^{-1.28} \tag{7.20}$$

(solid line in Figure 7.34), where q^*

$$q^* = \frac{q_s}{\sqrt{g\, R\, D_{50}}\, D_{50}} \tag{7.21}$$

is the dimensionless expression of q_s, which is bedload transport per unit width ($cm^2\, s^{-1}$). Figure 7.34 shows the equilibrium time for the different bedforms (color scheme in Figure 7.34) generated under the range of wave periods (symbol scheme in Figure 7.34) utilized in the present study, as a function of the dimensionless bedload transport per unit width. Despite the large dispersion, the fitted Equation 7.20 does a better job than Equations 7.17

and 7.18 at predicting the time at which the bed configuration reaches equilibrium conditions (R^2 = 0.92 and p-value= 0.02). In addition, for the case of relatively low sediment transport rates ($q^* < 10$) and long equilibrium times ($t_e > 1$ hr), all the experimental data lies within the 95% confidence interval.

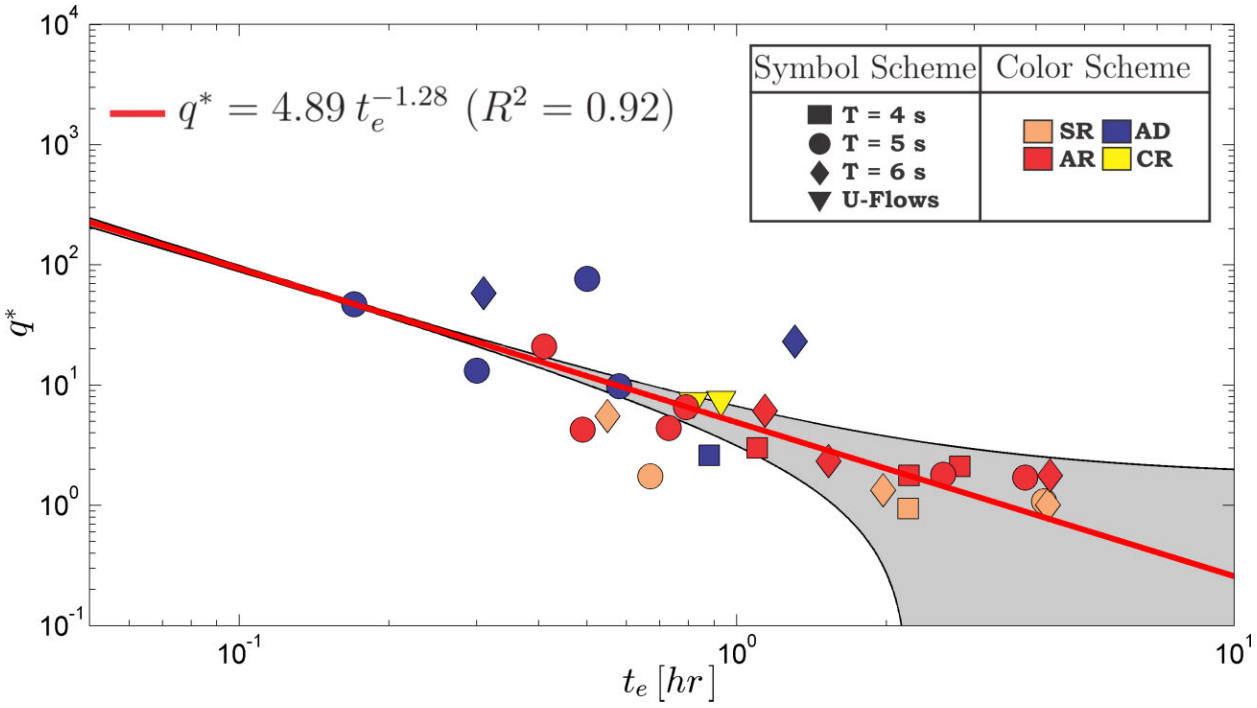

Figure 7.34: Equilibrium time as a function of the dimensionless bedload transport per unit width. The gray-shaded area represents the 95% confidence interval of the fitted function for the new proposed Equation (Equation 7.20). SR = Symmetric Ripples (light-orange), AR = Asymmetric Ripples (red), AD = Asymmetric Dunes (blue), and CR = Current Ripples (yellow).

7.5 Discussion

The evolution of bedforms from a flat bed was studied for a range of unidirectional, oscillatory and combined flow conditions over a 250 μm diameter sand bed. Based on the growth path described for the different types of flow, it can be concluded that the overall development (i.e., asymptotic growth) is clearly independent of the flow characteristics (Section 7.3). This result is consistent with the conclusion that could have been obtained if the results of

Sutherland and Hwang (1965) or Baas (1999) (unidirectional) were combined with the ones of Doucette and O'Donoghue (2006) (oscillatory), showing the same development curves to the present study. Furthermore, despite the difference in the morphological aspects (e.g., 2D vs 3D discussion in Section 7.3.2), the 'asymptotic growth' behavior is also independent on the final bedform stage. In other words, the general shape of the development curve is independent of the size (i.e., ripples vs dunes), shape (i.e., symmetric or rounded) and planform geometry (i.e., 2D vs 3D). A clear example of this result is the similar growth path of a two-dimensional symmetrical oscillatory ripple (Experiment 30, Figure 7.6) and a three-dimensional asymmetric rounded dune (Experiment 35, Figure 7.22). In addition to the independence on the flow characteristics (e.g., unidirectional vs combined flow) and the final bedform geometry (e.g., 2D vs 3D or CR vs SR), the development growth-path is also found to be grain-size independent. Faraci and Foti (2002) and the experiments herein (Table 7.1) were all conducted over a 0.25 mm diameter sand bed, whereas Lofquist (1978), Baas (1993) and Doucette and O'Donoghue (2006) conducted experiments over a wide range of grain sizes: D_{50} = 0.18 mm, D_{50} = 0.21 mm, D_{50} = 0.55 mm (Lofquist, 1978), D_{50} = 0.095 mm and D_{50} = 0.238 mm (Baas, 1993) and D_{50} = 0.44 mm (Doucette and O'Donoghue, 2006) and all results describe the same behavior. Therefore, it can be concluded that the development path described in Section 7.3 is ubiquitous for all types of subaqueous bedforms.

Consequent to the invariance of flow type (i.e., unidirectional, oscillatory or combined flow) on bedform development (Section 7.3), the analysis of the equilibrium time presents the same conclusion (symbol scheme in Figure 7.34). The different flow conditions (i.e., different velocities or periods) alter the sediment transport stages (through the SFD "trinity"), but no differences were found between different periods or flow types. However, the equilibrium time it is not independent of the final equilibrium stage for the particular cases of the bedforms generated in this study, and the larger bed morphologies (i.e., dunes) took the least amount of time to reach equilibrium conditions, since they were generated under the

most active sediment transport regimes. On the other hand, the smaller bedforms (i.e., ripples) formed in the lower sediment transport conditions, and hence required more time to reach their stable configuration. This result depends on the fact that for this particular grain size ($D_{50} = 250\mu$m), the larger bedforms only formed under high sediment transport rates and the small bedforms formed only under low transport stages. Furthermore, both sediment transport and bedform states have a strong correlation with grain size, and hence the relationship between equilibrium time and bed stage presented in Figure 7.34 should not be generalized for other grain sizes. For example, for coarser grain sizes large-scale gravel dunes can be generated under flow conditions that are just above the threshold for sediment transport (Carling, 1999), hence requiring a long time to reach their stable configuration.

It is important to note that all the results described in this chapter do not take into account hysteresis. The bedforms in this study were generated from an initial flat bed by a specific flow condition. Therefore, these results should not been extrapolated to bed morphologies that are generated by varying flows.

7.6 Conclusions

The development of bedforms was studied under a diverse range of unidirectional, oscillatory and combined flow conditions over an initially flat bed. Based on the results of previous work and the present results, several conclusions can be reached:

- The development-path or bedform growth exhibits the same general trend regardless of the flow type (e.g., unidirectional vs combined flow), bedform size (e.g., ripples vs dunes), bedform shape (e.g., symmetric or rounded), bedform planform geometry (e.g., 2D vs 3D) and sediment grain size.

- Bedform development can be divided into four main stages regardless of the flow conditions: (1) incipient bedforms, (2) growing bedforms, (3) stabilizing bedforms, and

(4) fully-developed bedforms. This division is consistent with the separation proposed by Baas (1994, 1999) for pure unidirectional flows.

- Stage 1 is defined from the genesis of the bedforms until the first signs of bedform growth. The dominant morphological feature for pure unidirectional and current-dominated combined flows started as longitudinal streaks that developed into very small three-dimensional ripples. On the other hand, for pure oscillatory and wave-dominated combined flows, the main juvenile bedform was transient rolling-grain ripples.

- Once the bed is fully covered with bed features, the bedform transitions to Stage 2 where the bedforms start to grow exponentially in time. This growth was proportionally to $\approx 1 - e^{-c\,t}$ and was successfully estimated by Equations 7.1 and 7.2. The large majority of the bedform enlargement takes place during this stage. The main mechanisms of bedform growth are sediment capturing and amalgamation with nearby bedforms.

- Stage 3 is defined as the temporal gap between the cessation of asymptotic growth and the time when the bed reaches equilibrium conditions. Compared with the growth in Stage 2, the enlargement during Stage 3 is minimal.

- Once the bedform reaches its equilibrium stage (Stage 4), the bed morphology remains in that regime until the flow conditions are changed. The equilibrium time t_e was defined by applying Equation 7.7 to the fitted data. The time of development was found to be inversely proportional to the amount of sediment transport occurring for that flow condition (Equations 7.21)

- During the fourth stage of development, the bedform wavelength and height fluctuate from their equilibrium mean wavelength and height. This variation is more marked for the case of three-dimensional bedforms, since the bed is constantly moving, with

bedforms merging and splitting and producing a relatively large range of active sizes.

- The behavior of bedforms during the fourth stage can be divided based on the final stage planform geometry. For the case of two-dimensional bedforms occurring only under pure oscillatory flows, there is a temporal separation between the time when the bed morphology reaches its equilibrium size and when the planform geometry becomes fully two-dimensional. In addition, three-dimensional bedforms generated under pure unidirectional, pure oscillatory and combined flows, exhibit a wider range of bedform sizes ($\sim$ 50% from the mean values) compared with two-dimensional oscillatory bedforms ($\sim$ 8% from the mean values). These results can be explained by the clear differences in the end state, with two-dimensional bedforms at planform-equilibrium being in a 'stable-equilibrium', whereas all three-dimensional bedforms are in a 'dynamic-equilibrium'.

Chapter 8

Unidirectional, Oscillatory and Combined Flow Bedform Indices

8.1 Introduction

In most field scenarios, stratigraphers have to make interpretation of paleoenviroments based on the cross-sectional form of preserved sedimentary structures (e.g., outcrops, cores). Therefore, geometrical analysis that examines the bedform indices can be essential to fully characterize the bedforms, and hence the paleoenviroment. Unfortunately, few studies report these variables, despite the fact that bedform indices (generally named ripple indices) were introduced almost half a century ago (Tanner, 1967). An explanation of their unpopularity lies in the fact that no study has assessed how useful or accurate these indices are in order to reconstruct paleoflows. Hence, based on the new experimental data presented herein, a detailed analysis of the most relevant bedform indices is made, with particular emphasis on their use to differentiate between unidirectional, oscillatory and combined flows.

8.2 Experimental Data

Tables 8.1 and 8.2 summarize the flow parameters and bedform characteristics of the 44 experiments conducted in the LOWST over a 250 μm sandy bed. The oscillatory flow velocities (U_o) were changed from 0 to 0.80 $m\,s^{-1}$, whilst the superimposed unidirectional flow velocities (U_u) were varied between 0 and 0.50 $m\,s^{-1}$ at three different periods (T = 4, 5 and 6 s).

Table 8.1: Summary of flow parameters and bedform characteristics.

#[a]	Init.[b] Cond.	T (s)	U_o ($m\,s^{-1}$)	U_u ($m\,s^{-1}$)	λ (m)	η (mm)	BI[c]	BSI[c]	BRI[c]	2D/3D[d]	Bedform[e] Type
01	00	04	0.25	0.00	0.22	34.8	06.3	0.96	0.40	2D	SR
02	00	04	0.25	0.10	0.15	20.5	07.4	1.39	0.45	2.5D	QAR
03	00	04	0.25	0.20	0.18	21.1	08.6	1.53	0.54	2.5D	AR
04	00	04	0.25	0.30	0.23	26.9	08.4	1.66	0.61	3D	ARR
05	00	04	0.25	0.40	0.51	35.6	14.3	2.36	0.72	3D	ARD
06	04	04	0.25	0.40	0.52	36.0	14.4	2.14	0.71	3D	ARD
07	00	04	0.30	0.00	0.20	31.0	06.5	1.04	0.41	3D	SR
08	00	05	0.20	0.00	21.20	35.3	06.1	0.97	0.36	2D	SR
09	13	05	0.20	0.00	18.50	33.1	05.7	1.00	0.39	3D	SR
10	11	05	0.20	0.00	16.20	23.6	07.1	0.98	0.42	3D	SR
11	00	05	0.20	0.10	14.60	36.4	09.3	1.17	0.52	3D	QAR
12	00	05	0.20	0.20	21.60	27.3	08.0	1.34	0.54	3D	QAR
13	01	05	0.20	0.20	20.20	30.0	06.7	1.32	0.53	3D	QAR
14	09	05	0.20	0.20	20.90	29.3	07.2	1.28	0.55	3D	QAR
15	00	05	0.20	0.30	26.90	27.6	08.8	1.96	0.61	3D	ARR
16	00	05	0.20	0.40	60.10	30.3	12.7	2.29	0.78	3D	ARD
17	00	05	0.20	0.50	88.40	44.6	11.7	3.20	0.88	3D	ARD
18	00	05	0.40	0.00	23.90	22.0	10.7	1.11	0.43	3D	SR
19	00	05	0.40	0.10	22.20	23.0	09.7	1.31	0.32	3D	QAR
20	00	05	0.40	0.20	21.00	20.7	10.5	1.31	0.68	3D	QARR
21	00	05	0.40	0.30	42.20	61.3	08.7	1.22	0.73	3D	QARR
22	00	05	0.40	0.40	102.10	98.3	10.4	4.20	0.89	2D[1]	ARD
23	17	05	0.40	0.40	105.30	102.3	10.3	4.16	0.92	2D[1]	ARD
25	00	05	0.50	0.40	123.20	153.0	08.1	3.10	0.63	2D[1]	ARD
26	41	06	0.10	0.20	0.22	23.2	09.5	1.97	0.53	3D	AR
27	00	06	0.10	0.50	0.49	35.5	13.8	1.72	0.52	3D	CR
28	28	06	0.15	0.40	0.56	37.9	14.9	3.26	0.58	3D	AD
29	39	06	0.20	0.00	0.25	42.0	06.0	1.04	0.37	2D	SR
30	00	06	0.25	0.00	0.20	32.1	06.2	1.08	0.42	2D	SR
31c	00	06	0.25	0.05	0.18	26.6	06.8	1.37	0.43	2.5D	SR
32	00	06	0.25	0.10	0.19	17.2	10.9	1.44	0.40	3D	QAR
33	00	06	0.25	0.20	0.17	17.6	09.8	1.45	0.45	3D	QAR
34	00	06	0.25	0.30	0.25	23.3	10.6	2.79	0.72	3D	ARR

[a] Experiment number

[b] Initial condition of the sediment bed at the beginning of the experiment: 00 indicates flat bed, other numbers indicate the number of the experiment run before.

[c] $BI = \lambda_\eta\,\eta^{-1}$ (Equation 8.1), $BSI = \lambda_s\,\lambda_l^{-1}$ (Equation 8.2) and $BRI = \lambda_{0.5\,s}\,\lambda_s^{-1}$ (Equation 8.3).

[d] 2D indicates two-dimensional bedforms, 2.5D indicates the presence of two-dimensional, and three-dimensional or wavy bedforms and 3D indicates three-dimensional bedforms. The superscript [1] indicates that the width of the flume was not large enough for bedforms to fully develop their planform geometry.

[e] SR = Symmetric Ripples, SD = Symmetric Dunes, AR = Asymmetric Ripples, ARR = Asymmetric Rounded Ripples, QAR = Quasi-Asymmetric Ripples, QARR = Quasi-Asymmetric Rounded Ripples, AD = Asymmetric Dunes, ARD = Asymmetric Rounded Dunes and CR = Current Ripples.

Table 8.2: Summary of flow parameters and bedform characteristics. (cont'd).

#[a]	Init.[b] Cond.	T (s)	U_o ($m\,s^{-1}$)	U_u ($m\,s^{-1}$)	λ (m)	η (mm)	BI[b]	BSI[c]	BRI[c]	2D/3D[d]	Bedform[e] Type
35	00	06	0.25	0.40	0.65	68.3	09.5	3.15	0.64	3D	ARD
36	00	06	0.25	0.50	1.30	123.0	10.6	3.69	0.82	3D	ARD
37	16	06	0.30	0.00	0.22	39.4	05.6	1.15	0.45	2.5D	SR
38	40	06	0.30	0.10	0.17	18.4	09.3	1.37	0.44	3D	QAR
39	42	06	0.30	0.20	0.30	38.8	07.8	1.46	0.51	3D	QAR
40	44	06	0.40	0.20	0.32	48.6	06.6	1.63	0.63	3D	ARR
41	45	06	0.40	0.30	0.74	84.2	08.8	2.17	0.72	3D[1]	ARD
42	00	06	0.50	0.00	0.28	32.3	08.7	1.14	0.41	3D	SR
43	29	06	0.50	0.30	0.56	31.0	18.0	3.33	0.71	3D	ARD
45	00	06	0.70	0.00	0.71	50.1	14.2	0.91	0.38	3D	SD
46	29	06	0.80	0.20	0.73	71.0	10.3	1.20	0.50	3D	SD
54	00	-	-	0.40	0.20	17.6	11.4	2.21	0.51	3D	CR
55	00	-	-	0.50	0.21	18.1	11.8	2.36	0.49	3D	CR

[a,b,c,d,e] See Table 8.1

8.3 Bedform Indices

Tanner (1967) discussed the uses of several bedform indices including

$$BI \;=\; \lambda_\eta\, \eta^{-1} \quad \text{Bedform Index} \tag{8.1}$$

$$BSI \;=\; \lambda_s\, \lambda_l^{-1} \quad \text{Bedform Symmetry Index.} \tag{8.2}$$

By plotting Equations 8.1 and 8.2, a dimensionless geometrical phase-space can be established for different bedforms generated by a variety of flows (Figure 8.1). Yokokawa (1995) highlighted the need to distinguish combined flow bedforms from oscillatory and unidirectional features by measuring a new bedform index, named the bedform roundness index, which can be plotted against BSI to generate a new geometrical-phase-space (Figure 8.2)

$$BRI \;=\; \lambda_{0.5\,s}\, \lambda_s^{-1} \quad \text{Bedform Roundness Index.} \tag{8.3}$$

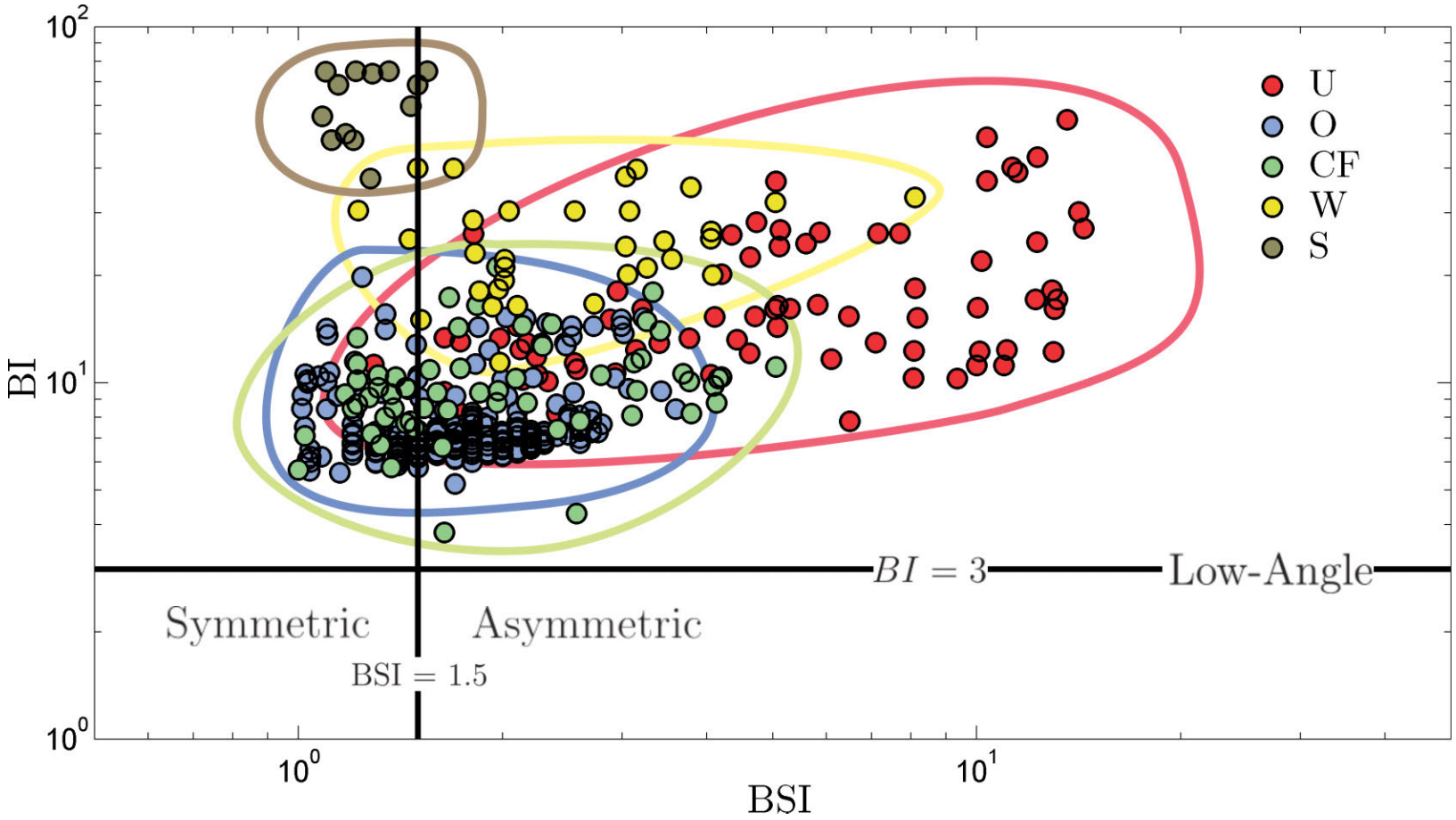

Figure 8.1: Bedform Index plotted against Bedform Symmetry Index. Data used comes from this study, Yokokawa (1995), Dumas et al. (2005), Venditti et al. (2005a), Yamaguchi and Sekiguchi (2010) and Martin and Jerolmack (2013). Bedform indices are shown for different type of flows, where U = unidirectional, O = oscillatory, CF = combined flows, W = wind and S = swash-zone bedforms.

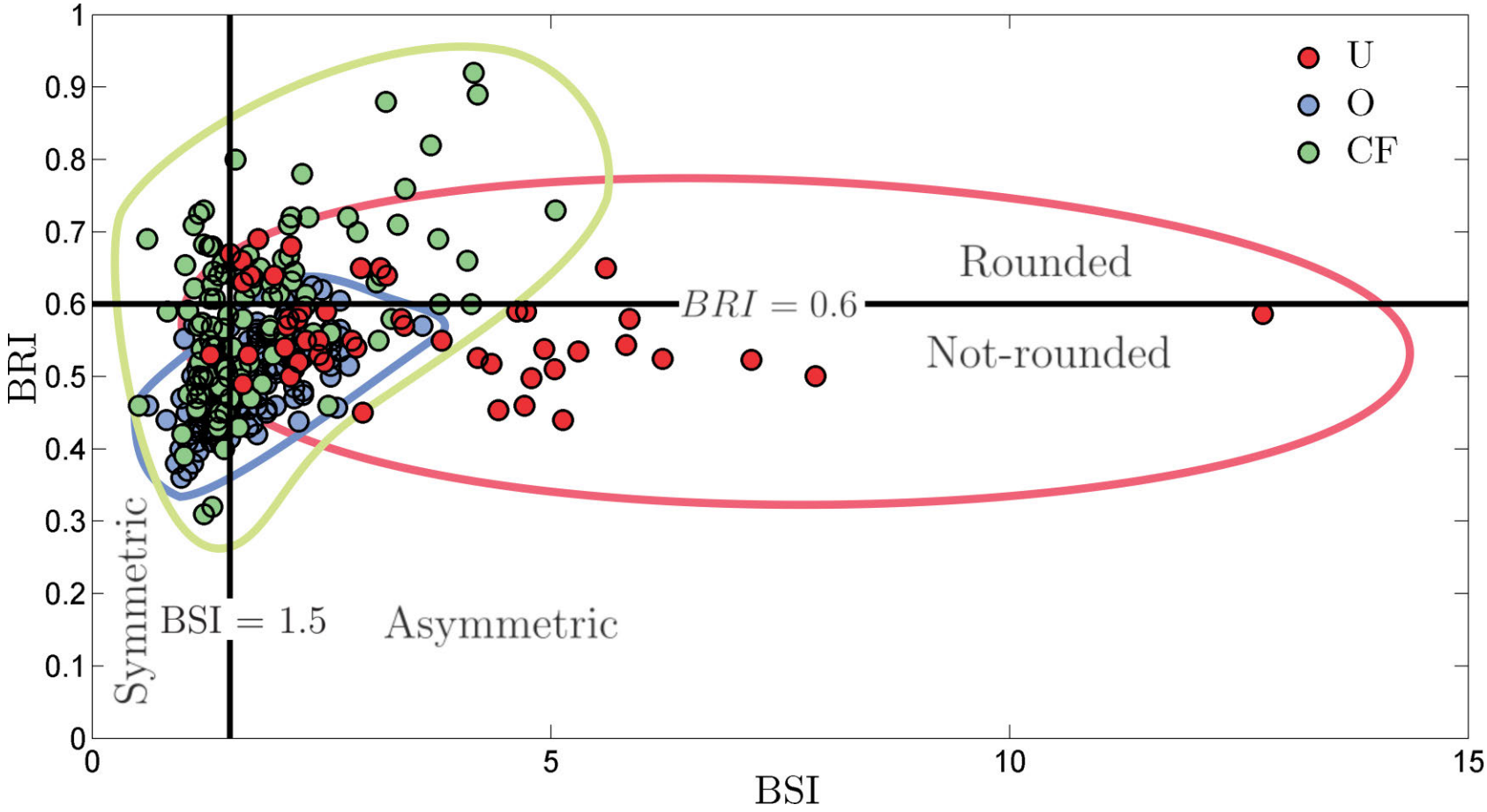

Figure 8.2: Bedform Roundness Index plotted against Bedform Symmetry Index. Data used comes from this study, Yokokawa (1995), Dumas et al. (2005), Venditti et al. (2005a), Yamaguchi and Sekiguchi (2010) and Martin and Jerolmack (2013). Bedform indices are shown for different types of flow, where U = unidirectional, O = oscillatory and CF = combined flows bedforms.

Although these dimensionless geometrical-phase-spaces do not show unique zones where only one type of flow condition exists, several trends can be observed (Figure 8.3):

Unidirectional Bedforms $60 > BI > 6$, $BSI > 1.2$ and $BRI \approx 0.5$

Oscillatory Bedforms $20 > BI > 5$, $BSI < 3.5$ and $BRI \lessapprox 0.5$

Combined Flow Bedforms $20 > BI > 3$, $BSI < 5$ and $BRI > 0.3$

Wind Bedforms $50 > BI > 10$ and $BSI < 8$

Swash-Zone Bedforms $100 > BI > 30$ and $BSI < 2$

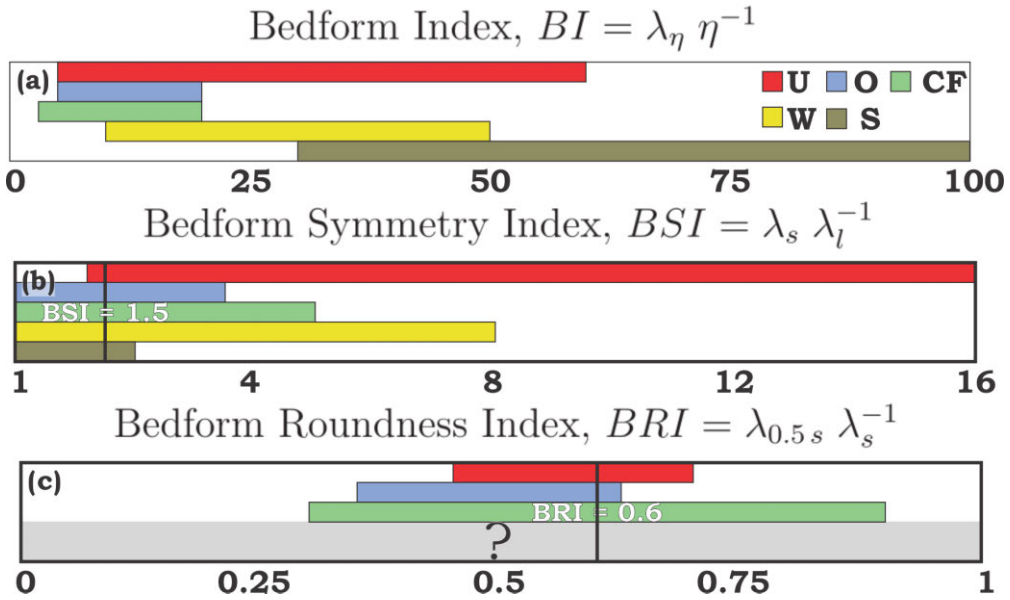

Figure 8.3: Graphical scheme that represents the range of (a) Bedform Index, (b) Bedform Symmetry Index and (c) Bedform Roundness Index, for different type of bedforms. U = unidirectional, O = oscillatory, CF = combined flows, W = wind and S = swash zone bedforms.

Figure 8.3 shows a graphical representation of the ranges of the bedform indices (Equations 8.1, 8.2 and 8.3) for different types of bedforms. Since there are no published data for BRI for wind (yellow) and swash (brown) bedforms, the discussion will only focus on the unidirectional, oscillatory and combined flow data sets. Unfortunately, none of the individual bedform indices by itself shows any promise to be a clear and unique measurement that

can be employed in the field to quickly distinguish between flow types. This result does not coincide with early results proposed by Yokokawa (1995) where a very clear distinction was found between unidirectional, oscillatory and combined flow bedforms. The pioneering work by Yokokawa (1995) was based on the relatively limited data of BRI at the time (N = 66), which did not include any observations in the overlapping zones. In some occasions, despite the multiple overlaps, the set of bedform indices can be used to define the flow type. For example, if a bedform has indices $BI = 25$, $BSI = 4$ and $BRI = 0.5$, although BSI and BRI does not provide any conclusive information, BI can be used to conclude unambiguously that the bedform was generated under unidirectional flows. This can be done in some very particular cases where some of the bedform indices lie within a range with no overlap (i.e., $BI > 20$ and $BRI > 0.7$). Nonetheless, there is a large subset of variables that does not lead to an answer, since none of the indices can unequivocally define one flow type (e.g., $BI = 12$, $BSI = 1.5$ and $BRI = 0.5$). In order to provide an alternative to the desired deterministic method (i.e., one set of bedform indices will unambiguously define one type of flow), a very simple multinomial logistic regression (Hosmer and Lemeshow, 2000) was performed using the MATLAB®(R2012a) Statistics Toolbox. Multinomial logistic regressions are one of the most common tools to analyze categorical data (Agresti, 1996). Thus the three different flow types (unidirectional, oscillatory and combined flows) are defined as the categorical variables with the bedform indices as the independent variables

$$\begin{aligned} U &= \mathfrak{f}(BI, BSI, BRI) \\ O &= \mathfrak{f}(BI, BSI, BRI) \\ CF &= \mathfrak{f}(BI, BSI, BRI) \end{aligned} \tag{8.4}$$

Hence, if a linear model is assumed and the experimental data from the pure unidirectional flows is chosen as a reference or base (Hosmer and Lemeshow, 2000), the log-odds or logits are

$$Z_{U,O}(BI, BSI, BRI) = -0.56\,BI - 0.37\,BSI - 4.75\,BRI + 9.74 \tag{8.5}$$

$$Z_{U,CF}(BI, BSI, BRI) = -0.16\ BI - 0.49\ BSI + 2.65\ BRI + 1.92 \tag{8.6}$$

where 9.74 and 1.92 are two constants and the rest of the values are the regression coefficients computed from the model. The R^2 of the regression coefficient is 0.56 and an average p-value is 0.01. Despite the relatively low R^2, the fact that the p-value$<$ 0.05 allows rejection of the null hypothesis, which makes the regression statistically significant. These logits (Equations 8.5 and 8.6) can be used to formulate a probabilistic model to obtain the likelihood of categorical variables (flow type) for an individual set of independent variables (bedform indices)

$$\mathcal{P}_u(BI, BSI, BRI) = \frac{1}{1 + e^{Z_{U,O}} + e^{Z_{O,CF}}} \tag{8.7}$$

$$\mathcal{P}_o(BI, BSI, BRI) = \frac{e^{Z_{U,O}}}{1 + e^{Z_{U,O}} + e^{Z_{O,CF}}} \tag{8.8}$$

$$\mathcal{P}_{CF}(BI, BSI, BRI) = \frac{e^{Z_{O,CF}}}{1 + e^{Z_{U,O}} + e^{Z_{O,CF}}}. \tag{8.9}$$

A set of examples of the use of Equations 8.7-8.9 are listed below (Table 8.3).

The values presented in Table 8.3 are a compilation of bedform indices from previous work and from measurements at the Lower-Colorado River in the Colorado River Wildlife Sanctuary near Austin, Texas (Figure 8.4). The field measurements were taken over 11 ripples (Figure 8.4c-d) located in different locations on a sandy river bed (Figure 8.4b). Equations 8.7-8.9 successfully predicted the flow type 23 times out of the 25 measurements ($\sim 92\%$). The lack of a perfect prediction (i.e., 25 out of 25) is expected due to the nature of the overlap between bedform geometries (Figure 8.3). In other words, since there is a large range of bedform geometries generated from a particular type of flow, any observation can lie close to the most likely geometry of other type of flow, generating the wrong prediction. Therefore multiple observations are required to minimize this error, and as illustrated in Table 8.3, the averaged percentage clearly predicts the right flow type.

In addition, the regression coefficients of the logits (Equations 8.5 and 8.6) can be used to characterize the relative weight (compared with the base case, unidirectional bedforms)

Table 8.3: Different probability distributions for flow type based on different bedform indices measured in the Lower-Colorado River and from previous studies.

Independent Variables			Categorical Variables (%)			Predicted[b]	Measured[b]
BI[a]	BSI[a]	BRI[a]	U[b]	O[b]	CF[b]		
32.0	7.0	0.50	**99.50**	00.00	00.50	U	U†
10.5	6.7	0.40	**56.95**	35.00	08.05	U	U†
12.0	5.0	0.30	**50.90**	39.33	09.77	U	U†
8.4	3.3	0.40	11.41	**77.03**	11.56	*O*	*U*†
12.0	5.0	0.50	**61.51**	18.38	20.10	U	U†
19.2	4.8	0.32	**92.07**	01.31	06.62	U	U†
11.3	5.0	0.40	**49.66**	36.32	14.02	U	U†
10.0	3.3	0.60	29.50	31.21	**39.29**	*CF*	*U*†
11.6	4.5	0.44	**50.54**	29.97	19.49	U	U†
9.5	6.0	0.39	38.44	**53.09**	08.47	*O*	*U*†
16.5	3.7	0.45	**75.61**	03.76	20.63	U	U†
Averaged Percentages			**56.01**	29.58	14.41	U	U†
6.4	1.0	0.31	0.01	**0.95**	0.04	O	O‡
7.2	1.2	0.42	0.03	**0.85**	0.12	O	O‡
3.9	1.0	0.50	0.01	**0.93**	0.07	O	O‡
4.6	1.2	0.65	0.02	**0.77**	0.21	O	O*
5.2	1.3	0.47	0.01	**0.90**	0.08	O	O*
4.4	1.6	0.63	0.02	**0.81**	0.17	O	O§
3.0	1.6	0.55	0.01	**0.93**	0.06	O	O§
3.6	1.4	0.50	0.01	**0.94**	0.05	O	O§
4.3	1.1	0.44	0.01	**0.94**	0.05	O	O§
4.1	1.0	0.35	0.00	**0.97**	0.02	O	O§
4.9	1.9	0.56	0.02	**0.85**	0.12	O	O††
4.7	1.0	0.50	0.01	**0.90**	0.09	O	O††
6.2	1.6	0.77	0.06	0.43	**0.51**	CF	CF$^{\wr}$
7.8	1.6	0.68	0.09	0.42	**0.49**	CF	CF$^{\wr}$

[a] $BI = \lambda_{\eta}\,\eta^{-1}$ (Equation 8.1), $BSI = \lambda_{s}\,\lambda_{l}^{-1}$ (Equation 8.2) and $BRI = \lambda_{0.5\,s}\,\lambda_{s}^{-1}$ (Equation 8.3).

[b] U = Pure Unidirectional Flows, O = Pure Oscillatory Flows and CF = Combined Flows. References = †Lower-Colorado Measurements, ‡Bagnold (1946),*Campbell (1966), §Faraci and Foti (2002), ††Admiraal et al. (2006) and $^{\wr}$Yokokawa et al. (1995)

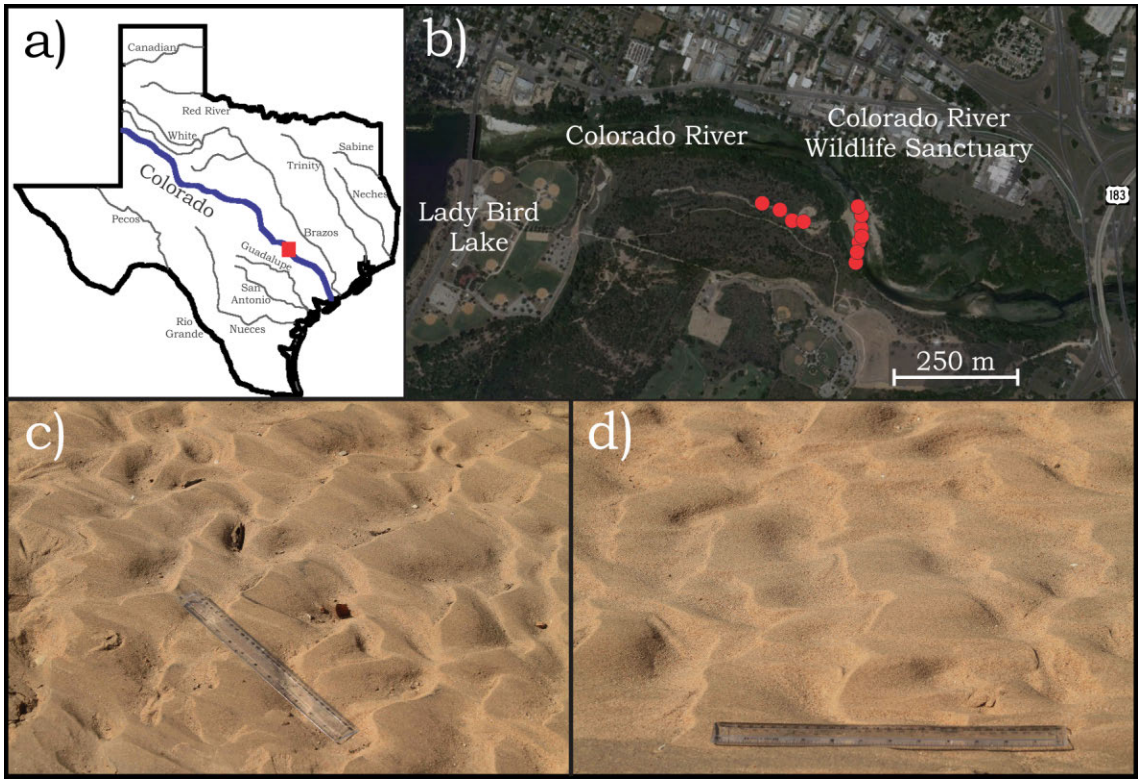

Figure 8.4: a) Location of the study area, Lower-Colorado River, near Austin, Texas. b) Approximate location of the ripple measurements represented by the red circles (Table 8.3). c-d) Unidirectional ripples from the location area.

of the different independent variables (i.e., bedform indices) in the probability. For example, the coefficients for BI are -0.56 for the comparison between oscillatory bedforms with unidirectional bedforms (U,O), and -0.16 for the comparison between combined flow bedforms with unidirectional bedforms (U,CF). Both coefficients are negative, so an increase in the value of BI will decrease the probability of either being generated by oscillatory or combined flow. In addition, since the coefficient for the U,O is smaller than the U,CF coefficient, it is less likely to be generated by oscillatory flows. The same thought process can be used to conclude that an increase in BSI will increase the probability of the bedform being generated under combined, rather than oscillatory flows, but yet it is more likely to be unidirectionally-generated. On the other hand, an increase in BRI increases the probability of unidirectional flows being the characteristic flow rather than oscillatory flow. However, a decrease in BRI reduces the probability of unidirectional flows compared with combined

flows.

8.3.1 Bedform Index

Between all the geometrical indices, the most documented in the literature is the Bedform Index (e.g., Dumas et al., 2005) or its inverse, the bedform steepness (e.g., Carling, 1999; van der Mark and Blom, 2007) given in Equation (8.1). Previous studies of combined flows have reported an abrupt change in the bedform wavelength between dunes and ripples (larger and small ripples in the nomenclature of Arnott and Southard, 1990; Dumas et al., 2005), a result that can influence the overall distribution of BI under combined flows. Dumas et al. (2005) reported that there is a gap in bedform wavelength between ≈ 0.30 and ≈ 1 m (green-shaded area in Figure 8.5), this conclusion being based on the lack of *equilibrium* wavelength bedforms (N = 159, squared symbols in Figure 8.5) in the 'size-gap' proposed. However, the experimental results presented in this chapter do not allow the same conclusion. Several equilibrium wavelengths for combined-flow ripples and dunes were observed in the 'size-gap' (triangles in Figures 8.5). Furthermore, as discussed in Chapter 7, the equilibrium value of the wavelength or height is not necessary a representative measure of the distribution of bed configuration sizes (Figure 8.6). Figure 8.6 not only presents an example of a bed state where the mean equilibrium wavelength (λ_e) is in the 'size-gap' domain, but also the associated equilibrium distribution of bedform sizes covers a wide range of sizes. However, it is important to note that the presence of these 'medium size' bedforms occurred only under flow conditions that had been previously unexplored (no squares in the green-shaded area in Figure 8.5). The experiments conducted by Arnott and Southard (1990) and Dumas et al. (2005) were conducted under unidirectional velocities up to 0.30 $m\,s^{-1}$ with grain sizes smaller than 0.17 mm (square symbols in Figure 8.5), and these bedforms were generally observed under unidirectional velocities greater than $0.30\,m\,s^{-1}$ (mean $\approx 0.40\,m\,s^{-1}$) with a $D_{50} = 0.25$ mm (triangle symbols in Figure 8.5). Furthermore, the large majority of the new combined flow experiments conducted in the LOWST with unidirectional velocities smaller

than $0.30\,m\,s^{-1}$ had wavelengths less than 0.30 m. Therefore, if only the mean values of the wavelength are considered, there might be a true size gap for wave-dominated combined flows, and the wavelength continuum is a representation of current-dominated combined flows. On the other hand, the gap probably is present only in the mean or equilibrium values of the wavelength, and if the whole dispersion of bed features is used multiple bedforms populate the 'size-gap'.

The mean equilibrium wavelength (λ_η) was plotted against the combined-flow water excursion d_o^+

$$d_o^+ = \frac{(U_u + U_o)\,T}{\pi} \tag{8.10}$$

to compare the dependence between the two variables with the classic oscillatory-flow relationship that relates bedform wavelength (λ_η) to the pure oscillatory water excursion length (d_o)

$$d_o = \frac{U_o\,T}{\pi}. \tag{8.11}$$

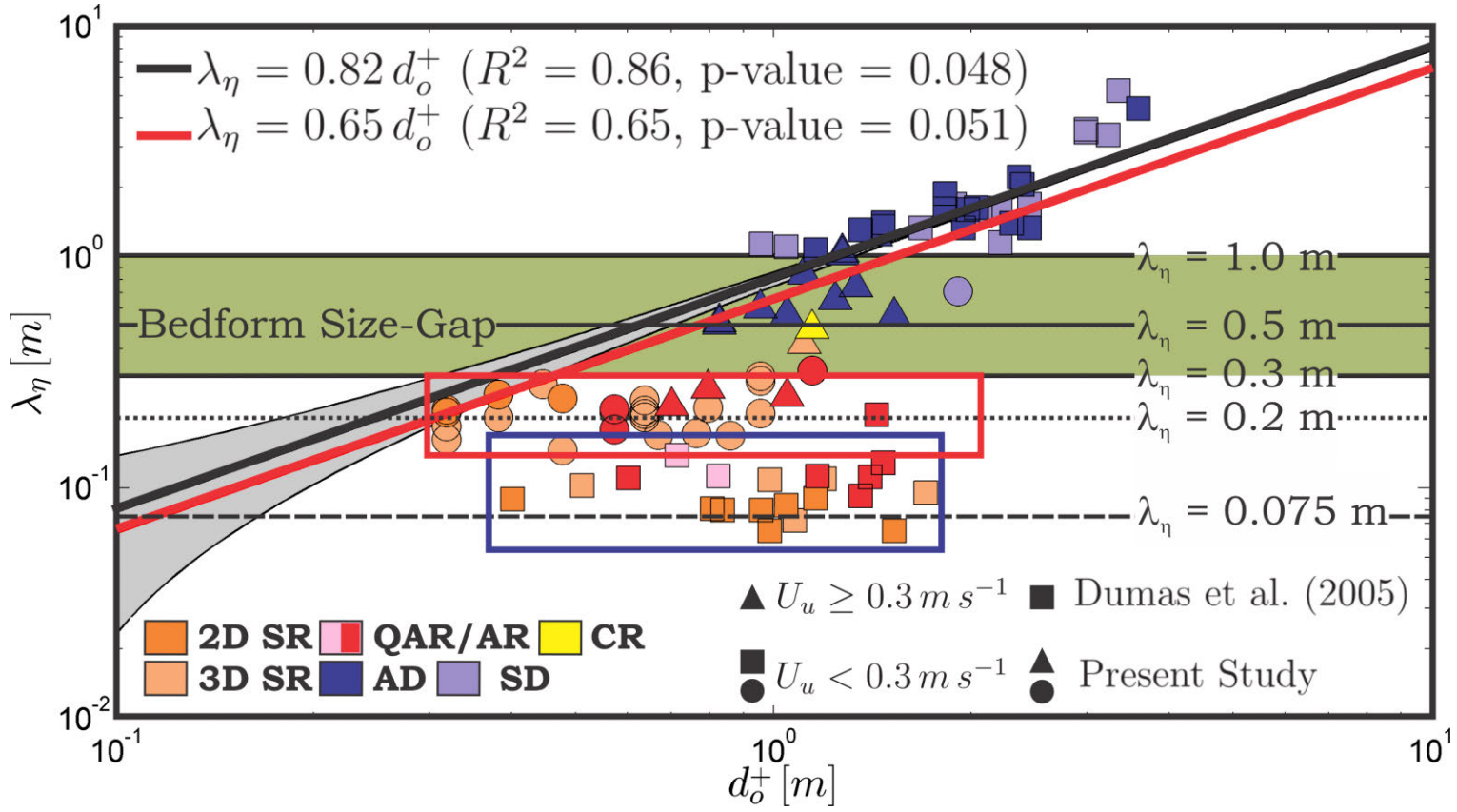

Figure 8.5: Bedform wavelength at equilibrium conditions as a function of the maximum combined-flow water excursion. Data from Dumas et al. (2005) (squares, sample size = 159) and new experiments at LOWST (circles and triangles, sample size = 44). Note that all the experimental data from Dumas et al. (2005) has $U_u < 0.3\, m\, s^{-1}$ (squares symbols). In addition, the large majority of the experiments with $U_u \geq 0.3\, m\, s^{-1}$ (triangles symbols) lie within the bedform size gap (green). The gray-shaded area represents the 95% confidence interval of the fitted function (black line, Equation 8.13). The red line represents the relationship between λ_η and d_o^+ for pure oscillatory orbital ripples (Clifton, 1976). 2D SR = Two-dimensional Symmetric Ripples (dark-orange), 3D SR = Three-dimensional Symmetric Ripples (light-orange), AR = Asymmetric Ripples (red), QAR = Quasi-asymmetric Ripples (pink), AD = Asymmetric Dunes (blue), SD = Symmetric Dunes (purple) and CR = Current Ripples (yellow). SR, QAR and AR do not scale with the flow (blue and red boxes); wavelength is independent of the water excursion.

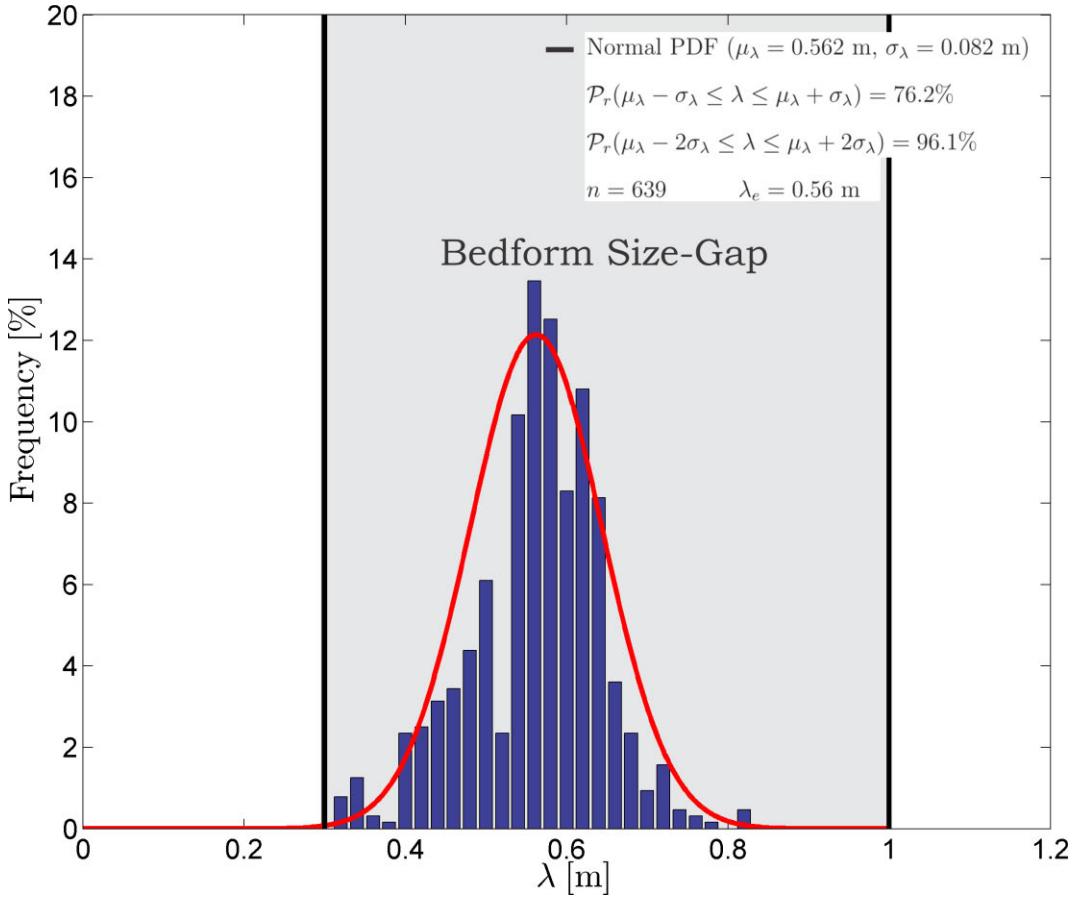

Figure 8.6: Histogram of bedform wavelength at equilibrium conditions for a three-dimensional asymmetric combined flow dune (Experiment 28). n is the number of measurements, P_r is the cumulative distribution function of the normal PDF (red line), λ_e is the equilibrium wavelength.

This type of relationship was first derived by Komar (1974) and later improved by Clifton (1976) to

$$\lambda_\eta = 0.65\, d_o, \tag{8.12}$$

and since then Equation (8.12) has been widely used in the geological community to predict paleoflow-depths (e.g., Dupré, 1984; Allen and Hoffman, 2005; Immenhauser, 2009). Relationships that simply relate the bedform size, which can be easily measured in the field, with the water excursion can be quickly used to back-calculate the water depth in the paleoenvironment. Therefore, based on their proven utility, a similar relationship can be proposed

for a subset of combined flow bedforms (data outside the red and blue boxes in Figure 8.5),

$$\lambda_\eta = 0.82\, d_o^+ \tag{8.13}$$

Like pure oscillatory and combined flow, a similar linear dependency is found in which the wavelength of dunes (previously named large ripples; e.g., Dumas et al., 2005) increase as the water excursion becomes larger. This result is consistent with previous studies under combined flows (Arnott and Southard, 1990; Dumas et al., 2005). Equation 8.13 (black line) and the 95% confidence interval (gray-shaded area) are plotted in Figure 8.5, showing the large amount of dispersion characteristic of bedforms (Figure 8.6). The fit of the experimental data was not able to account for the dispersion present in the data (symbols outside the gray-shaded area), although, no existing bedform predictor has been able to accomplish such a task (e.g., Raudkivi, 1997; Pedocchi and García, 2009b). Nevertheless, Equation 8.13 predicts a linear relationship between λ_η and d_o^+, and thus following the orbital/anorbital classification (Clifton, 1976), these bedforms can be classified as orbital.

On the other hand, similar to the experimental results of Dumas et al. (2005), the wavelength of SR, QAR and AR (small ripples in the nomenclature of Dumas et al., 2005) did not scale with the flow properties (i.e., the equilibrium wavelength was independent of the water excursion, symbols inside the blue and red box in Figure 8.5). This independence can be observed by the lack of an increment of the bedform wavelength as the combined flow orbital diameter is increased (symbols inside the blue and red box in Figure 8.5). Rather, the wavelength of oscillatory-flow and combined flow ripples remains constant at ~ 0.10 m for Dumas et al. (2005) ($D_{50} < 0.17$ mm; blue box in Figure 8.5) and ~ 0.20 m for the new combined flow experiments presented herein ($D_{50} = 0.25$ mm; red box in Figure 8.5). Hence, based on the behavior previously described, Dumas et al. (2005) classified such bedforms as anorbital. However, the wavelength of the bedforms present in the present study, which might be considered anorbital, have a wavelength that is twice as large as the characteristic

anorbital wavelength ($\lambda_\eta \sim 0.075 - 0.1$ m).

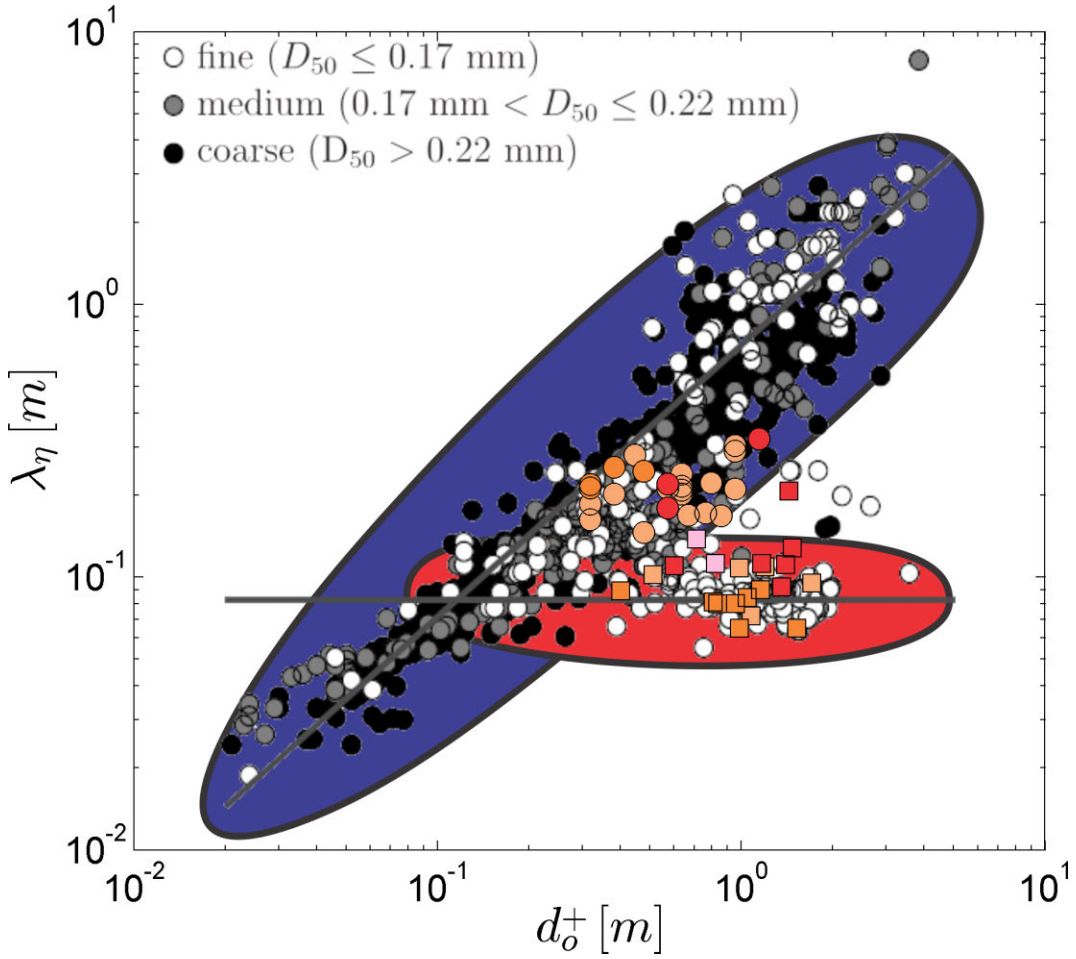

Figure 8.7: Experimental data relating d_o^+ with the wavelength spacing compiled by Pedocchi (2009) (pure oscillatory bedforms). In addition, the combined flow data inside the red and blue boxes from Figure 8.5 is plotted in color (for reference see Figure 8.5). The two lines corresponds to 'orbital' $\lambda_\eta = 0.65\, d_o$ (Equation 8.11) and 'anorbital' $\lambda_\eta = 0.075$ m trends. The blue and red-shaded zones are drawn to illustrate the range of orbital (blue) and anorbital (red) bedforms. Modify from Pedocchi (2009).

Nevertheless, despite this observation, the effects of grain size in the presence of orbital or anorbital bedforms is far from been understood (Cummings et al., 2009; Pedocchi, 2009). The presumably combined flow anorbital ripples in the present study generated with $D_{50} = 0.25$ mm lie within the large dispersion of orbital bedforms (colored circles in the blue-shaded area in Figure 8.7). However, it is hard to believe that the experimental data inside the red box in Figure 8.5 is actually scaling with d_o^+ as proposed by Figure 8.7 (blue-shaded area).

The combined flow anorbital ripples (symbols inside the red box in Figure 8.5) show no commensurate increase in bedform wavelength in a range between $d_o^+ = 0.3$ m and $d_o^+ = 1.15$ m, suggesting an anorbital classification. Therefore, it can be hypothesized that there might be some scaling effects between the anorbital wavelength and grain size. Unfortunately, the new experimental data presented in this study was unable to address such a grain size dependence, and further experimental work is required.

Similar to combined flow and oscillatory bedform wavelengths, the bedform index was found to have a strong relationship with the maximum combined-flow water excursion (d_o^+; Figure 8.8)

$$BI = 12.04\, d_o^{+\,0.32} \tag{8.14}$$

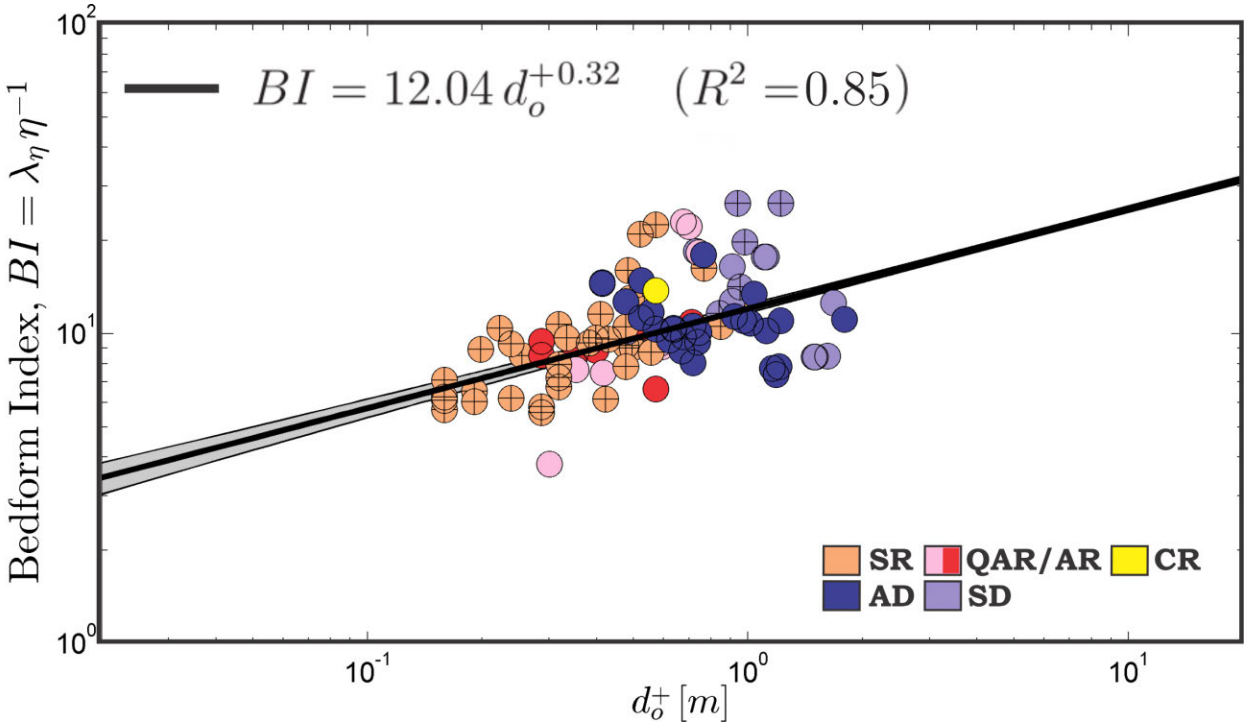

Figure 8.8: Bedform index as a function of the maximum combined-flow water excursion. The gray-shaded area represents the 95% confidence interval of the fitted function (Equation 8.14). SR = Symmetric Ripples (light-orange), AR = Asymmetric Ripples (red), QAR = Quasi-asymmetric Ripples (pink), AD = Asymmetric Dunes (blue), SD = Symmetric Dunes (purple) and CR = Current Ripples (yellow). Experimental data from Dumas et al. (2005) and the present study.

Figure 8.8 shows the linear regression (Equation 8.14) with a R-square of 0.85 (p-value = 0.0264, Appendix B.4) with the 95% confidence interval (gray-shaded area). Despite the natual dispersion, Equation 8.14 provides an overall good agreement with the experimental data. Furthermore, contrary to Equation 8.13, Equation 8.14 is able to represent (without accounting for the dispersion) all the combined flow bedforms from this study and the experimetal data from Dumas et al. (2005), including the anorbital bedforms.

8.3.2 Bedform Symmetry

One of the most clear descriptions that can be obtained from the cross-sectional geometry of bedforms in outcrops is the symmetry, and use of a quantitative value such as the bedform symmetry index is crucial to characterize this symmetry. To properly utilize this index, it is important to measure the lee and stoss side lengths using the distance between the trough and the crest, and not the trough and the brinkpoint (Allen, 1968). The separation between the crest and the brinkpoint is an important change in the cross-sectional geometry, but is independent of the change in symmetry (see section 8.3.3). Nevertheless, following the terminology proposed in chapter 5, the bedform symmetry can be classified as

$$\begin{array}{rrll} & BSI < & 1.3 & \text{Symmetric} \\ 1.3 < & BSI \geq & 1.5 & \text{Quasi-asymmetric} \\ & BSI < & 1.5 & \text{Asymmetric.} \end{array} \tag{8.15}$$

The presence of the unidirectional component in a given combined flow produces a net sediment transport downstream, which is reflected in the bedload transport (i.e., bedform migration). As preferential transport increases with the unidirectional flow velocities relative to the oscillatory component, the bedforms become oriented to this direction, thus producing an asymmetric profile. Figure 8.9 shows a range of cross-sectional geometries of different bedforms at equilibrium conditions with a fixed period (T = 4 s) and maximum orbital

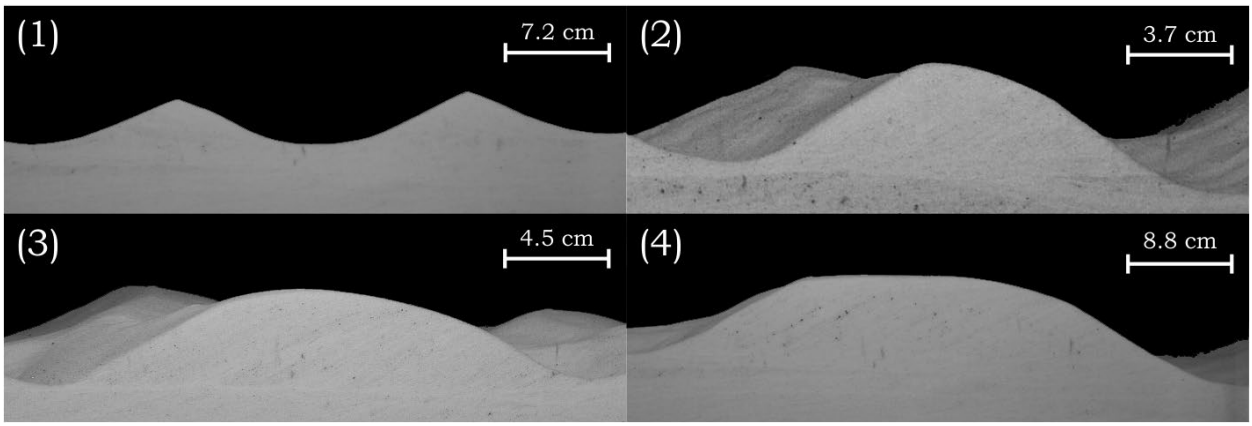

Figure 8.9: Different cross-sectional bedform geometries at equilibrium conditions. a) $BSI = 0.96$ - Experiment 01 ($T = 4$ s, $U_o = 0.25\,m\,s^{-1}$ and $U_u = 0\,m\,s^{-1}$), b) $BSI = 1.53$ - Experiment 03 ($T = 4$ s, $U_o = 0.25\,m\,s^{-1}$ and $U_u = 0.20\,m\,s^{-1}$), c) $BSI = 1.66$ - Experiment 04 ($T = 4$ s, $U_o = 0.25\,m\,s^{-1}$ and $U_u = 0.30\,m\,s^{-1}$) and d) $BSI = 2.36$ - Experiment 05 ($T = 4$ s, $U_o = 0.25\,m\,s^{-1}$ and $U_u = 0.40\,m\,s^{-1}$).

velocity ($U_o = 0.25\,m\,s^{-1}$) as the unidirectional flow is increased from $0\,m\,s^{-1}$ to $0.4\,m\,s^{-1}$. Therefore, the change between symmetric and asymmetric ripples is proportional to the relative amount of sediment transport generated by the unidirectional flow relative to the oscillatory flow. In addition, it was observed that BSI is also a function of the oscillation period (Figure 8.10)

$$\frac{BSI}{T_*} = 1.71 \times 10^{-10} \left(\frac{\theta_u}{\theta_o}\right)^{0.45} \tag{8.16}$$

where θ_u/θ_o is the ratio between the unidirectional and oscillatory Shields number and

$$T_* = T\nu/D_{50}^2 \tag{8.17}$$

is a dimensionless period. Equation 8.16 is a linear regression of the experimental data with an R^2 of 0.79 (p-value = 0.033, Appendix B.4; 95% confidence interval shown in the gray-shaded area in Figure 8.10). In addition, Equation 8.16 expresses two important behaviors of the BSI: i) it rises as the ratio between the unidirectional and oscillatory shear stress increases, and, ii) it exhibits a linear relationship with the dimensionless period T_*. Figure 8.10 shows the predictive power of Equation 8.16 for a range of oscillatory periods.

It can be observed that, despite the short range of oscillatory periods ($T = 4 - 9.4$ s), the relationship expressed by Equation 8.16 well predicts the degree of asymmetry for combined flows. However, Equation 8.16 does not show the asymptotic behavior necessary to predict the cases of pure oscillatory flows or pure unidirectional flows. Therefore, further experiments are needed to fully test this predictor and enlighten new physical processes that allow formulation of a universal equation for the bedform symmetry index.

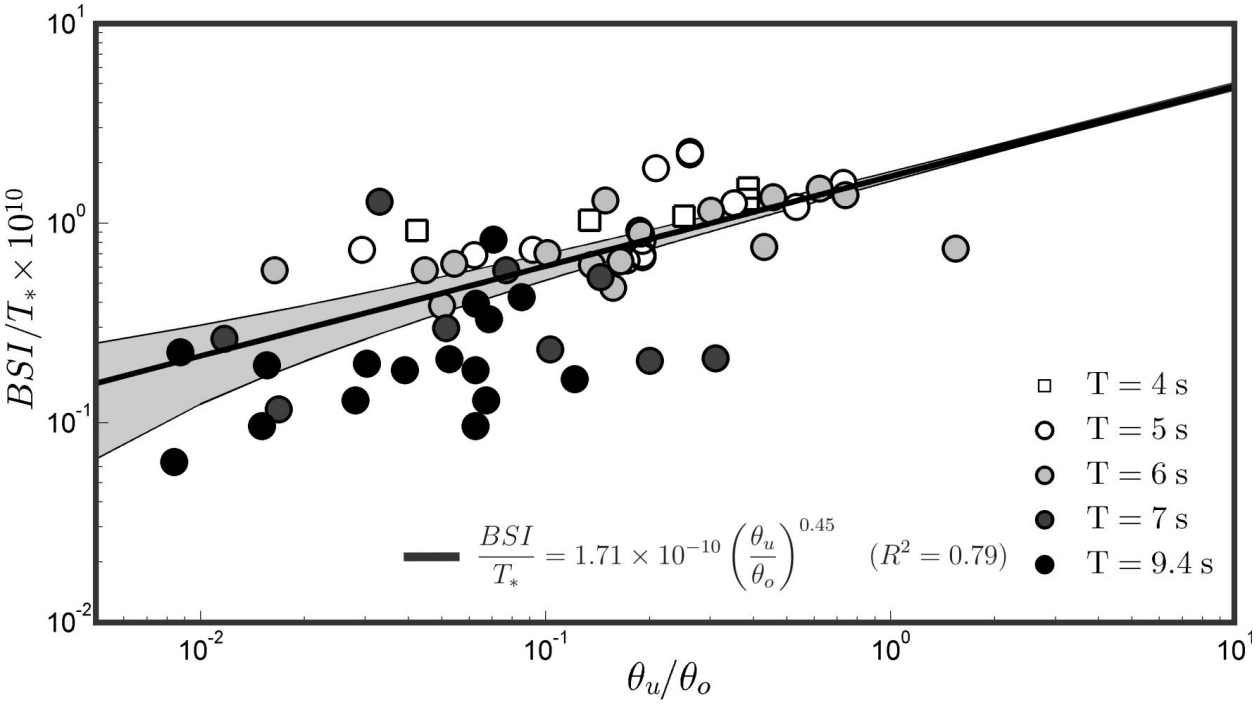

Figure 8.10: BSI/T_* as a function of the ratio between the current and wave Shields number (θ_c/θ_w), where T_* is the dimensionless wave period $T\nu/D_{50}^2$. The gray-shaded area represents the 95% confidence interval of the fitted function (Equation 8.16). Data from this study and Dumas et al. (2005).

8.3.3 Bedform Roundness

Bedforms with a rounded-stoss side have been described under relatively strong (below USPB conditions) unidirectional (e.g., Jopling and Forbes, 1979), oscillatory (e.g., Pedocchi and García, 2009b) and combined flows (e.g., Yokokawa, 1995). Figure 8.11 shows a range of different cross-sectional geometries at equilibrium conditions for pure oscillatory (Fig. 8.11a:

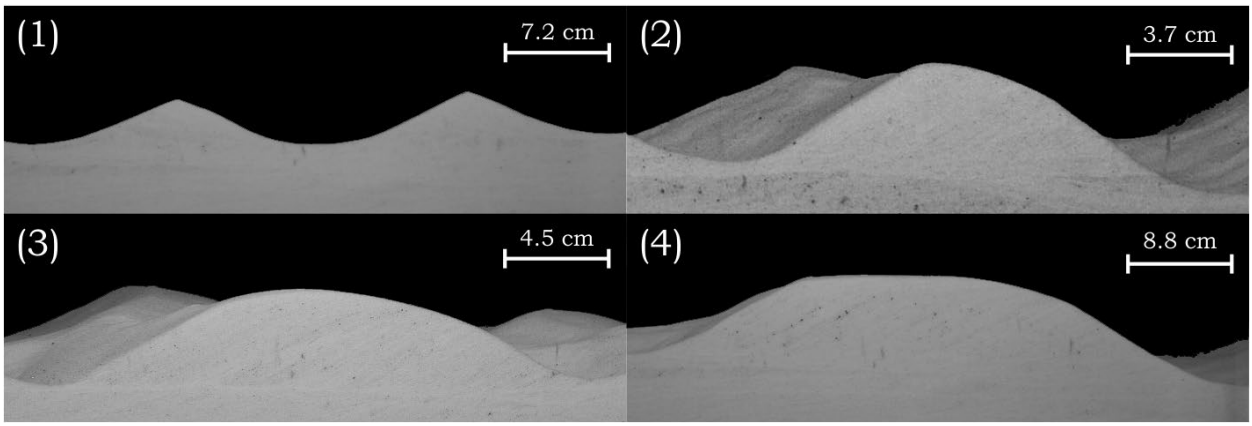

(a) Cross-sectional geometry of bedforms in the present study. (1) $BRI = 0.40$ - Experiment 01 ($T = 4$ s, $U_o = 0.25\,m\,s^{-1}$ and $U_u = 0\,m\,s^{-1}$), (2) $BRI = 0.54$ - Experiment 03 ($T = 4$ s, $U_o = 0.25\,m\,s^{-1}$ and $U_u = 0.20\,m\,s^{-1}$), (3) $BRI = 0.61$ - Experiment 04 ($T = 4$ s, $U_o = 0.25\,m\,s^{-1}$ and $U_u = 0.30\,m\,s^{-1}$) and (4) $BRI = 0.72$ - Experiment 05 ($T = 4$ s, $U_o = 0.25\,m\,s^{-1}$ and $U_u = 0.40\,m\,s^{-1}$). Flow direction from right to left.

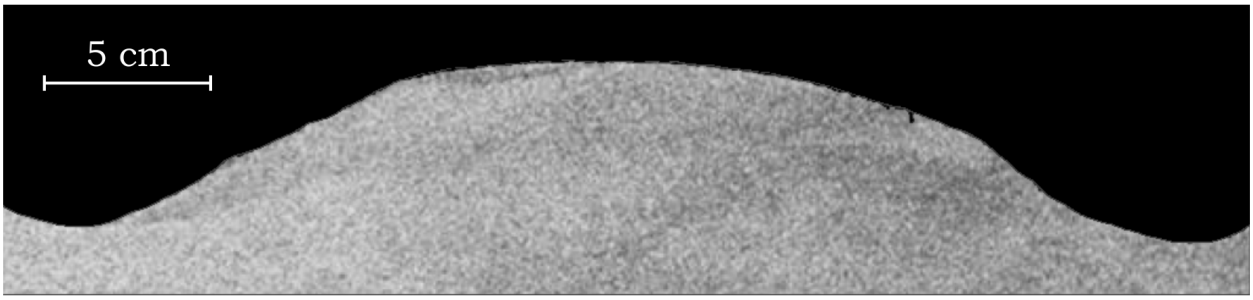

(b) Rounded ripple formed under pure unidirectional flows ($U_u = 0.45\,m\,s^{-1}$): $BRI = 0.61$. Flow direction from right to left. Modified from Jopling and Forbes (1979).

Figure 8.11: Different cross-sectional bedform geometries at equilibrium conditions.

1), combined (Fig. 8.11a: 2-4) and pure unidirectional (Fig. 8.11b) flows. Similar to the bedform symmetry index, the bedform roundness index increased as the unidirectional flow increases for a given period and oscillatory velocity (Figure 5.11 and Chapter 5). However, in these cases the same phenomenon occurred as the oscillatory velocity was increased. It is important to acknowledge that, in most cases, and especially for pure unidirectional and oscillatory flows, the roundness of the stoss side is a morphological representation of relatively high flow velocities and bed shear stresses. Hence, some of the bedforms generated under pure unidirectional and oscillatory flows are described as a transient stage or a gradual transition between ripples or dunes and USPB (e.g., Saunderson and Lockett, 1983; Bridge and Best, 1988; Pedocchi and García, 2009b). However, there is a set of combined flow

conditions where rounded bedforms are not generated under high shear stresses or close to the USPB transition. The additional process which rounds the bedforms in these combined flow conditions is associated with the flow reversal occurring under wave-dominated combined flows. Wave-dominated combined flows are such that the maximum shear stress at flow reversal (maximum oscillatory velocity in the upstream direction) is larger than the critical shear stress for sediment entrainment ($|\theta_{max}^{(-)}| > \theta_c$). Experiment 03 is used to illustrate this process, utilizing a sequence of cross-sectional pictures throughout a wave cycle (Figure 8.12). Wave-dominated combined flows are characterized by flow conditions where the current

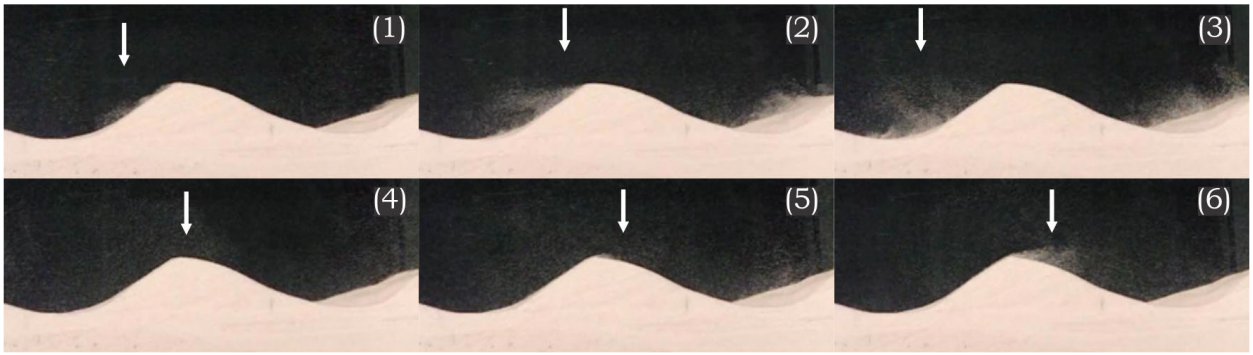

Figure 8.12: Sequence of pictures during a wave cycle for experiment 03 (wave-dominated combined flows), showing wave-reworking of the ripple crest. Pictures are temporally spaced at 0.61 s. Unidirectional flow from right to left. Bedform wavelength is 0.175 m. Since the bedforms are at equilibrium with the flow conditions, BRI remains unchanged at 0.54 for all the pictures.

boundary layer is not strong enough to prevent the wave boundary layer reversing the flow. Yet, the presence of the unidirectional flow produces a clear asymmetry in the flow near the bed (Figure 8.13) that is not only reflected in the bedform asymmetry, but also in the observed leeside (Figure 8.12:2) and stoss-side (Figure 8.12:6) flow separation eddies. When the direction of the oscillatory component and unidirectional flow coincide, flow separation is similar to that for unidirectional bedforms (Figure 8.12: 1-2, see section 3.2.2 or 3.2.3). On the other hand, the separation eddy (Figure 8.12:6) generated during flow reversal is generated under lower velocity conditions

(left side of the vertical lines in Figure 8.13a). This upstream flow separation eddy (Fig-

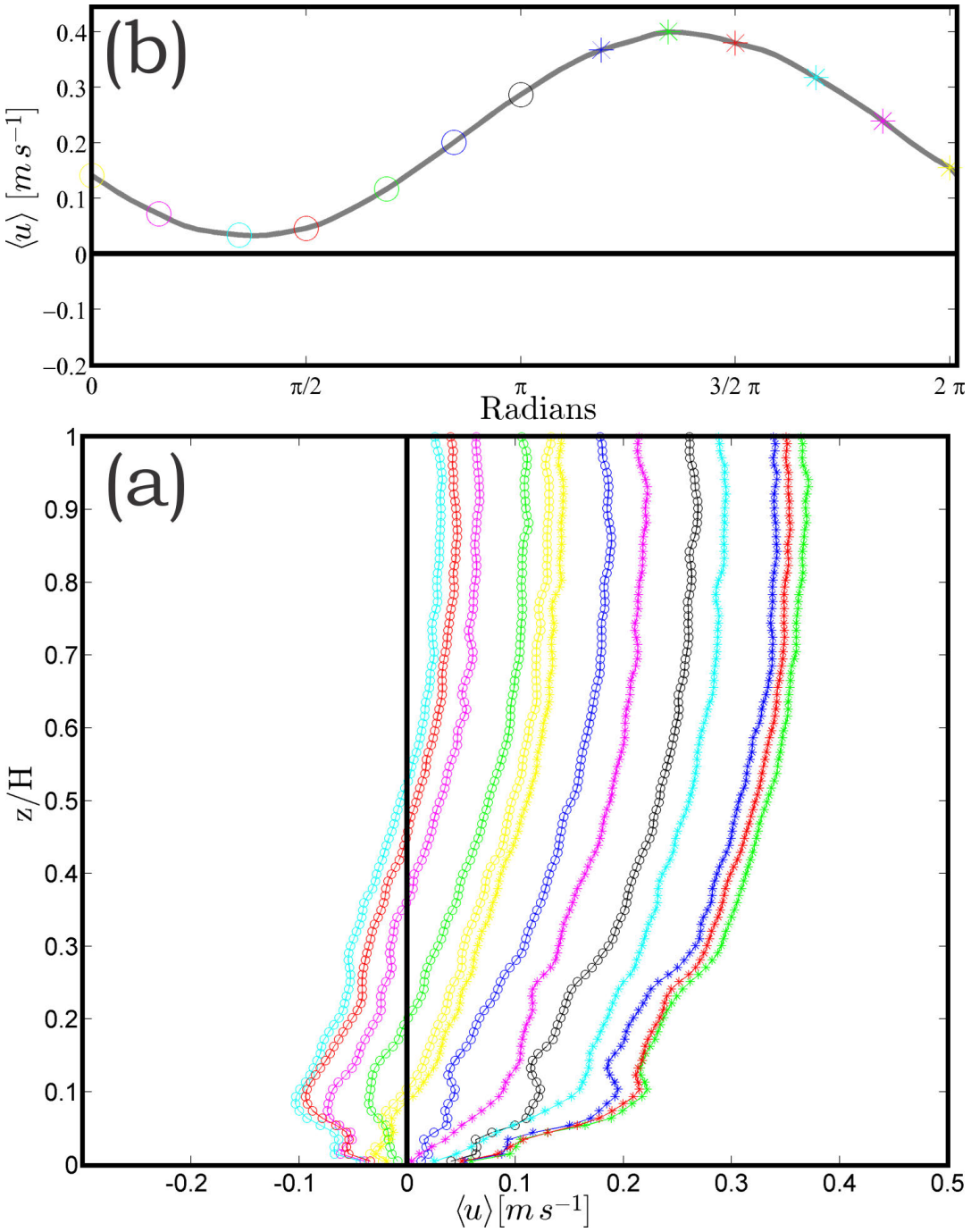

Figure 8.13: Velocity over a three-dimensional asymmetric combined flow ripple (Experiment 3). Oscillatory Condition: $U_o = 0.25\,m\,s^{-1}$ and $T = 4$ s. Unidirectional Condition: $U_u = 0.20\,m\,s^{-1}$. (a) Streamwise phase-averaged velocity profile along the oscillation cycle. (b) Streamwise phase-averaged velocity along the oscillation cycle at $z = 0.28$ m. The symbols correspond to the velocity profiles plotted in (a). Vertical (a) and horizontal (b) lines represent the zero velocity line.

ure 8.12: 6) does not have enough energy to fully mobilize the sediment on the stoss-side. Nonetheless, as the downstream eddy reverses, the eddy stays relatively close to the bed, thus 'reworking' the crest of the ripple, and making it relatively rounded (Figure 8.12: 3-5).

After detailed analysis, the bedform rounded index was found to be related to the ratio between the unidirectional and oscillatory Shields number (θ_u/θ_o) by the following equation (Figure 8.14)

$$BRI = 0.33 \left(\frac{\theta_u}{\theta_o}\right)^{0.30} + 0.40 \tag{8.18}$$

where the Shields numbers were computed using the unstratified, three-layer eddy viscosity formulation of Madsen and Grant (1976). Equation 8.18 is obtained by a linear regression of the experimental data (blue line in Figure 8.14). The R^2 of the fit is 0.78 (p-value =

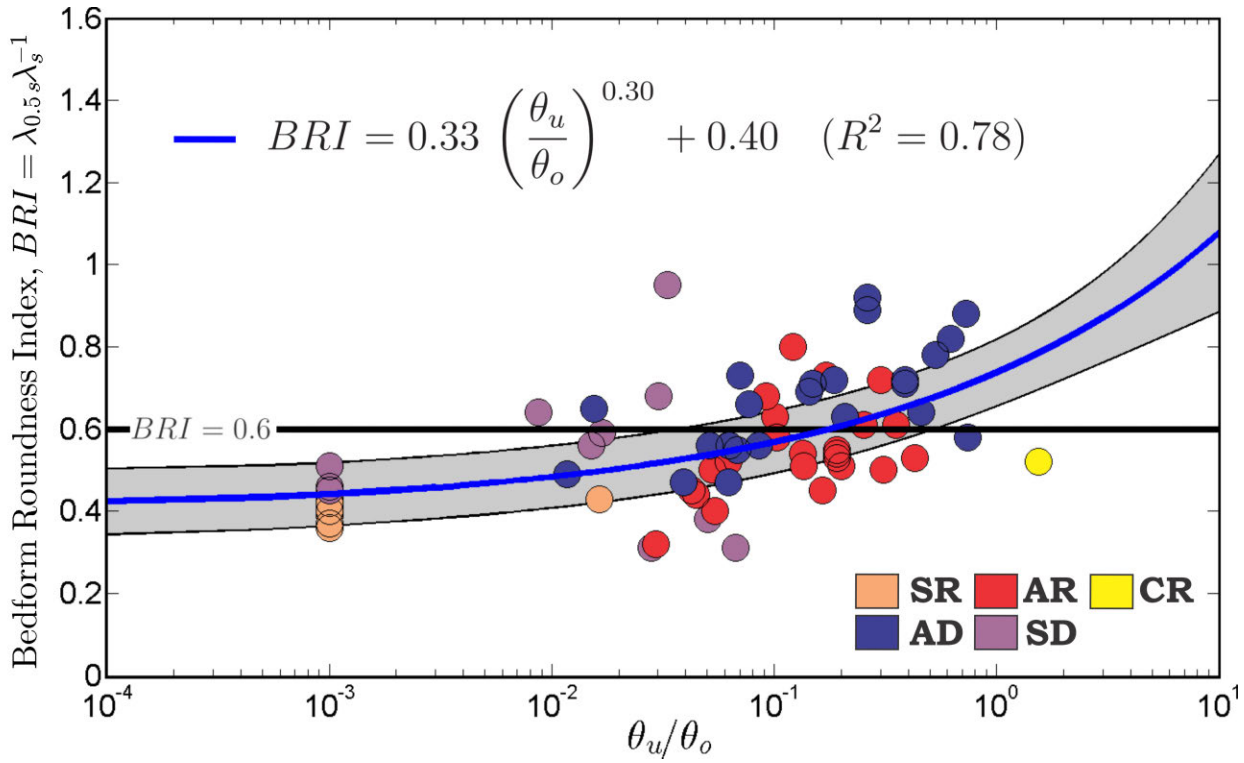

Figure 8.14: BRI as a function of the ratio between the unidirectional and oscillatory Shields number (θ_u/θ_o). The gray-shaded area represents the 95% confidence interval of the fitted function (Equation 8.18). SR = Symmetric Ripples (light-orange), AR = Asymmetric Ripples (red), AD = Asymmetric Dunes (blue), SD = Symmetric Dunes (purple) and CR = Current Ripples (yellow). Data from this study and Dumas et al. (2005).

0.046, Appendix B.4) with a relatively large, but expected, scatter (values outside the 95% confidence interval represented by the gray-shaded area in Figure 8.14). Despite the scatter, Equation 8.18 is able to represent the mean value of BRI observed for pure oscillatory flows

$$\lim_{U_u \to 0} BRI \to 0.40 \tag{8.19}$$

(Figure 8.14). On the other hand, Equation 8.16 does not show the asymptotic behavior necessary to predict the cases of pure unidirectional flows ($BRI \approx 0.5$).

8.4 Conclusions

A detailed analysis of the Bedform Index (BI), Bedform Symmetry Index (BSI) and Bedform Roundness Index (BRI) was made, with a particular emphasis on their use to differentiate between unidirectional, oscillatory and combined flows. This chapter proposes a new set of equations (Equations 8.7 to 8.9) that compute the probability of a bedform with a given cross-sectional geometry, defined with bedform indices (BI,BSI,BRI), being generated under unidirectional, oscillatory and combined flows. In order to characterize the indices with the flow conditions, three empirical relationships are proposed to relate (i) the bedform index with the combined-flow water excursion

$$BI = 12.04\, d_o^{+\,0.32}, \tag{8.20}$$

(ii) cross-sectional bedform symmetry with the Shields number ratio

$$\frac{BSI}{T_*} = 1.71 \times 10^{-10} \left(\frac{\theta_u}{\theta_o} \right)^{0.45} \tag{8.21}$$

and (iii) cross-sectional bedform roundness with the flow conditions

$$BRI = 0.33 \left(\frac{\theta_u}{\theta_o} \right)^{0.30} + 0.40 \tag{8.22}$$

In addition, unlike other combined flow studies (e.g., Dumas et al., 2005), a gradual size transition was observed between ripples and dunes. If only the mean values of wavelength are considered for the combined flow conditions with the unidirectional component less than $0.3\,m\,s^{-1}$, there might be a size gap between wavelengths $\approx$ 0.30 and $\approx$ 1 m. However, such a wavelength 'gap' was not observed under current-dominated combined flows ($U_u \geq 0.3\,m\,s^{-1}$). Moreover, such a gap is non-existent if the whole distribution of bedform sizes is taken into account.

Chapter 9

Conclusions and Future Research

This thesis presents new experimental data on bedform initiation and development under unidirectional, oscillatory and, more extensively, combined flows. In particular, this study was able to populate zones of the *Terra incognita* region previously defined in the literature (Southard, 1991). In this thesis, the stable bedform configurations under a diverse range of flow conditions were studied and divided into: *no motion (NM), 2D symmetric ripples (2D SR), 3D symmetric ripples (3D SR), 3D symmetric dunes (SD), 3D asymmetric ripples (AR), 3D quasi-asymmetric ripples (QAR), 3D asymmetric dunes (AD), 3D current ripples (CR), 3D current dunes (CD)* and *upper-stage plane bed (USPB)*. Each of these bedform stages was described, characterized and reproduced in dimensional and dimensionless phase diagrams. The experimental data collected under unidirectional flows larger than 0.30 $m\,s^{-1}$ allow expansion of the current understanding on bed configurations within the *Terra Incognita* zone, where the phase boundary between combined flow bedforms and current ripples was experimentally constrained. On the other hand, based on dimensionless analysis, the oscillatory and unidirectional mobility numbers were used to represent the dimensionless phase diagram under combined flows. This set of dimensionless numbers provides a better representation than previous studies that use a friction factor to compute the Shields number. In addition, a new nomenclature for combined flow bedforms is proposed, which includes the planform and cross-sectional geometries in order to better represent the bed morphologies. This new nomenclature was carefully designed to integrate both unidirectional and oscillatory bedforms. One of the main changes that allows integration with the nomenclature used in unidirectional flows is the reclassification of large ripples as dunes.

This change is a significant modification of the system of classification of oscillatory and combined flow bedforms where all bed states are called ripples. Furthermore, the introduction of the planform and cross-sectional geometries as properties to classify bedforms leads to the definition of a stable phase space for two-dimensional symmetrical ripples and three-dimensional quasi-asymmetrical ripples.

The bedform initiation and development experiments illuminated the similarity of the genesis and growth processes for all types of flows. This result was reflected in the same geometric pattern and development-path regardless of the flow conditions. Moreover, the development-path, or bedform growth, exhibits the same general trend for different bedform sizes (e.g., ripples vs dunes), bedform shape (e.g., symmetric or rounded), bedform planform geometry (e.g., 2D vs 3D) and sediment grain sizes. The development of the bed defects during the genesis of bedforms shows a strong relationship with the direction and magnitude of the shear stress throughout the oscillation cycle. If the condition possessed a symmetric shear stress, the defects grew and propagated symmetrically, whereas if the shear stress was asymmetric, the defects grew and propagated with a predominant downstream direction. Furthermore, for the case of current-dominated combined flow, the maximum upstream shear stress was not large enough to entrain sediment in the upstream direction, resulting in solely downstream sediment transport and bedform migration. The bedform development was able to be divided and characterized into four main stages : (1) incipient bedforms, (2) growing bedforms, (3) stabilizing bedforms, and (4) fully-developed bedforms, consistent with the separation proposed by Baas (1994, 1999) for pure unidirectional flows. Finally, a probabilistic model based on the bedform cross-sectional geometries is proposed in order to differentiate between unidirectional, oscillatory and combined flows from the preserved strata. This probabilistic model provides a significant improvement on the present tools to diagnose bedforms in the modern and ancient record.

Despite these new advances, the limitations of the present experiments, combined with the limited data set available in the literature, makes it impossible to address the effects of grain

size in the bed morphologies. Unfortunately, based on the grain size dependence of pure unidirectional and pure oscillatory flows bedforms, the effects of grain size might change the bed configuration significantly. It is expected that for sediments coarser than a critical grain size (still unknown), the stability field of ripples should vanish. Similarly, for sediments finer than a critical grain size, dunes would not form anymore or have a very small stability space. Furthermore, new work in sediment mixtures, in particular sand with silt/clay (e.g., Baas et al., 2011) has highlighted the significant role played by finer sediment in the development and final states of bedforms. Other issues besides grain size, which were not addressed in this thesis but may have a significant impact on bedform characteristics and evolution, are associated with the simplified flow field used in the present experiments. One of the most significant simplifications was the fact that the waves used in these experiments had a very well-defined sinusoidal shape with a unique oscillation period (symmetric waves). The effect of irregular waves (asymmetric waves), which are common in natural environments, can affect the overall geometry of the bedforms. In addition, coastal environments are characterized by a spectrum of wave periods and wave directions, effects that are thought to generate interference ripples (Davis, 1965), and were not considered herein. Hence, future field and laboratory experiments will require consideration of some, or all, of the above variables to move closer to bedforms that are found in the field.

Appendix A

Illustrative Videos

A.1 Cited Videos

A.1.1 Ch06 - 01*:T05O30U00_Genesis.avi*

Oscillatory Condition: $U_o = 0.30\,m\,s^{-1}$ and $T = 5$ s.

Unidirectional Condition: $U_u = 0.00\,m\,s^{-1}$

The experiment started from an initial defect, which was made by compacting the flat bed and generating a negative defect with a length ≈ 0.08 m, width ≈ 0.1 m and height ≈ 0.03 m. As the flow started, a characteristic geometric pattern was generated from the defect propagation by erosion of the edge of the original defect, and development of a crest and twin scour pits or 'horns' (Chapter 6). Despite the fact that no flow data was measured over the defect, it can be deduced by looking at the movie, that the flow separates from the defect edge, generating a zone of high instantaneous bed shear stresses large enough to move the sediment, mainly as bedload. As sediment gets transported both downstream and laterally, two-lobed horns form in the bed. Over time, the newly-formed feature becomes the new edge of a defect generating flow separation, which causes scour and development of a new feature; this process is repeated to form a train of defects in the direction of propagation. Unfortunately, due to the natural limitation of the facility, the area of view captured with the camera was relatively small (≈ 0.34 m long and ≈ 0.23 m wide) and unable to record the overall evolution of the defect as it further moved in the propagation direction.

Table A.1: Summary of flow parameters, bedform and video characteristics of *T05O30U00_Genesis.avi*.

Set	Exp	T (s)	U_o ($m\,s^{-1}$)	U_u ($m\,s^{-1}$)	D_*	U_H[a] ($m\,s^{-1}$)	$u_{*,M94}$[b] ($m\,s^{-1}$)	$u_{*,S97}$[c] ($m\,s^{-1}$)
01	01	05	0.30	0.00	6.06	0.00	0.026	0.025

u_* ($m\,s^{-1}$)	$\theta_{max}^{(+)}$[d]	$\theta_{max}^{(-)}$[e]	SSSI[f]	Temp (°C)	Duration[g] (min)	Frame Rate (fps)	V. Rep.[h] (min/sec)	V.L.[i] (min)
0.021	0.105	-0.113	1.07	18.0	46.83	60	RT	0.50

[a] Depth-averaged unidirectional velocity. UDVP data, computed with Equation 4.29.
[b] Predicted value based on Grant and Madsen (1979). [c] Predicted value based on Soulsby (1997).
[d] Maximum value through the oscillation cycle. UDVP data, computed with Equation 4.26.
[e] Minimum value through the oscillation cycle. UDVP data, computed with Equation 4.26.
[f] SSSI = Shear Stress Symmetry Index. [g] Experiment duration.
[h] Video Representation. RT = Real Time. [i] Video Length.

A.1.2 Ch07 - 01: *T06O25U00_Develop.wmv*

Oscillatory Condition: $U_o = 0.25\,m\,s^{-1}$ and $T = 6$ s.

Unidirectional Condition: $U_u = 0.00\,m\,s^{-1}$

The video shows two animations: on the left side of the video there is a sequence of pictures that show the evolution of the bedforms, and on the right side, there is a plot of the mean height (η - blue circles) and wavelength (λ - brown circles) as a function of time. There is a larger yellow circle in the diagram on the right side that indicates the mean height and wavelength represented in the image displayed on the left side. In addition, three vertical lines indicate the transitions of the four bedform development stages: (1) incipient bedforms, (2) growing bedforms, (3) stabilizing bedforms, and (4) fully-developed bedforms (see Chapter 7). Once the bedform reaches the fourth, or fully-developed bedform stage, the bedform is considered in morphodynamic equilibrium.

The experiment started from a flat bed. First, very small two-dimensional symmetrical ripples grew slowly from the sidewalls of the tunnel and propagated into the center of the channel. Fifteen to twenty minutes after the beginning of the experiment, the bed was completely covered by bedforms of a similar size to the initial ones, but with a three-dimensional

planform geometry. It is important to note that at this time the first measurements of height and wavelength were able to be computed, and hence all the time previous to this moment is listed as negative time. By a slow merging process, these ripples grew in size and the planform geometry became more two-dimensional as the bedforms started to amalgamate. During this merging stage, bedforms of all sizes were present on the bed. Larger bedforms stayed in a relative fixed position as smaller bedforms migrated into them forming even larger bedforms. This process culminated at the same time the bed reached a full two-dimensional planform geometry, where no further changes in height, wavelength and planform geometry were recorded, or 'stable equilibrium'. The experiment started from a flat bed. First, very small two-dimensional symmetrical ripples grew slowly from the sidewalls of the tunnel and propagated into the center of the channel. Fifteen to twenty minutes after the beginning of the experiment, the bed was completely covered by bedforms of a similar size to the initial ones, but with a three-dimensional planform geometry. It is important to note that at this time the first measurements of height and wavelength were able to be computed, and hence all the time previous to this moment is listed as negative time. By a slow merging process, these ripples grew in size and the planform geometry became more two-dimensional as the bedforms started to amalgamate. During this merging stage, bedforms of all sizes were present on the bed. Larger bedforms stayed in a relative fixed position as smaller bedforms migrated into them forming even larger bedforms. This process culminated at the same time the bed reached a full two-dimensional planform geometry, where no further changes in height, wavelength and planform geometry were recorded, or 'stable equilibrium'.

There are several important observations that can be made from this video:

- there is a temporal lag in the development history of 2D oscillatory bedforms between the time required for these bedforms to reach equilibrium sizes (i.e., $\eta_t \sim 0.9\,\eta_e$ and $\lambda_t \sim 0.9\,\lambda_e$) and the time to reach equilibrium planform geometry (i.e., the time for the bed to be fully 2D). This is shown in the video when the experiment reaches the fourth, or fully-developed, bedform stage and the bed is still not at planform equilibrium.

- that despite the two-dimensionality of the initial and final stages of the bed configuration, the bedforms always transition to a three-dimensional stage when transitioning between two-dimensional configurations. This characteristic property of oscillatory flows was also observed in the experiments reported by Pedocchi (2009).

- that for the case of two-dimensional oscillatory ripples, once the bed reached the final equilibrium the bedforms stopped their migration and established a very defined wavelength and height that stayed fixed over time without any variations. These wavelengths and heights will persist until the flow condition is changed, and then the bed will break the two-dimensionality to rearrange itself to a new equilibrium stage that is stable with the new flow condition. This 'stable equilibrium' behavior is a fundamental characteristic of two-dimensional oscillatory ripples, not seen in any other type of flow type or bedform.

Table A.2: Summary of flow parameters, bedform and video characteristics of *T06O25U00_Develop.wmv*.

#[a]	Init.[b] Cond.	T (s)	U_o ($m\,s^{-1}$)	U_u ($m\,s^{-1}$)	λ (m)	η (mm)	BI[c]	BSI[c]	BRI[c]
01	00	06	0.25	0.0	0.25	42.00	6.23	1.08	0.42

2D/3D[d]	A/S[e]	nR/R[f]	Bedform[g] Type	Temp (°C)	Eq. Time[h] (hr)	Duration[i] (hr)	Frame Rate (fps)	V. Rep.[j] (min/sec)	V.L.[k] (min)
2D	S	nR	SR	20.5	2.83	15.5	42	15.5	1.93

[a] Experiment number: s at the end of the name indicates that smaller bedforms were observed superimposed on the larger ones.

[b] Initial condition of the sediment bed at the beginning of the experiment: 00 indicates flat bed, other numbers indicates the number of the experiment run before.

[c] $BI = \lambda_\eta\,\eta^{-1}$, $BSI = \lambda_s\,\lambda_l^{-1}$ and $BRI = \lambda_{0.5\,s}\,\lambda_s^{-1}$, equation 3.32.

[d] 2D indicates two-dimensional bedforms

[e] A stands for asymmetric ($BSI > 2$) and S for symmetric ($BSI < 2$)

[f] nR stands for not-rounded ($BRI < 0.6$) and R stands for rounded ($BRI > 0.6$).

[g] SR = Symmetric Ripples. [h] Time until flow-bedform equilibrium.

[i] Experiment duration. [j] Video Representation. [k] Video Length.

A.2 Additional Videos

In the following appendix, there is a list of several key videos generated to illustrate the development and behavior of the bedforms in the thesis.

A.2.1 Experiment 3 - *T04O25U20.wmv*

Oscillatory Condition: $U_o = 0.25\,m\,s^{-1}$ and $T = 4$ s.

Unidirectional Condition: $U_u = 0.20\,m\,s^{-1}$

The experiment started from a flat bed. Initially, small ripples slowly grew from the sidewalls of the tunnel and propagated into the center of the tunnel with a clear downstream alignment. This propagation was not homogeneous along the bed, leaving some areas of the bed free of bedforms. Ten to fifteen minutes after the beginning of the experiment, the bed was completely covered by bedforms. At this time, the bed was populated by small asymmetrical ripples with a wide range of sizes. Soon after these ripples had covered the bed, differential transport allowed the "faster" ripples to agglomerate with the "slower" ripples, thereby generating larger three-dimensional combined-flow ripples. Unlike Experiment 30 (A.1.2), once the bed reached a final equilibrium stage, the bedforms moved and adjusted in a 'dynamic equilibrium' with the instantaneous flow and sediment transport conditions. The diversity of sizes seen in the video, which is an inheritance condition of a dynamic equilibrium, are considered to be the 'normal' stage of the bedform, where there is not a unique equilibrium wavelength and height but a spectrum of values. The difference between a bedform with a spectrum of sizes and multiple superimposed bedforms can be distinguished by a clear break in the size distribution (i.e, the presence of a bi- or tri-modal distribution). Unless specifically mentioned in the existence of a superposition of bedforms, all three-dimensional bedforms are in dynamic equilibrium and their wavelength and height reported is the mean of the sizes (see Chapter 7).

Table A.3: Summary of flow parameters, bedform and video characteristics of *T04O25U20.wmv*.

#[a]	Init.[b] Cond.	T (s)	U_o ($m\,s^{-1}$)	U_u ($m\,s^{-1}$)	λ (m)	η (mm)	BI[c]	BSI[c]	BRI[c]
03	00	04	0.25	0.2	0.18	21.1	08.6	1.53	0.54

2D/3D[d]	A/S[e]	nR/R[f]	Bedform[g] Type	Temp (°C)	Eq. Time[h] (hr)	Duration[i] (hr)	Frame Rate (fps)	V. Rep[j] (min/sec)	V.L.[k] (min)
2.5D	A	nR	AR^{c}	17.5	2.91	18.0	74	18	1.12

[a] Experiment number: s at the end of the name indicates that smaller bedforms were observed superimposed on the larger ones.
[b] Initial condition of the sediment bed at the beginning of the experiment: 00 indicates flat bed, other numbers indicates the number of the experiment run before.
[c] $BI = \lambda_\eta\,\eta^{-1}$, $BSI = \lambda_s\,\lambda_l^{-1}$ and $BRI = \lambda_{0.5\,s}\,\lambda_s^{-1}$, equation 3.32.
[d] 2D indicates two-dimensional bedforms
[e] A stands for asymmetric ($BSI > 2$) and S for symmetric ($BSI < 2$)
[f] nR stands for not-rounded ($BRI < 0.6$) and R stands for rounded ($BRI > 0.6$).
[g] AR = Asymmetric Ripples and ^{c} = Current-Dominated Combined Flows.
[h] Time until flow-bedform equilibrium. [i] Experiment duration.
[j] Video Representation. [k] Video Length.

A.2.2 Experiment 23 - *T05O40U40fromT05O20U40.wmv* and *T05O40U40fromT05O20U40_CloseUP.avi*

Oscillatory Condition: $U_o = 0.40\,m\,s^{-1}$ and $T = 5$ s.

Unidirectional Condition: $U_u = 0.40\,m\,s^{-1}$

The experiment (T05O40U40fromT05O20U40.wmv) started from the final equilibrium condition of Experiment 17 ($U_o = 0.20\,m\,s^{-1}$, $T = 5$ s and $U_u = 0.40\,m\,s^{-1}$). This flow condition generated appreciable immediate entrainment, suspending large amounts of sediment. In general, high transport conditions promote rapid initiation of bedforms (Venditti et al., 2005a) but in this case, since the bed possessed bedforms already, the flow slowly modified the pre-existing bedforms. As these bedforms evolved, they quickly grew in size. This growth was limited by the scaling imposed by the width of the flume. At this point, the bedform three-dimensionality was eliminated. The wavelength exhibited by these dunes was ≈ 1 m and was interpreted as the equilibrium wavelength. The large velocities gener-

ated when the unidirectional and oscillatory flows were directionally-coincident produced the greatest downstream bedform migration. In addition, during these conditions, separation eddies forming in the lee side of the asymmetric combined-flow dunes were strong enough to mobilize sediment, leading to the development of small upstream migrating ripples. These small ripples persisted only while the recirculation eddies entrained sediment. This process can be seen in the close-up video (T05O40U40fromT05O20U40_CloseUP.avi).

Table A.4: Summary of flow parameters, bedform and video characteristics of *T05O40U40fromT05O20U40.wmv*.

#[a]	Init.[b] Cond.	T (s)	U_o ($m\,s^{-1}$)	U_u ($m\,s^{-1}$)	λ (m)	η (mm)	BI[c]	BSI[c]	BRI[c]
23	16	05	0.40	0.40	1.05	102.30	10.3	4.16	0.92
2D/3D[d]	A/S[e]	nR/R[f]	Bedform[g] Type	Temp (°C)	Eq. Time[h] (hr)	Duration[i] (hr)	Frame Rate (fps)	V. Rep[j] (min/sec)	V.L.[k] (min)
2D[1]	A	R	ARD[ς]	17.0	-	00.8	15	1.808	0.57

[a] Experiment number: s at the end of the name indicates that smaller bedforms were observed superimposed on the larger ones.

[b] Initial condition of the sediment bed at the beginning of the experiment: 00 indicates flat bed, other numbers indicates the number of the experiment run before.

[c] $BI = \lambda_\eta\,\eta^{-1}$, $BSI = \lambda_s\,\lambda_l^{-1}$ and $BRI = \lambda_{0.5\,s}\,\lambda_s^{-1}$, equation 3.32.

[d] 2D indicates two-dimensional bedforms. The superscript [1] indicates that the width of the flume was not large enough for bedforms to fully develop their planform geometry.

[e] A stands for asymmetric ($BSI > 2$) and S for symmetric ($BSI < 2$)

[f] nR stands for not-rounded ($BRI < 0.6$) and R stands for rounded ($BRI > 0.6$).

[g] AR = Asymmetric Rounded Dune and [ς] = Current-Dominated Combined Flows.

[h] Time until flow-bedform equilibrium.

[i] Experiment duration.

[j] Video Representation.

[k] Video Length.

Table A.5: Summary of flow parameters, bedform and video characteristics of *T05O40U40fromT05O20U40_CloseUP.avi*.

#[a]	Init.[b] Cond.	T (s)	U_o ($m\,s^{-1}$)	U_u ($m\,s^{-1}$)	λ (m)	η (mm)	BI[c]	BSI[c]	BRI[c]
23	16	05	0.40	0.40	1.05	102.30	10.3	4.16	0.92
2D/3D[d]	A/S[e]	nR/R[f]	Bedform[g] Type	Temp (°C)	Eq. Time[h] (hr)	Duration[i] (hr)	Frame Rate (fps)	V. Rep[j] (min/sec)	V.L.[k] (min)
$2D^1$	A	R	ARD[ς]	17.0	-	00.8	15	RT	0.73

[a] Experiment number: s at the end of the name indicate that smaller bedforms were observed superimposed on the larger ones.

[b] Initial condition of the sediment bed at the beginning of the experiment: 00 indicates flat bed, other numbers indicates the number of the experiment run before.

[c] $BI = \lambda_\eta\,\eta^{-1}$, $BSI = \lambda_s\,\lambda_l^{-1}$ and $BRI = \lambda_{0.5\,s}\,\lambda_s^{-1}$, equation 3.32.

[d] 2D indicates two-dimensional bedforms. The superscript [1] indicates that the width of the flume was not large enough for bedforms to fully develop their planform geometry.

[e] A stands for asymmetric ($BSI > 2$) and S for symmetric ($BSI < 2$)

[f] nR stands for not-rounded ($BRI < 0.6$) and R stands for rounded ($BRI > 0.6$).

[g] AR = Asymmetric Rounded Dune and [ς] = Current-Dominated Combined Flows.

[h] Time until flow-bedform equilibrium. [i] Experiment duration.

[j] Video Representation. RT = Real Time. [k] Video Length.

Appendix B

Significance of Correlations

B.1 Chapter 05

Table B.1: Significance of correlations for fits in Chapter 5

Equation	$BSI = A\,U_u + B$ (Equation 5.5)		
A	B	R^2	p-value
4.40	1.0	0.68	0.036
Equation	$BRI = A\,U_u + B$ (Equation 5.5)		
A	B	R^2	p-value
0.64	0.42	0.62	0.042

B.2 Chapter 06

Table B.2: Significance of correlations for fits in Chapter 6

Equation	$\frac{\lambda_{DS}}{\lambda_{US}}(t) = \alpha\, t + \beta$ (Equation 6.1)			
Set	Exp	$\alpha \times 10^{-2}$ $[s^{-1}]$	$R^2(\alpha)$	p-value(α)
01	01	0.05	0.69	0.04
01	02	0.41	0.68	0.05
01	03	0.02	0.90	0.02
01	04	0.05	0.67	0.03
02	01	4.26	0.63	0.03
02	02	3.79	0.70	0.04
02	03	3.04	0.70	0.03
02	04	3.14	0.69	0.04
03	01	0.02	0.62	0.03
03	02	3.04	0.56	0.04
03	03	7.47	0.71	0.04
Equation	$\alpha = \gamma\ (SSSI - 1)^{\phi}$ (Equation 6.2)			
γ	ϕ	R^2	p-value	
0.035	0.6	0.82	0.04	

B.3 Chapter 07

Table B.3: Significance of correlations for Table 7.1

Equations	$\eta_t(t) = \eta_e \left(1 - e^{-c_\eta t}\right)$ (Equation 7.1) $\lambda_t(t) = \lambda_e \left(1 - e^{-c_\lambda t}\right)$ (Equation 7.2)							
#	η_e (mm)	c_η (hr^{-1})	$R^2(\eta)$	p-value(η)	λ_e (m)	c_λ (hr^{-1})	$R^2(\lambda)$	p-value(λ)
1	34.8	0.99	0.95	0.005	0.22	0.87	0.96	0.006
2	20.5	0.75	0.60	0.028	0.15	1.01	0.56	0.042
3	21.1	0.89	0.65	0.044	0.18	0.47	0.82	0.012
4	26.9	2.02	0.40	0.021	0.23	1.80	0.56	0.040
5	35.6	1.34	0.45	0.048	0.51	6.90	0.45	0.035
8	35.3	0.82	0.97	0.009	0.21	0.65	0.98	0.009
11	36.4	0.69	0.66	0.035	0.15	0.24	0.46	0.042
12	27.3	2.10	0.87	0.022	0.22	1.24	0.91	0.010
15	27.6	2.68	0.63	0.027	0.27	2.72	0.48	0.047
16	30.3	2.20	0.50	0.034	0.60	0.98	0.45	0.030
17	44.6	0.06	0.85	0.029	0.88	0.06	0.85	0.024
18	22.0	2.79	0.62	0.036	0.20	3.48	0.53	0.026
19	23.0	4.30	0.43	0.036	0.17	3.17	0.35	0.021
20	20.7	2.65	0.43	0.027	0.21	2.48	0.43	0.042
21	61.3	0.93	0.92	0.007	0.58	0.77	0.93	0.008
22	98.3	0.98	0.89	0.023	1.02	0.93	0.79	0.034
25	153.0	0.06	0.47	0.040	1.23	0.96	0.47	0.047
27	35.5	6.10	0.97	0.007	0.49	0.86	0.96	0.008
30	32.1	0.45	0.94	0.007	0.20	0.48	0.97	0.008
31	26.6	0.70	0.63	0.050	0.18	2.50	0.39	0.046
32	17.2	0.55	0.92	0.005	0.19	0.37	0.91	0.009
33	17.6	1.47	0.43	0.047	0.17	0.89	0.36	0.037
34	23.3	2.15	0.62	0.047	0.25	1.42	0.51	0.026
35	68.3	1.78	0.64	0.044	0.65	1.52	0.42	0.027
36	123.0	3.36	0.78	0.023	1.30	1.61	0.69	0.047
42	32.3	3.67	0.45	0.028	0.28	3.94	0.45	0.021
54	17.6	1.36	0.72	0.030	0.20	3.69	0.76	0.035
55	18.1	2.09	0.63	0.040	0.21	2.82	0.78	0.025

Table B.4: Significance of correlations for fits in Chapter 7

Equation	$U_u = A\, t_e^B + C$ (Equation 7.17)			
A	B	C	R^2	p-value
0.2695	-0.333	0.274	0.55	0.04
Equation	$U_u = A\, t_e^B + C$ (Equation 7.18)			
0.2185	-0.508	0.272	0.63	0.03
Equation	$q^* = A\, t_e^B$ (Equation 7.20)			
A	B		R^2	p-value
4.89	-1.28		0.92	0.02

B.4 Chapter 08

Table B.5: Significance of correlations for fits in Chapter 8

Equation	$\lambda_\eta = A\, d_o^+$ (Equation 8.12)	
A	R^2	p-value
0.65	0.65	0.051

Equation	$\lambda_\eta = A\, d_o^+$ (Equation 8.13)	
A	R^2	p-value
0.82	0.86	0.048

Equation	$BI = A\, d_o^{+\,B}$ (Equation 8.14)		
A	B	R^2	p-value
12.04	0.32	0.85	0.026

Equation	$\frac{BSI}{T_*} = A\left(\frac{\theta_u}{\theta_o}\right)^B$ (Equation 8.16)		
A	B	R^2	p-value
1.71×10^{-10}	0.45	0.79	0.033

Equation	$BRI = A\left(\frac{\theta_u}{\theta_o}\right)^B + C$ (Equation 8.18)			
A	B	C	R^2	p-value
0.33	0.30	0.40	0.78	0.046

References

Abramowitz, M. and **Stegun, I. A.** (1972) *Handbook of mathematical functions with formulas, graphs, and mathematical tables*: Courier Dover Publications, 1046 pp.

Acarlar, M. and **Smith, C.** (1987a) A study of hairpin vortices in a laminar boundary layer. Part 1. Hairpin vortices generated by a hemisphere protuberance. *Journal of Fluid Mechanics*, **175**, no. 1, 1–41.

Acarlar, M. and **Smith, C.** (1987b) A study of hairpin vortices in a laminar boundary layer. part 2. hairpin vortices generated by fluid injection. *Journal of Fluid Mechanics*, **175**, no. 1, 43–83.

Admiraal, D., Musalem-Jara, R., García, M. and **Niño, Y.** (2006) Vortex trajectory hysteresis above self-formed vortex ripples. *Journal of Hydraulic Research*, **44**, no. 4, 437–450.

Adrian, R. (2007) Hairpin vortex organization in wall turbulence. *Physics of Fluids*, **19**, no. 4, 041301.

Adrian, R. and **Liu, Z.** (2002) Observation of vortex packets in direct numerical simulation of fully turbulent channel flow. *Journal of Visualization*, **5**, no. 1, 9–19.

Adrian, R., Meinhart, C. and **Tomkins, C.** (2000) Vortex organization in the outer region of the turbulent boundary layer. *Journal of Fluid Mechanics*, **422**, no. 1, 1–54.

Agnew, R. (1965) A two layer theory for unsteady flow, In: Proceedings of the 2nd Australasian conference on hydraulics and fluid mechanics, December 1965 Australian Institution of Engineers, Sidney, A97–A115.

Agresti, A. (1996) *An Introduction to Categorical Data Analysis*: 2nd Edition. *Probability and Statistics*. Wiley-Interscience, 400 pp.

Allen, J. R. L. (1962) Asymmetrical ripple marks and the origin of cross-stratification. *Nature*, **194**, no. 4824, 167–169.

Allen, J. R. L. (1968) *Current Ripples: Their Relation to Patterns of Water and Sediment Motion*: 1st Edition. Elsevier Science Publishing Co. Inc.,U.S., 446 pp.

Allen, J. R. L. (1976) Bed forms and unsteady processes: Some concepts of classification and response illustrated by common one-way types. *Earth Surface Processes*, **1**, no. 4, 361–374.

Allen, J. R. L. (1979) Initiation of transverse bedforms in oscillatory bottom boundary layers. *Sedimentology*, **26**, no. 6, 863–865.

Allen, J. R. L. (1982) Simple-models for the shape and symmetry of tidal sand waves .2. Dynamically stable symmetrical equilibrium forms. *Marine Geology*, **48**, no. 1-2, 51–73.

Allen, J. R. L. (1983) River bedforms: Progress and problems, In: *Modern and Ancient Fluvial Systems* (Eds. J. Collinson and J. Lewin), Blackwell Science Ltd, *Special Publications 6 of the International Association of Sedimentologists*, 19–33.

Allen, J. R. L. and **Friend, P. F.** (1976) Relaxation time of dunes in decelerating aqueous flows. *Journal of the Geological Society*, **132**, no. 1, 17–26.

Allen, P. A. (1985) Hummocky cross-stratification is not produced purely under progressive gravity waves. *Nature*, **313**, 562–564.

Allen, P. A. and **Hoffman, P. F.** (2005) Extreme winds and waves in the aftermath of a Neoproterozoic glaciation. *Nature*, **433**, no. 7022, 123–127.

Amos, C. L., Bowen, A., Huntley, D. and **Lewis, C.** (1988) Ripple generation under the combined influences of waves and currents on the Canadian continental shelf. *Continental Shelf Research*, **8**, no. 10, 1129–1153.

Amos, C. L., Bowen, A. J., Huntley, D. A., Judge, J. T. and **Li, M. Z.** (1999) Ripple migration and sand transport under quasi-orthogonal combined flows on the scotian shelf. *Journal of Coastal Research*, **15**, no. 1, 1–14.

Amos, C. L., Li, M. Z. and **Choung, K. S.** (1996) Storm-generated, hummocky stratification on the outer-scotian shelf. *Geo-Marine Letters*, **16**, no. 2, 85–94.

Andersen, K. H. (2001) A particle model of rolling grain ripples under waves. *Physics of Fluids*, **13**, no. 1, 58–64.

Anthony, E. (2009) *Shore Processes and their Palaeoenvironmental Applications*: 1st Edition. *Developments in Marine Geology, Vol. 4*. Elsevier, Hungary, 519 pp.

Armstrong, M. A. (1983) *Basic Topology*: Springer, 272 pp.

Arnott, R. W. and **Southard, J. B.** (1990) Exploratory flow-duct experiments on combined-flow bed configurations, and some implications for interpreting storm-event stratification. *Journal of Sedimentary Research*, **60**, no. 2, 211–219.

Ashley, G. M. (1990) Classification of large-scale subaqueous bedforms: A new look at an old problem-SEPM Bedforms and Bedding Structures. *Journal of Sedimentary Petrology*, **60**, no. 1, 160–172.

Baas, J. H. (1993) Dimensional analysis of current ripples in recent and ancient depositional environments. Ph.D. thesis, Utrecht University, 199 pp.

Baas, J. H. (1994) A flume study on the development and equilibrium morphology of current ripples in very fine sand. *Sedimentology*, **41**, no. 2, 185–209.

Baas, J. H. (1999) An empirical model for the development and equilibrium morphology of current ripples in fine sand. *Sedimentology*, **46**, no. 1, 123–138.

Baas, J. H., Best, J. L. and **Peakall, J.** (2011) Depositional processes, bedform development and hybrid bed formation in rapidly decelerated cohesive (mud–sand) sediment flows. *Sedimentology*, **58**, no. 7, 1953–1987.

Baas, J. H., Oost, A. P., Sztano, O. K., Boer, P. L. and **Postma, G.** (1993) Time as an independent variable for current ripples developing towards linguoid equilibrium morphology. *Terra Nova*, **5**, no. 1, 29–35.

Bagnold, R. A. (1946) Motion of waves in shallow water. interaction between waves and sand bottoms (with comments from Taylor, G.). *Proceedings of the Royal Society A: Mathematical, Physical and Engineering Sciences*, **187**, no. 1008, 1–18.

Bagnold, R. A. (1966) An approach to the sediment transport problem from general physics: Physiographic and hydraulic studies of rivers. U.S. Geological Survey Professional Paper 422-I, U.S. Geological Survey, 47 pp.

Baird, D. M. (1962) Ripple marks. *Journal of Sedimentary Research*, **32**, no. 2, 332–334.

Bakker, W. T. (1974) Sand concentration in an oscillatory flow, In: Proceedings of the 14th International Conference on Coastal Engineering, ASCE, Copenhagen 1129–1148.

Bartholdy, J., Flemming, B. W., Bartholom, A. and **Ernstsen, V. B.** (2005) Flow and grain size control of depth-independent simple subaqueous dunes. *Journal of Geophysical Research*, **110**, no. F04S16, 12.

Basilici, G., de Luca, P. H. V. and **Poiré, D. G.** (2012) Hummocky cross-stratification-like structures and combined-flow ripples in the Punta Negra Formation (Lower-Middle Devonian, Argentine Precordillera): A turbiditic deep-water or storm-dominated prodelta inner-shelf system? *Sedimentary Geology*, **267–268**, 73–92.

Bechteler, W., Vogel, G. and **Vollmers, H.** (1991) Model investigations on the sediment transport of a lower alpine river, In: *Fluvial Hydraulics of Mountain Regions* (Eds. A. Armanini and G. D. Silvio), Lecture Notes in Earth Sciences Edition, Springer-Verlag, 179–194.

Bendat, J. S. and **Piersol, A. G.** (2000) *Random Data: Analysis & Measurement Procedures*: 3rd Edition. Wiley-Interscience, 594 pp.

Bennett, S. J. and **Best, J. L.** (1995) Mean flow and turbulence structure over fixed, two-dimensional dunes: implications for sediment transport and bedform stability. *Sedimentology*, **42**, no. 3, 491–513.

Bennett, S. J. and **Best, J. L.** (1996) Mean flow and turbulence structure over fixed ripples and the ripple-dune transition, In: *Coherent Flow Structures in Open Channels* (Eds. P. J. Ashworth, S. J. Bennett, J. L. Best and S. J. McLelland), John Wiley, Hoboken, N. J., 67–125.

Best, J. L. (1992) On the entrainment of sediment and initiation of bed defects: insights from recent developments within turbulent boundary layer research. *Sedimentology*, **39**, no. 5, 797–811.

Best, J. L. (1993) On the interactions between turbulent flow structure, sediment transport and bedform development: some considerations from recent experimental research, In: *Turbulence: Perspectives on Flow and Sediment Transport* (Eds. N. Clifford, J. French and J. Hardisty), Wiley, Chichester; New York, 61–92.

Best, J. L. (2005) Kinematics, topology and significance of dune-related macroturbulence: some observations from the laboratory and field, In: *Fluvial Sedimentology VII* (Eds. M. D. Blum, S. B. Marriott and S. F. Leclair), Blackwell Pub., Malden, MA, *Special Publication Number 35 International Association of Sedimentologists*, 41–60.

Best, J. L., Buffin-Bélanger, T., Kirkbride, A. and **Reid, I.** (2001a) Visualisation of coherent flow structures associated with particle clusters: Temporal and spatial characterisation revealed using ultrasonic doppler velocity profiling, In: *Gravel-Bed Rivers 2000 CD-ROM* (Eds. T. J. Nolan and C. R. Thorne), *Special Publication of the New Zealand Hydrological Society.*

Best, J. L., Kirkbride, A. and **Peakall, J.** (2001b) Mean flow and turbulence structure in sediment-laden gravity currents: new insights using ultrasonic doppler velocity profiling, In: *Particulate Gravity Currents* (Eds. W. McCaffrey, B. Kneller and J. Peakall), *Special Publication of the International Association of Sedimentologists, 31*, 159–172.

Best, J. L. and **Kostaschuk, R.** (2002) An experimental study of turbulent flow over a low-angle dune. *Journal of Geophysical Research-Oceans*, **107**, no. C9, 3135.

Best, J. L., Kostaschuk, R. A. and **Villard, P. V.** (2001c) Quantitative visualization of flow fields associated with alluvial sand dunes: Results from the laboratory and field using ultrasonic and acoustic doppler anemometry. *Journal of Visualization*, **4**, no. 4, 373–381.

Bijker, E. (1967) Some considerations about scales for coastal models with moveable bed. Tech. Rep. 50, Delft Hydraulics Laboratory, 142 pp.

Blasius, H. (1910) Über die abhängigkeit der formen der riffeln und geschiebebänke vom gefälle. *Zeitschrift für Bauwesen*, **60**, 466–472.

Blondeaux, P. and **Vittori, G.** (1994) Wall imperfections as a triggering mechanism for Stokes-layer transition. *Journal of Fluid Mechanics*, **264**, 107–135.

Bourgeois, J. (1980) A transgressive shelf sequence exhibiting hummocky cross-stratification: the Cape Sebastian Sandstone (Upper Cretaceous), southwestern Oregon. *Journal of Sedimentary Petrology*, **50**, no. 3, 681–702.

Brenchley, P. (1985) Storm influenced sandstone beds. *Modern Geology*, **9**, 369–396.

Brevik, I. (1980) Flume experiment on waves and currents II. Smooth bed. *Coastal Engineering*, **4**, 89–110.

Brevik, I. (1981) Oscillatory rough turbulent boundary layers. *Journal of the Waterways Port Coastal and Ocean Division*, **107**, no. 3, 175–188.

Brevik, I. and **Bjørn, A.** (1979) Flume experiment on waves and currents. I. Rippled bed. *Coastal Engineering*, **3**, 149–177.

Bridge, J. S. and **Best, J. L.** (1988) Flow, sediment transport and bedform dynamics over the transition from dunes to upper-stage plane beds: implications for the formation of planar laminae. *Sedimentology*, **35**, no. 5, 753–763.

Bridge, J. S. and **Demicco, R.** (2008) *Earth Surface Processes, Landforms and Sediment Deposits*: 1. Cambridge University Press, United Kingdom, 815 pp.

Brownlie, W. R. (1981) Prediction of flow depth and sediment discharge in open channels. Ph.D. thesis, California Institute of Technology, Pasadena, California, 443 pp.

Campbell, C. V. (1966) Truncated wave-ripple laminae. *Journal of Sedimentary Research*, **36**, no. 3, 825–828.

Cantwell, B. J. (1981) Organized motion in turbulent flow. *Annual Review of Fluid Mechanics*, **13**, 457–515.

Cao, Z. (1997) Turbulent bursting-based sediment entrainment function. *Journal of Hydraulic Engineering*, **123**, no. 3, 233–236.

Carling, P. A. (1999) Subaqueous gravel dunes. *Journal of Sedimentary Research*, **69**, no. 3, 534–545.

Carstens, M. R., Neilson, F. M. and **Altinbilek, H. D.** (1969) Bed forms generated in laboratory under an oscillatory flow. Analytical and experimental study. Technical Memorandum 28, U. S. Army Corps of Engineers, Coastal Engineering Research Center, 102 pp.

Carstensen, S., Sumer, B. M. and **Fredsœ, J.** (2010) Coherent structures in wave boundary layers. part 1. oscillatory motion. *Journal of Fluid Mechanics*, **646**, 169–206.

Catano, Y. A. (2006) Burial of short cylinders induced by local scour and bedform migration under waves plus currents. Ph.D. thesis, University of Illinois at Urbana-Champaign, 211 pp.

Cheel, R. J. and **Leckie, D. A.** (1993) Hummocky cross-stratification, In: *Sedimentology review* (Ed. V. P. Wright), 1, Blackwell Publishing Ltd., Oxford, UK, 103–122.

Christensen, K. T. and **Adrian, R. J.** (2001) Statistical evidence of hairpin vortex packets in wall turbulence. *Journal of Fluid Mechanics*, **431**, 433–443.

Christoffersen, J. B. and **Jonsson, I. G.** (1985) Bed friction and dissipation in a combined current and wave motion. *Ocean Engineering*, **12**, no. 5, 387–423.

Clauser, F. H. (1956) The turbulent boundary layer, In: *Advances in Applied Mechanics* (Eds. H. L. Dryden, R. V. Mises and T. V. Karman), 4, Academic Press Inc., 1–51.

Clifton, H. E. (1976) Wave-formed sedimentary structures-a conceptual model, In: *Beach and nearshore sedimentation* (Eds. J. Davis, R. A. and R. L. Ethington), *Society of Economic Paleontologists and Mineralogists Special Publication 24*, 126–148.

Clifton, H. E. and **Dingler, J. R.** (1984) Wave-formed structures and paleoenvironmental reconstruction. *Marine Geology*, **60**, no. 1-4, 165–198.

Coleman, J. M. (1969) Brahmaputra river: Channel processes and sedimentation. *Sedimentary Geology*, **3**, no. 2-3, 129–239.

Coleman, S. E. and **Eling, B.** (2000) Sand wavelets in laminar open-channel flows. *Journal of Hydraulic Research*, **38**, no. 5, 331–338.

Coleman, S. E., Fedele, J. J. and **García, M. H.** (2003) Closed-conduit bed-form initiation and development. *Journal of Hydraulic Engineering*, **129**, 956–965.

Coleman, S. E. and **Melville, B. W.** (1996) Initiation of bed forms on a flat sand bed. *Journal of Hydraulic Engineering*, **122**, no. 6, 301–310.

Coleman, S. E. and **Nikora, V. I.** (2011) Fluvial dunes: initiation, characterization, flow structure. *Earth Surface Processes and Landforms*, **36**, no. 1, 39–57.

Coles, D. E. (1956) The law of the wake in the turbulent boundary layer. *Journal of Fluid Mechanics*, **1**, 191–226.

Collins, J. I. (1964) The effect of currents on the mass transport of progressive water waves. *Journal of Geophysical Research*, **69**, no. 6, 1051–1057.

Corea, W. C. (1978) A method for synthesizing sedimentary structures generated by migrating bedforms. Master's thesis, Massachusetts Institute of Technology, 58 pp.

Corea, W. C. (1981) Flume studies of large-scale cross-stratification produced by migrating bed forms. Ph.D. thesis, Massachusetts Institute of Technology, 181 pp.

Cummings, D. I., Dumas, S. and **Dalrymple, R. W.** (2009) Fine-grained versus coarse-grained wave ripples generated experimentally under large-scale oscillatory flow. *Journal of Sedimentary Research*, **79**, no. 2, 83–93.

Dalrymple, R. W. and **Rhodes, R. N.** (1995) Estuarine dunes and bars, In: *Geomorphology and sedimentology of estuaries* (Ed. G. M. E. Perillo), Elsevier, 359–422.

Darwin, G. M. (1884) On the formation of ripple-marks in sand. *Proceedings of the Royal Society London*, **36**, 18–43.

Davis, R. A. (1965) Underwater study of ripples, southeastern Lake Michigan. *Journal of Sedimentary Research*, **35**, no. 4, 857–866.

Deacon, G. (1894) Discussion of paper on 'Estuaries by H.L. Partiot, In: Proceedings of the Institution of Civil Engineers CXVIII, 47–189.

Devauchelle, O., Malverti, L., Lajeunesse, E., Lagrée, P., Josserand, C. and **Nguyen Thu-lam, K.** (2010) Stability of bedforms in laminar flows with free surface: From bars to ripples. *Journal of Fluid Mechanics*, **642**, 329–348.

Dinehart, R. L. (2002) Bedform movement recorded by sequential single-beam surveys in tidal rivers. *Journal of Hydrology*, **258**, 25–39.

Dingler, J. R. (1974) Wave formed ripples in nearshore sands. Ph.D. thesis, University of California at San Diego, USA., 136 pp.

Dingler, J. R. and **Inman, D. L.** (1976) Wave-formed ripples in nearshore sands, In: Proceedings of the 15th Coastal Engineering Conference, ASCE New York, 2109–2126.

Dott, R. H. and **Bourgeois, J.** (1982) Hummocky stratification: significance of its variable bedding sequences. *Bulletin of the Geological Society of America*, **93**, no. 8, 663–680.

Doucette, J. S. (2002) Geometry and grain-size sorting of ripples on low-energy sandy beaches: Field observations and model predictions. *Sedimentology*, **49**, 483–503.

Doucette, J. S. and **O'Donoghue, T.** (2006) Response of sand ripples to change in oscillatory flow. *Sedimentology*, **53**, no. 3, 581–596.

Du Buat, P. (1786) *Principes d'hydraulique*: De l'Imprimerie de Monsieur, Paris, 453 pp.

Duke, W. L. (1990) Geostrophic circulation or shallow marine turbidity currents? The dilemma of paleoflow patterns in strom-influenced prograding shoreline systems. *Journal of Sedimentary Research*, **60**, no. 6, 870–883.

Duke, W. L., Arnott, R. W. C. and **Cheel, R. J.** (1991) Shelf sandstones and hummocky cross-stratification: new insights on a stormy debate. *Geology*, **19**, no. 6, 625–628.

Dumas, S. and **Arnott, R.** (2006) Origin of hummocky and swaley cross-stratification - the controlling influence of unidirectional current strength and aggradation rate. *Geology*, **34**, no. 12, 1073–1076.

Dumas, S., Arnott, R. and **Southard, J. B.** (2005) Experiments on oscillatory-flow and combined-flow bed forms: Implications for interpreting parts of the shallow-marine sedimentary record. *Journal of Sedimentary Research*, **75**, no. 3, 501–513.

Dupré, W. R. (1984) Reconstruction of paleo-wave conditions during the late Pleistocene from marine terrace deposits, Monterey Bay, California. *Marine Geology*, **60**, no. 1-2, 435–454.

Earnshaw, H. C. and **Greated, C. A.** (1998) Dynamics of ripple bed vortices. *Experiments in Fluids*, **25**, no. 3, 265–275.

Faraci, C. and **Foti, E.** (2002) Geometry, migration and evolution of small-scale bedforms generated by regular and irregular waves. *Coastal Engineering*, **47**, no. 1, 35–52.

Faraci, C., Foti, E. and **Musumeci, R. E.** (2008) Waves plus currents at a right angle: The rippled bed case. *Journal of Geophysical Research*, **113**, C07018.

Fernandez, R., Best, J. L. and **Lopez, F.** (2006) Mean flow, turbulence structure, and bed form superimposition across the ripple-dune transition. *Water Resources Research*, **42**, W05406.

Folk, R. L. (1976) Rollers and ripples in sand, streams and sky: rhythmic alteration of transverse and longitudinal vortices in three orders. *Sedimentology*, **23**, no. 5, 649–668.

Fredsoe, J. (1984) Turbulent boundary layer in wave-current motion. *Journal of Hydraulic Engineering*, **110**, no. 8, 1103–1120.

Fredsøe, J., Andersen, K. H. and **Mutlu Sumer, B.** (1999) Wave plus current over a ripple-covered bed. *Coastal Engineering*, **38**, no. 4, 177–221.

Fredsøe, J. and **Deigaard, R.** (1992) *Mechanics of Coastal Sediment Transport*: *Advanced Series in Ocean Engineering*. World Scientific Publishing Company, 392 pp.

Gad el Hak, M. and **Bandyopadhyay, P. R.** (1994) Reynolds number effects in wall-bounded turbulent flows. *Applied Mechanics Reviews*, **47**, no. 8, 307–364.

Gallagher, E. L. (2003) A note on megaripples in the surf zone: evidence for their relation to steady flow dunes. *Marine Geology*, **193**, no. 3-4, 171–176.

García, C. M., Cantero, M. I., Jackson, P. R. and **García, M. H.** (2004) Characterization of the flow turbulence using water velocity signals recorded by Acoustic Doppler Velocimeters. Civil engineering studies, Hydraulic engineering series 75, University of Illinois at Urbana-Champaign.

García, C. M., Cantero, M. I., Niño, Y. and **García, M. H.** (2005) Turbulence measurements with acoustic doppler velocimeters. *Journal of Hydraulic Engineering*, **131**, no. 12, 1062–1073.

García, M. H. (2008) *Sedimentation engineering : processes, measurements, modeling, and practice*: American Society of Civil Engineers, Reston Va., 1132 pp.

Gee, D. (1974) Sediment transport in non-steady flow. Technical report 22-3, University of California, Hydraulic Engineering Laboratory, 93 pp.

Grant, W. D. and **Madsen, O. S.** (1979) Combined wave and current interaction with a rough bottom. *Journal of Geophysical Research*, **84**, no. C4, 1797–1808.

Grass, A. J. (1983) The influence of boundary layer turbulence on the mechanics of sediment transport, In: *Mechanics of Sediment Transport, Proc. Euromech. 156* (Eds. B. M. Sumer and A. Muller), A. A. Balkema, Rotterdam, 3–18.

Green, M., Rowley, C. and **Haller, G.** (2007) Detection of lagrangian coherent structures in three-dimensional turbulence. *Journal of Fluid Mechanics*, **572**, no. 1, 111–120.

Greenwood, B. and **Sherman, D. J.** (1986) Hummocky cross-stratification in the surf zone: flow parameters and bedding genesis. *Sedimentology*, **33**, no. 1, 33–45.

Gyr, A. and **Schmid, A.** (1997) Turbulent flows over smooth erodible sand beds in flumes. *Journal of Hydraulic Research*, **35**, no. 4, 525–544.

Haidari, A. and **Smith, C.** (1994) The generation and regeneration of single hairpin vortices. *Journal of Fluid Mechanics*, **277**, no. 1, 135–162.

Hamblin, A. P., Duke, W. L. and **Walker, R. G.** (1979) Hummocky-cross stratification: Indicator of storm-dominated shallow-marine environments. *AAPG Bulletin*, **63**, 460–461.

Harms, J. C. (1969) Hydraulic significance of some sand ripples. *Geological Society of America Bulletin*, **80**, no. 3, 363–396.

Harms, J. C., Southard, J., Spearing, D. and **Walker, R.** (1975) *Depositional environments as interpreted from primary sedimentary structures and stratification sequences*: 2. Society of Economic Paleontologists and Mineralogists, 161 pp.

Hasanat Zaman, M. and **Baddour, E.** (2011) Interaction of waves with non-colinear currents. *Ocean Engineering*, **38**, no. 4, 541–549.

Heathershaw, A. D. and **Thorne, P. D.** (1985) Sea-bed noises reveal role of turbulent bursting phenomenon in sediment transport by tidal currents. *Nature*, **316**, no. 6026, 339–342.

Héquette, A., Hemdane, Y. and **Anthony, E. J.** (2008) Sediment transport under wave and current combined flows on a tide-dominated shoreface, northern coast of France. *Marine Geology*, **249**, no. 3-4, 226–242.

Hertwig, D., Leitl, B. and **Schatzmann, M.** (2011) Organized turbulent structures - link between experimental data and LES. *Journal of Wind Engineering and Industrial Aerodynamics*, **99**, no. 4, 296–307.

Hino, M., Kashiwayanagi, M., Nakayama, A. and **Hara, T.** (1983) Experiments on the turbulence statistics and the structure of a reciprocating oscillatory flow. *Journal of Fluid Mechanics*, **131**, no. 131, 363–400.

Honji, H., Kaneko, A. and **Matsunaga, N.** (1980) Flows above oscillatory ripples. *Sedimentology*, **27**, no. 2, 225–229.

Hosmer, D. W. and **Lemeshow, S.** (2000) *Applied logistic regression*: 2nd Edition. Wiley-Interscience, 392 pp.

Howard, J. D. (1971) Comparison of the beach-to-offshore sequence in modern and ancient sediments, In: *Recent Advances in Paleoecology and Ichnology: Short Course Lecture Notes* (Eds. J. Howard, J. Valantine and J. Warme), American Geological Institute: Washington, DC., 148–183.

Howard, J. D. (1972) Trace fossils as criteria for recognizing shorelines in the stratigraphic record, In: *Recognition of Ancient Sedimentary Environments* (Eds. J. Rigby and W. Hamblin), Spec. Publ. Soc. Econ. Paleont. Miner., 215–255.

Hussain, A. K. M. F. and **Reynolds, W. C.** (1970) The mechanics of an organized wave in turbulent shear flow. *Journal of Fluid Mechanics*, **41**, no. 02, 241–258.

Ikeda, H. (1983) Experiments on bedload transport, bed forms, and sedimentary structures using fine gravel in the 4-meter-wide flume. Tech. Rep. 2, Environmental Research Center, University of Tsukuba, 72 pp.

Immenhauser, A. (2009) Estimating palaeo-water depth from the physical rock record. *Earth-Science Reviews*, **96**, no. 1-2, 107–139.

Inman, D. and **Bowen, A.** (1963) Flume experiments on sand transport by waves and currents, In: Proceedings of 18th Conference On Coastal Engineering, Mexico City, November 1962 American Society of Civil Engineers, 137–150.

Ito, M., Ishigaki, A., Nishikawa, T. and **Saito, T.** (2001) Temporal variation in the wavelength of hummocky cross-stratification: Implications for storm intensity through Mesozoic and Cenozoic. *Geology*, **29**, no. 1, 87–89.

Jackson, R. G. (1976) Sedimentological and fluid-dynamic implications of the turbulent bursting phenomenon in geophysical flows. *Journal of Fluid Mechanics*, **77**, no. 03, 531–560.

Jensen, B. L., Sumer, B. M. and **Fredsœ, J.** (1989) Turbulent oscillatory boundary layers at high reynolds numbers. *Journal of Fluid Mechanics*, **206**, 265–297.

Johns, B. (1975) The form of the velocity profile in a turbulent shear wave boundary layer. *Journal of Geophysical Research*, **80**, 5109–5112.

Johns, B. (1977) Residual flow and boundary shear stress in the turbulent bottom layer beneath waves. *Journal of Physical Oceanography*, **7**, no. 5, 733–738.

Johnson, R. W. (1998) *Handbook of Fluid Dynamics*: 1st Edition. CRC Press, 1952 pp.

Jonsson, I. G. (1966) Wave boundary layers and friction factors, In: Proceedings of 10th Conference on Coastal Engineering 1, American Society Of Civil Engineers, New York, 127–148.

Jonsson, I. G. (1980) A new approach to oscillatory rough turbulent boundary layers. *Ocean Engineering*, **7**, no. 1, 109–152.

Jopling, A. V. and **Forbes, D. L.** (1979) Flume study of silt transportation and deposition. *Geografiska Annaler. Series A, Physical Geography*, **61**, no. 1/2, 67–85.

Kajiura, K. (1968) A model of the bottom boundary layer in water waves. *Bulletin of the Earthquake Research Institute*, **46**, 75–123.

Kaneko, A. and **Honji, H.** (1979) Double structures of steady streaming in the oscillatory viscous flow over a wavy wall. *Journal of Fluid Mechanics*, **93**, no. 04, 727–736.

Kemp, P. H. and **Simons, R. R.** (1982) The interaction between waves and a turbulent current: Waves propagating with the current. *Journal of Fluid Mechanics*, **116**, 227–250.

Kemp, P. H. and **Simons, R. R.** (1983) The interaction of waves and a turbulent current: Waves propagating against the current. *Journal of Fluid Mechanics*, **130**, 73–89.

Kennedy, J. F. (1969) The formation of sediment ripples, dunes, and antidunes. *Annual Review of Fluid Mechanics*, **1**, 147–168.

Kennedy, J. F. and **Falcon, M.** (1965) Wave generated sediment ripples. Hydrodynamics Laboratory Report 86, Massachusetts Institute of Technology, 55 pp.

Kleinhans, M. G. (2001) The key role of fluvial dunes in transport and deposition of sand-gravel mixtures, a preliminary note. *Sedimentary Geology*, **143**, no. 1-2, 7–13.

Kleinhans, M. G. (2005) Phase diagrams of bed states in steady, unsteady, oscillatory and mixed flows, In: *Principles of Sedimentation and Erosion Engineering in Rivers, Estuaries and Coastal Seas* (Ed. L. van Rijn), Aqua, Blokzijl, Netherlands, Q1 Q16 .

Kline, S. J., Reynolds, W. C., Schraub, F. A. and **Runstadler, P. W.** (1967) The structure of turbulent boundary layers. *Journal of Fluid Mechanics*, **30**, no. 04, 741–773.

Komar, P. D. (1974) Oscillatory ripple marks and the evaluation of ancient wave conditions and environments. *Journal of Sedimentary Research*, **44**, no. 1, 169–180.

Komar, P. D. (1976) *Beach processes and sedimentation*: 2nd Edition. Prentice Hall, 544 pp.

Komar, P. D. and **Miller, M. C.** (1975) The initiation of oscillatory ripple marks and the development of plane-bed at high shear stresses under waves. *Journal of Sedimentary Research*, **45**, no. 3, 697–703.

Kostaschuk, R. (2000) A field study of turbulence and sediment dynamics over subaqueous dunes with flow separation. *Sedimentology*, **47**, no. 3, 519–531.

Kostaschuk, R. and **Villard, P.** (1996) Flow and sediment transport over large subaqueous dunes: Fraser River, Canada. *Sedimentology*, **43**, no. 5, 849–863.

Kraus, N., Lohnnann, A. and **Cabrera, R.** (1994) New acoustic meter for measuring 3D laboratory flows. *Journal of Hydraulic Engineering*, **120**, 406–412.

Lapointe, M. (1992) Burst-like sediment suspension events in a sand bed river. *Earth Surface Processes and Landforms*, **17**, no. 3, 253–270.

Launder, B. E. and **Spalding, D. B.** (1972) *Mathematical Models of Turbulence*: Academic Press, New York, NY, 169 pp.

Leclair, S. F. and **Bridge, J. S.** (2001) Quantitative interpretation of sedimentary structures formed by river dunes. *Journal of Sedimentary Research*, **71**, no. 5, 713–716.

Leclair, S. F., Bridge, J. S. and **Wang, F.** (1997) Preservation of cross-strata due to migration of subaqueous dunes over aggrading and non-aggrading beds: Comparison of experimental data with theory. *Geoscience Canada*, **24**, 55–66.

Leeder, M. R. (1983) On the interactions between turbulent flow, sediment transport and bedform mechanics in channelized flows, In: *Modern and Ancient Fluvial Systems* (Eds. J. Collinson and J. Lewin), Blackwell Science Ltd, *Special Publications 6 of the International Association of Sedimentologists*, 584 pp .

Lemmin, U. and **Rolland, T.** (1997) Acoustic velocity profiler for laboratory and field studies. *Journal of Hydraulic Engineering*, **123**, no. 12, 1089–1098.

Lhermitte, R. and **Lemmin, U.** (1994) Open-channel flow and turbulence measurement by high resolution doppler sonar. *Journal of Atmospheric and Oceanic Technology*, **11**, no. 5, 1295–1308.

Li, M. Z. and **Amos, C. L.** (1999a) Field observations of bedforms and sediment transport thresholds of fine sand under combined waves and currents. *Marine Geology*, **158**, no. 1-4, 147–160.

Li, M. Z. and **Amos, C. L.** (1999b) Sheet flow and large wave ripples under combined waves and currents: field observations, model predictions and effects on boundary layer dynamics. *Continental Shelf Research*, **19**, no. 5, 637–663.

Lighthill, M. J. (1954) The response of laminar skin friction and heat transfer to fluctuations in the stream velocity. *Proceedings of the Royal Society of London. Series A, Mathematical and Physical Sciences*, **224**, no. 1156, 1–23.

Liu, H. K. (1957) Mechanics of sediment-ripple formation. *Journal of the Hydraulics Division*, **83**, no. 2, 1–23.

Lodahl, C. R., Sumer, B. M. and **Fredsøe, J.** (1998) Turbulent combined oscillatory flow and current in a pipe. *Journal of Fluid Mechanics*, **373**, 313–348.

Lofquist, K. E. B. (1978) Sand ripple growth in an oscillatory-flow water tunnel. Technical paper 78-5, U.S. Army, Corps of Engineers, Coastal Engineering Research Center., 101 pp.

Longuet-Higgins, M. S. and **Stewart, R. W.** (1960) The changes in amplitude of short gravity waves on steady non-uniform currents. *Journal of Fluid Mechanics*, **10**, no. 4, 565–583.

Lopez, F. and **García, M. H.** (2001) Mean flow structure of open-channel flow through non-emergent vegetation. *Journal of Hydraulic Engineering*, **127**, 392–402.

Lu, S. S. and **Willmarth, W. W.** (1973) Measurements of the structure of the Reynolds stress in a turbulent boundary layer. *Journal of Fluid Mechanics*, **60**, no. 03, 481–511.

Madsen, O. S. and **Grant, W. D.** (1976) Quantitative description of sediment transport by waves, In: 15th International Conference on Coastal Engineering, ASCE. 2, 1093–1112.

Martin, R. L. and **Jerolmack, D. J.** (2013) Origin of hysteresis in bedform response to unsteady flows. *Water Resources Research*.

Mathisen, P. P. and **Madsen, O. S.** (1996a) Waves and currents over a fixed rippled bed 1. bottom roughness experienced by waves in the presence and absence of currents. *Journal of Geophysical Research*, **101**, no. C7, 16533–16542.

Mathisen, P. P. and **Madsen, O. S.** (1996b) Waves and currents over a fixed rippled bed 2. bottom and apparent roughness experienced by currents in the presence of waves. *Journal of Geophysical Research*, **101**, no. C7, 16543–16550.

Mathisen, P. P. and **Madsen, O. S.** (1999) Waves and currents over a fixed rippled bed 3. bottom and apparent roughness for spectral waves and currents. *Journal of Geophysical Research*, **104**, no. C8, 18447–18461.

McLean, S. R., Ribberink, J. S., Dohmen-Janssen, C. M. and **Hassan, W. N.** (2001) Sand transport in oscillatory sheet flow with mean current. *Journal of Waterway, Port, Coastal, and Ocean Engineering*, **127**, 141–151.

McLelland, S. J. and **Nicholas, A. P.** (2000) A new method for evaluating errors in high-frequency ADV measurements. *Hydrological Processes*, **14**, 351–366.

Met-Flow (2002) *UVP Monitor Users Guide*. Met-Flow SA, Lausanne, Switzerland.

Meyer-Peter, E. and **Müller, R.** (1948) Formulas for bed-load transport, In: Proceedings of the 2nd International IAHR Congress, Stockholm, Sweden 39–64.

Miche, M. (1951) Le pouvoir réfléchissant des ouvrages maritimes exposés à l'action de la houle. *Annals des Ponts et Chaussess*, **121**, 285 – 319.

Mogridge, G. R. and **Kamphuis, J.** (1972) Experiments on bed form generation by wave action, In: Proceedings of the 13th Coastal Engineering Conference, Vancouver 1123–1142.

Mulder, T., Razin, P. and **Faugeres, J. C.** (2009) Hummocky cross-stratification-like structures in deep-sea turbidites: Upper Cretaceous Basque basins (Western Pyrenees, France). *Sedimentology*, **56**, no. 4, 997–1015.

Myrhaug, D., Holmedal, L. E., Simons, R. R. and **MacIver, R. D.** (2001) Bottom friction in random waves plus current flow. *Coastal Engineering*, **43**, no. 2, 75–92.

Myrow, P. M., Fischer, W. and **Goodge, J. W.** (2002) Wave-modified turbidites: combined-flow shoreline and shelf deposits, Cambrian, Antarctica. *Journal of Sedimentary Research*, **72**, no. 5, 641–641.

Myrow, P. M. and **Southard, J. B.** (1991) Combined-flow model for vertical stratification sequences in shallow marine storm-deposited beds. *Journal of Sedimentary Research*, **61**, no. 2, 202–202.

Newton, S. I. (1687) *The mathematical principles of natural philosophy*: Oxford University, 320 pp.

Nezu, I. and **Nakagawa, H.** (1993) *Turbulence in Open-Channel Flows*: Balkema, 286 pp.

Nezu, I. and **Rodi, W.** (1986) Open-channel flow measurements with a laser doppler anemometer. *Journal of Hydraulic Engineering*, **112**, no. 5, 335–355.

Niño, Y., Lopez, F. and **García, M.** (2003) Threshold for particle entrainment into suspension. *Sedimentology*, **50**, no. 2, 247–263.

Nielsen, P. (1979) Some basic concepts of wave sediment transport. Series paper 20, Inst. Hydrodynamics and Hydraulic Engineering (ISVA), Technical University of Denmark, 160 pp.

Nielsen, P. (1981) Dynamics and geometry of wave-generated ripples. *Journal of Geophysical Research*, **86**, no. 7, 6467–6472.

Nikora, V. and **Goring, D.** (1998) Adv measurements of turbulence: Can we improve their interpretation? *Journal of hydraulic engineering*, **124**, no. 6, 630–634.

O'Donoghue, T. and **Clubb, G. S.** (2001) Sand ripples generated by regular oscillatory flow. *Coastal Engineering 44*, **44**, 101–115.

O'Donoghue, T., Doucette, J., van der Werf, J. and **Ribberink, J.** (2006) The dimensions of sand ripples in full-scale oscillatory flows. *Coastal Engineering*, **53**, no. 12, 997–1012.

Ojha, S. P. and **Mazumder, B. S.** (2010) Turbulence characteristics of flow over a series of 2D bed forms in the presence of surface waves. *Journal of Geophysical Research*, **115**, no. F04016, 15.

Olabarrieta, M., Warner, J. C. and **Kumar, N.** (2011) Wave-current interaction in Willapa Bay. *Journal of geophysical research*, **116**, no. C12014, 27.

Oost, A. P. and **Baas, J. H.** (1994) The development of small scale bedforms in tidal environments: an empirical model for unsteady flow and its applications. *Sedimentology*, **41**, no. 5, 883–903.

Paola, C. and **Borgman, L.** (1991) Reconstructing random topography from preserved stratification. *Sedimentology*, **38**, no. 4, 553–565.

Passchier, S. and **Kleinhans, M. G.** (2005) Observations of sand waves, megaripples, and hummocks in the dutch coastal area and their relation to currents and combined flow conditions. *Journal of Geophysical Research*, **110**, no. F4, 1–15.

Pedocchi, F. (2009) Bed morphology and sediment transport under oscillatory flow. Ph.D. thesis, University of Illinois at Urbana-Champaign, 177 pp.

Pedocchi, F. and **García, M. H.** (2009a) Friction coefficient for oscillatory flow: The rough-smooth turbulent transition. *Journal of Hydraulic Research*, **47**, no. 4, 438–444.

Pedocchi, F. and **García, M. H.** (2009b) Ripple morphology under oscillatory flow: 1. prediction. *Journal of Geophysical Research*, **144**, C12014.

Pedocchi, F. and **García, M. H.** (2009c) Ripple morphology under oscillatory flow: 2. experiments. *Journal of Geophysical Research*, **114**, C12015.

Pedocchi, F. and **García, M. H.** (2012) Acoustic measurement of suspended sediment concentration profiles in an oscillatory boundary layer. *Continental Shelf Research*, **46**, 87–95.

Peregrine, D. (1976) Interaction of water waves and currents, In: *Advances in Applied Mechanics* (Ed. C.-S. Yih), 16, Elsevier, 9–117.

Perillo, M. M., Pedocchi, F., Best, J. L. and **García, M. H.** (2009) Exploratory experiments on ripple morphology under combined flows, In: *6th IAHR Symposium on River, Coastal and Estuarine Morphodynamics (RCEM 2009)* (Eds. C. A. Vionnet, M. H. García, E. M. Latrubesse and G. M. E. Perillo), 2, Taylor and Francis Group, London, Enschede, The Netherlands, 793–798.

Prandtl, L. (1904) über flüssigkeitsbewegung bei sehr kleiner reibung, In: Verhandlungen des dritten Internationalen mathematikerkongresses in Heidelberg .

Prandtl, L. (1925) Bericht über untersuchungen zur ausgebildeten turbulenz. *Zeitschrift für angewandte Mathematik und Mechanik*, **5**, no. 2, 136–139.

Prave, A. R. and **Duke, W. L.** (1990) Small-scale hummocky cross-stratification in turbidites: a form of antidune stratification? *Sedimentology*, **37**, no. 3, 531–539.

Prins, A. and **de Vries, M.** (1971) *On dominant discharge concepts for rivers*: Technische Hogeschool Delft, Waterloopkundig Laboratorium, Delft, Netherlands, 22 pp.

Raudkivi, A. J. (1963) Study of sediment ripple formation. *Journal of the Hydraulics Division*, **89**, no. HY6, 15–33.

Raudkivi, A. J. (1997) Ripples on stream bed. *Journal of Hydraulic Engineering*, **123**, no. 1, 58–64.

Reesink, A. J. and **Bridge, J.** (2009) Influence of bedform superimposition and flow unsteadiness on the formation of cross strata in dunes and unit bars part 2, further experiments. *Sedimentary Geology*, **222**, no. 3-4, 274–300.

Reynolds, O. (1883) An experimental investigation of the circumstances which determine whether the motion of water shall be direct or sinuous, and of the law of resistance in parallel channels. *Proceedings of the Royal Society A: Mathematical, Physical and Engineering Sciences*, **35**, 84–99.

Ribberink, J. and **Al-Salem, A.** (1994) Sediment transport in oscillatory boundary layers in cases of rippled beds and sheet flow. *Journal of Geophysical Research*, **99**, no. C6, 12707 12727.

Richards, K. J. (1980) The formation of ripples and dunes on an erodible bed. *Journal of Fluid Mechanics*, **99**, no. 03, 597–618.

Robinson, S. K. (1991) Coherent motions in the turbulent boundary layer. *Annual Review of Fluid Mechanics*, **23**, 601–639.

Rubin, D. M. and **Hunter, R. E.** (1982) Bedform climbing in theory and nature. *Sedimentology*, **29**, no. 1, 121–138.

Sato, S. (1987) Oscillatory boundary layer flow and sand movement over ripples. Ph.D. thesis, University of Tokyo, Japan, 135 pp.

Saunderson, H. C. and **Lockett, F. P. J.** (1983) Flume experiments on bedforms and structures at the dune-bed transition, In: *Modern and Ancient Fluvial Systems* (Eds. J. Collinson and J. Lewin), Blackwell Science Ltd, *Special Publications 6 of the International Association of Sedimentologists*, 584 pp. .

Schlichting, H. (1979) *Boundary-layer theory*: McGraw-Hill, New York, 817 pp.

Sekiguchi, T. and **Sunamura, T.** (2004) Effects of bed perturbation and velocity asymmetry on ripple initiation: wave-flume experiments. *Coastal Engineering*, **50**, no. 4, 231–239.

Sekiguchi, T. and **Yokokawa, M.** (2008) Effect of wave period on combined-flow bedforms: a flume experiment, In: Marine Sandwave and River Dune Dynamics 281–284.

Sequeiros, O. E. (2008) Bedload transport, self acceleration, downstream sorting, and flow dynamics of turbidity currents. Ph.D. thesis, University of Illinois at Urbana-Champaign, 190 pp.

Shields, A. (1936) *Anwendung der Aehnlichkeitsmechanik und der Turbulenzforschung auf die Geschiebebewegung.* 26. Mitteilungen der Preußischen Versuchsanstalt fr Wasserbau, Berlin: Preuischen Versuchsanstalt fr Wasserbau., 1-26 pp.

Simons, D. B., Richardson, E. V. and **Nordin Jr, C. F.** (1965) Bedload equation for ripples and dunes. Tech. rep., US Geological Survey, 9 pp.

Sleath, J. (1984) *Sea Bed Mechanics*: John Wiley & Sons Inc, USA, 335 pp.

Sleath, J. F. (1991) Velocities and shear stresses in wave-current flows. *Journal of Geophysical Research*, **96**, no. C8, 15237–15244.

Sleath, J. F. A. (1987) Turbulent oscillatory flow over rough beds. *Journal of Fluid Mechanics*, **182**, no. -1, 369–409.

Smith, G. J. and **Jacobi, R. D.** (2001) Tectonic and eustatic signals in the sequence stratigraphy of the Upper Devonian Canadaway Group, New York State. *AAPG Bulletin*, **85**, no. 2, 325–357.

Smits, A. J., McKeon, B. J. and **Marusic, I.** (2011) Highreynolds number wall turbulence. *Annual Review of Fluid Mechanics*, **43**, 353–375.

Sommer, H. J. (2008) polygeom.m. MATLAB Central File Exchange, Retrieved April 26, 2011. URL `http://www.mathworks.com/matlabcentral/fileexchange/319-polygeom-m`

Sontek (2011) ADV Beam Geometry.
URL `http://www.sontek.com/xmedia/products/adv-beam-geometry_001.gif`

Soulsby, R. L. (1980) Selecting record length and digitization rate for near-bed turbulence measurements. *Journal of Physical Oceanography*, **10**, no. 2, 208–219.

Soulsby, R. L. (1997) *Dynamics of marine sands : a manual for practical applications*: Telford, London, 249 pp.

Soulsby, R. L. and **Clarke, S.** (2005) Bed shear-stresses under combined waves and currents on smooth and rough beds. Tech. Rep. TR 137, HR Wallingford.

Soulsby, R. L., Hamm, L., Klopman, G., Myrhaug, D., Simons, R. and **Thomas, G.** (1993) Wave-current interaction within and outside the bottom boundary layer. *Coastal Engineering*, **21**, no. 1-3, 41–69.

Southard, J. B. (1991) Experimental determination of bed-form stability. *Annual Review of Earth and Planetary Sciences*, **19**, no. 1, 423–455.

Southard, J. B. and **Boguchwal, L. A.** (1990) Bed configurations in steady unidirectional water flows; part 2, synthesis of flume data. *Journal of Sedimentary Research*, **60**, no. 5, 658–679.

Southard, J. B. and **Dingler, J. R.** (1971) Flume study of ripple propagation behind mounds on flat sand beds. *Sedimentology*, **16**, no. 3–4, 251–263.

Southard, J. B., Lambie, J. M., Federico, D. C., Pile, H. T. and **Weidman, C. R.** (1990) Experiments on bed configurations in fine sands under bidirectional purely oscillatory flow, and the origin of hummocky cross-stratification. *Journal of Sedimentary Research*, **60**, no. 1, 1–17.

Stokes, W. L. (1950) Some unusual ripple marks from the Triassic of Utah. *The Journal of Geology*, **58**, no. 2, 153–155.

Sutherland, A. J. and **Hwang, L. S.** (1965) A study of dune geometry and dune growth on a sand bed. Technical Memorandum 65-5, W.M. Keck Laboratory of Hydraulics and Water Resources, Division of Engineering and Applied Science, California Institute of Technology., Pasadena, CA.

Swift, D., Hudelson, P., Brenner, R. and **Thompson, P.** (1987) Shelf construction in a foreland basin: storm beds, shelf sandstones, and shelf-slope depositional sequences in the Upper Cretaceous Mesaverde Group, Book Cliffs, Utah. *Sedimentology*, **34**, 423–457.

Swift, D. J. P., Figueiredo, A. G., Freeland, G. L. and **Oertel, G. F.** (1983) Hummocky cross-stratification and megaripples; a geological double standard? *Journal of Sedimentary Research*, **53**, no. 4, 1295–1317.

Takeda, Y. (1991) Development of an ultrasound velocity profile monitor. *Nuclear Eng. and Design*, **126**, 277–284.

Takeda, Y., Fischer, W. E. and **Sakakibara, J.** (1994) Decomposition of the modulated waves in a rotating couette system. *Science*, **263**, 502–505.

Tanner, W. F. (1964) Eolian ripple marks in sandstone. *Journal of Sedimentary Research*, **34**, no. 2, 432–433.

Tanner, W. F. (1965) High-index ripple marks in the swash zone. *Journal of Sedimentary Research*, **35**, no. 4, 968.

Tanner, W. F. (1967) Ripple mark indices and their uses. *Sedimentology*, **9**, no. 2, 89–104.

Theodorsen, T. (1952) Mechanism of turbulence, In: Proceedings of the Second Midwestern Conference on Fluid Mechanics: 1719 March Ohio State University, Columbus, OH,.

Thorne, P. D., Williams, J. J. and **Davies, A. G.** (2002) Suspended sediments under waves measured in a large-scale flume facility. *Journal of Geophysical Research*, **107**, no. C8, 3178.

Tillman, R. (1985) A spectrum of shelf sands and sandstones, In: *Shelf Sands and Sandstones* (Eds. D. Swift, R. Walker and R. Tillman), Society of Economic Paleontologists and Mineralogists (SEPM), *SEPM Short Courses, Vol 13*, 1–46.

Tinterri, R. (2011) Combined flow sedimentary structures and the generic link between sigmoidal- and hummocky-cross stratification. *GeoActa, Bologna*, **10**, 1–43.

Traykovski, P., Hay, A., Irish, J. and **Lynch, J.** (1999) Geometry, migration, and evolution of wave orbital ripples at leo-15. *Journal of Geophysical Research*, **104**, no. C1, 1505 1524.

Tropea, C. (1983) A note concerning the use of a one-component lda to measure shear stress terms. *Experiments in Fluids*, **1**, no. 4, 209–210.

Uchiyama, Y., McWilliams, J. C. and **Restrepo, J. M.** (2009) Wave-current interaction in nearshore shear instability analyzed with a vortex force formalism. *Journal of Geophysical Research*, **114**, no. C06021, 15.

van der Mark, C. and **Blom, A.** (2007) A new and widely applicable bedform tracking tool. CE&M Research Report 2007R-003/WEM-002., Faculty of Engineering Technology, University of Twente.

van Rijn, L. C. (1982) Equivalent roughness of alluvial bed. *Journal of the Hydraulics Division*, **118**, no. 10, 1215–1218.

van Rijn, L. C. (1984a) Sediment transport, part i: Bed load transport. *Journal of Hydraulic Engineering*, **110**, no. 10, 1431–1456.

van Rijn, L. C. (1984b) Sediment transport, part iii: Alluvial roughness. *Journal of Hydraulic Engineering*, **110**, no. 12, 1733–1754.

van Rijn, L. C. (1986) *Manual sediment transport measurements*. Delft Hydraulics Laboratory, Delft, The Netherlands.

van Rijn, L. C. (2006) *Principles of sediment transport in rivers, estuaries and coastal seas*: Aqua Publications, Amsterdam, 690 pp.

Vanoni, V. A. (2006) *Sedimentation Engineering*: American Society of Civil Engineers Publications, 432 pp.

Venditti, J. G., Church, M. A. and **Bennett, S. J.** (2005a) Bed form initiation from a flat sand bed. *Journal of Geophysical Research*, **110**, F01009.

Venditti, J. G., Church, M. A. and **Bennett, S. J.** (2005b) On the transition between 2D and 3D dunes. *Sedimentology*, **52**, no. 6, 1343–1360.

Venditti, J. G., Church, M. A. and **Bennett, S. J.** (2006) On interfacial instability as a cause of transverse subcritical bed forms. *Water Resources Research*, **42**, W07423.

von Kármán, T. (1930) Mechanische Ähnlichkeit und turbulenz. *Nachrichten von der Gesellschaft der Wissenschaften zu Gttingen, Fachgruppe 1 (Mathematik)*, **5**, 58–76.

Vongvisessomjai, S. (1984) Oscillatory ripple geometry. *Journal of Hydraulic Engineering*, **110**, 247–266.

Voulgaris, G. and **Trowbridge, J.** (1998) Evaluation of the acoustic doppler velocimeter (adv) for turbulence measurements. *Journal of Atmospheric and Oceanic Technology*, **15**, 272–288.

Wiberg, P. L. and **Harris, C. K.** (1994) Ripple geometry in wave-dominated environments. *Journal of Geophysical Research-Oceans*, **99**, no. C1, 775789.

Williams, J. (1996) Turbulent flow in rivers, In: *Advances in Fluvial Dynamics and Stratigraphy* (Eds. P. A. Carling and M. R. Dawson), Wiley, 1–32.

Williams, P. B. and **Kemp, P. H.** (1971) Initiation of ripples on flat sediment beds. *Journal of the Hydraulics Division*, **97**, no. 6, 505–522.

Willis, A. and **Kerswell, R.** (2008) Coherent structures in localized and global pipe turbulence. *Physical review letters*, **100**, no. 12, 1–4.

Willmarth, W. W. and **Lu, S. S.** (1972) Structure of the reynolds stress near the wall. *Journal of Fluid Mechanics*, **55**, no. 01, 65–92.

Xu, J. (2005) Observations of plan-view sand ripple behavior and spectral wave climate on the inner shelf of San Pedro Bay, California. *Continental Shelf Research*, **25**, no. 3, 375–396.

Yalin, M. (1992) *River Mechanics*: 1st Edition. Pergamon Press Ltd., 235 pp.

Yalin, M. and **Karahan, E.** (1979) On the geometry of ripples due to waves, In: Proceedings of the Coastal Engineering Conference 2, 1776–1786.

Yalin, M. S. (1964) Geometrical properties of sand waves. *Journal of the Hydraulics Division*, **90**, 105–119.

Yalin, S. and **Russell, R. C. H.** (1962) Similarity in sediment transport due to waves, In: In Proceedings of the 8th Coastal Engineering Conference, Mexico City 1123–1142.

Yamaguchi, N. and **Sekiguchi, H.** (2010) Effects of settling and preferential deposition of sediment on ripple roundness under shoaling waves. *Journal of Sedimentary Research*, **80**, no. 9, 781–790.

Yokokawa, M. (1995) Combined-flow ripples: genetic experiments and applications for geologic records. *Earth and Planetary Sciences, Memoirs, Series D*, **29**, 1–38.

Yokokawa, M., Masuda, F. and **Endo, N.** (1995) Sand particle movement on migrating combined-flow ripples. *Journal of Sedimentary Research*, **65**, no. 1, 40–44.

Zhou, J., Adrian, R., Balachandar, S. and **Kendall, T.** (1999) Mechanisms for generating coherent packets of hairpin vortices in channel flow. *Journal of Fluid Mechanics*, **387**, no. 1, 353–396.